Synthesis of M/Fe/S Clusters Relevant to Biological Systems and Minerals.

by

Charalampos Kalyvas

A dissertation submitted in partial fulfillment
of the requirements for the degree of
Doctor of Philosophy
(Chemistry)
In The University of Michigan
2008

Doctoral Committee

Professor Dimitri N. Coucouvanis. Chair
Professor Vincent L. Pecoraro
Professor David P. Ballou
Assistant Professor Hashim M. Al-Hashimi

Dedication

To my family and friends

Acknowledgements

I would like to thank my advisor, Professor Dimitri Coucouvanis for his support and guidance throughout the years, and for the vast amount of knowledge I obtained by working in his group. Also I would like to thank the members of my committee, for their valuable input and guidance that expanded the perspective of this work even further and Dr. Jeff Kampf and Dr. Yiannis Sanakis for their hard work in obtaining experimental data and valuable discussions.

A special thanks goes to all the people, post-docs, graduate and undergraduate students, that I had the opportunity to work with in the lab, for their help and support either through direct work or through the valuable discussions and exchange of ideas, and above all the pleasant environment that they created.

Finally, nothing of this would be possible without the support of my family and my friends, through the good and bad times, that helped me keep a balance. Thank you.

Table of Contents

List of Figures

List of Tables

List of Appendices

Abstract

The synthesis and characterization of three series of iron sulfur clusters is presented with relevance to biological systems and minerals. The synthesis, crystallographic structures and reactivity of these clusters is presented along with preliminary spectroscopic characterization including magnetic susceptibility measurements, cyclic voltammetry, infra-red and Mössbauer spectroscopy. The first series of compounds includes iron sulfur nitrosyl clusters with tetra-, hexa-, and octanuclear core structures. The interconversions between these three cores and their reactivity are presented. Comparative spectroscopic characterization provides experimental evidence supporting that the best description for iron-bound nitric oxide is NO^-. These clusters can serve as model compounds that can help to elucidate the interactions of nitric oxide with iron sulfur proteins in biological systems. The second series of compounds includes heterometalic iron sulfur chloride clusters containing a pentlandite like M_8S_6 core, with the heterometal being nickel, copper or cobalt. The clusters presented provides several new complexes that can serve as structural and electronic models for the natural occurring pentlandites, and the systematic synthesis provides a methodology for the expansion of the M_8S_6 core to additional metals. The third series includes metal iron sulfur nitrosyl clusters containing a pentlandite like M_8S_6 core, with the metal being molybdenum, nickel, cobalt. Both chloro and nitrosyl clusters are compared in terms of synthesis and electronic properties, and the possibility of these clusters to serve as potential building blocks for extended networks that could serve as multi-electron heterogeneous catalysts is discussed.

Chapter 1
Introduction

1.1. Background

The field of inorganic chemistry, as the term suggests, traditionally has been linked to the study of metals, elements that were not considered to participate in living systems. At that time living systems were believed to consist of carbon, hydrogen, nitrogen, oxygen, phosphorus and sulfur. As science advanced, several metals were found to be essential to living systems, but the real interest of inorganic chemists in biological systems came with the discovery in recent decades of metalloenzymes that are recognized as extremely significant components of biological processes. This enabled the use of several concepts of coordination chemistry, spectroscopy and synthetic inorganic chemistry to become integral part in the arsenal used to understand biological processes.

Presently there are eleven elements recognized to be required for all forms of life (H, C, N, O, Na, Mg, P, S, Cl, K, Ca), an additional thirteen elements essential for most living forms (B, F, Si, V, Cr, Mn, Fe, Co, Ni, Cu, Zn, Se, Mo, I), and seven elements that are required for some species (As, Br, Sr, Cd, Sn, Ba, W). For humans, the essential elements are from the first two categories with the exception of silicon and boron.[1]

Transition metals in particular are important for nearly all biological processes including lewis acid base catalysis, electron transfer, functional group transfer, redox catalysis, energy storage and biomineralization.

1.1.1 Abundance of the elements and bioavailability.

In the universe, hydrogen and helium are the most abundant elements, followed by oxygen, carbon, nitrogen, neon and iron [2]. The first six are gases, making iron the most abundant heavier element. As the solar systems formed, the heavier atoms aggregated to form rocky planets while the lighter atoms formed gaseous planets. Since earth is a rocky planet, iron is consequently the most abundant element on Earth. While the earth's core is believed to consist largely of an iron-nickel alloy constituting 35% of the mass of the Earth as a whole, iron makes up only about 5% of the Earth's uppermost layer, the crust.

The abundance of elements on earth and its crust crust can be used as a measure of elemental availability for biological systems. However, the abundance alone is not a sufficient criterion for the utilization of an element; abundance has to be combined with chemical availability of an element in solid or soluble forms, from which organisms can effectively acquire the element. In this respect, the abundance of elements in the aqueous phases of earth is particularly relevant to the biological use of elements on earth.

As seen from the abundance graphs (Figures 1.1 and 1.2) [2], although first row transition metals are abundant on the earths crust, in the oceans their availability is limited, with the only notable exception being molybdenum that forms soluble ions and is the most abundant transition metal in the oceans, nevertheless, still in nanomolar concentrations. This correlates with the fact that molybdenum and tungsten are the only second and third row transition elements that have known biological functions. Besides the abundance and availability however, a chemical element must be exploitable by organisms for their metabolic functions and survival, and therefore elements such as lithium or aluminum although relatively abundant and available, are not used in biological processes.

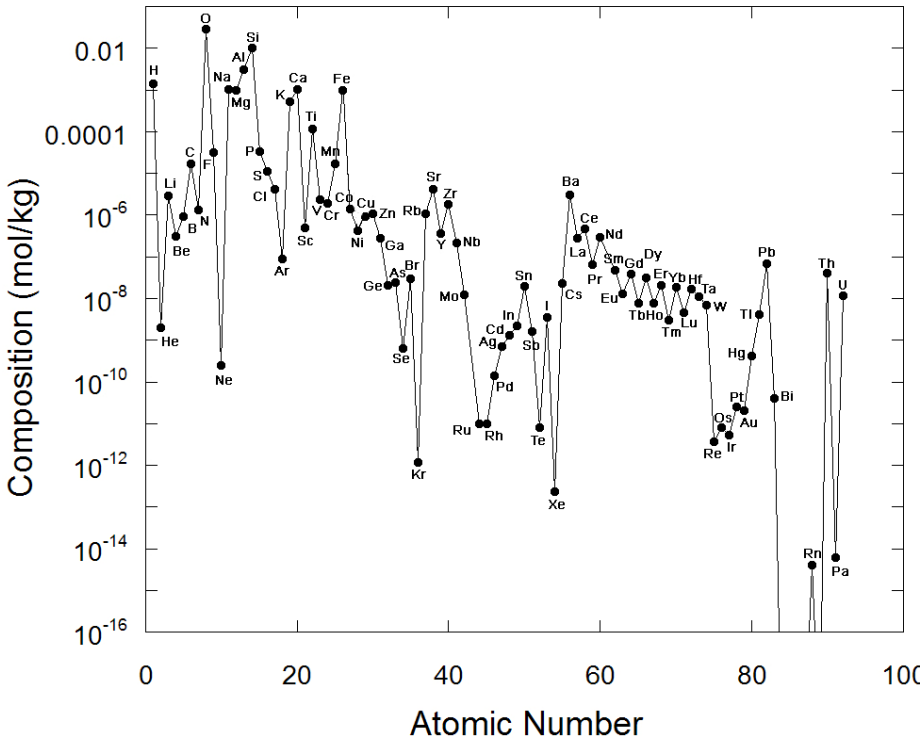

Figure 1.1. The abundance of elements in the Earth's crust shown on logarithmic scale. The concentration values are obtained from reference [2].

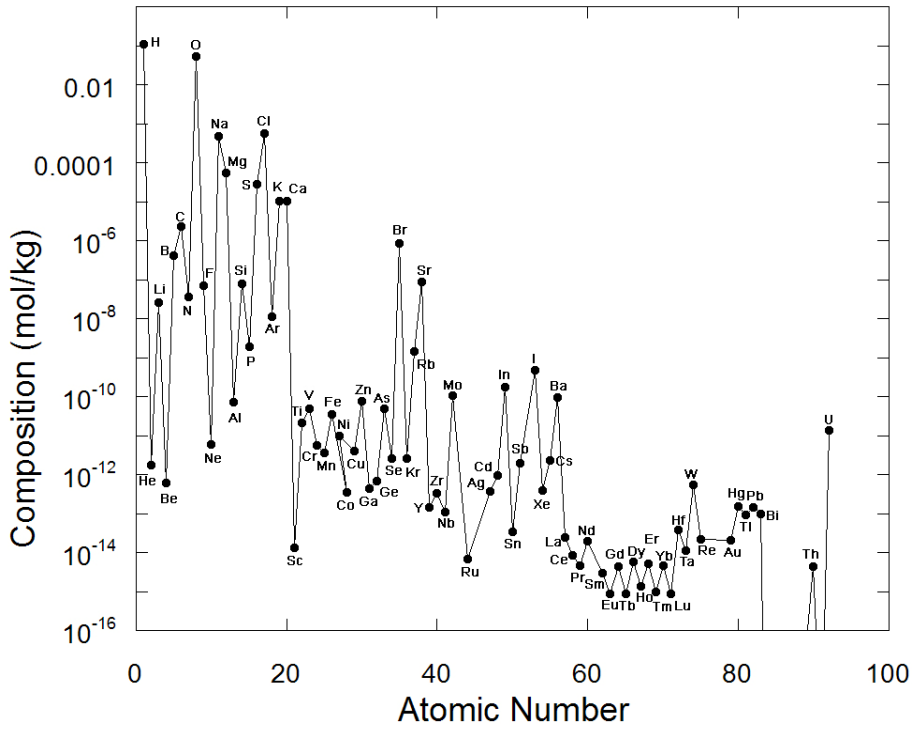

Figure 1.2. The abundance of elements in the Oceans shown on logarithmic scale. The concentration values are obtained from reference [2].

1.1.2 Metalloenzymes

The essential metal ions, when associated with polypeptides or ribonucleotides, can help catalyze a huge variety of unique chemical reactions and perform specific physiological functions, whereas proteins or ribonucleotides alone are not sufficient to perform all the reactions needed for life. The metals used for these purposes are called metal cofactors, and besides being used as catalytic centers, they can also serve as structural factors enabling specific conformations and folding in proteins necessary for their proper function. These metals are bound to the protein through atoms containing lone pairs, typically N, O and S found in the side chains of aminoacids although in some instances backbone oxygen or nitrogen atoms are used as well. The most common donor atoms for metals in proteins are sulfur of cysteines and methionines, nitrogen atoms of histidines and oxygen atoms of glutamates, aspartates and tyrosinates. Cysteine, histidine, aspartate and glutamate can serve also as bridging ligands between two metals.

Although metal ions can provide considerable versatility, the simple coordination to the various donor atoms from protein residues is not sufficient for all the biological requirements. Therefore, besides directly incorporating single metal ions in proteins, nature through evolution, has selected other inorganic or organic ligands for metal centers. The two most common constructs of non-protein origin are iron sulfur proteins and tetrapyrroles (including hemes, chlorophylls and corrins). These prosthetic groups are mainly used for electron transfer as their redox potentials can be tuned over large ranges. It should be noted that once nature learned to produce a specific cofactor, the same cofactor is utilized for as many purposes as possible. Therefore, hemes are found as carriers and activators of oxygen, and iron sulfur clusters in regulatory proteins that are used to interact with RNA and DNA, for redox sensing, and in dehydration reactions.

There are also additional cofactors used for specific reactions, especially for small molecule activation, including interesting metal clusters [3] such as the FeMo cofactor of nitrogenase, consisting of a (homocitrate)$MoFe_7S_9X$ (X=O or N) cluster [4], that is used for the reduction of dinitrogen to ammonia, the H-center of hydrogenases, consisting of a $[Fe_4S_4]$-SCys-$Fe_2(dtn)(CO)_2(CN)_2$ (dtn = di(thiomethyl)amine) or a $Ni(SCys)_2Fe(CN)_2(CO)$ cluster, that is used for the reversible reduction of protons to dihydrogen [5], and the Mn Cluster of Photosystem II, consisting of a Mn-Mn_3CaO_4 cluster [6, 7], that is used for the oxidation of water to dioxygen.

1.2 Iron Sulfur Clusters in biological systems

Iron Sulfur clusters are one of the most ubiquitous and functionally versatile prosthetic groups of proteins in nature [8-11]. There are more than 120 distinct types of enzymes and proteins known to contain iron sulfur clusters, reflecting the chemical versatility of both iron and sulfur. As it will be discussed, along with the availability of iron sulfur clusters in nature, these enzymes are believed to be evolutionary ancient prosthetic groups fundamental for life processes [12], especially in times where the oxygen levels on earth were in much lower levels than today.

1.2.1 Iron Sulfur Clusters and the Origins of Life

There are several theories involving the origin of life with the “RNA world” theory [13-16] being the most prominent and widely accepted. In the early 1990’s however, another theory emerged, based on the presence of iron sulfur compounds both in minerals and in biological systems, that lead to the “iron-sulfur world” theory [17-19]. According to this theory, the origins of early life occurred not in bulk solution in the oceans, but on

mineral surfaces (e.g. iron pyrites) near deep hydrothermal vents in the ocean, the so called “Black Smokers”. Although this theory is not without serious dispute [20, 21], it provides an attractive explanation for the large usage of iron sulfur clusters as prosthetic groups in a plethora of enzymes.

Physical compartmentation from the environment and self-organization of self-contained redox reactions are the most conserved attributes of living things; hence inorganic matter with such attributes would be life’s most likely forebear. The proposal is that life evolved in structured iron monosulfide precipitates in a seepage site of a hydrothermal mound at a redox, pH and temperature gradient between sulfide-rich hydrothermal fluid and iron(II)-containing waters of the Hadean ocean floor. The naturally arising, three-dimensional compartmentation observed within fossilized seepage-site metal sulfide precipitates indicates that these inorganic compartments were the precursors of cell walls and membranes found in free-living prokaryotes. The known capability of FeS and NiS to catalyze the synthesis of acetyl-methylsulfide from carbon monoxide and methylsulfide, constituents of hydrothermal fluid, indicates that pre-biotic syntheses occurred at the inner surfaces of these metal-sulfide-walled compartments. Furthermore this restrained reacted products from diffusing into the ocean, and thus provided sufficient concentrations of reactants to forge the transition from geochemistry to biochemistry. The chemistry of what is known as the RNA-world could have taken place within these naturally forming, catalytic-walled compartments to give rise to replicating systems. Sufficient concentrations of precursors to support replication would have been synthesized in situ geochemically and biogeochemically, with FeS (and NiS) centers playing the central catalytic role [22-24]. An illustration of the processes described can be seen in Figure 1.3.

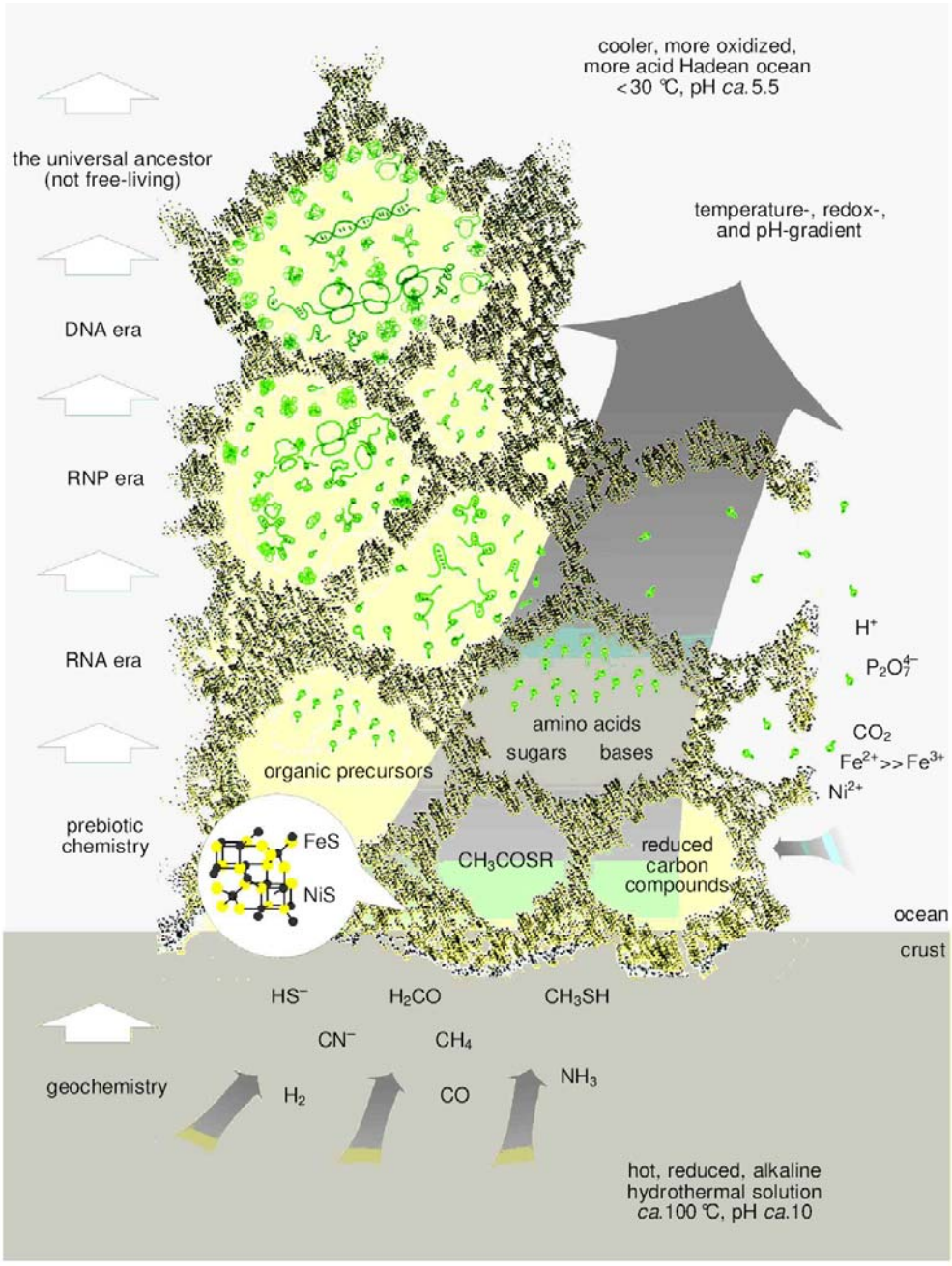

Figure 1.3. A model for the origin of life at a redox, pH and temperature gradient at a submarine hydrothermal vent. Figure taken from reference 23

1.2.2 Iron Sulfur Proteins

1.2.2.1. Structure

Iron sulfur clusters are most commonly found in three distinct forms and are widely used throughout biological systems. These forms are the [2Fe-2S], [3Fe-4S] and [4Fe-4S] clusters (Figure 1.2). These three clusters, along with Rubredoxins that contain a single iron tetrahedrally coordinated to four cysteine ligands, are the metal centers of the iron sulfur proteins. The [2Fe-2S] is a dimer with the two irons bridged by μ_2-S atoms, the [4Fe-4S] is a cubane like cluster with the four irons bridged by μ_3-S atoms and the [3Fe-4S] cluster can be viewed as a cubane in which one iron is missing. In all the cases, the iron atoms are four coordinated with the coordination sphere being completed generally by cysteines, although occasionally histidine, serine, or backbone amide ligation at a single iron atom is observed. However, there are also enzymes containing larger and more complex iron sulfur clusters (Figure 1.4), such as in nitrogenase that contains a [8Fe-7S] (P-Cluster) and a [Mo-7Fe-9S] (FeMoco) cluster, carbon monoxide dehydrogenase containing a [Ni-4Fe-5S] cluster. In addition, there are enzymes in which a [4Fe-4S] cluster is bridged directly via a cysteine ligand to another metallic center, such as in the cases of iron only hydrogenase Fe_4S_4-SCys-$Fe_2(dtn)(CO)_2(CN)_2$, in sulfite reductase which the [4Fe-4S] cluster is bound to a heme and in acetyl-coenzyme A synthase with a [2Ni-4Fe-4S] core.

In terms of binding to the protein, the cysteine ligand (or ligands) completes the tetrahedral coordination environment of the iron in iron sulfur proteins. And in general, the Cys-X-X-Cys motif is fairly reserved in the sequence of the proteins. Although there are seemingly no particular stereochemical requirements for the number of X residues

being two, interestingly, it is very similar to the zinc binding domain of zinc finger proteins [25].

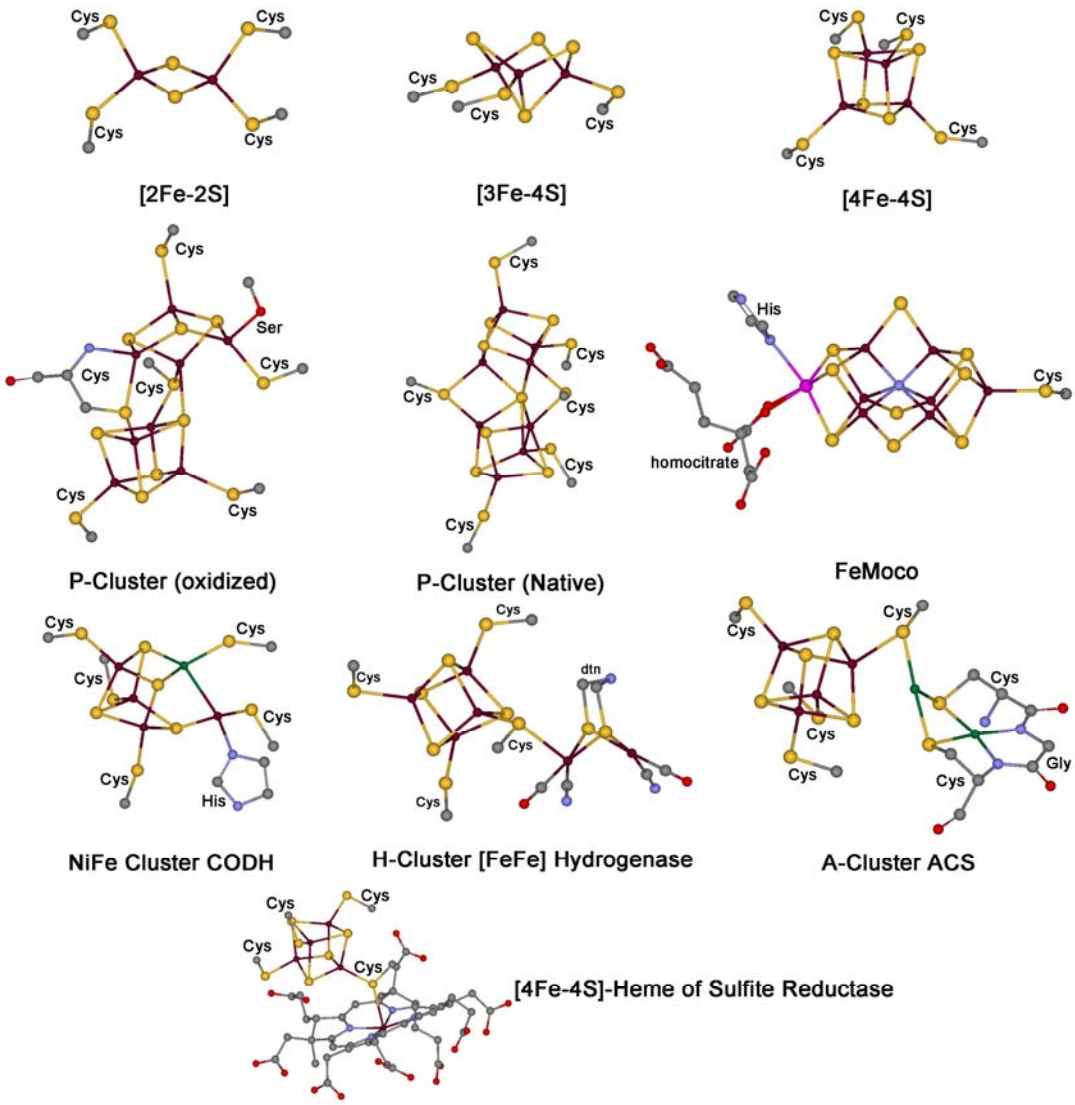

Figure 1.4 Structures of different arrangements of Fe Sulfur clusters in biological systems. Obtained from protein crystal structures.[2Fe-2S] [26], [3Fe-4S] and [4Fe-4S] [27], oxidized P-Cluster [28], native P-Cluster and FeMoco [4], NiFe Cluster [29], H-Cluster [30], A-Cluster [31], [4Fe-4S]-Heme [32]

1.2.2.2 Function

As mentioned previously, iron sulfur proteins are used in a variety of important physiological processes [11], mainly as electron transport proteins but also as catalytic centers and as sensors or regulators. In table 1.1 several biological functions of iron sulfur proteins are summarized.

For electron transfer reactions, biological systems utilize iron sulfur clusters as the active redox center for several reasons.[33-39]

1. The electron transfer protein must be capable of one electron reduction-oxidation. Most redox active organic molecules are not capable to effectively carry out this process, whereas metal centers are
2. Electron transfer is faster when the free energy difference between the donor and the acceptor is somewhat negative, but not too much. Therefore, the reduction potential must be fine tuned to be in between those of the donor and the acceptor when the same protein donates and accepts electrons. Consequently as the potential of metallic centers (and clusters) can be regulated over a wide range by their coordination environment they are used in a large variety of biological systems.
3. Efficiency of electron transfer pathways is enhanced by shortening the distance between the two centers, which is achieved in metals by large "conducting" cofactors like heme or metal clusters.
4. The reorganization energy on passing from one redox state to the other is minimized in metals by special coordinating geometries that are favorable

for both redox states of the metal, or possibly by distributing the electron over several metal ions.

Function	Cluster	Protein
Electron Transfer	$Fe(Cys)_4$	Rubredoxin, Desulforedoxin
	[2Fe-2S] and/or [3Fe-4S] and/ or [4Fe-4S]	Ferredoxins, Fe only hydrogenase, fumarate reductase
	[4Fe-4S]	High Potential Iron Protein, Nitrogenase Fe-Protein, Trimethylamine dehydrogenase
Coupled e^-/H^+ transfer	2Fe-2S	Rieske Proteins
	P-Cluster	Nitrogenase MoFe-Protein
Catalysis of non-redox reactions	[4Fe-4S]	Hydrolyases
Catalysis of redox reactions	H-Cluster	Fe only Hydrogenase
	[4Fe-4S]-heme	Sulfite reductase
	A-Cluster	Acetyl-Coenzyme A synthase
Stabilization of protein structure for DNA repair	[4Fe-4S]	Endonuclease III, MutY
Regulation of gene expression	[2Fe-2S]	SoxR, IscR
	[4Fe-4S] and [2Fe-2S]	FNR
	[4Fe-4S]	Iron Regulatory Protein
Regulation of enzyme activity	[2Fe-2S]	Ferrochelatase
	[4Fe-4S]	Glutamine PRPP amidotransferase
Redox mediated generation of free radicals	[4Fe-4S]	Biotin Synthase, anaerobic ribonucleotide reductase
Disulfide reduction	[4Fe-4S]	Ferredoxin:thioredoxin reductase

Table 1.1. Summary of biological functions of Iron Sulfur cluster containing proteins. Abbreviations used: MutY Mutator locus, SoxR Sulfur Oxidizing Regulatory enzyme, IscR Iron Sulfur Cluster Regulating enzyme, FNR Fumarate Nitrate Reduction enzymes, PRPP phosphoribosylpyrophosphate

In all the cases for Iron Sulfur proteins the iron redox couple used is Fe(II)/Fe(III); therefore, $Fe(Cys)_4$ and [2Fe-2S] proteins have one redox couple while [4Fe-4S] has three redox couples, with the $[4Fe\text{-}4S]^{0/1+}$ couple being observed only in two iron sulfur proteins [40, 41] although there are not enough evidence support a biological function. Potentially the [3Fe-4S] cluster should have three redox couples; however, only one redox couple has been established so far.

$$Fe^{II}(SCys)_4 \rightleftharpoons Fe^{III}(SCys)_4$$

$$[Fe_2S_2]^{+} \rightleftharpoons [Fe_2S_2]^{2+}$$

$$[Fe_3S_4]^{0} \rightleftharpoons [Fe_3S_4]^{+1}$$

$$[Fe_4S_4]^{0} \rightleftharpoons [Fe_4S_4]^{1+} \rightleftharpoons [Fe_4S_4]^{2+} \rightleftharpoons [Fe_4S_4]^{3+}$$

Figure 1.5. Biologically relevant redox couples of iron sulfur proteins

The potentials of the proteins can be tuned within a specific range by the protein environment [38]; Rubredoxins have an effective range of +30mV to -80mV, and [2Fe-2S] ferredoxins have a range of -150mV to -450mV. The 0/+1 couple of [3Fe-4S] ferredoxins [42] has a narrow range from -120mV to -150mV; however, in the [7Fe-8S] ferredoxins that contain a $[Fe_3S_4]$ and a $[Fe_4S_4]$ cluster the range of this couple increases dramatically and potentials range from -130mV to -450mV. For $[Fe_4S_4]$ clusters, there are two couples observed, the +1/+2 couple in ferredoxins, and the +2/+3 couple in High Potential Iron Proteins (HiPIP). In [4Fe-4S] ferredoxins the range of potentials lies between -270mV and -430mV, in [7Fe-8S] ferredoxins, between -400mV and -660mV, and in [8Fe-8S] ferredoxins, containing two $[Fe_4S_4]$ clusters, the range is from -400mV to -500mV. In HiPIPs, that are part of a superfamily of electron transfer proteins

encountered in aerobic photosynthetic bacteria [43], there is a range of potentials from +80mV to +500mV. Higher photosynthetic organisms including plants, have instead of HiPIPs [2Fe-2S] proteins known as Rieske Proteins [43]. In these, the [Fe_2S_2] cluster is coordinated to two cysteine and two histidine residues with a highly conserved Cys-X-His-X-Gly-Cys-X_{12-44}-Cys-X-Cys-His with the binding residues underlined while the remaining two cysteine residues, in most cases, form a disulfide bond that stabilizes the structure [44]. In the photosynthetic pathway the role of Rieske proteins, along with a cytochrome b and cytochrome c, are to oxidize hydroquinones and transfer electrons to their respective acceptors, cytochrome c or plastocyanin. Hydroquinones bind directly to the Rieske protein and are oxidized and lose protons, while other Rieske type proteins function in dioxygenases that convert aromatic compounds into cis-arene diols. In both cases the electron transfer is coupled to proton transfer; therefore, Rieske Proteins are described as coupled e^-/H^+ transport proteins [45, 46], a role that is presumed, due to the presence of serine, for the P-Cluster of nitrogenase [28, 47] as well. Although in the case of the P-Cluster it is yet to be confirmed.

As catalytic centers, iron sulfur clusters can be divided into redox active and non-redox active. In the first case, the examples include Fe only hydrogenases catalyzing the reversible reduction of protons to dihydrogen [5, 48, 49], sulfite reductase that catalyzes the reduction of sulfite (HSO_3^-) to sulfide (HS^-) [32, 50-53], and Acetyl Coenzyme A synthase (Acetyl-CoA synthase) that condenses a methyl group, CO and CoA to Acetyl-CoA [54-58]. In all cases an [Fe_4S_4] cluster is directly bound via a cysteine residue to another metallic center that is the active catalytic center, and in that sense, the [Fe_4S_4] cluster acts solely as an electron carrier, although by coupling directly to the catalytic site, the electron transfer to the substrate is instantaneous.

In non redox catalytic reactions, the [Fe_4S_4] cluster is bound to three cysteine residues while the fourth iron is typically bound to a hydroxylate ligand [59]. These are enzymes of the hydrolyase family with the most well studied enzyme being aconitase, a widely distributed enzyme in nature that catalyses the stereospecific isomerization of citrate to isocitrate via consecutive dehydration-hydration reactions [60-64]. As the iron sulfur cluster can shift electrons between the metals and the ligands it can lead to polarization of attached or surrounding groups. In aconitase, the hydroxyl-bound iron serves as a Lewis acid, which is able to abstract a hydroxyl and a proton from the substrate and reattaching it to a previously dehydrated substrate with the positions of the carbons inverted [63]. During the reaction, coordination of the iron changes from four coordinated to six coordinated and the iron slightly distances itself from the remaining cluster. Due to this feature, aconitase in the presence of oxygen loses this iron and forms an [Fe_3S_4] cluster, which consequently in the 70's had lead to the assumption that aconitase is a [3Fe-4S] protein, as the protein was not isolated in strictly anaerobic conditions.

The sensitivity to oxygen and the ability of aconitase to reactivate in the presence of iron makes aconitase a sensing and regulatory protein. The sensitivity of iron sulfur clusters to oxygen is being exploited by Nature in sensing and signaling [61, 62, 65-67]. An example of this function is the SoxR/SoxS system. SoxR is a transcriptional activator in which the [Fe_2S_2] cluster is in the +1 oxidation state under physiological conditions and inactive since its potential is high even at aerobic conditions. In the presence of O_2^- the [Fe_2S_2] cluster is oxidized to the +2 oxidation state, activating the enzyme and inducing a single gene, soxS, that in turn triggers a complex stress-response, resulting in

the synthesis of proteins protective against oxidative stress, such as SOD (superoxide dismutase), a DNA repair enzyme ENDO IV, and others.[61]

A final example is the role of iron sulfur proteins in radical generation. These iron sulfur proteins, known as radical SAM enzymes, utilize S-adenosylmethionine (SAM) as a cofactor to generate radicals [68-72]. Their catalytic roles include glycyl radical formation, rearrangement reactions, cofactor biosynthesis, repair of UV induced DNA damage, and possibly even more yet unknown functions. This is due to the oxygen sensitivity and lability of the iron sulfur clusters in Radical SAM enzymes and mainly spectroscopic techniques are used in order to identify the clusters. These proteins have a conserved motif of Cys-X-X-X-Cys-X-X-Cys, with no other cysteines, suggesting that the catalytic [Fe_4S_4] cluster most likely contains one non cysteine ligand [73-78] similar to the coordination of the [Fe_4S_4] cluster in hydrolases discussed previously.

1.2.2.3 Synthetic models and physical properties

Since the discovery of iron sulfur clusters as parts of proteins, these clusters have been studied spectroscopically and by synthetic models, [11, 37, 79, 80], to an extent that in several cases, protein crystallography merely confirmed the results obtained by other methods.

Spectroscopically, iron sulfur proteins have been extensively studied with a variety of methods including Mössbauer, EPR, NMR, ENDOR and other spectroscopic techniques [61, 81-88], in order to elucidate the electronic properties of these clusters. These studies reveal that in all cases iron is either high spin Fe(II) (S=2) or high spin Fe(III) (S=5/2) that are always overall antiferromagnetically coupled. It should be noted however, that in the cases of [Fe_3S_4] and [Fe_4S_4] clusters, iron pairs can be

ferromagnetically coupled. For the $[Fe_2S_2]^{2+}$ cluster, both irons are Fe(III) and because of antiferromagnetic coupling give an EPR silent S=0 state, while in the reduced $[Fe_2S_2]^{+}$ cluster the system becomes localized Fe(III)/Fe(II) with S=1/2 and an EPR signal at g=1.94. The $[Fe_3S_4]^{+}$ cluster is again 3Fe(III) and antiferromagnetic coupling yields a S=1/2 ground state with g values centered around 2.01. The one electron reduced $[Fe_3S_4]^{0}$ cluster contains one S=5/2 Fe(III) and a delocalized Fe(II)/Fe(III) dimer in which the charge on the individual irons is 2.5 and S=9/2, with the net spin being S=2. In the $[Fe_4S_4]^{2+}$ cluster, there are formally 2Fe(III) and 2Fe(II) centers that form two mixed valence S=9/2 pairs antiferromagnetically coupled to give an S=0 EPR silent ground state. With the addition of one electron, the ground state consists of a mixed valence S=9/2 pair and an all ferrous S=4 pair, with overall S=1/2 state, for $[Fe_4S_4]^{+}$. In oxidized HiPIPs the $[Fe_4S_4]^{3+}$ cluster has a ground state consisting of a mixed valence S=9/2 pair coupled antiferromagnetically to a ferric S=5 pair, giving rise to a S=1/2 ground state. However, in this case there can be shifts of the mixed valence pair from one side of the cube to another, giving an average of distinct Fe(III) and Fe(II) sites, which is also a possible model for the electronic structure of $[Fe_4S_4]^{3+}$ clusters.

As mentioned previously there can be ferromagnetic coupling between iron pairs in $[Fe_3S_4]$ and $[Fe_4S_4]$ clusters. This coupling allows the delocalization of spins to occur without spin inversion, reducing the energy involved in such processes, and providing additional stability to these high spin states. Consequently, high spin systems are more efficient for electron transfer [89-91].

Besides spectroscopic characterization of the iron sulfur proteins, synthetic models [42, 49, 79, 92, 93] have been proven of equal importance in elucidating the electronic structure of iron sulfur clusters. Up to date there have been models for several types of

the iron sulfur clusters presented in Figure 1.4. Model clusters of $[Fe_2S_2]$ [94, 95] and $[Fe_4S_4]$ [96-98] are known from the early 70's, although the synthesis on new models still continues [99, 100], in order to obtain more detailed information about the nature and function of these clusters.

In terms of synthesis, the approaches that have been used are as follows:

1. The use of monomeric iron, thiols and sulfur under various conditions provide a wide range of iron sulfur clusters. This includes cubic $[Fe_4S_4(L)_4]^{n-}$ (L=halogens, thiols phosphines) [92, 101], prismatic $[Fe_6S_6X_6]^{3-}$ (X=halogens) [102], octanuclear $[Fe_8S_6I_8]^{n-}$ [103], adamantane like $[Fe_4(SPh)_6Cl_4]^{2-}$ [104], planar $[Fe_3S_4(SR)_4]^{2-}$ [105], planar $[Fe_6S_9(SR)_2]^{4-}$ [106], and in the most recent example, a structural analogue to the $[Fe_8S_7]$ P-Cluster of nitrogenase, $Fe_8S_7(SR)_4(SR')$ [107] in which the use of extremely bulky thiols enabled the creation of a "carbon cage" in which the cluster lies.
2. The use of small dimeric or cubic clusters as building blocks for the assembly of higher nuclearity clusters. The method has enabled the formation of clusters of fused cubane structures both with iron only, such as $Fe_8S_8(PR_3)_8$ [108] and $Fe_{16}S_{16}(PR_3)_{16}$ [109], and also in M/Fe/S clusters with a core structure of $[M_2Fe_6S_8]$ (M = Mo[110, 111], V[112]). Other clusters synthesized by this method include the single-bridged double cubane $[(Fe_4S_4Cl_4)_2S]^{4-}$ [113] and double-bridged double cubanes of $[(MoFe_3S_4)_2(\mu_2\text{-}S)(\mu_2\text{-}X)]$ ($X=S^{2-}$, OH^-, N_3^-) [114]

Synthetic analogues for the whole H-Cluster of hydrogenase have not been synthesized but extremely valuable information has been obtained from the synthesis of

dimeric iron sulfur carbonyl clusters and their interaction with protons [115-119]. For the A-Cluster of Acetyl CoA synthase [120, 121], and the Sulfite reductase cluster [122-124], adequate structural models have been obtained, while for the NiFe cluster of CODH, the existing models so far [125, 126], do not have the exact topology of metals as found in the enzyme.

1.3. Nitric Oxide in Biology

Nitric oxide is a neutral gaseous molecule with one unpaired electron; therefore it is a free radical, isoelectronic to O_2^+. The electron is delocalized in the π^* molecular orbitals and NO remains monomeric in solution. The neutral charge contributes greatly in the diffusability of NO through membranes and its solubility in water is comparable to that of CO_2 and O_2.

For a long time NO had only been considered as a poisonous gas and a significant environmental pollutant, generated by the incomplete burning of N_2. The poisonous nature of NO was regarded to be, as its analogues, CO and CN^-, the irreversible binding to metal centers, and therefore it affected the respiratory process. As a strong ligand, the coordination chemistry of NO had been well documented; however, the use of NO as a ligand for biologically relevant systems was mainly to mimic biological oxygen activators. In these metalloenzymes, characterization of the unstable oxygenated species is extremely difficult or even impossible, making the stable NO an effective probe of the structure (both geometric and electronic) and function of these enzymes.

However, in the 1980's it was discovered that NO is a physiologically generated molecule, responsible for smooth muscle relaxation, a discovery that was awarded the Nobel Prize in Physiology and Medicine in 1998 to Robert F. Furchgott, Louis J. Ignarro,

and Ferid Murad. Since its initial discovery, NO has been implicated in a large number of physiological systems, and is now recognized as a regulator of blood pressure, vascular tone, neural signaling and immunological function. Consequently in the last 30 years, there has been an exponential increase in biological research involving nitric oxide, with about 15000 research articles published in the last 5 years, and since 1997, there has been a journal dedicated to the biology and chemistry of Nitric Oxide [127].

As a signaling molecule involved in so many important processes, it is currently linked with a plethora of pathological conditions, including diabetes, hypertension, cancer, memory disorders, and drug addiction, and therefore is widely used as a drug and its chemistry and biology has been extensively studied. It comes with no surprise, however; that the physiology of nitric oxide is directly related to its metal binding abilities, and therefore understanding the chemistry of nitric oxide with respect to metalloenzymes is of vital importance. Since iron is the most widely used transition element in biology the study of iron nitrosyl complexes is particularly important.

1.3.1 Biological synthesis of Nitric Oxide.

Nitric oxide is generated in the cells of animals by a series of enzymes, the Nitric Oxide Synthases (NOS) [128-131], which are unique in the complexity of their organization and include a multitude of various cofactors. There are three types of NOS, neural NOS (nNOS), epithelial NOS (eNOS) and inducible NOS (iNOS), and they all catalyze the five electron oxidation of an arginine nitrogen by molecular oxygen coupled to the oxidation of NADPH and the overall reaction is:

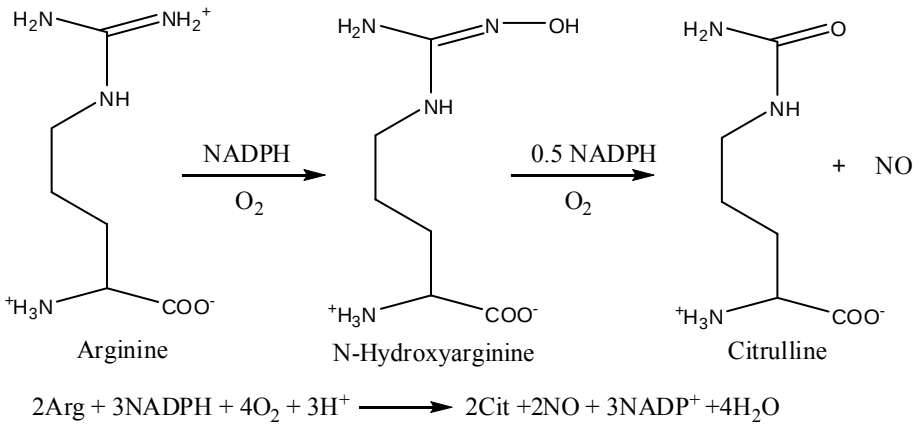

Figure 1.6. NOS synthesis of NO from arginine.

Two of the three NOSs are constitutively expressed in cells (cNOS) and synthesize NO in response to increased Ca^{2+} levels, or in some cases, by independent stimuli like shear stress. These are the neural NOS (nNOS) and epithelial NOS (eNOS). The third type is an inducible NOS (iNOS) that is expressed only in some tissues, such as lung epithelium, and typically is synthesized in response to inflammatory or pro-inflammatory mediators; therefore, expression of iNOS might be linked to host defense or immune response modulation, although its expression is linked with inflammatory diseases.

The enzyme comprises an N-terminal oxygenase domain and a C-terminal reductase domain with an approximately 30 amino acid recognition sequence for the Ca^{2+} binding protein calmodulin (CaM) that is located between the two domains. The oxygenase domain contains a heme, and binds tetrahydrobiopterin and L-Arginine; the heme is the active site where NO formation occurs. The reductase domain varies in length among the NOS and participates in cellular targeting. This domain binds FMN, FAD and NADPH.

During NO synthesis, the reductase flavins acquire electrons from NADPH and transfer them to the heme iron, permitting it to bind and activate oxygen and catalyze NO synthesis. In cNOS the electron transfer is triggered by CaM binding, which explains the regulation by Ca^{2+}. In iNOS however, CaM binding is irreversible, consistent with iNOS being constantly active once assembled. In terms of mechanism, although it is not completely elucidated, the heme acts in a P450 type of mechanism, with the iron bound to the porphyrin ring and a cysteine residue, with one site open for O_2 coordination. In the first step, oxygen binds to the iron and after a two electron reduction, forms a peroxo-Fe species, which by protonation and loss of water forms the active oxo-Fe species that reacts with arginine forming N-hydroxyarginine. The second oxygen with the addition of one electron forms a peroxo-Fe species that is believed to interact directly with the substrate, producing citrulline and NO.

Besides the regular production of nitric oxide by the NOS enzymes, NO can be generated by non enzymatic activity, mainly from nitrate reduction [132], a process that occurs under high acidic conditions such as in the stomach; and therefore, it has been suggested that NO can act as a defense system from swallowed pathogenic microorganisms. Other instances that NOS independent NO synthesis occurs is under pathogenic conditions, such as ischemia in which NO accumulates in the tissues and binds to a variety of heme proteins.

1.3.2. Biological function of Nitric Oxide

The biological function of nitric oxide can be beneficial for the organism or deleterious. Unlike most small signaling molecules, the biological effects of NO are determined by their chemical reactions, such as binding to the regulatory heme in soluble

guanylate cyclase (sGC) participating in muscle relaxation, rather than traditional indirect protein receptor-ligand interactions. The primary target of NO, sGC, is the enzyme catalyzing the conversion of Guanosine-5′-triphosphate (GTP) to cyclic Guanosine-3′-5′-monophosphate (cGMP), by activating the enzyme. The activation, although not completely defined, involves the coordination of NO to a heme iron, and this leads to the dissociation of the trans Histidine ligand, which induces conformational changes to the protein that lead to its activity [133].

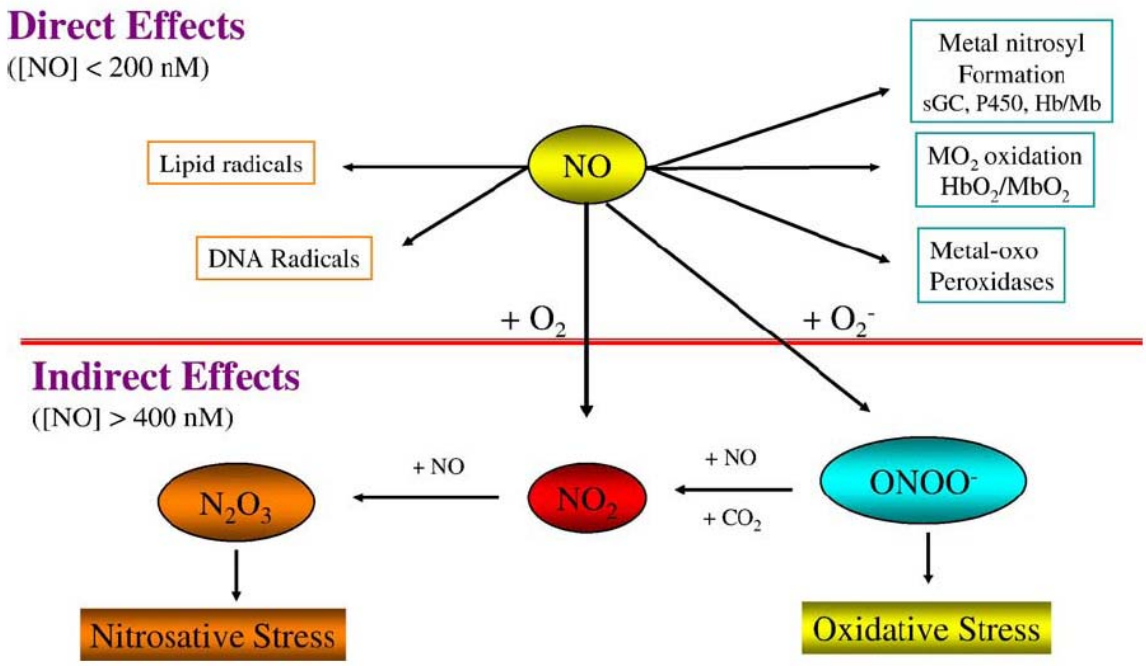

Figure 1.7. Chemical biology of NO distinguished between direct and indirect effects. Taken from reference [134]

The biological effects of NO can be divided into direct and indirect effects depending on the concentration of NO in the cell or tissue [134] (Figure 1.7). The indirect effects occur from formation of reactive nitrogen species (RNS). These species, like reactive oxygen species, are derived from the interaction of the NO radical resulting in the formation of more persistent species that induce multiple biological effects. The best

understood RNS occurs form the reaction of NO with O_2^-, forming peroxynitrite $ONOO^-$, which is much more reactive and damaging than its precursors. It causes oxidation of thiols, nitrates, and protein tyrosine residues, and it damages mitochondria through the increase of Ca^{2+} efflux. It also damages DNA by making single strand breaks and causing overexpression of poly(ADP-ribose) polymerase used for DNA repair; therefore, it leads to an energy deficit to the cell [135, 136].

Direct effects of NO include interaction with oxyhemoglobin and myoglobin to form nitrite at a high rate, making nitrate the major endpoint in NO metabolism. It also binds to several heme enzymes, such as cytochrome oxidase, catalase and cytochrome P450, and also to iron sulfur proteins, mainly catalytic iron sulfur clusters such as aconitase.

In the nervous system, NO acts as a signaling molecule, by release into the synaptic cleft through free diffusion. This is a difference of NO with the majority of neurotransmitters that typically act as ion channel activators causing the release of Na^+ ions in the synaptic cleft. Part of the NO function in the nervous system is to activate cGS and produce GMP. Besides cGS activation, there are indications for additional functions of NO in the nervous system although such mechanisms remain unclear.[137-139]

In the cardiovascular system [140-142], NO interacts primarily with hemoglobin directly, but it also acts indirectly through the formation of S-nitrosothiol derivatives of cysteine and glutathione that are potent vasodilators. Interaction of NO with hemoglobin occurs initially at the heme iron, when hemoglobin is in the tense state. When in the relaxed state, NO actually migrates from the heme to a cysteine residue (β-Cys93 in humans) forming an S-nitrosylated adduct (SNO-Hb). In general, as NO is present at low concentrations in tissues, and hence in red blood cells, it does not interact with cytosolic

hemoglobin that is the bulk O_2 transporter, but with hemoglobin on the plasma membrane of the red blood cells. As red blood cells transport O_2 from the lungs, oxygenation favors the formation of the relaxed state and hence formation of SNO-Hb. In the vascular periphery, deoxygenation is associated with transition to the tense state, so that in the membrane population of hemoglobin, where hemoglobin interacts with the cytoplasmic domain of a band 3 protein, AE1, NO is transferred from the hemoglobin cysteine to the AE1 protein.

1.3.3. Interactions of NO with Iron Sulfur proteins

The main interaction of NO with iron proteins is with heme proteins that bind oxygen. Iron sulfur clusters are usually air sensitive, and cells have developed methods of protecting these proteins from oxygen; similar mechanisms of protecting these proteins by NO are also likely to exist. In the electron transport proteins, the iron sulfur cluster is buried inside the protein and therefore somewhat inaccessible to NO. However, it is possible that NO can interfere with the biosynthesis of iron sulfur clusters by binding to iron and preventing it from being taken up during assembly of the cofactor [143-147].

Nevertheless, in catalytic and regulatory iron sulfur clusters in which the cluster lies near the surface, NO can directly interact with the protein and examples of such behavior have been reported for Aconitase, Endonuclease III and SoxR. In all of these cases, NO affects the activation/inactivation of these enzymes in a reversible manner, and as such, NO can act as a regulator for the physiological or pathophysiological activity of these enzymes. The NO-modified iron sulfur clusters exhibit a characteristic g=2.04 EPR signal, making the observation of NO binding observable in tissues [148-152].

In mitochondrial aconitase, an enzyme participating in the Krebs cycle, the [Fe_4S_4] cluster is bound to three cysteine residues, leaving one iron partially exposed to participate in the isomerization of citrate to isocitrate. The interaction with NO occurs by direct binding to the exposed iron and therefore, inhibits the activity of the enzyme. In vivo, it has been shown that NO does not remove the iron and form a [Fe_3S_4] cluster, but rather it forms a stable reversible protein-bound iron nitrosyl complex. In prolonged exposure to NO, it is possible that removal of iron occurs, leading to the inactivated form of the enzyme. After complete loss of one iron, the [Fe_3S_4] cluster functions as an iron-responsive protein. Therefore, NO can act as a regulator for both activities of aconitase under physiological conditions, or at pathological conditions [61, 153, 154]

Endonuclease III is a DNA repair enzyme that hydrolyzes N-glycosydic bonds between damaged bases and the DNA backbone. The enzyme contains a [Fe_4S_4] cluster that is essential for proper folding to produce active enzyme, but it is not the catalytic center of the enzyme. Unlike other [4Fe-4S] proteins it is resistant to both oxidation and reduction; however, NO interacts with the protein forming detectable dinitrosylated iron species. This leads to complete inactivation of enzymatic activity, which can be restored under aerobic growth conditions without new protein synthesis. It has been suggested that inactivation by NO might be beneficial in preventing excessive generation of DNA breaks caused by the DNA glycosylase activity of endonuclease III. Moreover, if the specific cellular repair activity is compromised, the inactivated proteins will accumulate in the cells, which can contribute to onset of neurodegenerative diseases [155].

SoxR, is a bacterial [2Fe-2S] transcription factor protein that functions as a sensor of oxidative stress and part of the MerR family of transcriptional activators. Under oxidative stress, the SoxR protein enhances the transcription of the soxS gene up to 100-

fold, enabling the soxS gene to initiate the production of various antioxidant and repair proteins. As in the case of endonuclease III, the role of the [Fe_2S_2] cluster of SoxR is structural and not catalytic. However the enzyme is active only when the cluster is oxidized and since both the apo-SoxR and the reduced SoxR bind to DNA with similar affinity, it is believed that oxidation of the [Fe_2S_2] cluster induces conformational change on the protein and therefore activates the enzyme. Structurally [156], the [Fe_2S_2] cluster is located on the surface of the protein, and is therefore accessible to reactive oxygen species and NO, and it is also in close proximity to the DNA binding site. The key feature is the asymmetric distribution of charges from protein residues near the [Fe_2S_2] cluster. As the cluster upon electron transfer alters its charge, the protein has to rearrange in order to compensate the charge and consequently alters the bending of the bound DNA strand. This is somewhat surprising because nitrosylation of iron sulfur centers typically causes inactivation of the enzyme while in this case; the enzyme is activated by nitrosylation. The nitrosylated SoxR enzyme is stable when purified SoxR is used, but in bacteria, it is unstable making the regulatory process reversible in vivo [157].

As mentioned previously, the nitrosylated iron sulfur clusters exhibit a characteristic g=2.04 EPR signal. This signal is attributed to dinitrosylated iron sulfur species (DNIS) with a general formula $(NO)_2Fe(SR)_2$, that can be bound to the protein or free in solution. However, in most of the enzymes it has been shown that the cluster remains bound to the protein and nitrosylation is reversible. Given that besides the EPR signal similarity to DNIS, there is no other evidence on the exact nature of protein bound nitrosylated iron sulfur clusters, further studies on iron sulfur nitrosyl clusters are necessary to elucidate the interaction of nitric oxide with iron sulfur proteins.

1.3.4 The Metal-Nitric Oxide bond.

As previously discussed, nitric oxide is an essential molecule in biological processes, and the center of attention for researchers from a broad range of fields. For inorganic chemists, nitric oxide is a fascinating molecule as it can be described with three different electronic descriptions, and thus affecting the oxidation state of the metal.

These electronic configurations are NO^+, radical $NO\cdot$, and NO^-. According to the molecular orbital diagram of NO, the HOMO in NO^+ would be a σ orbital, while for $NO\cdot$ and NO^- the HOMO orbital is a π* orbital with one and two electrons respectively. Therefore, in terms of a simple angular overlap approach, NO^+ would give linear complexes, while $NO\cdot$ and NO^- would give bent complexes. However, as shown by Enemark and Feltham in what is now consider a classic review on Metal-Nitrosyl bonding [158], there is significant mixing of d metal orbitals with both σ and π* orbitals of NO and therefore, metal-nitrosyls should be considered as covalent entities rather than individual units with a typical metal-ligand interaction. According to these molecular orbital diagrams, the linear or bent nature of the M-NO bond depends on the total number of electrons of both the metal and the nitrosyl, and not on the formal charges of the two species.

In order to address the covalent nature of the M-NO bond, Enemark and Feltham proposed the $\{M\text{-}(NO)_x\}^n$ notation, with x being the number of nitrosyls bound to a metal, and n the sum of d metal electrons and π* electrons of NO. This notation provides adequate predictions and explanations for the geometry of the M-NO bond. For example, for a six coordinated $\{M\text{-}NO\}^6$ species, the molecular orbital diagrams predict that a C_{4v} geometry with a linear M-NO bond is more energetically favorable than the C_s geometry with bent M-NO bond. The same diagrams predict that a six coordinated $\{M\text{-}NO\}^8$

species will prefer the C_s geometry. This preference is confirmed crystallographically, by the linear Fe-NO bond (178º) in $[Fe(CN)_5(NO)]^{2-}$ and the bent Co-NO bond (114º) in $[Co(NH_3)_5(NO)]^{2+}$, since the complexes are described as $\{M\text{-}NO\}^6$ and $\{M\text{-}NO\}^8$ respectively.

However, this method gives the same $\{M\text{-}(NO)_x\}^n$ notation regardless of the formal oxidation sate of NO, making the M-NO bond angle insufficient for assigning formal oxidations on NO and consequently the metal. For example, in $[Fe(CN)_5(NO)]^{2-}$, the cyanides are -1 ions and the total charge of the complex is -2; therefore, if we assume NO^+, the iron should be in the +2 oxidation state to balance the charge. Since NO^+ does not contain any π^* electrons and Fe(II) is a d^6 metal, the Enemark-Feltham notation is $\{Fe\text{-}NO\}^6$. The same result is obtained if we assume NO^-, since the iron has to be in the +4 oxidation state to compensate the charge. Since NO^- has two π^* electrons and Fe(IV) is a d^4 metal, once again the notation is $\{Fe\text{-}NO\}^6$. Further proof that the angular overlap model is too simplistic for describing the M-NO bond, comes from the stretching vibrations in M-NO complexes. According to bond order, NO^+ will have a higher N-O stretching vibration than NO^-. In the two isoelectronic $\{M\text{-}NO\}^6$ complexes $[Fe(CN)_5(NO)]^{2-}$ and $[Mn(CN)_5(NO)]^{3-}$, the bond is linear. However, the N-O stretching vibration differs by $200cm^{-1}$, which is a difference large enough to assign different formal oxidations on the nitrosyl, and this is contradicting the linearity of the M-NO bond in both cases, when using the angular overlap model approach.

As a conclusion, the bond angle cannot be used as a criterion for determining the formal oxidation states of the metal in metal-nitrosyl complexes. Such an assignment of formal charges, has to come from extensive spectroscopic characterization using a variety

of techniques, since neither the N-O stretching vibration is sufficient on its own, due to the high overlap between the vibrations of the three nitric oxide oxidation states.

Of biological interest, the most significant are the $\{Fe\text{-}NO\}^7$ and $\{Fe\text{-}NO\}^8$ units that can be found in heme and iron-sulfur containing proteins, with six or five coordinated and four coordinated geometries respectively. For four coordinated mononitrosyl complexes, Enemark and Feltham predicted that there is no significant energetic difference between linear C_{3v} and bent C_s conformations, with the linear being slightly favorable. In six or five coordinated complexes, both $\{Fe\text{-}NO\}^7$ and $\{Fe\text{-}NO\}^8$ units should be bent; however, there are several five-coordinated $\{Fe\text{-}NO\}^7$ complexes that contain linear Fe-NO bonds and the Enemark-Feltham model had to be reevaluated. As it was suggested by extended spectroscopic investigations [159] and more recently shown by theoretical calculations [160], this discrepancy is due to significant mixing between the $3d_z^2$ and $4p_z$ orbitals. The mixing leads to distortions of the d_z^2 orbital, in which the lobe trans to the NO is elongated while the lobe on the side of NO decreases significantly and therefore the orbital cannot be used for binding making the π- bonding interactions stronger and therefore the molecule assumes a linear Fe-NO conformation. In six coordinated complexes, the presence of the ligand trans to NO lowers the $4p_z$ contribution to the molecular orbitals used for NO binding and therefore the bent conformation is obtained. A similar effect has been shown to happen in C_{3v} four and five coordinated complexes [161], suggesting that any bonding interactions trans to NO would cause the M-NO bond to bend.

1.4. Iron Sulfur clusters in minerals.

As mentioned above, the ubiquitous presence of iron sulfur clusters in Nature has led to the notion that these clusters are evolutionary archaic enzymes. There are theories that life itself was formed on volcanic composites on the ocean floor, which were rich in iron sulfur minerals and provided the raw materials for the incorporation of iron sulfur clusters to proteins.

There are at least 166 known minerals containing iron as a necessary component, of which, several consist of iron and sulfur; these include pyrite (FeS_2), pyrrhotite ($Fe_{1-x}S$), chalcopyrite ($CuFeS_2$), and pentlandite $(Fe,Ni)_9S_8$. In the Earth's crust, however, iron is mainly found combined with oxygen as iron oxide in minerals such as hematite (Fe_2O_3) and magnetite (Fe_3O_4).

In Nature, sulfur can be found as the pure element as well as sulfide and sulfate minerals. Natural occurrence of elemental sulfur derives from volcanic emissions from hydrothermal vents, and from bacterial action on decaying sulfur-containing organic matter. Common naturally occurring sulfur compounds include the sulfide minerals, such as pyrite (iron sulfide), cinnabar (mercury sulfide), galena (lead sulfide), sphalerite (zinc sulfide) and stibnite (antimony sulfide), and the sulfates, such as gypsum (calcium sulfate), alunite (potassium aluminium sulfate), and barite (barium sulfate).

Minerals are defined as naturally occurring substances that are formed through geological processes and have characteristic chemical compositions, highly ordered atomic structures and specific physical properties. Rocks, by comparison, are aggregates of minerals and need not have specific chemical compositions. Minerals range in composition from pure elements and simple salts to very complex silicates with thousands of known forms. Rocks are classified in terms of being igneous, sedimentary

or metamorphic forms. Igneous rocks are formed from cooling of molten magma, either on the surface as volcanic lava cools, or below the surface of the earth, within other rock compartments, and this relatively slow process causes fractional crystallization of minerals. Sedimentary rocks are formed near the surface of the earth, from deposition of clastic sediments (formed from small segments of other rocks by weathering), organic matter (such as from corals), or chemical precipitates (from evaporation of surface water bodies). Finally, metamorphic rocks are the result transformation of previous rock formations under high pressure and/or temperature, within the earth.

Sulfide-containing minerals are of igneous origin, and are the main source of ores of copper (chalcopyrite, bornite), lead (galena), silver (acanthite) and nickel (pentlandite). As these minerals are of igneous origin, their formation and composition depends on their fractional crystallization from molten rock. The sulfides melt at or above 1000 ºC, and are in the form or monosulfide solid solution (MSS) from which the minerals form upon cooling. The study of MSS is of particular interest, both for understanding the process of formation and for industrial purposes in extracting the ores. These studies include the pentlandite minerals, and better understanding of the process of formation is of great importance in the extraction of nickel.

Pentlandites are minerals of the general formula M_9S_8, but have a variety of compositions, with nickel and iron being the main components; however, cobalt, silver and lead are found as well. Structurally, the pentlandites belong to the *Fm3m* space group with four M_9S_8 units per cell. The 36 metals are distributed over 32 tetrahedral and 4 octahedral (4b) sites while the 32 sulfur atoms are in a pseudo cubic close packing arrangement distributed over 8 c and 24 e equipoints in four and five coordination geometries. There are additionally 4 octahedral (4a), 24 octahedral (24d) and 32

tetrahedral (32f) interstitial (vacant) sites. Nickel is mainly found in tetrahedral sites, while iron is preferred for the octahedral sites. The composition, however, is close to $(Fe_{4.5}Ni_{4.5})S_8$ although it can vary in different specimens [162-167].

Thermal studies [168-170] on pentlandites show that the crystal structure of the pentlandite, might have additional vacant sites or excess of metals; depending on the metal ratio, in particular the ratio of Fe to (Fe + Ni).

Cobalt is also found in structures similar to pentlandites or as a component of naturally occurring pentlandites, but in general, it tends to crystallize as Co_9S_8 from MSS mixtures containing Fe,Ni and Co. Recently [171], it has been shown that the enthalpy of formation of Co_9S_8 is slightly higher than the enthalpy of formation of $(Fe_5Ni_4)S_8$, providing some insight into the exclusion of cobalt from the majority of natural occurring pentlandites. The same studies have shown that increased stability is associated with the Co_9S_8 structure over the Co_8S_8 structure.

As mentioned, the exact distribution of the metals in pentlandites is not known, and studies at a theoretical level are being performed in order to better understand the stability of these minerals, and in this sense, model compounds can help to elucidate the fine details of the formation of these minerals.

1.5 Scope of the Thesis

In chapter 2 the synthesis, characterization and reactivity of iron sulfur nitrosyl clusters is presented. These clusters are analogous to the iron sulfur clusters containing halogens and thiols and their synthesis and interconversions are discussed in terms of possible pathways of formation. Spectroscopic characterization and electrochemical measurements are reported At this level it would be ill-advised to imply any direct

relevance to biological systems and the interaction of nitrosyl with iron sulfur proteins, although potentially these clusters can be used to further understand the electronic structure and properties of iron sulfur nitrosyl clusters, which in turn, will help to better understand the modes of interaction between nitrosyl and iron sulfur proteins.

In chapter 3 the synthesis and characterization of heterometallic iron sulfur chloride clusters containing the pentlandite core structure with the heterometals being copper, nickel and cobalt, is presented. Possible pathways of formation are discussed along with some spectroscopic properties. The synthesis follows a systematic approach and some mechanistic pathways of iron sulfur clusters are conceptually derived. These clusters can provide useful information on the exact topology of the metals in the pentlandite minerals as their properties are comparable and can potentially be used as building blocks for the synthesis of new materials with exciting electronic and chemical properties.

Finally in chapter 4, the reported clusters are extensions of the clusters presented in chapter 3 to nitrosyl derivatives and are a link between the clusters presented in the two previous chapters. Synthetic pathways, spectroscopic and electrochemical measurements are reported and comparison between the chloro and nitrosyl analogues is made. The differences and similarities provide a better understanding on the properties of the clusters and the ligands discussed in the previous two chapters.

1.6 References

[1] I. Bertini, H.B. Gray, E.I. Stiefel, J.S. Valentine, Biological inorganic chemistry : structure and reactivity, University Science Books, 2007.
[2] R.S. Carmichael, Practical handbook of physical properties of rocks and minerals, CRC Press, Boca Raton, 1989.
[3] D.C. Rees, Annual Review of Biochemistry 71 (2002) 221.
[4] O. Einsle, F.A. Tezcan, S.L.A. Andrade, B. Schmid, M. Yoshida, J.B. Howard, D.C. Rees, Science 297 (2002) 1696.
[5] J.C. Fontecilla-Camps, A. Volbeda, C. Cavazza, Y. Nicolet, Chemical Reviews 107 (2007) 4273.
[6] S. Shigehiro, M. Nakasako, N. Dohmae, M. Tsujimura, K. Tokoi, M. Odaka, M. Yohda, N. Kamiya, I. Endo, Nature Structural Biology 5 (1998) 347.
[7] B. Loll, J. Kern, W. Saenger, A. Zouni, J. Biesiadka, Nature 438 (2005) 1040.
[8] D.C. Johnson, D.R. Dean, A.D. Smith, M.K. Johnson, Annual Review of Biochemistry 74 (2005) 247.
[9] X.Y. Cui, C.L. Joannou, M.N. Hughes, R. Cammack, FEMS Microbiol. Lett. 98 (1992) 67.
[10] J. Imsande, Plant Physiology and Biochemistry 37 (1999) 87.
[11] H.I. Lee, L.M. Cameron, J. Christiansen, P.D. Christie, R.C. Pollock, R. Song, M. Sorlie, W.H. Orme-Johnson, D.R. Dean, B.J. Hales, B.M. Hoffman, Q-band ENDOR studies of the nitrogenase MoFe protein under turnover conditions - Substrate-inhibitor-binding to and metal-ion valencies of the FeMo-cofactor, Paramagnetic Resonance of Metallobiomolecules, 2003, pp. 150.
[12] R.H. Wickrama, Space Life Sciences 4 (1973) 341.
[13] W. Gilbert, Nature 319 (1986) 618.
[14] M. Bleyman, C. Woese, Genetics 60 (1968) 162.
[15] P.J. Unrau, D.P. Bartel, Nature 395 (1998) 260.
[16] E. Szathmary, Trends in Genetics 15 (1999) 223.
[17] C. Huber, G. Wachtershauser, Science 281 (1998) 670.
[18] G. Wachtershauser, Science 289 (2000) 1307.
[19] J. Washington, Origins of Life and Evolution of the Biosphere 30 (2000) 53.
[20] S.P. Chu, S. Elliott, M.E. Maltrud, Chemosphere 50 (2003) 223.
[21] D.S. Ross, Astrobiology 8 (2008) 267.
[22] M.J. Russell, R.M. Daniel, A.J. Hall, J.A. Sherringham, Journal of Molecular Evolution 39 (1994) 231.
[23] G.D. Cody, Annual Review of Earth and Planetary Sciences 32 (2004) 569.
[24] W. Martin, M.J. Russell, Philosophical Transactions of the Royal Society of London Series B-Biological Sciences 358 (2003) 59.
[25] I.L. Alberts, K. Nadassy, S.J. Wodak, Protein Science 7 (1998) 1700.
[26] R. Morales, M.H. Chron, G. Hudry-Clergeon, Y. Petillot, S. Norager, M. Medina, M. Frey, Biochemistry 38 (1999) 15764.
[27] C.D. Stout, E.A. Stura, D.E. McRee, Journal of Molecular Biology 278 (1998) 629.
[28] J.W. Peters, M.H.B. Stowell, S.M. Soltis, M.G. Finnegan, M.K. Johnson, D.C. Rees, Biochemistry 36 (1997) 1181.

[29] T.I. Doukov, T.M. Iverson, J. Seravalli, S.W. Ragsdale, C.L. Drennan, Science 298 (2002) 567.
[30] Y. Nicolet, C. Piras, P. Legrand, C.E. Hatchikian, J.C. Fontecilla-Camps, Structure with Folding & Design 7 (1999) 13.
[31] V. Svetlitchnyi, H. Dobbek, W. Meyer-Klaucke, T. Meins, B. Thiele, P. Romer, R. Huber, O. Meyer, Proceedings of the National Academy of Sciences of the United States of America 101 (2004) 446.
[32] B.R. Crane, L.M. Siegel, E.D. Getzoff, Science 270 (1995) 59.
[33] H.B. Gray, J.R. Winkler, Annual Review of Biochemistry 65 (1996) 537.
[34] T. Pascher, J.P. Chesick, J.R. Winkler, H.B. Gray, Science 271 (1996) 1558.
[35] R. Langen, I.J. Chang, J.P. Germanas, J.H. Richards, J.R. Winkler, H.B. Gray, Science 268 (1995) 1733.
[36] J.L. Liao, D.N. Beratan, Biophys. J. 87 (2004) 1369.
[37] S. Wherland, H.B. Gray, Proceedings of the National Academy of Sciences of the United States of America 73 (1976) 2950.
[38] F. Capozzi, S. Ciurli, C. Luchinat, Structure and Bonding 90 (1998) 127.
[39] P.J. Stephens, D.R. Jollie, A. Warshel, Chemical Reviews 96 (1996) 2491.
[40] M.L. Guo, F. Sulc, M.W. Ribbe, P.J. Farmer, B.K. Burgess, Journal of the American Chemical Society 124 (2002) 12100.
[41] M. Hans, W. Buckel, E. Bill, Journal of Biological Inorganic Chemistry 13 (2008) 563.
[42] M.K. Johnson, R.E. Duderstadt, E.C. Duin, Advances in Inorganic Chemistry 47 (1999) 1.
[43] B. Schoepp, M. Brugna, E. Lebrun, W. Nitschke, Advances in Inorganic Chemistry 47 (1999) 335.
[44] L.M. Carruthers, C.L. Closken, K.L. Link, S.N. Mahapatro, M. Bikram, J.L. Du, S.S. Eaton, G.R. Eaton, Inorg. Chem. 38 (1999) 3529.
[45] L.M. Hunsicker-Wang, A. Heine, Y. Chen, E.P. Luna, T. Todaro, Y.M. Zhang, P.A. Williams, D.E. McRee, J. Hirst, C.D. Stout, J.A. Fee, Biochemistry 42 (2003) 7303.
[46] R. Camba, Y.S. Jung, L.M. Hunsicker-Wang, B.K. Burgess, C.D. Stout, J. Hirst, F.A. Armstrong, Biochemistry 42 (2003) 10589.
[47] R. Silaghi-Dumitrescu, D.M. Kurtz, L.G. Ljungdahl, W.N. Lanzilotta, Biochemistry 44 (2005) 6492.
[48] M. Frey, Chembiochem 3 (2002) 153.
[49] X.M. Liu, S.K. Ibrahim, C. Tard, C.J. Pickett, Coordination Chemistry Reviews 249 (2005) 1641.
[50] L. Champier, N. Sibille, B. Bersch, B. Brutscher, M. Blackledge, J. Coves, Biochemistry 41 (2002) 3770.
[51] B.R. Crane, L.M. Siegel, E.D. Getzoff, Biochemistry 36 (1997) 12101.
[52] B.R. Crane, L.M. Siegel, E.D. Getzoff, Biochemistry 36 (1997) 12120.
[53] T.A. Hansen, Antonie Van Leeuwenhoek International Journal of General and Molecular Microbiology 66 (1994) 165.
[54] J. Seravalli, S.Y. Zhao, S.W. Ragsdale, Biochemistry 38 (1999) 5728.
[55] T.A. Jackson, E. Yikilmaz, A.F. Miller, T.C. Brunold, J. Am. Chem. Soc. 125 (2003) 8348.
[56] C.L. Drennan, J.W. Peters, Curr. Opin. Struct. Biol. 13 (2003) 220.
[57] S.W. Ragsdale, M. Kumar, Chemical Reviews 96 (1996) 2515.

[58] D.J. Evans, Coordination Chemistry Reviews 249 (2005) 1582.
[59] D.H. Flint, R.M. Allen, Chemical Reviews 96 (1996) 2315.
[60] W.E. Walden, Proceedings of the National Academy of Sciences of the United States of America 99 (2002) 4138.
[61] M.C. Kennedy, W.E. Antholine, H. Beinert, J. Biol. Chem. 272 (1997) 20340.
[62] T.A. Rouault, Nature Chemical Biology 2 (2006) 406.
[63] M.M. Werst, M.C. Kennedy, A.L.P. Houseman, H. Beinert, B.M. Hoffman, Biochemistry 29 (1990) 10533.
[64] K. Hantke, Current Opinion in Microbiology 4 (2001) 172.
[65] O.A. Lukianova, S.S. David, Current Opinion in Chemical Biology 9 (2005) 145.
[66] P.J. Kiley, H. Beinert, Current Opinion in Microbiology 6 (2003) 181.
[67] M.C. Kennedy, Role of iron-sulfur proteins in gene regulation, Metal Ions in Biological Systems, Vol 32, 1996, pp. 579.
[68] C.J. Walsby, D. Ortillo, J. Yang, M.R. Nnyepi, W.E. Broderick, B.M. Hoffman, J.B. Broderick, Inorg. Chem. 44 (2005) 727.
[69] J.B. Broderick, D. Coucouvanis, Current Opinion in Chemical Biology 7 (2003) 157.
[70] J.B. Broderick, C. Walsby, W.E. Broderick, C. Krebs, W. Hong, D. Ortillo, B.H. Huynh, B.M. Hoffman, Abstracts of Papers of the American Chemical Society 223 (2002) A25.
[71] J. Cheek, C. Krebs, B.H. Huynh, J.B. Broderick, Journal of Inorganic Biochemistry 86 (2001) 176.
[72] J. Cheek, J.B. Broderick, Journal of Biological Inorganic Chemistry 6 (2001) 209.
[73] S. Costanzo, S. Menage, R. Purrello, R.P. Bonomo, M. Fontecave, Inorg. Chim. Acta 318 (2001) 1.
[74] D.W. Chen, C. Walsby, B.M. Hoffman, P.A. Frey, Journal of the American Chemical Society 125 (2003) 11788.
[75] P.A. Frey, O.T. Magnusson, Chemical Reviews 103 (2003) 2129.
[76] P.A. Frey, Faseb Journal 17 (2003) A791.
[77] H.J. Sofia, G. Chen, B.G. Hetzler, J.F. Reyes-Spindola, N.E. Miller, Nucleic Acids Research 29 (2001) 1097.
[78] B.M. Hoffman, Accounts of Chemical Research 36 (2003) 522.
[79] R.H. Holm, Accounts of Chemical Research 10 (1977) 427.
[80] D.C. Yoch, R.P. Carithers, Microbiological Reviews 43 (1979) 384.
[81] A.X. Trautwein, E. Bill, E.L. Bominaar, H. Winkler, Structure and Bonding 78 (1991) 1.
[82] R.H. Holm, P. Kennepohl, E.I. Solomon, Chemical Reviews 96 (1996) 2239.
[83] I. Bertini, S. Ciurli, C. Luchinat, Structure and Bonding 83 (1995) 1.
[84] L. Noodleman, C.Y. Peng, D.A. Case, J.M. Mouesca, Coordination Chemistry Reviews 144 (1995) 199.
[85] H. Sticht, P. Rosch, Progress in Biophysics & Molecular Biology 70 (1998) 95.
[86] H. Cheng, J.L. Markley, Annual Review of Biophysics and Biomolecular Structure 24 (1995) 209.
[87] B. Guigliarelli, P. Bertrand, Advances in Inorganic Chemistry 47 (1999) 421.
[88] E.I. Solomon, X.J. Xie, A. Dey, Chemical Society Reviews 37 (2008) 623.
[89] E.L. Bominaar, S.A. Borshch, J.J. Girerd, Journal of the American Chemical Society 116 (1994) 5362.

[90] E.L. Bominaar, C. Achim, S.A. Borshch, J.J. Girerd, E. Munck, Inorganic Chemistry 36 (1997) 3689.
[91] F. Malatesta, F. Nicoletti, V. Zickermann, B. Ludwig, M. Brunori, Febs Letters 434 (1998) 322.
[92] P.V. Rao, R.H. Holm, Chemical Reviews 104 (2004) 527.
[93] P. Zanello, Coord. Chem. Rev. 83 (1988) 199.
[94] J.J. Mayerle, R.B. Frankel, R.H. Holm, J.A. Ibers, W.D. Phillips, J.F. Weiher, Proceedings of the National Academy of Sciences of the United States of America 70 (1973) 2429.
[95] J.J. Mayerle, S.E. Denmark, B.V. Depamphilis, J.A. Ibers, R.H. Holm, Journal of the American Chemical Society 97 (1975) 1032.
[96] B.A. Averill, Herskovi.T, R.H. Holm, J.A. Ibers, Journal of the American Chemical Society 95 (1973) 3523.
[97] L. Que, J.R. Anglin, M.A. Bobrik, A. Davison, R.H. Holm, Journal of the American Chemical Society 96 (1974) 6042.
[98] Depamphi.Bv, B.A. Averill, Herskovi.T, L. Que, R.H. Holm, Journal of the American Chemical Society 96 (1974) 4159.
[99] T.A. Scott, C.P. Berlinguette, R.H. Holm, H.C. Zhou, Proc. Natl. Acad. Sci. U. S. A. 102 (2005) 9741.
[100] E.P.L. van der Geer, Q. Li, G. van Koten, R. Gebbink, B. Hessen, Inorganica Chimica Acta 361 (2008) 1811.
[101] H. Ogino, S. Inomata, H. Tobita, Chemical Reviews 98 (1998) 2093.
[102] M.G. Kanatzidis, W.R. Hagen, W.R. Dunham, R.K. Lester, D. Coucouvanis, J. Am. Chem. Soc. 107 (1985) 953.
[103] S. Pohl, W. Saak, Angewandte Chemie-International Edition in English 23 (1984) 907.
[104] D. Coucouvanis, M. Kanatzidis, E. Simhon, N.C. Baenziger, J. Am. Chem. Soc. 104 (1982) 1874.
[105] K.S. Hagen, A.D. Watson, R.H. Holm, J. Am. Chem. Soc. 105 (1983) 3905.
[106] G. Christou, R.H. Holm, M. Sabat, J.A. Ibers, Journal of the American Chemical Society 103 (1981) 6269.
[107] Y. Ohki, Y. Ikagawa, K. Tatsumi, J. Am. Chem. Soc. 129 (2007) 10457.
[108] C. Goh, B.M. Segal, J.S. Huang, J.R. Long, R.H. Holm, J. Am. Chem. Soc. 118 (1996) 11844.
[109] H.C. Zhou, R.H. Holm, Inorganic Chemistry 42 (2003) 11.
[110] J. Han, M. Koutmos, S. Al Ahmad, D. Coucouvanis, Inorganic Chemistry 40 (2001) 5985.
[111] K.D. Demadis, C.F. Campana, D. Coucouvanis, Journal of the American Chemical Society 117 (1995) 7832.
[112] C. Hauser, E. Bill, R.H. Holm, Inorg. Chem. 41 (2002) 1615.
[113] P.R. Challen, S.M. Koo, W.R. Dunham, D. Coucouvanis, Journal of the American Chemical Society 112 (1990) 2455.
[114] D. Coucouvanis, P.R. Challen, S.M. Koo, W.M. Davis, W. Butler, W.R. Dunham, Inorganic Chemistry 28 (1989) 4181.
[115] E.J. Lyon, I.P. Georgakaki, J.H. Reibenspies, M.Y. Darensbourg, Angewandte Chemie-International Edition 38 (1999) 3178.

[116] E.J. Lyon, I.P. Georgakaki, J.H. Reibenspies, M.Y. Darensbourg, Journal of the American Chemical Society 123 (2001) 3268.
[117] J.D. Lawrence, H.X. Li, T.B. Rauchfuss, M. Benard, M.M. Rohmer, Angewandte Chemie-International Edition 40 (2001) 1768.
[118] F. Gloaguen, J.D. Lawrence, M. Schmidt, S.R. Wilson, T.B. Rauchfuss, Journal of the American Chemical Society 123 (2001) 12518.
[119] A.K. Justice, T.B. Rauchfuss, S.R. Wilson, Angewandte Chemie-International Edition 46 (2007) 6152.
[120] T.C. Harrop, D.T. Song, S.J. Lippard, J. Am. Chem. Soc. 128 (2006) 3528.
[121] P.V. Rao, S. Bhaduri, J.F. Jiang, D. Hong, R.H. Holm, Journal of the American Chemical Society 127 (2005) 1933.
[122] L.S. Cai, J.A. Weigel, R.H. Holm, Journal of the American Chemical Society 115 (1993) 9289.
[123] L.S. Cai, R.H. Holm, Journal of the American Chemical Society 116 (1994) 7177.
[124] J. Zhou, Z.G. Hu, E. Munck, R.H. Holm, J. Am. Chem. Soc. 118 (1996) 1966.
[125] R.H. Holm, S. Ciurli, J.A. Weigel, Prog. Inorg. Chem. 38 (1990) 1.
[126] R. Panda, Y.G. Zhang, C.C. McLauchlan, P.V. Rao, F.A.T. de Oliveira, E. Munck, R.H. Holm, J. Am. Chem. Soc. 126 (2004) 6448.
[127] V.K.K. Praneeth, C. Nather, G. Peters, N. Lehnert, Inorg. Chem. 45 (2006) 2795.
[128] D.J. Stuehr, Biochimica Et Biophysica Acta-Bioenergetics 1411 (1999) 217.
[129] F. Cutruzzola, Biochimica Et Biophysica Acta-Bioenergetics 1411 (1999) 231.
[130] A.C.F. Gorren, B. Mayer, Biochemistry-Moscow 63 (1998) 734.
[131] A.A. Nedospasov, Biochemistry-Moscow 63 (1998) 744.
[132] J.L. Zweier, A. Samouilov, P. Kuppusamy, Biochimica Et Biophysica Acta-Bioenergetics 1411 (1999) 250.
[133] D.P. Ballou, Y. Zhao, P.E. Brandish, M.A. Marletta, Proc. Natl. Acad. Sci. U. S. A. 99 (2002) 12097.
[134] D.D. Thomas, L.A. Ridnour, J.S. Isenberg, W. Flores-Santana, C.H. Switzer, S. Donzelli, P. Hussain, C. Vecoli, N. Paolocci, S. Ambs, C.A. Colton, C.C. Harris, D.D. Roberts, D.A. Wink, Free Radical Biology and Medicine 45 (2008) 18.
[135] M.P. Murphy, Biochimica Et Biophysica Acta-Bioenergetics 1411 (1999) 401.
[136] S. Tamir, S. Burney, S.R. Tannenbaum, Chem. Res. Toxicol. 9 (1996) 821.
[137] D.S. Bredt, S.H. Snyder, Annual Review of Biochemistry 63 (1994) 175.
[138] J.P. Bolanos, A. Almeida, Biochimica Et Biophysica Acta-Bioenergetics 1411 (1999) 415.
[139] V.G. Bashkatova, K.S. Rayevsky, Biochemistry-Moscow 63 (1998) 866.
[140] D.J. Singel, J.S. Stamler, Annual Review of Physiology 67 (2005) 99.
[141] O. Tashimo, T. Ishibashi, J. Yoshida, H. Tsuchida, M. Nishio, Nitric Oxide-Biology and Chemistry 9 (2003) 148.
[142] M.S. Wolin, C.A. Davidson, P.M. Kaminski, R.P. Fayngersh, K.M. Mohazzab, Biochemistry-Moscow 63 (1998) 810.
[143] J.C. Drapier, Methods 11 (1997) 319.
[144] C.E. Cooper, Biochimica Et Biophysica Acta-Bioenergetics 1411 (1999) 290.
[145] A.R. Butler, I.L. Megson, Chem. Rev. 102 (2002) 1155.
[146] F.W. Flitney, I.L. Megson, D.E. Flitney, A.R. Butler, Br. J. Pharmacol. 107 (1992) 842.
[147] J.A. McCleverty, Chem. Rev. 104 (2004) 403.

[148] B. Kalyanaraman, Methods Enzymol. 268 (1996) 168.
[149] A. Mulsch, D.J. Lurie, I. Seimenis, B. Fichtlscherer, M.A. Foster, Free Radical Biology and Medicine 27 (1999) 636.
[150] A.F. Vanin, D.I. Aliev, Stud. Biophys. 97 (1983) 223.
[151] A.M. Komarov, J.H. Kramer, I.T. Mak, W.B. Weglicki, Mol. Cell. Biochem. 175 (1997) 91.
[152] T. Yoshimura, S. Fujii, H. Yokoyama, H. Kamada, Chem. Lett. (1995) 309.
[153] R. Radi, Chemical Research in Toxicology 9 (1996) 828.
[154] K. Asanuma, K. Iijima, N. Ara, T. Koike, J. Yoshitake, S. Ohara, T. Shimosegawa, T. Yoshimura, Nitric Oxide-Biology and Chemistry 16 (2007) 395.
[155] P.A. Rogers, L. Eide, A. Klungland, H. Ding, DNA Repair 2 (2003) 809.
[156] S. Watanabe, A. Kita, K. Kobayashi, K. Miki, Proceedings of the National Academy of Sciences of the United States of America 105 (2008) 4121.
[157] H.G. Ding, B. Demple, Proceedings of the National Academy of Sciences of the United States of America 97 (2000) 5146.
[158] J.H. Enemark, R.D. Feltham, Coord. Chem. Rev. 13 (1974) 339.
[159] C.A. Brown, M.A. Pavlosky, T.E. Westre, Y. Zhang, B. Hedman, K.O. Hodgson, E.I. Solomon, J. Am. Chem. Soc. 117 (1995) 715.
[160] J. Conradie, A. Ghosh, J. Inorg. Biochem. 100 (2006) 2069.
[161] J. Conradie, D.A. Quarless, H.F. Hsu, T.C. Harrop, S.J. Lippard, S.A. Koch, A. Ghosh, J. Am. Chem. Soc. 129 (2007) 10446.
[162] V. Rajamani, C.T. Prewitt, Canadian Mineralogist 13 (1975) 75.
[163] V. Rajamani, C.T. Prewitt, Canadian Mineralogist 12 (1973) 178.
[164] V. Rajamani, C.T. Prewitt, American Mineralogist 60 (1975) 39.
[165] H.B. Gray, Manohara.Pt, J. Pearlman, R.F. Riley, Chemical Communications (1965) 62.
[166] S.D. Scott, E. Gasparrini, Canadian Mineralogist 12 (1973) 165.
[167] S.R. Hall, J.M. Stewart, Canadian Mineralogist 12 (1973) 169.
[168] K. Tsukimura, H. Nakazawa, T. Endo, O. Fukunaga, Physics and Chemistry of Minerals 19 (1992) 203.
[169] V. Rajamani, Economic Geology 71 (1976) 795.
[170] V. Rajamani, A.J. Naldrett, Economic Geology 73 (1978) 82.
[171] H.R. Chauke, D. Nguyen-Manh, P.E. Ngoepe, D.G. Pettifor, S.G. Fries, Physical Review B 66 (2002).

Chapter 2
Interconversions of Iron Sulfur Nitrosyl clusters containing $[Fe_8S_6]$, $[Fe_6S_6]$, $[Fe_4S_4]$ and $[Fe_4S_3]$ core structures.

2.1 Introduction

Nitric oxide plays a significant role as a signaling molecule in biological systems, in regulating blood pressure, neurotransmission and immune response [1-3]. The importance of NO in several physiological and pathophysiological processes in mammals [4, 5] has led to the wide use of organic and organometallic NO donor prodrugs in clinical treatments [6-8]. The interaction of NO with iron proteins [9], including Iron Sulfur clusters [10, 11], is one of the most important biological reactions in which NO participates. As a result, investigations on Iron/Sulfur/Nitrosyl clusters are of great importance. Of the various iron-sulfur nitrosyl clusters known, $(NH_4)[Fe_4S_3(NO)_7]$ [12], also known as the Roussin black salt, is the most well studied member. It is also recognized as an important physiological NO donor [13-15] in living cells.

In addition, the Roussin black salt is one of the few iron/sulfur clusters that possesses the sulfur voided $[Fe_4S_3]$ cuboidal subunit found in the core of the MoFe cofactor of Nitrogenase [16] (figure 2.1). Other clusters possessing structural subunits of similar topology include $[MoFe_3S_3]$ [17-19] and $[MS_3Fe_4S_3]$ (M=Mo,V) [20] clusters. In our investigations towards synthetic models for the nitrogenase clusters, the reactivity of

$[Fe_4S_3(NO)_7]^-$ was initially explored as a potential building block in the synthesis of clusters relevant to the FeMo cofactor of Nitrogenase.

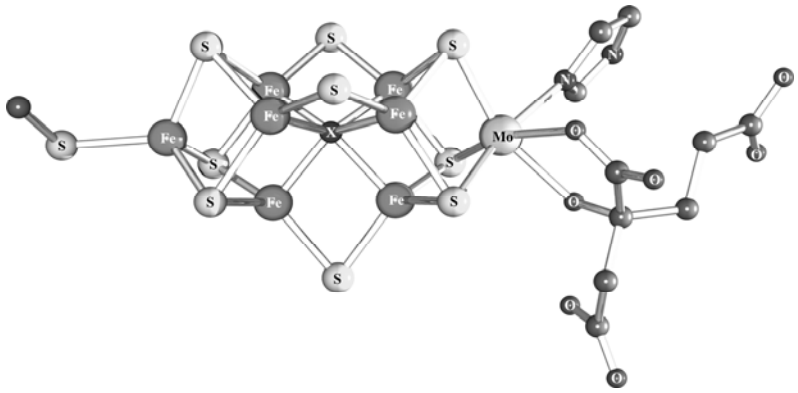

Figure 2.1. Structure of the FeMo cofactor of nitrogenase. The structure can be viewed as two M_4S_3 cuboidal units bridged by three μ_3-S atoms and a μ_6-X (X=C,N or O) interstitial atom.

In this chapter, synthesis and reactivity of some Iron/Sulfur/Nitrosyl clusters derived from the Roussin black salt are presented and interconversions of these clusters elucidate their functional and electronic properties.

2.2 Experimental Section

All the reactions were performed under nitrogen atmosphere in a glove box or by using standard Shlenck line techniques. The solvents used were distilled and degassed prior to use, except for DMF that was only degassed. The following compounds, $(NH_4)Fe_4S_3(NO)_7$ [21], $(PPN)_2Fe_4(CO)_{13}$ [22], Benzyl Trisulfide Bz_2S_3 [23], and potassium anthracenite [24] have been synthesized according to published procedures, while Bu_4NSH, $[Fe(H_2O)_6](BF_4)_2$, Tri-*n*-propylphospine PPr_3, NO and $NOBF_4$ have been purchased from commercial sources.

IR spectra were collected on a Perkin Elmer Spectrum BX FT-IR spectrometer (mid-IR) and a Nicolet 740 FT-IR spectrometer (Far-IR) in KBr pellets; mass spectra

were collected on a Micromass LCT Time-of-Flight mass spectrometer; electronic spectra collected on a Varian CARY 1E UV-Visible spectrometer; and cyclic voltammetry experiments were carried out on a glassy carbon working electrode and Ag/AgCl reference electrode in saturated AgCl/KCl aqueous solution, with 0.1M Bu_4NPF_6 as supporting electrolyte on a EG&G Princeton Potentiostat/Galvanostat model 263A. The redox potentials are reported vs. SCE. Magnetic susceptibility measurements were carried out on a MPMS SQUID magnetometer and the data were corrected for diamagnetic contributions. X-Band EPR spectra were collected on a Bruker EMX electron spin resonance spectrometer equipped with a Varian liquid nitrogen cryostat at approximately 100K. Elemental analysis was performed by the Microanalytical Laboratory at the University of Michigan. Mössbauer spectra were obtained with the high-sensitivity Mössbauer spectrometer in the Institute of Materials Science, NCSR "Demokritos" Athens, Greece, courtesy of Dr. Yiannis Sanakis.

2.2.1 Bis (Bis(triphenylphospine)iminium) hexasulfido-octairon-octanitrosyl, $(PPN)_2[Fe_8S_6(NO)_8)]$ *(Reaction 1).*

$(NH_4)[Fe_4S_3(NO)_7]$ (0.50g ,0.87 mmol) and $(PPN)_2[Fe_4(CO)_{13}]$ (2.17g 1.30 mmol) were dissolved in 20 ml MeCN and allowed to stir for 24h. The precipitate obtained by filtration was washed with 5 ml MeCN before being dissolved in 15ml DMF. The resulting solution was layered with ~ 150 ml ether, affording 0.80 g of a black crystalline product.

Yield 0.41 mmol, 94% of $(PPN)_2[Fe_8S_6(NO)_8]$ based on sulfur.

Elemental analysis calculated for $(PPN)_2[Fe_8S_6(NO)_8]\cdot DMF$ $C_{75}H_{67}N_{11}O_9P_4S_6Fe_8$ C: 44.39%, H: 3.33%, N: 7.59% Found; C: 44.75%, H: 3.48%, N: 7.36%.

IR (KBr, cm^{-1}): 3054(w), 2690(m), 2928(m), 2868(w), 1684(vs)(ν_{N-O}), 1427(m), 1263(m), 1113(m), 797(w), 744(w), 723(m), 690(m), 550(m), 532(m), 526(w), 495(w).

MS (ESI^-, m/z): 878.6 $Fe_8S_6(NO)_8^-$, 788.2 $Fe_8S_6(NO)_5^-$, 707.2 $Fe_6S_6(NO)_6^-$, 647.3 $Fe_6S_6(NO)_4^-$, 617.3 $Fe_6S_6(NO)_3^-$, 587.3 $Fe_6S_6(NO)_2^-$, 471.5 $Fe_4S_4(NO)_4^-$, 441.5 $Fe_4S_4(NO)_3^-$, 411.52 $Fe_4S_4(NO)_2^-$, and several smaller molecular weight fragments were observed below 400.

MS (ESI^+, m/z): 537.8 PPN^+

UV/Vis (DMF solution, nm): 268, 273(sh), 280(sh)

CV (DMF solution, 0.017 M): $E_{1(rev)}$ = -482 mV, $E_{2(rev)}$ = -616 mV, $E_{-3(rev)}$ = -1202 mV, $E_{4(rev)}$ = -1295 mV

2.2.2 Bis (Bis(triphenylphospine)iminium) hexasulfido-hexairon-hexanitrosyl, $(PPN)_2[Fe_6S_6(NO)_6)]$

Method A *(Reaction 2)*:

$(PPN)[Fe_4S_3(NO)_7]$ (0.50g, 0.47 mmol) and $(PPN)_2[Fe_4(CO)_{13}]$ (0.78g, 0.47 mmol) were dissolved in 20ml MeCN, followed by the addition of Bz_2S_3 (0.39g, 1.40 mmol) and the resulting mixture was heated under reflux for 24 hours. After cooling at room temperature, the precipitate obtained by filtration was washed with 5 ml MeCN and dissolved in 15ml DMF. The resulting solution was layered with ~ 150 ml ether, affording 0.88 g of a black crystalline product.

Yield 0.49 mmol, 79% of $(PPN)_2[Fe_6S_6(NO)_6]$, based on total Fe content.

Method B *(Reaction 3):*

$(PPN)_2[Fe_8S_6(NO)_8]$ (0.23g, 0.12 mmol) was dissolved in 10ml DMF and Bz_2S_3 (0.1g, 0.36 mmol) was added and the solution stirred for 24h. The solution was filtered and layered with ~ 100 ml ether, affording 0.18g of black crystalline product.

Yield 0.10 mmol, 84% of $(PPN)_2[Fe_6S_6(NO)_6]$.

Elemental analysis calculated for $(PPN)_2[Fe_6S_6(NO)_6]$, $C_{72}H_{60}N_8O_6P_4S_6Fe_6$ C: 48.46%, H: 3.39%, N: 6.28%. Found; C: 47.90%, H: 3.65%, N: 7.33% .

IR (KBr, cm^{-1}): 2690(m), 2928(m), 2868(w), 1679(vs) (ν_{N-O}), 1669(vs) (ν_{N-O}), 1435(m), 1262(m), 1116(m), 803(w), 743(w), 723(m), 692(m), 687(m), 546(m), 531(m), 523(w), 498(w).

MS (ESI^-, m/z): 1245.31 $(PPN)Fe_6S_6(NO)_6^-$, 707.26 $Fe_6S_6(NO)_6^-$, 647.27 $Fe_6S_6(NO)_4^-$, 617.28 $Fe_6S_6(NO)_3^-$, 587.28 $Fe_6S_6(NO)_2^-$, 557.31 $Fe_6S_6(NO)^-$, 471.49 $Fe_4S_4(NO)_4^-$, 441.49 $Fe_4S_4(NO)_3^-$, 411.52 $Fe_4S_4(NO)_2^-$, and several smaller molecular weight fragments were observed below 400.

MS (ESI^+, m/z): 537.78 PPN^+

UV/Vis (DMF solution, nm): 266, 273(sh), 280(sh), 336(sh)

CV (DMF solution, 0.019 M): $E_{1(rev)}$ = -690 mV, , $E_{2(rev)}$ = -1521 mV

2.2.3 Bis (Bis(triphenylphospine)iminium) tetrasulfido-tetrairon-tetranitrosyl, $(PPN)_2[Fe_4S_4(NO)_4]$.

Method A *(Reaction 4):*

$(PPN)[Fe_4S_3(NO)_7]$ (0.50g, 0.47 mmol) and $(PPN)_2[Fe_4(CO)_{13}]$ (1.17g, 0.70 mmol) were dissolved in 20ml MeCN, followed by the addition of Bu_4NSH (0.13g, 0.47 mmol) in 5ml MeCN and the mixture was heated under reflux for 24 h. After cooling at room temperature, the resulting precipitate obtained by filtration was washed with 5ml MeCN, extracted with ~ 15 ml DMF and layered with ~ 100 ml ether, affording 0.35g of microcrystalline product.

Yield 0.23 mmol, 24.5 % of $(PPN)_2Fe_4S_4(NO)_4$ based on sulfur.

Elemental analysis calculated for $(PPN)_2[Fe_4S_4(NO)_4]$ $C_{72}H_{60}N_6O_4P_4S_4Fe_4$ C: 55.39%, H: 3.90%, N: 5.43%. Found; C: 51.49%, H: 3.49%, N: 5.96%.

Method B *(Reaction 5):*

$(PPN)_2[Fe_8S_6(NO)_8]$ (0.20g, 0.10 mmol) and Bu_4NSH (0.17g, 0.62 mmol) were dissolved in 10ml DMF and heated at 80 ºC for 24h. The resulting mixture was cooled at room temperature, filtered, and the solution layered with ~ 100 ml ether, affording 0.22g of microcrystalline product.

Yield 0.14 mmol, 68.75% of $(PPN)_2Fe_4S_4(NO)_4$.

Elemental analysis calculated for $(PPN)_2[Fe_4S_4(NO)_4]$ $C_{72}H_{60}N_6O_4P_4S_4Fe_4$ C: 55.39%, H: 3.90%, N: 5.43%. Found; C: 52.04%, H: 4.10%, N: 5.88%.

IR (KBr, cm^{-1}): 2690(m), 2928(m), 2868(w), 1652(vs) ($\nu_{N\text{-}O}$), 1435(m), 1262(m), 1116(m), 803(w), 743(w), 723(m), 692(m), 687(m), 546(m), 531(m), 523(w), 498(w).

MS (ESI^-, m/z): 471.5 $Fe_4S_4(NO)_4^-$, 441.5 $Fe_4S_4(NO)_3^-$, 411.5 $Fe_4S_4(NO)_2^-$and several smaller molecular weight fragments were observed below 400.

MS (ESI^+, m/z): 537.7 PPN^+

UV/Vis (DMF solution, nm): 266, 273(sh), 280(sh)

CV (DMF solution, 0.022 M): $E_{1(rev)}$ = -202 mV, $E_{2(rev)}$ = -1279 mV

2.2.4. Isolation of Bis(Bis(triphenylphospine)iminium) tetrasulfido-tetrairon-hexanitrosyl, $(PPN)_2[Fe_4S_4(NO)_6]$ *(Reaction 6).*

$(NH_4)[Fe_4S_3(NO)_7]$ (0.20g, 0.35 mmol) and $(PPN)_2[Fe_4(CO)_{13}]$ (0.87g 0.52 mmol) were dissolved in 15ml MeCN, the mixture was cooled to -20°C followed by the addition of a 2ml solution of Bu_4NSH (0.05g, 0.19 mmol) in MeCN. The mixture was stirred for 8h at -20°C, filtered, and the precipitate was washed with MeCN and extracted with ~ 5 ml DMF and layered with ~ 50 ml ether, left for 2 days in the freezer, filtered again to

remove any $(PPN)_2[Fe_4S_4(NO)_4]$ that formed and the filtrate layered with additional 100 ml ether, affording 0.08g of green brown microcrystalline product.

Yield 0.07 mmol, 14% of $(PPN)_2[Fe_4S_4(NO)_6]$ based on $[Fe_4S_3(NO)_7]^-$

Elemental analysis for $(PPN)_2[Fe_4S_4(NO)_6]\cdot 2DMF$ $C_{78}H_{74}N_{10}O_8P_4S_4Fe_4$ C: 53.38%, H: 4.25%, N: 7.98%. Found, C: 53.92%, H: 4.20%, N: 7.33%

IR (KBr, cm^{-1}): 2962(w), 2930(w), 2861(w), 1700(vs) ($\nu_{N\text{-}O}$), 1668(vs) ($\nu_{N\text{-}O}$), 1435(m), 1262(m), 1115(m), 840(w), 746(w), 723(m), 692(m), 687(m), 546(m), 531(m), 523(w), 496(w).

MS (ESI^-, m/z): 525.4 $Fe_4S_4(NO)_6^-$, 495.6 $Fe_4S_4(NO)_5^-$, 467.8 $Fe_4S_4(NO)_4^-$ 438.1 $Fe_4S_4(NO)_3^-$

MS (ESI^+, m/z): 535.3 PPN^+

2.2.5 Reduction of $(PPN)_2[Fe_8S_6(NO)_8]$ with potassium anthracenite. *(Reaction 7)*

$(PPN)_2[Fe_8S_6(NO)_8]$ (0.2 g, 0.10mmol) was dissolved in 20ml THF followed by the dropwise addition of potassium anthracenite 0.11M in THF (4.2 ml, 0.43 mmol) and the mixture stirred overnight. This caused the formation of an oily precipitate and a deeply colored solution. The mixture was filtered and the THF filtrate was layered with ca. 100 ml ether while the precipitate was washed with THF, dissolved in ~ 10ml DMF and layered with ~ 100ml ether. Both fractions afforded black crystalline material.

THF fraction gave 0.08g of microcrystalline $(PPN)_4[Fe_8S_6(NO)_8]$ while the DMF fraction gave 0.12g of crystalline $K_4[Fe_8S_6(NO)_8]\cdot 13DMF$

Tetra (Bis(triphenylphospine)iminium) hexasulfido-octairon-octanitrosyl, $(PPN)_4[Fe_8S_6(NO)_8]$

Yield 0.03 mmol, 30% of $(PPN)_4[Fe_8S_6(NO)_8]$

Elemental analysis calculated for $(PPN)_4[Fe_8S_6(NO)_8]$ $C_{144}H_{120}Fe_8N_{12}O_8P_8S_6$ C:57.01%, H: 3.99%, N: 5.54%. Found C:56.32%, H:4.10%, N:5.46%

IR (KBr, cm^{-1}): 3053(w), 2926(w), 2865(w), 1738 (m) ($\nu_{N\text{-}O}$),1686(vs) ($\nu_{N\text{-}O}$), 1437(m), 1256(m), 1114(m), 745(w), 723(m), 692(m), 549(w), 533(m), 497(m).

MS (ESI^-) m/z: 879 $Fe_8S_6(NO)_8^-$, 788 $Fe_8S_6(NO)_5^-$, 707 $Fe_6S_6(NO)_6^-$, 647 $Fe_6S_6(NO)_4^-$, 617 $Fe_6S_6(NO)_3^-$, 587 $Fe_6S_6(NO)_2^-$, 470 $Fe_4S_4(NO)_4^-$, 441 $Fe_4S_4(NO)_3^-$

MS (ESI^+) m/z: 538 PPN^+

Tetrakis Potassium hexasulfido-octairon-octanitrosyl, $K_4[Fe_8S_6(NO)_8]\cdot 13DMF$

Yield 0.06 mmol, 60% of $K_4[Fe_8S_6(NO)_8]\cdot 13DMF$

Elemental analysis calculated for $K_4[Fe_8S_6(NO)_8]\cdot 13DMF$ $C_{42}H_{98}Fe_8N_{22}O_{22}S_6$ C:24.50%, H: 4.80%, N: 14.97%. Found C:26.02%, H:5.31%, N:15.28%

IR (KBr, cm^{-1}): 2926(w), 2874(w), 1738(m) ($\nu_{N\text{-}O}$),1682(vs) ($\nu_{N\text{-}O}$), 1495(m), 1437(m), 1411(m), 1387(m), 1256(m), 1098(m), 664(m), 583(w).

MS (ESI^-, m/z): 918 $KFe_8S_6(NO)_8^-$, 879 $Fe_8S_6(NO)_8^-$, 863 , 849 $Fe_8S_6(NO)_7^-$, 816, 793 $Fe_7S_6(NO)_7^-$, 763 $Fe_7S_6(NO)_6^-$, 703 $Fe_7S_6(NO)_4^-$, 674 $Fe_7S_6(NO)_3^-$, 647 $Fe_6S_6(NO)_4^-$, 471 $Fe_4S_4(NO)_4^-$, 439 $Fe_4S_3(NO)_4^-$, 409 $Fe_4S_3(NO)_3^-$.

MS (ESI^+, m/z): Low m/z unidentifiable peaks.

2.2.6 Reactions of $(PPN)_2[Fe_8S_6(NO)_8]$ with oxidizing agents.

a) With O_2 *(Reaction 8)*.

$(PPN)_2[Fe_8S_6(NO)_8]$ (0.2g, 0.11 mmol) was dissolved in 10ml DMF and O_2 was bubbled through the solution for 5 min. The mixture was stirred for 1h and filtered to remove a light brown powder and layered with ether affording 0.10g of crystalline

material, which was identified as $[Fe(DMF)_6][Fe_6S_6(NO)_6]$ by IR, MS and Unit Cell determination.

Yield 0.08 mmol, 75.64 % of $[Fe(DMF)_6][Fe_6S_6(NO)_6]$

IR (KBr, cm^{-1}): 2961(w), 2926(w), 2873(w) 1705(vs) (ν_{N-O}),1684(vs) (ν_{N-O}), 1666(vs) (ν_{C-O}), 1643(vs) (ν_{C-O}), 1495(w), 1456(w), 1431(w), 1411(w), 1375(m), 1249(w), 1109(m), 1060(w), 865(w), 802(w), 757(w), 686(m), 681(m), 582(w).

MS (ESI^-, m/z): Identical to $[Fe_6S_6(NO)_6]^{2-}$ described in Reaction 2 above.

MS (ESI^+, m/z): 538 $Fe(DMF)_6^+$, 354 $Fe(DMF)_4^+$, 277 $Fe(DMF)_3^+$, 247, 210, 174

b) With $[Fe(Cp)_2]PF_6$ *(Reaction 9)*

$(PPN)_2[Fe_8S_6(NO)_8]$ (0.2g, 0.11 mmol) was dissolved in 10ml DMF and $[Fe(Cp)_2]PF_6$ (0.14g, 0.42 mmol) was added. The mixture was stirred overnight, filtered, and the filtrate layered with ether, affording 0.05g of crystalline $[Fe(DMF)_6][Fe_6S_6(NO)_6]$ as identified by IR and MS.

Yield 0.04 mmol, 37.8 % of $[Fe(DMF)_6][Fe_6S_6(NO)_6]$

c) With SCl_2 *(Reaction 10)*

$(PPN)_2[Fe_8S_6(NO)_8]$ (0.2g, 0.11 mmol) was dissolved in 20 ml dichloroethane prior to the dropwise addition of a 10% SCl_2 solution in dichloroethane (0.07 ml, 0.11 mmol) and the solution was stirred for 1h. The mixture was filtered and the precipitate was dissolved in DMF and layered with ether, affording a powder that was identified by IR as $[Fe(DMF)_6][Fe_6S_6(NO)_6]$.

The filtrate of this solution was layered with ~ 20ml ether, filtered to remove a white powder of PPNCl, and then layered with additional 40ml ether to obtain 0.08g light green needle shaped crystals of $(PPN)[FeCl_3(NO)]$.

The unit cell was identical to the known (PPN)[$Fe(CO)_3(NO)$] complex [25], and displayed IR characteristic peaks at 1794cm^{-1} (ν_{N-O}) and 350cm^{-1} (ν_{Fe-Cl}). Elemental analysis confirmed that the crystals are (PPN)[$FeCl_3(NO)$], apparently isomorphous to the (PPN)[$Fe(CO)_3(NO)$]complex, and the NO stretching frequency is comparable to the reported value from CH_2Cl_2 solutions of (PPN)[$FeCl_3(NO)$] at 1802cm^{-1}[26].

Yield 0.17 mmol, 80% of (PPN)[$FeCl_3(NO)$]

Elemental analysis for (PPN)[$FeCl_3(NO)$] $C_{36}H_{30}N_2OP_2Cl_3Fe$ C: 59.17%, H: 4.14%, N: 3.83%. Found; C: 58.86%, H: 3.99%, N: 3.66%.

IR (KBr, cm^{-1}): 3052(w), 2917(w), 2848(w), 1794(vs) (ν_{N-O}), 1436(s), 1244(s), 1114(s), 998(w), 795(w), 749(m), 723(s), 692(s), 550(s), 533(m), 500(m), 350(s) (ν_{Fe-Cl})

2.2.7 Reactions of $(PPN)_2[Fe_8S_6(NO)_8]$ with $NOBF_4$ and NO gas.

a) With $NOBF_4$ *(Reaction 11)*

$(PPN)_2[Fe_8S_6(NO)_8]$ (0.2g, 0.11 mmol) was dissolved in 20ml dichloroethane and a solution of $NOBF_4$ (0.09g, 0.77 mmol) in 2 ml THF was added dropwise. The mixture stirred for 1 hour and filtered. The precipitate was dissolved in DMF and layered with ether, affording $[Fe(DMF)_6][Fe_6S_6(NO)_6]$ as confirmed by IR and MS, while the dichloroethane filtrate was layered with ether, affording a mixture of black crystals, identified as by IR and MS as (PPN)$[Fe_4S_3(NO)_7]$, and a white powder that was identified by IR as $PPN(BF_4)$.

(PPN)$[Fe_4S_3(NO)_7]$

IR (KBr, cm^{-1}): 3051(w), 3052(w), 1797(s) (ν_{N-O}), 1762(vs) (ν_{N-O}), 1731(vs) (ν_{N-O}), 1703(vs) (ν_{N-O}), 1586(m), 1482(w), 1438(s), 1286(s), 1270(m), 1186(w), 1115(s)

1073(w), 1025(w), 997(m), 743(m), 722(s), 692(s), 688(s), 661(w), 615(w), 545(s), 532(s), 526(m), 500(s), 459(w)

b) With NO *(Reaction 12)*

$(PPN)_2[Fe_8S_6(NO)_8]$ (0.2g, 0.11 mmol) was placed in a Schlenk line flask and dissolved in 20 ml DMF. The flask was connected to an oil bubbler and using a needle, NO gas was allowed to bubble through the solution for 5 min under vigorous stirring. The solution was then filtered and the solvent removed under vacuum. The remaining 0.16g black powder was identified by IR and MS as $(PPN)[Fe_4S_3(NO)_7]$ (yield 69.5% based on iron)

2.2.8 Reactions of $(PPN)_2[Fe_6S_6(NO)_6]$ with Fe^{2+} or Fe^0

a) With $Fe(H_2O)_6(BF_4)_2$ / PPr_3 *(Reaction 13)*

$(PPN)_2[Fe_6S_6(NO)_6]$ (0.2g, 0.11mmol) and $Fe(H_2O)_6(BF_4)_2$ (0.08g, 0.24 mmol) were suspended in 20ml of THF/MeCN 1:1 ratio, and PPr_3 (0.05ml, 0.25 mmol) was added dropwise. The mixture was stirred overnight, filtered, and the solution layered with ether, affording 0.12g of crystalline material. The material was identified as $(PPN)_2[Fe_8S_6(NO)_8]$ by IR, MS and cyclic voltammetry, without any evidence suggesting the presence of a different species.

Yield 0.06mmol, 55% of $(PPN)_2[Fe_8S_6(NO)_8]$

b) With $Fe(CO)_5$ *(Reaction 14)*

$(PPN)_2[Fe_6S_6(NO)_6]$ (0.2g, 0.11mmol) was dissolved in a solution of 20ml THF/MeCN 1:1 ratio and $Fe(CO)_5$ (0.03ml, 0.23mmol) was added dropwise. The mixture was stirred overnight, filtered, and the filtrate layered with ether, affording 0.10g of a

microcrystalline material. The material was identified as $(PPN)_2[Fe_8S_6(NO)_8]$ by IR and MS.

Yield 0.05mmol, 46% of $(PPN)_2[Fe_8S_6(NO)_8]$.

2.2.9 Reactions of $(PPN)_2[Fe_6S_6(NO)_6]$ with $NOBF_4$ and NO gas.

a) With $Fe(H_2O)_6(BF_4)_2$ /$NOBF_4$ *(Reaction 15)*

$(PPN)_2[Fe_6S_6(NO)_6]$ (0.2g, 0.11 mmol) and $Fe(H_2O)_6(BF_4)_2$ (0.08g, 0.23mmol) were dissolved in 20ml dichloroethane, followed by the addition of $NOBF_4$ (0.06g, 0.51mmol). The mixture was stirred for 4 hours, filtered and the filtrate was layered with ether, affording 0.12g $(PPN)[Fe_4S_3(NO)_7]$ (yield 70% based on iron) as verified by IR and MS.

b) With NO *(Reaction 16)*

$(PPN)_2[Fe_6S_6(NO)_6]$ (0.2g, 0.11 mmol) was placed in a Schlenk line flask and dissolved in 20 ml DMF. The flask was connected to an oil bubbler and using a needle, NO gas was allowed to bubble through the solution for 5 min under vigorous stirring. The solution was then filtered and the solvent removed under vacuum. The remaining 0.13g of black powder were identified by IR and MS as $(PPN)[Fe_4S_3(NO)_7]$ (yield 84% based on iron)

2.2.10. Crystallographic Data

All diffraction data were collected at the University of Michigan X-Ray facility, at low temperatures ranging from 85(2) to 123(2) K to avoid decay during data collection, using a Siemens SMART CCD-based X-Ray diffractometer equipped with an LT-2 low temperature device and normal focus Mo-target X-ray tube (λ = 0.71073 Å). All

diffraction data were processed with SADABS for absorption correction. The positions of heavy atoms were found by direct methods in E-maps using the software solution program in SHELXTL v.6.1. Subsequent cycles of least-squares refinement followed by difference Fourier synthesis produced the positions of the remaining non-hydrogen atoms; they were refined anisotropically unless stated otherwise. All hydrogen atoms were placed in ideal positions and refined as riding atoms with individual (or group if appropriate) isotropic thermal displacement parameters. The compounds $(PPN)_2[Fe_8S_6(NO)_8]$ (Table 2.1), $(PPN)_2[Fe_6S_6(NO)_6]\cdot 2DMF$ (Table 2.2), $K_4[Fe_8S_6(NO)_8]\cdot 13DMF$ (Table 2.3) and $(PPN)_2[Fe_4S_4(NO)_6]$ (Table 2.4) have been structurally characterized. All space group assignments were determined based on systematic absences and intensity statistics and were confirmed by the program XPREP of the SHELXTL package.

$(PPN)_2[Fe_8S_6(NO)_8]$	
Color	Black
Habit	Block
Size (mm)	0.28 x 0.32 x 0.40
Formula	$C_{76}H_{70}Fe_8N_{10}O_9P_4S_6$
Weight ($g \cdot mol^{-1}$)	2017.43
Crystal System	Triclinic
Space Group	P -1
Unit Cell (Å) (a,b,c, α,β,γ)	10.8007(11)
	14.6681(15)
	14.9851(15)
	117.4000(10)
	97.671(2)
	96.071(2)
Volume ($Å^3$)	2050.8(4)
Z	1
Temperature (K)	123(2)
Absorption coefficient	1.634
F(0,0,0)	1024
θ range (deg)	2.95 to 28.33
Reflections	27863
Limiting indices	-14<h<14,
	-19<k<19,
	-19<l<19
R_{int}	0.0192
Data / restraints / parameters	18424/3/1010
R_1, wR_2 [I>2σ(I)]	0.0305, 0.0796
R_1, wR_2 (all data)	0.0393, 0.0853
GooF (F^2)	1.019

Table 2.1. Crystallographic and refinement data for $(PPN)_2[Fe_8S_6(NO)_8]$

$(PPN)_2[Fe_6S_6(NO)_6]\cdot 2DMF$	
Color	Black
Habit	Block
Size (mm)	0.44 x 0.30 x 0.26
Formula	$C_{78}H_{74}Fe_6N_{10}O_8P_4S_6$
Weight ($g\cdot mol^{-1}$)	1930.81
Crystal System	Triclinic
Space Group	P -1
Unit Cell (Å) (a,b,c, α,β,γ)	13.0510(14)
	13.3561(14)
	13.3741(14)
	118.473(2)
	91.213(2)
	95.004(2)
Volume ($Å^3$)	2036.2(4)
Z	1
Temperature (K)	150(2)
Absorption coefficients	1.334
F(0,0,0)	988
Θ range (deg)	3.00 to 28.33
Reflections	28490
Limiting indices	-17 < h < 17
	-17 < k < 17
	-17 < l < 17
R_{int}	0.0256
Data / restraints / parameters	9974 / 0 / 502
R_1, wR_2 [I>2σ(I)]	0.0284, 0.0716
R_1, wR_2 (all data)	0.0384, 0.07711
GooF (F^2)	1.022

Table 2.2. Crystallographic and refinement data for $(PPN)_2[Fe_6S_6(NO)_6]\cdot 2DMF$

$K_4[Fe_8S_6(NO)_8]\cdot 13DMF$	
Color	Black
Habit	Needle
Size (mm)	0.18 x 0.20 x 0.40
Formula	$C_{39}H_{91}Fe_8K_4N_{21}O_{21}S_6$
Weight ($g\cdot mol^{-1}$)	1985.89
Crystal System	Triclinic
Space Group	P -1
Unit Cell (Å) (a,b,c, α,β,γ)	12.1213(15)
	15.5851(19)
	22.2184(27)
	88.524(2)
	85.214(2)
	68.149(2)
Volume ($Å^3$)	3882(1)
Z	2
Temperature (K)	123(2)
Absorption coefficients	1.9021
F(0,0,0)	2040
θ range (deg)	1.84 to 28.33
Reflections	85250
Limiting indices	$-16 < h < 16$
	$-20 < k < 20$
	$-29 < l < 29$
R_{int}	0.0491
Data / restraints / parameters	19256 / 0 / 931
R_1, wR_2 [$I>2\sigma(I)$]	0.0546, 0.1726
R_1, wR_2 (all data)	0.0917, 0.2008
GooF (F^2)	1.027

Table 2.3. Crystallographic and refinement data for $K_4[Fe_8S_6(NO)_8]\cdot 13DMF$

$(PPN)_2[Fe_4S_4(NO)_6]$	
Color	Brown
Habit	Needle
Size (mm)	0.60 x 0.04 x 0.04
Formula	$C_{78}H_{74}Fe_4N_{10}O_8P_4S_4$
Weight ($g \cdot mol^{-1}$)	1754.99
Crystal System	Triclinic
Space Group	P -1
Unit Cell (Å) (a,b,c, α,β,γ)	10.951(6)
	12.345(7)
	28.632(15)
	90.021(9)
	94.034(9)
	90.127(9)
Volume ($Å^3$)	3861(4)
Z	2
Temperature (K)	123(2)
Absorption coefficients.	0.991
F(0,0,0)	1808
θ range (deg)	1.80 to 19.27
Reflections	32467
Limiting indices	$-10 < h < 10$
	$-11 < k < 11$
	$-26 < l < 26$
R_{int}	0.1486
Data / restraints / parameters	6428 / 0 / 978
R_1, wR_2 [$I>2\sigma(I)$]	0.0573, 0.1372
R_1, wR_2 (all data)	0.1235, 0.1781
GooF (F^2)	1.029

Table 2.4. Crystallographic and refinement data for $(PPN)_2[Fe_4S_4(NO)_6]$

2.3 Results and Discussion

In the case of Metal-Nitrosyl complexes, assignment of formal oxidation states for both the metal and the nitrosyl ligand is not trivial. This is due to the highly covalent nature of the M-NO bond in which the ligand can be described as NO^+, $NO\cdot$ or NO^-. It has been recognized that the best method of describing M-NO complexes is by treating them as functional groups using the Enemark-Feltham notation [27] $\{M(NO)_x\}^n$,where n is the number of electrons located on the d orbitals of the metal and the π^* orbitals of NO. An advantage of this method, is that electronic relationships between similar metal-nitrosyl species can be derived without the need to specify in advance the formal oxidation states of the metal and the NO ligands individually.

For the $[Fe_4S_3(NO)_7]^-$ cluster that consists of one $\{FeNO\}^7$ and three $\{Fe(NO)_2\}^9$ functional groups, the most recent description based on DFT calculations and UV spectroscopy [28] is that the cluster is better described as an 4Fe(III)/ $7NO^-$ system. In this description, both $\{FeNO\}^7$ and $\{Fe(NO)_2\}^9$ units consist of high spin Fe(III) S=5/2 atoms antiferromagnetically coupled to NO^- S=1 molecules, giving rise to the $\{FeNO\}^7$ S=3/2 and $\{Fe(NO)_2\}^9$ S=1/2 units respectively. In addition, the $\{FeNO\}^7$ S=3/2 unit is antiferromagnetically coupled to the three $\{Fe(NO)_2\}^9$ S=1/2 units leading to an overall S=0 ground state for the $[Fe_4S_3(NO)_7]^-$ cluster.

In earlier studies, however [29], the $[Fe_4S_3(NO)_7]^-$ cluster had been described as a Fe(0)/3Fe(I) system with NO^+, based on Huckel calculations, and the interconversions between the $[Fe_4S_3(NO)_7]^-$, $[Fe_2S_2(NO)_4]^{2-}$ and $[Fe_4S_4(NO)_4]$ clusters that occur, according to the following non stoichiometric equations:

$$[Fe_2S_2(NO)_2]^{2-} \underset{OH^-}{\overset{H^+}{\rightleftharpoons}} [Fe_4S_3(NO)_7]^- \underset{Na/Hg}{\overset{S_8}{\rightleftharpoons}} Fe_4S_4(NO)_4 \quad \text{(eq. 1)}$$

The assignment of the NO ligands as NO^+ by Glidewell and Hoffman et al. [29] in 1985, although consistent with the reactivity of the clusters, was mainly implied by the results rather than the calculations on spin densities and charges as was done in the recent calculations by Jarowska et al. [28] in 2006. In addition, these studies from Glidewell and Hoffman were done almost 10 years before the introduction of the Fe(III)-NO^- description by Solomon et al. [30] regarding the S=3/2 $\{FeNO\}^7$ species.

As it will become evident from the discussion below, the assignment of the NO ligands as NO^- provides a better interpretation of the results presented in this chapter, whenever such a distinction is necessary. It should be noted though, that the assignment of the iron oxidation states in the Roussin Black Salt as Fe(III) is rather simplistic, as it does not comply with the overall chemical behavior of the cluster. Furthermore, in the calculations made by Jarowska, excited states containing Fe(II)-NO^0 descriptions lie very close in energy to the ground state, implying that in these Fe/S/NO clusters charge transfer from the nitrosyl to the metal and vice versa is readily accessible.

Despite the preference for the NO^- description, the studies of Glidewell and Hoffman [29] provide an elegant explanation for the behavior of the Fe/S/NO clusters, as they predict the fragmentation of these clusters to smaller units upon oxidation or reduction. The basis of this fragmentation is the presence of antibonding orbitals (with respect to the iron framework) beneath and above the HOMO orbital, in both the $[Fe_4S_3(NO)_7]^-$ and $[Fe_4S_4(NO)_4]$ clusters. In our perspective, the concept that these conversions of Fe/S/NO clusters could occur through a fragmentation mechanism is a very important feature, and as it will be demonstrated, provides a rationalization for the behavior of the clusters presented in this chapter.

2.3.1 Synthesis and Reactivity

The clusters reported herein can be described as interconversions between tetra-, hexa-, and octa- [FeS(NO)] fragments derived from the $[Fe_4S_3(NO)_7]^-$ cluster as shown in Scheme 2.2. Most of the reactions have been proven reversible by treating the complexes with the appropriate reagents. In general, these conversions, given the variety of reagents tested and conditions employed, appear to be the most thermodynamically stable members of this family of clusters.

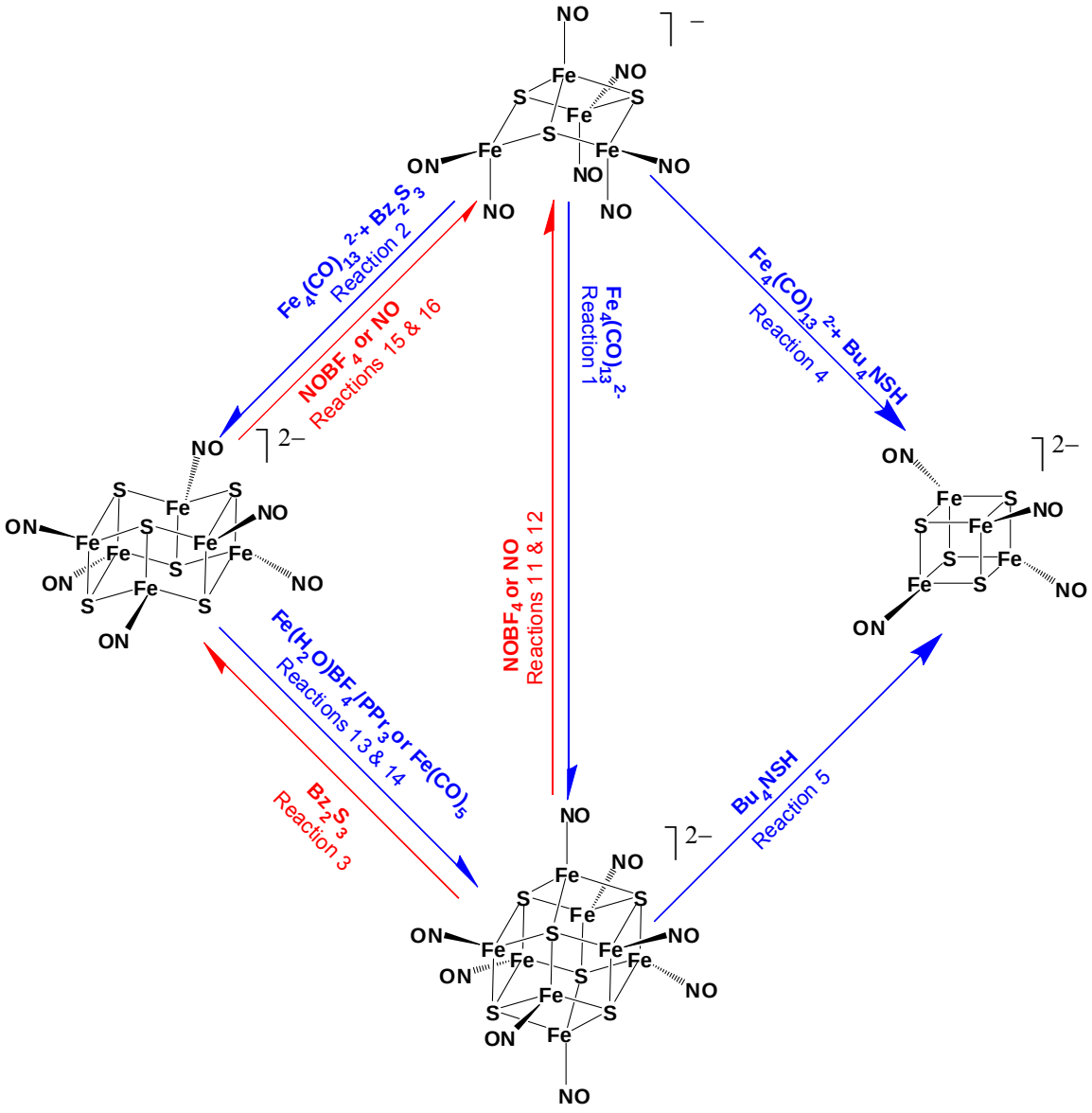

Figure 2.2: The interconversions between the Fe/S/NO clusters presented in this chapter

The octanuclear iron-sulfur nitrosyl cluster $(PPN)_2[Fe_8S_6(NO)_8]$ is obtained in high yield from the reaction of $(NH_4)[Fe_4S_3(NO)_7]$ with $(PPN)_2[Fe_4(CO)_{13}]$ in a 2:3 ratio (Reaction 1). This reaction appears to proceed through the abstraction of nitrosyls from $[Fe_4S_3(NO)_7]^-$ by the $[Fe_4(CO)_{13}]^{2-}$ cluster and the possible formation of an $[Fe_4S_3(NO)_4]^-$ intermediate, which subsequently self couples to form the $[Fe_8S_6(NO)_8]^{2-}$ cluster. Other products of this reaction that have been verified by IR and MS are $(PPN)[Fe(CO)_3(NO)]$ and a small amount of $(PPN)[Fe_4N(CO)_{12}]$. Although the reported synthesis of $(PPN)[Fe(CO)_3(NO)]$ is from $PPNNO_2$ and $Fe(CO)_5$ [31], in this case it seems to have been obtained from the reaction of the abstracted NO with $[Fe_4(CO)_{13}]^{2-}$, or fragments of it, given the labile nature of iron carbonyl clusters. The $[Fe_4N(CO)_{12}]^-$ cluster derives from a concurrent side reaction of $Fe_3(CO)_9$ with $[Fe(CO)_3(NO)]^-$ [32]. The reaction process was not followed spectroscopically because of the nature of the compounds involved that contain very strong interfering spectroscopic signals. In addition, the use of isotopic labeling with ^{57}Fe to show if the $[Fe_4(CO)_{13}]^{2-}$ cluster is involved as an iron source for the formation of $[Fe_8S_6(NO)_8]^{2-}$ has not been pursued because of the synthetic limitations (low yields and/or multi step processes) and cost of such an experiment. Taking into account the observed products and the high yield (94% based on Sulfur), a possible stoichiometric overall reaction is the following (eq. 2):

$$4[Fe_4S_3(NO)_7]^- + 3[Fe_4(CO)_{13}]^{2-} \longrightarrow 2[Fe_8S_6(NO)_8]^{2-} + 12[Fe(CO)_3(NO)]^- + 3CO \quad \text{(eq. 2)}$$

The use of excess of $(PPN)_2[Fe_4(CO)_{13}]$ with a 2:3 $(NH_4)[Fe_4S_3(NO)_7]$: $(PPN)_2[Fe_4(CO)_{13}]$ ratio instead of the stoichiometric 4:3, was chosen as an alternative to increase the amount of PPN^+ ion in the mixture. Otherwise, the use of $(PPN)[Fe_4S_3(NO)_7]$ would require heating during the reaction, as it is less reactive than

its NH_4^+ analogue, and the $[Fe_8S_6(NO)_8]^{2-}$ cluster is unstable at prolonged heating at high temperatures.

Besides the reactions with sulfur donors as seen in Figure 2.2, the $[Fe_8S_6(NO)_8]^{2-}$ cluster reacts with oxidizing agents, such as $FeCp_2$, O_2 and SCl_2 (Reactions 8, 9 and 10 from the experimental section) forming $[Fe_6S_6(NO)_6]^{2-}$ as the main product in all cases. The reaction seems to proceed through removal of iron from the cluster as in coordinating solvents L, the isolated product is $[Fe(II)L_6][Fe_6S_6(NO)_6]$, while in non coordinating solvents there is formation of a brown powder that is presumed to contain iron, but was not further characterized. The only exception is in the reaction with SCl_2, that in addition to $[Fe(DMF)_6][Fe_6S_6(NO)_6]$, $(PPN)[FeCl_3(NO)]$ was also isolated and characterized. This behavior is in accordance to the more oxidized nature of $[Fe_6S_6(NO)_6]^{2-}$ that contains $2\{FeNO\}^8$ and $4\{FeNO\}^7$ units, compared to the $[Fe_8S_6(NO)_8]^{2-}$ cluster that contains $6\{FeNO\}^8$ and $2\{FeNO\}^7$ units. A general reaction (eq. 3) relating the two clusters can be written as:

$$[Fe_8S_6(NO)_8]^{2-} \longrightarrow [Fe_6S_6(NO)_6]^{2-} + 2\{FeNO\}^8 + 2e^- \quad \text{(eq. 3)}$$

The fate of the unstable $\{FeNO\}^8$ units is the formation of more stable Fe species such as $[FeL_6]^{2+}$ and $[FeCl_3(NO)]^-$ described above. In the presence of S^0, as in the case of Bz_2S_3, these $\{FeNO\}^8$ units could theoretically be utilized to form Fe/S/NO clusters, although there is no experimental evidence to support or refute this conversion.

Upon treatment of $(PPN)_2[Fe_8S_6(NO)_8]$ with eight equivalents of $NOBF_4$ (Reaction 11) the components of the mixture of products obtained were identified as $[Fe^{II}(DMF)_6][Fe_6S_6(NO)_6]$, $(PPN)[Fe_4S_3(NO)_7]$ and $PPNBF_4$. Assuming that NO^- is the best description for the nitrosyl in $[Fe_4S_3(NO)_7]^-$, the formation of both clusters from NO^+ can be explained by the oxidation of $(PPN)_2[Fe_8S_6(NO)_8]$ in order to reduce NO^+. In this

case the stoichiometric reaction of $(PPN)_2[Fe_8S_6(NO)_8]$ to form two $(PPN)[Fe_4S_3(NO)_7]$ clusters requires six additional NO^-, which means that six NO^+ have to be converted to NO initially, and then by internal oxidation, NO^- ions are formed. For the first reduction to NO, these six electrons can be provided by the oxidation of three $[Fe_8S_6(NO)_8]^{2-}$ to $[Fe_6S_6(NO)_6]^{2-}$ in accordance to equation 3 above. The reaction of $(PPN)_2[Fe_8S_6(NO)_8]$ with gaseous NO (Reaction 12) affords, as expected, $(PPN)[Fe_4S_3(NO)_7]$ exclusively.

The yield of $(PPN)_2[Fe_6S_6(NO)_6]$ (Reaction 2) is unreasonably high, assuming that $[Fe_4S_3(NO)_7]^-$ is the only source of Fe, as implied in the synthesis of $(PPN)_2[Fe_8S_6(NO)_8]$, and therefore, it appears that the $[Fe_4(CO)_{13}]^{2-}$ cluster provides additional iron. Furthermore, it is known that $[Fe(CO)_3(NO)]^-$, upon reaction with elemental sulfur, produces $[Fe_4S_4(NO)_4]^-$ [33], so the pathway for the formation of $(PPN)_2[Fe_6S_6(NO)_6]$ via reaction 2 seems to be more complicated than the initial formation of $(PPN)_2[Fe_8S_6(NO)_8]$ and the further reaction with Bz_2S_3 as shown by reactions 1 and 3 (Figure 2.2).

$(PPN)_2[Fe_6S_6(NO)_6]$ can react with $Fe(CO)_5$ or $[Fe(H_2O)_6](BF_4)_2/PPr_3$ (reactions 13 and 14) to produce $(PPN)_2[Fe_8S_6(NO)_8]$ as the only identified product, although in yields of about 50%. This unexpected behavior can be rationalized if the $[Fe_6S_6(NO)_6]^{2-}$ cluster is labile in solution and breaks into smaller fragments of Fe(NO) units that recombine to form the $[Fe_8S_6(NO)_8]^{2-}$ cluster, which is more stable under reducing conditions. In the case where $NOBF_4$ was used with $[Fe(H_2O)_6](BF_4)_2$, the only product obtained was $[Fe_4S_3(NO)_7]^-$ which is in accordance to the more oxidized nature of $[Fe_4S_3(NO)_7]^-$ (assuming NO^-). Furthermore, formation of only $[Fe_4S_3(NO)_7]^-$ is also observed when gaseous NO is used, as in the case of $(PPN)_2[Fe_8S_6(NO)_8]$

It is noteworthy to mention that the $(PPN)_2[Fe_4S_4(NO)_4]$ cluster has not been isolated in this oxidation level previously. The IR spectrum shows a NO stretch at 1652cm^{-1}, which is lower than the 1760cm^{-1} and 1700cm^{-1} bands reported for $Fe_4S_4(NO)_4$ and $[Fe_4S_4(NO)_4]^-$ respectively [33]. The lower frequency of the NO stretching vibration in the $[Fe_4S_4(NO)_4]^{2-}$ cluster is consistent with the expected increase in the Fe-NO backbonding. Elemental analysis also is consistent with the $(PPN)_2[Fe_4S_4(NO)_4]$ formula; however, we were not able to obtain a satisfactory crystal structure due to the high distortion of the PPN cation in the crystal lattice. Nevertheless, the presence of a cubic $Fe_4S_4(NO)_4$ cluster and two PPN cations was confirmed.

Regarding the synthesis of $(PPN)_2[Fe_4S_4(NO)_4]$ through reaction 3, the yield (24.5%) based on total sulfur, which is the limiting reagent, is particularly low compared to the other two clusters. This makes the alternative route via reaction 5, which gives a cleaner product with higher yield (68%), the preferred method of synthesis. Electronically, the $[Fe_4S_4(NO)_4]^{2-}$ cluster can be described as consisting of $2\{FeNO\}^7$ and $2\{FeNO\}^8$ units, being related to $[Fe_8S_6(NO)_8]^{2-}$ according to the following reaction:

$$[Fe_8S_6(NO)_8]^{2-} + 2S^{2-} \longrightarrow 2[Fe_4S_4(NO)_4]^{2-} + 2e^- \quad \text{(eq. 4)}$$

The loss of two electrons required for this reaction, have to be donated to a species capable of accepting electrons, with the best candidates being H^+ or another $[Fe_8S_6(NO)_8]^{2-}$ cluster. Provided that $[Fe_8S_6(NO)_8]^{2-}$ can receive at most 2 electrons per cluster, the latter cannot act as the only electron acceptor, or the maximum yield of the reaction would be less than the yield obtained.

Overall, the reactivity of the Fe/S/NO clusters presented in this chapter, exhibit a common feature that enables the interconversions between them. This feature is the kinetic lability of these species in solution in which they break into smaller Fe/S/NO

fragments, consequently leading to rearrangements and formation of the species presented herein. It is noted in particular, that for the $[Fe_6S_6(NO)_6]^{2-}$ and the $[Fe_4S_4(NO)_4]^{2-}$ clusters the basic repeating fragment can be described as $[Fe_2S_2(NO)_2]^-$. This fragmentation to dimers in solution is also demonstrated in the case of Fe/S/Cl species through the conversion of $[Fe_6S_6Cl_6]^{3-}$ to $[Fe_4S_4Cl_4]^{2-}$ by substitutions of the counterion [34].

The isolation of $(PPN)_2[Fe_4S_4(NO)_6]$ can be regarded as an example of this lability of the clusters in solution. Although it has been observed few times in mixtures, by means of its characteristic 1700cm^{-1}, 1668cm^{-1} N-O stretching frequency in the infrared spectrum, this species has only been isolated in a pure form once, and in low yields. Therefore, this cluster can be better described as a "trapped" intermediate, rather than a final product of a reaction.

The structure of the $(PPN)_2[Fe_4S_4(NO)_6]$ cluster can be perceived as a combination of two $[Fe_2S_2(NO)_3]^-$ dimers sharing an edge. There are two possible pathways that these dimers might form. The first pathway is through dissociation of the $[Fe_4S_3(NO)_7]^-$ cluster to two fragments, $[Fe_2S_2(NO)_3]^-$ and $[Fe_2S(NO)_4]$. The latter, by abstraction of NO and the addition of sulfur, can lead to the $[Fe_2S_2(NO)_2]^-$ fragment that is the basic repeating unit in the formation of $[Fe_4S_4(NO)_4]^{2-}$, while the first will lead to the $[Fe_4S_4(NO)_6]^{2-}$ as demonstrated schematically in Figure 2.3. This mechanism can possibly explain the difficulty in isolating the $[Fe_4S_4(NO)_6]^{2-}$ cluster, as the conditions of the reaction that favor the removal of NO will also favor the conversion of the $[Fe_2S_2(NO)_3]^-$ fragment to the more stable $[Fe_2S_2(NO)_2]^-$ fragment.

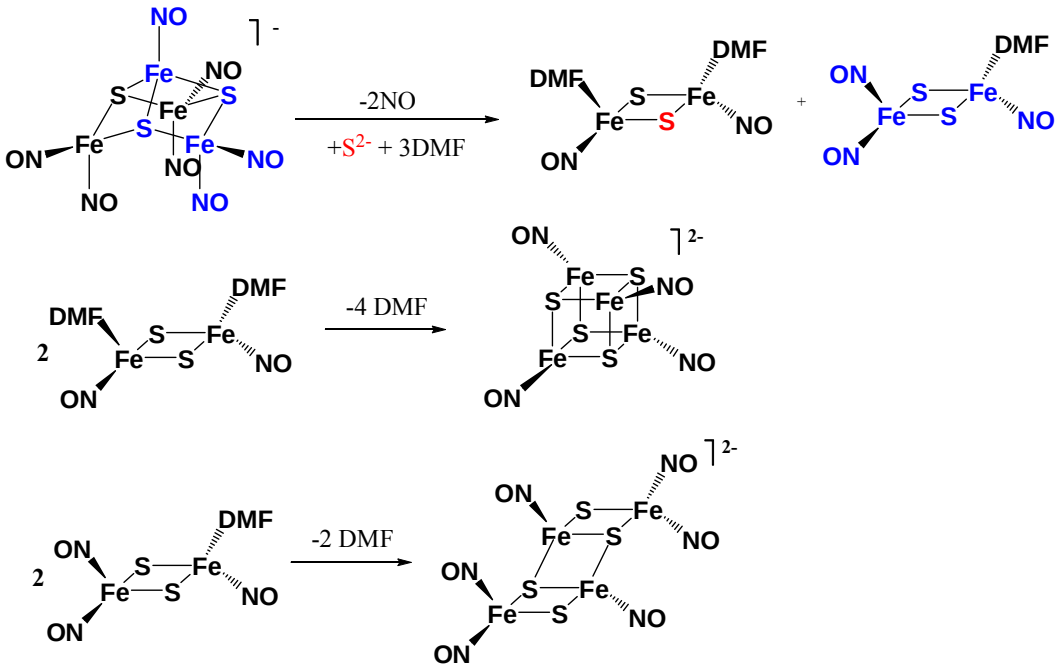

Figure 2.3. Proposed fragmentation of $[Fe_4S_3(NO)_7]^-$ that leads to the formation of $[Fe_4S_4(NO)_4]^{2-}$ and $[Fe_4S_4(NO)_6]^{2-}$.

The other possible pathway for the formation of $[Fe_4S_4(NO)_6]^{2-}$ can be the addition of NO to $[Fe_2S_2(NO)_2]^-$ fragments, which is rather unlikely to be followed in the reaction of $[Fe_4S_3(NO)_7]^-$ with $[Fe_4(CO)_{13}]^{2-}$, but would be more likely to be followed in a reaction of $[Fe_4S_4(NO)_4]^{2-}$ with NO. Unfortunately under an NO atmosphere, $[Fe_4S_4X_4]^{2-}$ (X=NO, Cl) clusters will form $[Fe_4S_3(NO)_7]^-$ very fast, preventing the isolation of $[Fe_4S_4(NO)_6]^{2-}$. In addition, the lack of a unique UV spectrum of $(PPN)_2[Fe_4S_4(NO)_6]$ combined with the extensively overlapping UV spectra of both the $[Fe_4S_3(NO)_7]^-$ and $[Fe_4S_4(NO)_4]^{2-}$ clusters (Figure 2.4) will prevent the detection of the $(PPN)_2[Fe_4S_4(NO)_6]$ cluster in solution.

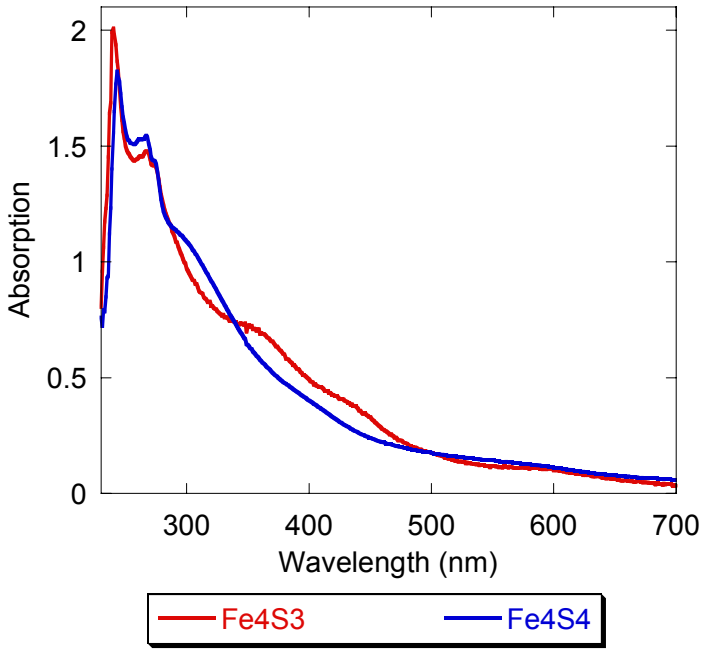

Figure 2.4. UV/Vis spectra of $(PPN)_2[Fe_4S_3(NO)_7]$ and $(PPN)_2[Fe_4S_4(NO)_4]$

2.3.2 Structural Description

The crystallographic structure determination of $(PPN)_2[Fe_8S_6(NO)_8]$ (Figure 2.5) reveals a cubic arrangement of iron with μ_4-sulfides capping the faces of the cube. The cluster has average Fe-Fe and Fe-S distances of 2.66 Å and 2.26 Å respectively. The nitrosyl groups are almost linearly bound to the irons with mean Fe-NO distances of 1.67Å and Fe-N-O angles of 177.2º.

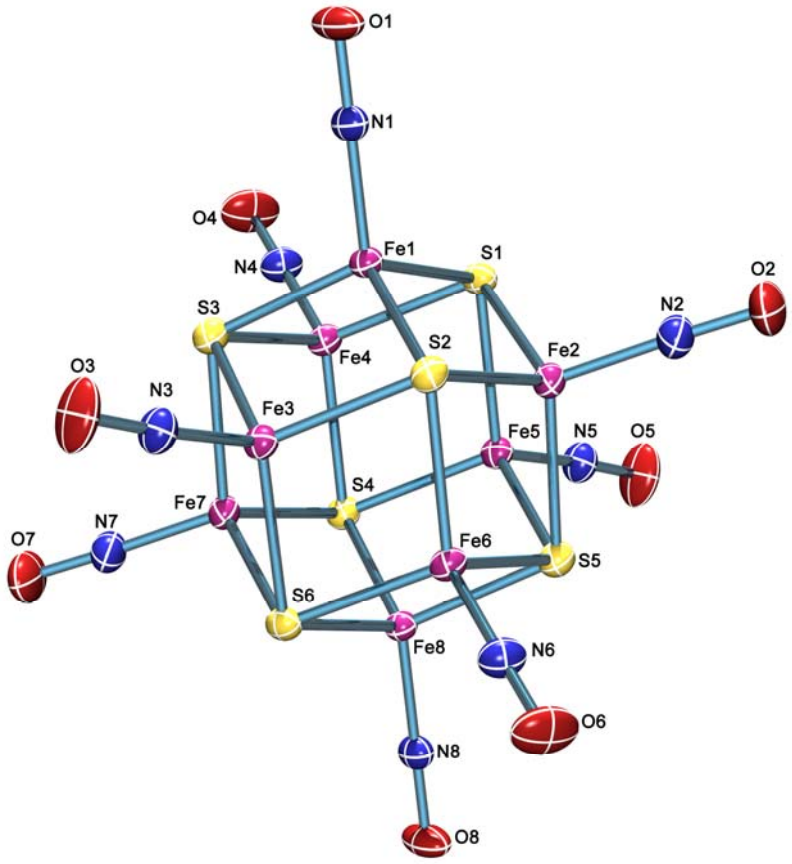

Figure 2.5. Ortep diagram of $[Fe_8S_6(NO)_8]^{2-}$ Showing thermal ellipsoids with 50% probability.

This cubic $[Fe_8S_6]$ type of arrangement is also known in the $(Et_4N)_3Fe_8S_6I_8$ [35], $(PhCH_2NEt_3)_4Fe_8S_6I_8$, $[Fe(dppe)(MeCN)_4]_2Fe_8S_6I_8$ [36] and $Fe_8S_6(PCy_3)_4Cl_4$ [37]

clusters. Comparison of interatomic distances in these clusters (Table 2.5) reveals a more compact structure for the $[Fe_8S_6(NO)_8]^{2-}$ cluster.

Cluster	Fe-Fe (Å)	Fe-S(Å)	Fe-X(Å)
$(PPN)_2[Fe_8S_6(NO)_8]$	2.659	2.265	1.674
$(Et_4N)_3Fe_8S_6I_8$	2.723	2.315	2.535
$(PhCH_2NEt_3)_4Fe_8S_6I_8$	2.704	2.317	2.59
$[Fe(dppe)(MeCN)_4]_2Fe_8S_6I_8$	2.698	2.319	2.593
$Fe_8S_6(PCy_3)_4Cl_4$	2.698	2.309	2.218 (Fe-Cl) 2.422 (Fe-PCy_3)

Table 2.5. Comparison of average interatomic distances between different $[Fe_8S_6X_8]^{x-}$ clusters

Upon the reduction of $[Fe_8S_6(NO)_8]^{2-}$ with potassium anthracenite the two electron reduced cluster $K_4[Fe_8S_6(NO)_8]\cdot 13DMF$ has been synthesized (Figure 2.6). The $[Fe_8S_6(NO)_8]^{4-}$ cluster does not show any significant structural change from the initial cluster, although the average Fe-Fe and N-O distances are slightly elongated in accordance to the increase of electron density in antibonding orbitals within the cluster. Furthermore, the crystal structure of the intermediate trivalent cluster $(PPN)_3[Fe_8S_6(NO)_8]$ has been obtained as well, although the synthesis of this cluster was not reproducible, and is presented herein for comparison purposes only (see Appendix 1 for crystallographic data and structure). Table 2.6 illustrates the structural data obtained for all three $[Fe_8S_6(NO)_8]^{n-}$ (n = 2,3,4) clusters.

Cluster	Fe-Fe(Å)	Fe-S(Å)	Fe-N(Å)	N-O(Å)	Fe-N-O angle
$[Fe_8S_6(NO)_8]^{2-}$	2.659	2.265	1.674	1.181	177.12º
$[Fe_8S_6(NO)_8]^{3-}$	2.666	2.268	1.673	1.191	175.70º
$[Fe_8S_6(NO)_8]^{4-}$	2.684	2.265	1.670	1.205	173.57º

Table 2.6. Comparison of average interatomic distances in $[Fe_8S_6(NO)_8]^{n-}$ clusters (n = 2,3 and 4)

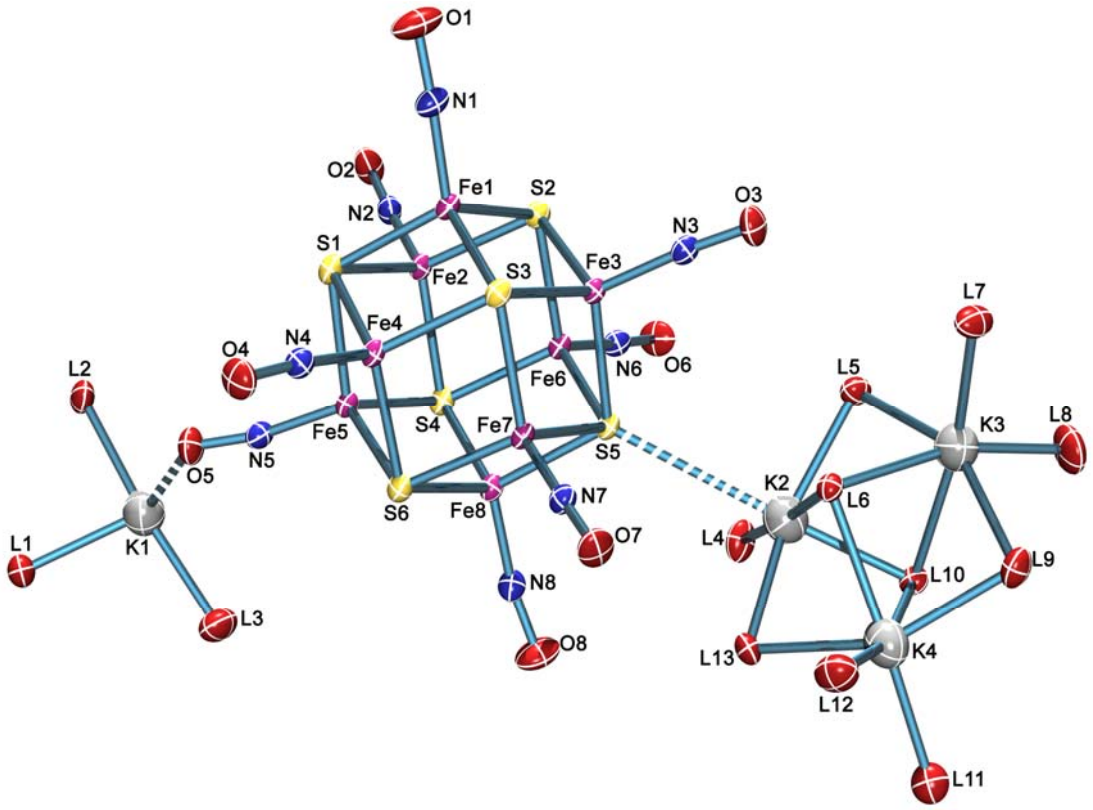

Figure 2.6. Ortep diagram of $K_4[Fe_8S_6(NO)_8]\cdot 13DMF$ with 50% probability ellipsoids. Dashed lines represent the short contacts of the potassium ions to the cluster. DMF molecules have been omitted for clarity except their oxygen atoms (labeled L) coordinated to potassium ions.

As seen in Figure 2.6, there are some notable features. The first one is the short contact between a nitrosyl group and a potassium ion with the K1-O5 distance of 2.385Å that can be considered as direct coordination, since it is comparable to the K-O distances of the coordinated DMF molecules, and thus within the range of 2.396Å to 2.511Å. The Fe5-N5-O5 angle is 169.5º while interestingly enough, the smallest angle is that of Fe8-N8-O8 at 168.3º, which does not seem to be in proximity with any potassium ion or solvent molecule. The other short contact denoted is the 3.305Å distance between K2 and S5 that satisfies the pseudo-octahedral coordination of K2, which applies for K3 and K4 as well. This implies a nucleophilic nature of the sulfide groups of the $[Fe_8S_6(NO)_8]$ clusters, one that has also been observed for the $[Fe_4S_3(NO)_7]^-$ cluster [38].

The crystal structure of $(PPN)_2[Fe_6S_6(NO)_6]$ (Figure 2.7) exhibits a $[Fe_6S_6]$ prismatic core configuration with average Fe-Fe and Fe-S distances at 2.651Å and 2.22Å respectively. Additionally, the nitrosyls are bound to iron with an average angle of 175.3º, while the Fe-N and N-O distances are 1.670Å and 1.180Å respectively.

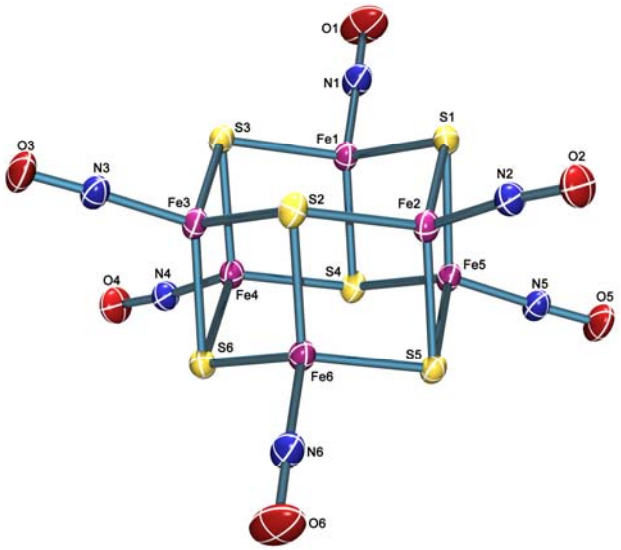

Figure 2.7. Ortep diagram of $[Fe_6S_6(NO)_6]^{2-}$ Showing thermal ellipsoids with 50% probability.

Cluster	Fe-Fe (Å)	Fe-S (Å)	Fe-X (Å)	N-O (Å)	Fe-NO angle
$(PPN)_2[Fe_6S_6(NO)_6]$	2.651	2.220	1.669	1.180	175.30º
$(Et_4N)_2[Fe_6S_6(NO)_6]$	2.659	2.221	1.659	1.176	175.83º
$(Bu_4N)_2[Fe_6S_6(NO)_6]$	2.642	2.219	1.664	1.184	174.17º
$[Fe_6S_6Cl_6]^{3-}$	2.764	2.275	2.223	-	-
$[Fe_6S_6Br_6]^{3-}$	2.746	2.271	2.363	-	-
$[Fe_6S_6I_6]^{3-}$	2.736	2.257	2.537	-	-
$[Fe_6S_6(p\text{-}^{-}O\text{-}C_6H_4\text{-}Me)_6]^{3-}$	2.760	2.276	1.880	-	-
$[Fe_6S_6(p\text{-}^{-}O\text{-}C_6H_4\text{-}OMe)_6]^{3-}$	2.782	2.295	1.870	-	-

Table 2.7. Comparison of the average interatomic distances between different $[Fe_6S_6X_6]^{n-}$ clusters

The $[Fe_6S_6(NO)_6]^{2-}$ cluster has been synthesized previously either as a Et_4N^+ [39], or a Bu_4N^+ [40] salt, but these were byproducts of other reaction pathways. The same prismatic core structure has been also observed in the clusters $[Fe_6S_6X_6]^{3-}$ (X= Cl^- [34], Br^- [41], I^- [42], p-$^-$O-C_6H_4-Me[43], p-$^-$O-C_6H_4-OMe [44]). As in the case of $[Fe_8S_6(NO)_8]^{2-}$ cluster, the $[Fe_6S_6(NO)_6]^{2-}$ is more compact with smaller average distances compared to the $[Fe_6S_6X_6]^{3-}$ analogues (Table 2.7), and, as expected there is no difference when changing the counter ion.

Crystallographic determination of $(PPN)_2[Fe_4S_4(NO)_6]$ reveals an unusual $[Fe_4S_4]$ core configuration that can be described as the fusion of two $[(NO)_2Fe(\mu_2\text{-}S)_2Fe(NO)]^-$ anionic dimers to give a nido $[Fe_4S_4(NO)_6]^{2-}$ cluster (Figure 2.8) with an inter-dimer Fe-Fe distance of 2.77 Å and an average intra-dimer Fe-Fe distance of 2.68Å. The Fe-NO distances are almost equivalent at 1.66Å (1.65-1.67Å) with average Fe-N-O bond angles of 167º within the range of 163º -171º.

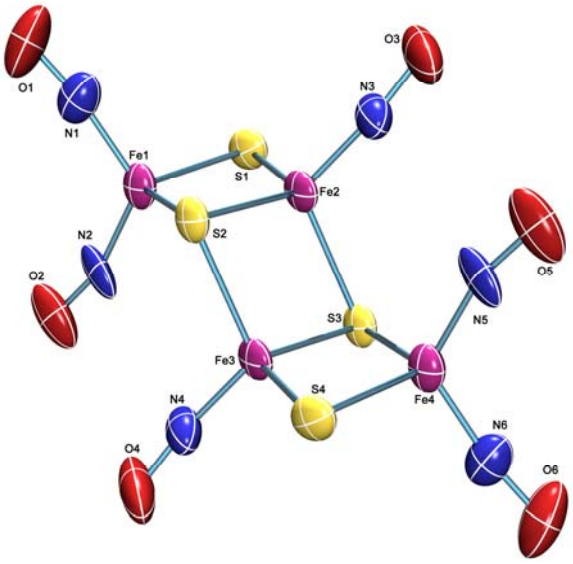

Figure 2.8. Ortep diagram of $[Fe_4S_4(NO)_6]^{2-}$ showing ellipsoids with 50% probability.

2.3.3. Spectroscopic Characterization

As mentioned previously, due to the highly covalent nature of the M-NO bond there is great ambiguity in the assignment of the oxidation state of NO in metal nitrosyl complexes and therefore the formal oxidation states of the metals.

As presented in Table 2.8, the formal oxidation state of iron for the clusters presented herein, can vary from -1 to +3, although the Enemark-Feltham notation can provide satisfactory explanations for the electronic behavior of the $[Fe_8S_6NO)_8]^{2-}$, $[Fe_6S_6(NO)_6]^{2-}$ and $[Fe_4S_4(NO)_4]^{2-}$ clusters that have been studied, since they consist of $\{FeNO\}^n$ units. Based on the molecular orbital diagrams [27] for the four coordinated C_{3v} $\{FeNO\}^n$ units, the expected electronic configurations are S=3/2 for $\{FeNO\}^7$ and S=1 for $\{FeNO\}^8$ which are consistent with a high spin pseudotetrahedral configuration of iron.

Cluster	Enemark-Feltham	Formal Oxidation of Fe		
		NO^+	NO·	NO^-
$[Fe_8S_6(NO)_8]^{2-}$	$2\{FeNO\}^7$, $6\{FeNO\}^8$	6Fe(0), 2Fe(I)	6Fe(I), 2Fe(II)	6Fe(II), 2Fe(III)
$[Fe_6S_6(NO)_6]^{2-}$	$4\{FeNO\}^7$, $2\{FeNO\}^8$	2Fe(0), 4Fe(I)	2Fe(I), 4Fe(II)	2Fe(II), 4Fe(III)
$[Fe_4S_4(NO)_4]^{2-}$	$2\{FeNO\}^7$, $2\{FeNO\}^8$	2Fe(0), 2Fe(I)	2Fe(I), 2Fe(II)	2Fe(II), 2Fe(III)
$[Fe_4S_3(NO)_7]^-$	$\{FeNO\}^7$, $3\{Fe(NO)_2\}^9$	3Fe(-1), Fe(I)	3Fe(I), 3Fe(II)	4Fe(III)
$[Fe_4S_4(NO)_6]^{2-}$	$2\{FeNO\}^8$, $2\{Fe(NO)_2\}^8$	4Fe(0)	2Fe(I), 2Fe(II)	4Fe(III)

Table 2.8. Comparative table of the theoretical assignment of iron oxidation levels based on the possible oxidation states of the nitrosyl ligand.

Other than Fe/S/NO clusters, the only four coordinated $\{FeNO\}^n$ units with sulfur ligation that have been structurally characterized are $(Et_4N)[Fe(S^tBu)_3NO]$ [45] and $(PPN)[Fe(SPh)_3NO]$ [46] which are the only examples. These $\{FeNO\}^7$ complexes have been described as an S=3/2 Fe(III)-NO^- system and their spectroscopic properties are presented along with those of the three Fe/S/NO clusters in Table 2.9

Compound	Fe-N dist. (Å)	Fe-N-O angle (º)	$\nu_{(N-O)}$ (cm^{-1})	EPR signal
$[Fe_8S_6(NO)_8]^{2-}$	1.674	177.12	1684	Silent
$[Fe_6S_6(NO)_6]^{2-}$	1.669	175.30	1679	Silent
$[Fe_4S_4(NO)_4]^{2-}$	-	-	1654	Silent
$[Fe(S^tBu)_3NO]^-$	1.711	174.18	1704	3.84, 3.16, 2.01
$[Fe(SPh)_3NO]^-$	1.682	164.51	1726	3.76, 2.01

Compound	μ_{eff} (50K)	μ_{eff} (300K)	δ ($mm \cdot s^{-1}$)	ΔE_Q
$[Fe_8S_6(NO)_8]^{2-}$	3.24	5.86	0.38	0.24
$[Fe_6S_6(NO)_6]^{2-}$	2.90	5.86	0.26	0.32
$[Fe_4S_4(NO)_4]^{2-}$	3.42	6.29	0.28	0.20
$[Fe(S^tBu)_3NO]^-$	3.91	3.97	0.26	0.46
$[Fe(SPh)_3NO]^-$	3.66	3.83	-	-

Table 2.9. Comparative table of structural and spectroscopic data for four coordinated Fe/S/NO compounds. Values for $[Fe(S^tBu)_3NO]^-$ taken from Ref. 43. EPR and Mössbauer measurements of $[Fe(S^tBu)_3NO]^-$ are reported at 4.2K while for the other three compounds at 78K.

Structural data for $[Fe_8S_6(NO)_8]^{2-}$ and $[Fe_6S_6(NO)_6]^{2-}$ show M-N-O angles at 172.9º-178.8º and Fe-N distances of 1.669Å-1.674Å. The Fe-NO bond is short enough to be consistent with a considerable amount of multiple bond character, and the Fe-N-O angles approach linearity, which is consistent with theoretical data [47].

The Mössbauer spectra of $[Fe_8S_6(NO)_8]^{2-}$, $[Fe_6S_6(NO)_6]^{2-}$ and $[Fe_4S_4(NO)_4]^{2-}$ show a single doublet that is consistent with delocalized charge of the irons, and exhibit isomer shifts of 0.29mm·s^{-1}, 0.18mm·s^{-1} and 0.20mm·s^{-1} respectively at 250K. At 78K the δ values increase to 0.37mm·s^{-1}, 0.26mm·s^{-1} and 0.28mm·s^{-1}, suggesting that an equivalent increase is expected to occur at 4.2K, a temperature that we were unable to obtain due to experimental restrictions at this time. In comparison to the 0.26mm·s^{-1} of $(Et_4N)[Fe(S^tBu)_3NO]$ and the typical range for Fe(III) in similar coordination [48], the Mossbauer spectra of these clusters appear to be in the range for high spin Fe(III) systems. Indicating that the best description for the nitrosyl ligands is NO^-, and consequently the clusters can be described as Fe(III)/Fe(II) delocalized systems. It should be noted however, that even with NO^- that gives the maximum oxidation states for the irons, the values are $Fe^{+2.25}$, $Fe^{+2.66}$ and $Fe^{+2.5}$ for the $[Fe_8S_6(NO)_8]^{2-}$, $[Fe_6S_6(NO)_6]^{2-}$ and $[Fe_4S_4(NO)_4]^{2-}$ clusters respectively. By comparison with the equivalent $[Fe_4S_4]^{2+}$ and $[Fe_6S_6]^{3+}$ cores ($Fe^{+2.5}$ systems) with halogens or thiols [34] that exhibit isomer shifts in the range of 0.41-0.50mm·s^{-1} the nitrosyl analogues appear to be considerably closer to an all-ferric state. This inconsistency can be attributed to the "non-innocent" nature of NO ligands [49] due to the covalent nature of the Fe-NO bond. In such a bond, electron density is removed from the metal causing it to appear more oxidized. The larger isomer shift of $[Fe_4S_4(NO)_4]^{2-}$ (δ= 0.20 mm·s^{-1} at 250K) compared with those reported for $[Fe_4S_4(NO)_4]^n$ (n=0, -1) [33] that are δ= 0.092 mm·s^{-1} and δ= 0.156 mm·s^{-1}, respectively at 300K, is in accordance to a more electron rich core, which also indicates that for Fe/S/NO clusters the increase in isomer shift with the addition of electrons is not as large as in the case of Fe/S/X (X=halogen, thiol) clusters.

By plotting the isomer shift of the known Fe/S/NO clusters that contain $FeS_3(NO)$ coordination and comparing those to the values reported for $FeS_3(SR)$ clusters [50] (Figure 2.9) it is clear that the values follow a similar trend, shifted to lower isomer shifts, a trend that appears as well with the temperature change from 78K to 300K.

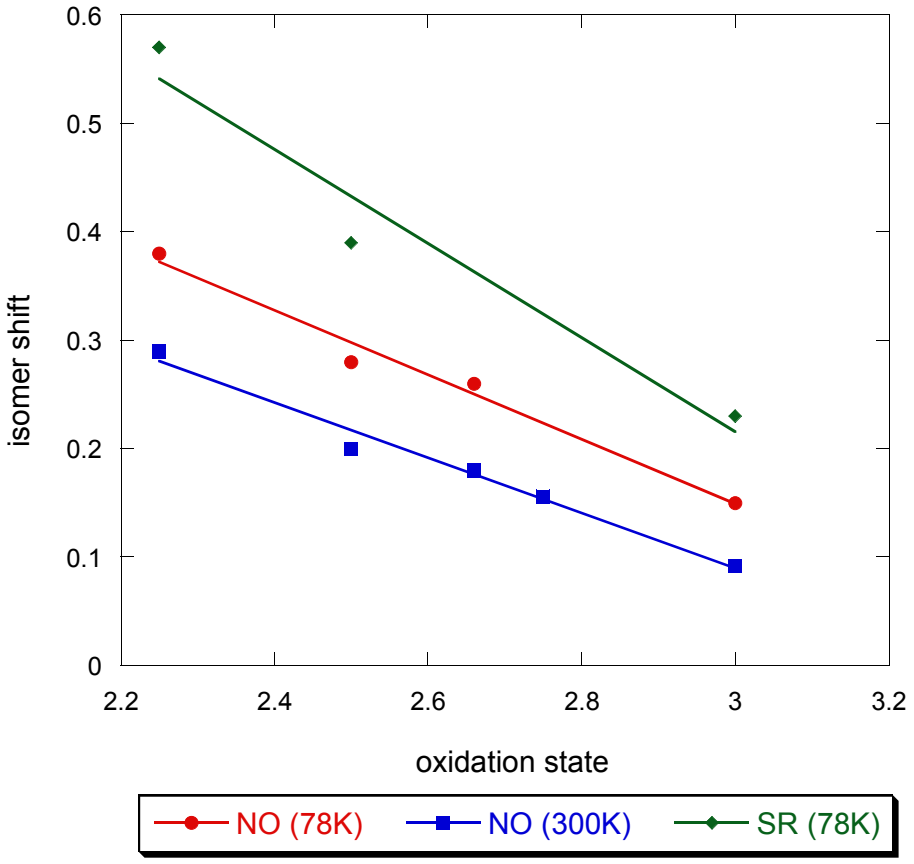

Figure 2.9. Distribution plots of ^{57}Fe isomer shifts for Fe/S/L clusters at 78K and 300K for different average oxidation states of the clusters. The values used for $FeS_3(SR)$ are from reference [50], while the $FeS_3(NO)$ are from the $[Fe_8S_6(NO)]^{2-}$ ($Fe^{+2.25}$), $[Fe_6S_6(NO)_6]^{2-}$ ($Fe^{+2.66}$), $[Fe_4S_4(NO)_4]^{2-}$($Fe^{+2.5}$) clusters reported herein and the $[Fe_4S_4(NO)_4]^{-}$ ($Fe^{+2.75}$ at 300K only) $[Fe_4S_4(NO)_4]^{0}$ (Fe^{+3}) from reference [33]

Electron Paramagnetic Resonance spectra (frozen DMF solutions at 78K) showed that the ground state of all three Fe/S/NO clusters is S=0, which is consistent with antiferromagnetic coupling of the even number of $\{FeNO\}^8$ (S=1) and $\{FeNO\}^7$ (S=3/2) units. For $(PPN)_2[Fe_8S_6(NO)_8]$, however, an EPR signal with a g value of 1.995 was detected shown in Figure 2.10, which by comparison to a $CuSO_4$ standard (10^{-4} M in

DMF) and according to corrected double integral analysis [51] was shown to be less than 10% of the total concentration.

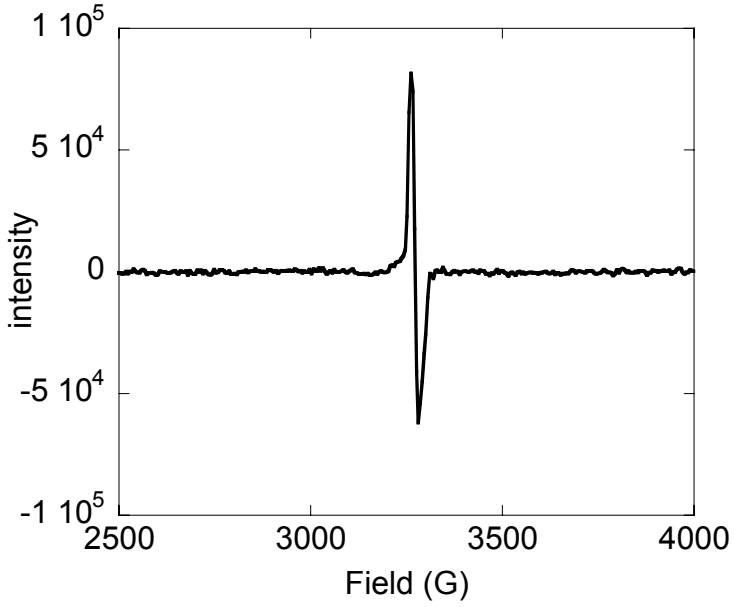

Figure 2.10. X-Band EPR spectrum obtained of a DMF solution of $(PPN)_2[Fe_8S_6(NO)_8]$. The signal corresponds to a species with a concentration less than 10% of the total concentration.

The nature and the origin of this weak signal remains uncertain, although it has been observed in several attempts from different batches of $(PPN)_2[Fe_8S_6(NO)_8]$, suggesting that it might not be due to impurities in the sample. In addition, the EPR signal is also affected by the solvent, since by using dichloroethane instead of DMF, the signal decreases more than 80%. This behavior can be explained if there is dissociation of $(PPN)_2[Fe_8S_6(NO)_8]$ in solution that gives rise to species with odd number of $\{FeNO\}^7$ and $\{FeNO\}^8$ units, with donor solvents favoring the dissociation more than non-coordinative solvents. The signal area cannot be directly correlated to the extent of this dissociation because as the solution freezes gradually, the rate of dissociation decreases significantly, leaving only a small fraction of the EPR active species.

Variable temperature magnetic susceptibility measurements at 5000Oe for all three Fe/S/NO clusters (Figure 2.11) show the expected behavior for Fe/S clusters that are antiferromagnetically coupled. The effective magnetic moments for the $[Fe_8S_6(NO)_8]^{2-}$ cluster ranges from μ_{eff} = 1.38 (4.0K) to μ_{eff} = 5.86 (300K), for $[Fe_6S_6(NO)_6]^{2-}$ ranges from μ_{eff} = 1.82 (4.0K) to μ_{eff} = 5.86 (300K) and for $[Fe_4S_4(NO)_4]^{2-}$ ranges from μ_{eff} = 1.44 (4.0K) to μ_{eff} = 6.29 (300K)

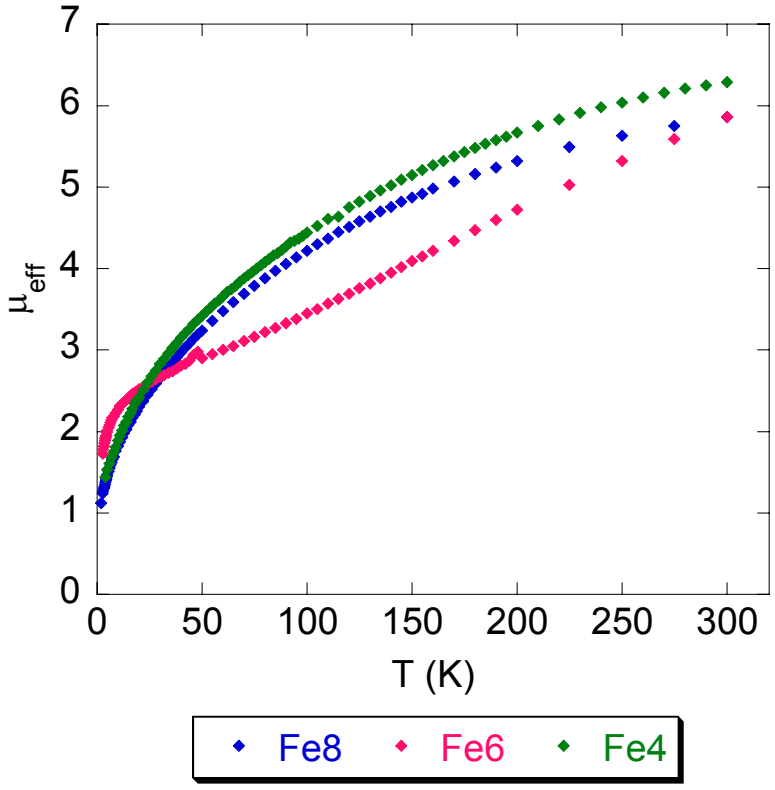

Figure 2.11. Temperature dependence of the effective magnetic moment for $(PPN)_2[Fe_8S_6(NO)_8]$, $(PPN)_2[Fe_6S_6(NO)_6]$ and $(PPN)_2[Fe_4S_4(NO)_4]$

2.3.4 Electrochemical Properties

The electrochemical properties of the Fe/S/NO clusters presented in Figure 2.2 have been studied by means of cyclic voltammetry. All species show two reversible reduction waves between 0 and -1.6V, with the exception of $(PPN)_2[Fe_8S_6(NO)_8]$ (Figure 2.12) which shows an unusual two pair of waves of unequal height, with half wave potentials of $E_{1(rev)}$ = -480 mV, $E_{2(rev)}$ = -620 mV, $E_{3(rev)}$ = -1200 mV, $E_{4(rev)}$ = -1300 mV. This is typically attributed to the presence of two different species and in this case can be viewed as the dissociation of $[Fe_8S_6(NO)_6]^{2-}$ in solution.

At this point it is helpful to address the expected reductions for the Fe/S/NO species in this chapter. Assuming NO^- ligation, the expected reduction couples are those of Fe(III)/Fe(II). Therefore, $(PPN)_2[Fe_8S_6(NO)_8]$ (6Fe(II), 2Fe(III)) should exhibit two reductions, $(PPN)_2[Fe_6S_6(NO)_6]$ (2Fe(II), 4Fe(III)) four reductions, $(PPN)_2[Fe_4S_3(NO)_7]$ (4Fe(III)) four reductions and $(PPN)_2[Fe_4S_4(NO)_4]$ (2Fe(II),2Fe(III)) two reductions.

The voltammogram of $(PPN)_2[Fe_6S_6(NO)_6]$ (Figure 2.13) shows two reversible reductions at -690 mV and -1520 mV, while the reported voltammogram for $(Et_4N)[Fe_6S_6(NO)_6]$[39] shows four waves at -730 mV, -900 mV, -1400 mV and -1640 mV (Table 2.10). This inconsistent electrochemical behavior of the two $[Fe_6S_6(NO)_6]^{2-}$ clusters could be explained either by counterion effects that alter the potentials or by impurities in the $(Et_4N)[Fe_6S_6(NO)_6]$ cluster. Change of counterion is possible to cause only two reduction waves to be visible in the 0V to -2V window or cause the overlap of the two reductions potentials, which would give rise to a two electron reduction wave. For $(PPN)_2[Fe_4S_3(NO)_7]$ (Figure 2.14), and $(PPN)_2[Fe_4S_4(NO)_4]$ (Figure 2.15) clusters,

the only difference to the reported values [33, 52] are the actual positions of the reduction potentials, that can be attributed to effects from the counter-ion.

Cluster	Observed potentials			
$(PPN)_2[Fe_8S_6(NO)_8]$	-480mV	-620mV	-1200mV	-1300mV
$(PPN)_2[Fe_6S_6(NO)_6]$	-690mV		-1520mV	
$(Et_4N)_2[Fe_6S_6(NO)_6]$[39]	-730mV	-900mV	-1400mV	-1640mV
$(PPN)_2[Fe_4S_4(NO)_4]$	-200mV		-1280mV	
$Fe_4S_4(NO)_4$[33]	+130mV		-650mV	
$(PPN)[Fe_4S_3(NO)_7]$	-660mV		-1370mV	-1940mV
$(Et_4N)[Fe_4S_3(NO)_7]$[52]	-680mV		-1260mV	-1750mV

Table 2.10. Electrochemical comparison between the reported Fe/S/NO clusters and their PPN^+ analogues reported in this chapter

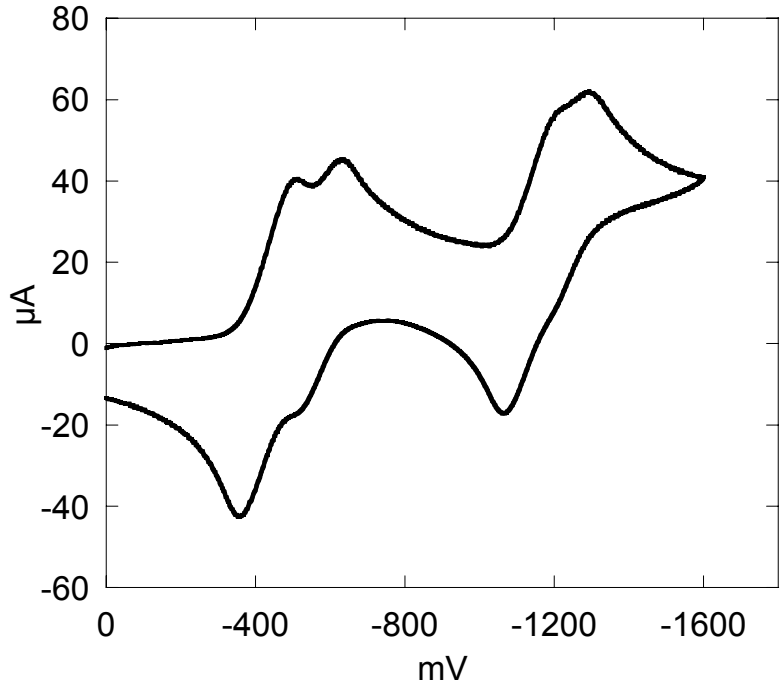

Figure 2.12. Cyclic voltammogram of $(PPN)_2[Fe_8S_6(NO)_8]$ from 0 to -1.6 V in DMF

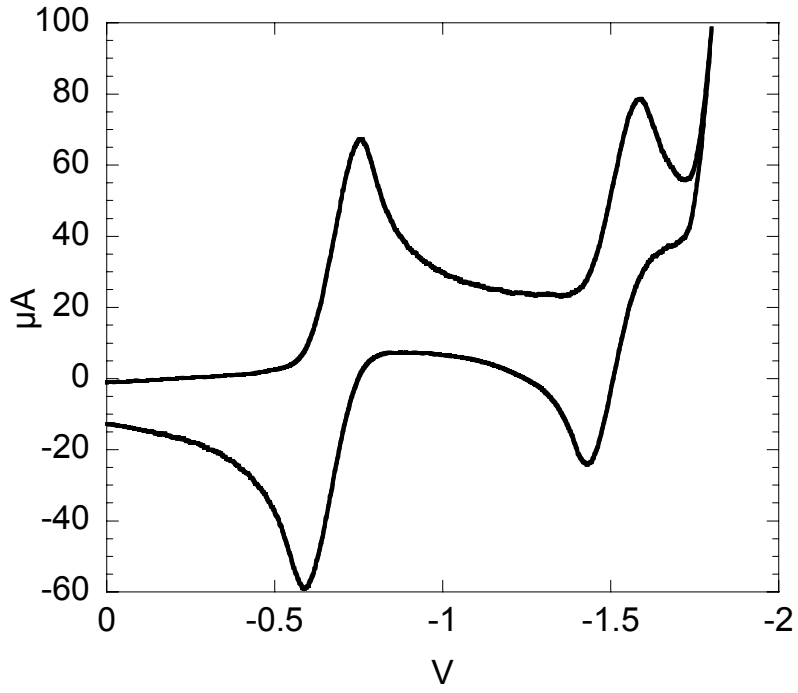

Figure 2.13. Cyclic voltammogram of $(PPN)_2[Fe_6S_6(NO)_6]$ from 0 to -1.8 V in DMF

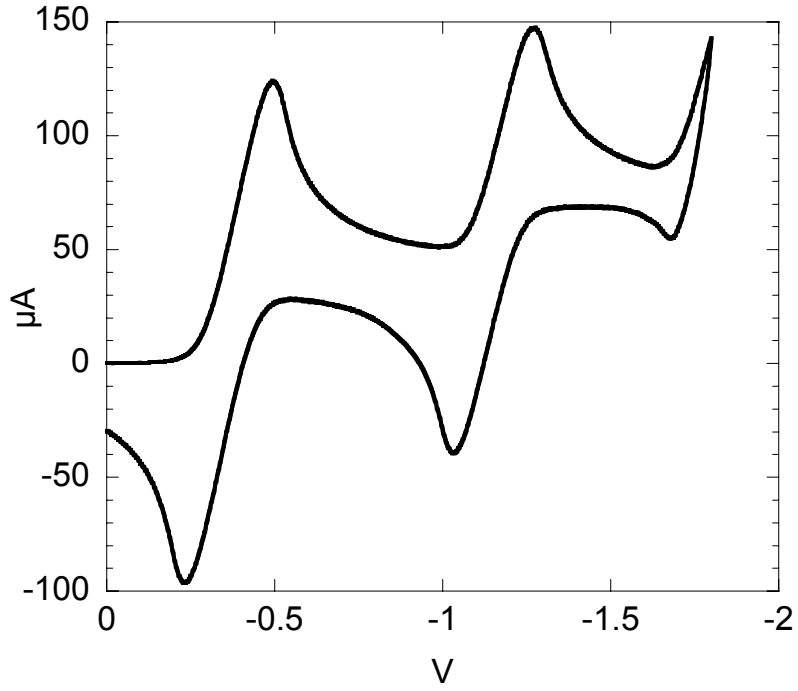

Figure 2.14. Cyclic voltammogram of $(PPN)_2[Fe_4S_3(NO)_7]$ from 0 to -1.8 V in DMF

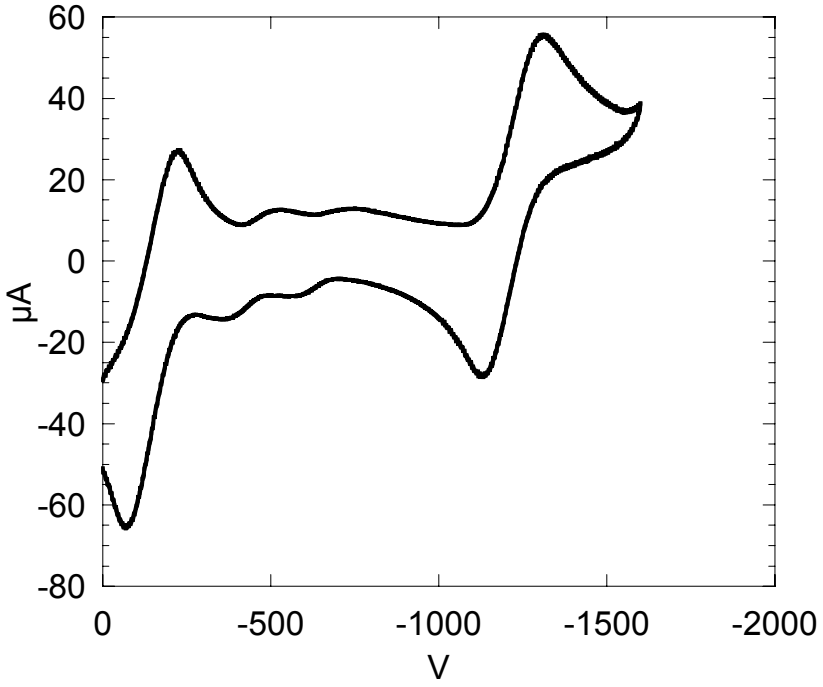

Figure 2.15. Cyclic voltammogram of $(PPN)_2[Fe_4S_4(NO)_4]$ from 0 to -1.6 V in DMF. The two small peaks at -0.5V are contamination from $(PPN)_2[Fe_8S_6(NO)_8]$ used as starting material

The unusual cyclic voltammetry of $(PPN)_2[Fe_8S_6(NO)_8]$ was investigated further in an attempt to determine the nature of the species involved. The voltammogram was repeated several times from different batches and the presence of the two closely spaced reduction waves was always observed, even when using different scan rates, temperatures and solvents. In addition the voltammogram of the reduced $(PPN)_4[Fe_8S_6(NO)_8]$ cluster exhibited the same four wave pattern.

Analysis to elucidate the electrochemical properties of this cluster is based on the descriptions presented by Piero Zanello [53]. This analysis is only performed for the first two waves because the poor resolution of the last two waves prevents the extrapolation of any useful information. The ΔE_p of the forward peak and the reverse peak varies from 80mV to 250mV with increasing scan rates, suggesting quasi-reversible reductions. In different batches of $(PPN)_2[Fe_8S_6(NO)_8]$, the ratio of the two forward currents is not

strictly constant, but changes between 0.8-0.95, suggesting that two species might be present in the initial material as a mixture. The possibility of equilibrium between two species could not be excluded, as the ratio of the two peaks varies also with variations in scan rate, temperature, and solvent system, even within the same sample.

One characteristic that was found constantly throughout the experiments, is the ratio of reverse (i_{pr}) to forward current (i_{pf}) that shows a $i_{pr}/i_{pf}>1$ for the first reduction and $i_{pr}/i_{pf}<1$ for the second reduction, which also provides an explanation for the unequal heights of the two waves. The ratio i_{pr}/i_{pf} was calculated using the following empirical equation:

$$\frac{i_{pr}}{i_{pf}} = \frac{(i_{pr})_0}{i_{pf}} + \frac{0.485 \cdot (i_f)_0}{i_{pf}} + 0.086 \qquad \text{(eq. 5)}$$

The properties of a quasi-reversible electron transfer are the increase in ΔE_p with scan rate (v), a non constant $i_{pf}/v^{1/2}$ ratio, and the shift of the potential of the forward wave E_{pf} towards more negative potentials with increases in scan rate. In addition, if the transfer coefficient α is greater than 0.5, then the forward peak is sharper than the reverse peak, and thus $i_{pr}/i_{pf}>1$, or if $\alpha<0.5$ then the opposite effect is observed; only if α is 0.5 will the peaks be of the same height. The simplest explanation for these two waves is that there might be two consecutive electron transfers with different extents of reversibility, which affect the ratio of the currents observed.

Nevertheless, there are other possibilities of a more complex system that have to be examined as well, and these would be electron transfers coupled to chemical reactions. For a C_rE_r mechanism (reversible reaction followed by electron transfer) the diagnostic criteria besides $i_{pr}/i_{pf}>1$ is the increase of the ratio as the scan rate increases, a shift in E_{pf} to less negative potentials with increase of scan rate, and a decrease in the $i_{pf}/v^{1/2}$ ratio with

increase of scan rate. For the E_rC_i mechanism (electron transfer followed by an irreversible chemical reaction), besides $i_{pr}/i_{pf}<1$ that progressively increases with scan rate and reaches values close to 1, there is also a shift in E_{pf} to more negative potentials with increase scan rate, and a constant or small decrease $i_{pf}/v^{1/2}$ ratio. As evident from the criteria above, the presence of quasi-reversible reductions influences some of the diagnostic criteria of electron coupled chemical reactions, and due to the fact that the two signals are overlapping, the determination of thermodynamic and kinetic parameters would not be valid at this point.

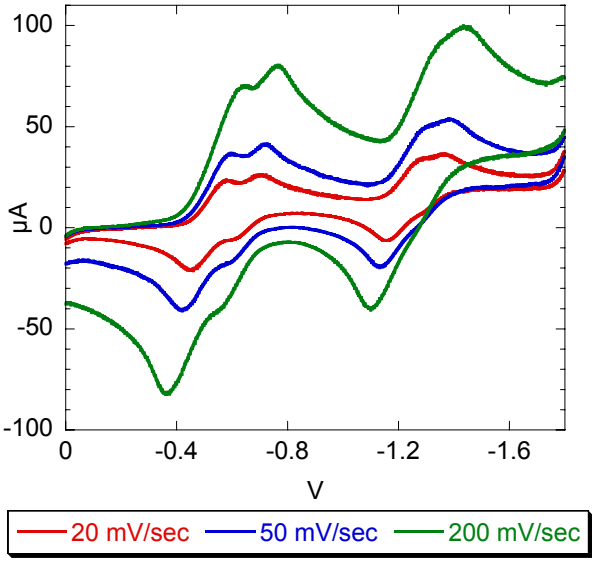

Figure 2.16. Scan rate comparison for $(PPN)_2[Fe_8S_6(NO)_8]$ at room temperature.

	E_{pf} (mV)	Scan Rate (mV/sec)	ΔE_p (mV)	i_{pr}/i_{pf}	$i_{pf}/v^{1/2}$	$i_{pr}/v^{1/2}$
	-584	20	134	1.299	5.088	6.608
1st wave	-598	50	174	1.518	5.049	7.666
	-638	200	276	1.655	4.698	7.775
	-708	20	132	0.605	5.804	3.512
2nd wave	-720	50	154	0.801	5.784	4.632
	-766	200	228	0.925	5.412	5.008

Table 2.11. Electrochemical parameters for the two first waves of $(PPN)_2[Fe_8S_6(NO)_8]$

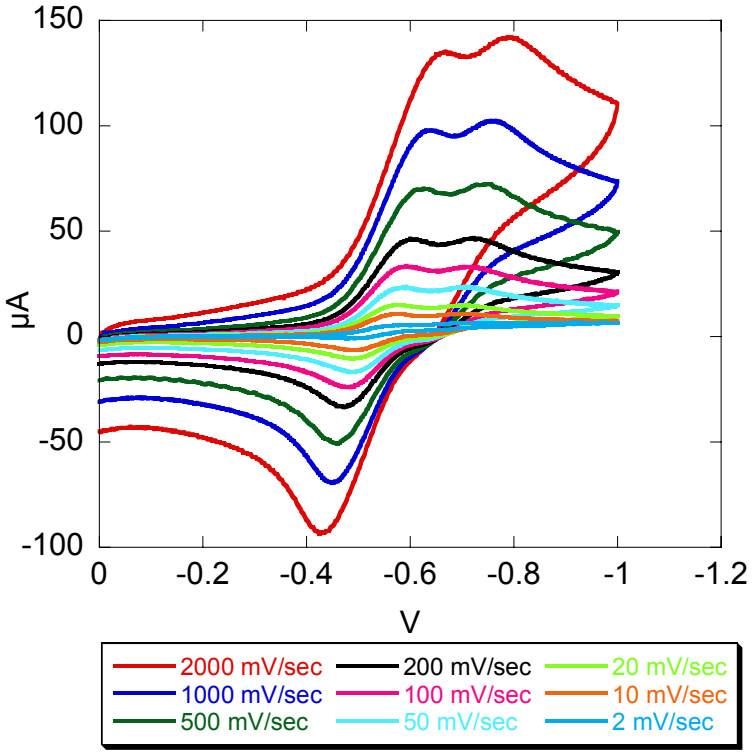

Figure 2.17. Scan rate comparison for $(PPN)_2[Fe_8S_6(NO)_8]$ at room temperature from 0 to -1V

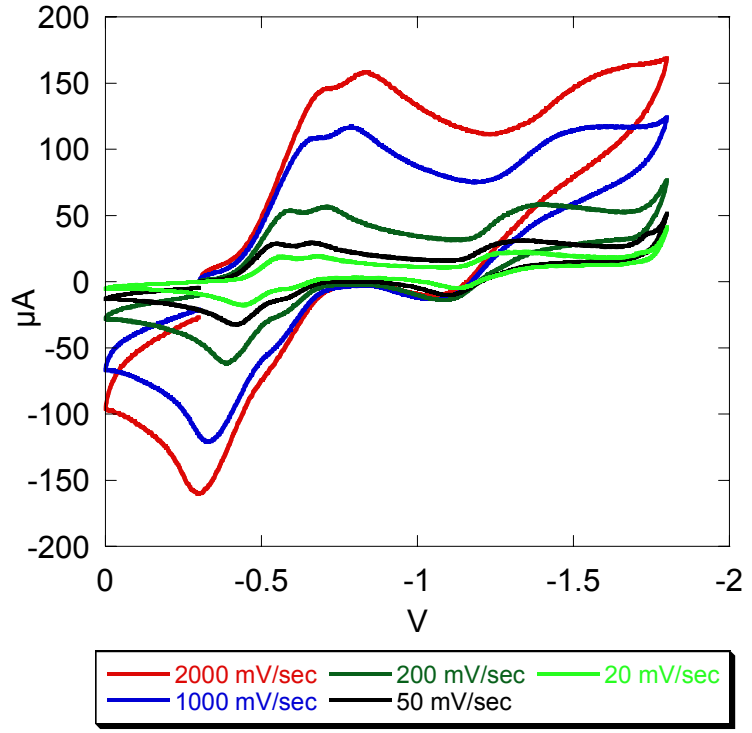

Figure 2.18. Scan rate comparison for $(PPN)_2[Fe_8S_6(NO)_8]$ at room temperature from -0.3 to -1.8V

	E_{pf} (mV)	Scan Rate (mV/sec)	ΔE_p (mV)	i_{pr}/i_{pf}	$i_{pf}/v^{1/2}$	$i_{pr}/v^{1/2}$
	-576	10	86	1.117	3.127	3.525
	-580	20	90	1.190	3.133	3.729
	-588	50	100	1.242	3.035	3.768
1st wave	-596	100	118	1.252	3.059	3.850
	-606	200	132	1.257	3.010	3.785
	-626	500	168	1.292	2.886	3.728
	-636	1000	188	1.344	2.776	3.730
	-668	2000	238	1.382	2.667	3.686
	-700	10	78	0.422	3.216	1.358
	-706	20	92	0.590	3.108	1.851
	-706	50	92	0.540	3.091	1.669
2nd wave	-710	100	96	0.571	3.049	1.759
	-724	200	108	0.575	3.024	1.740
	-742	500	140	0.607	2.980	1.808
	-760	1000	142	0.590	2.921	1.723
	790	2000	196	0.678	2.819	1.913

Table 2.12. Electrochemical parameters for the two first waves of $(PPN)_2[Fe_8S_6(NO)_8]$ from 0 to -1V

As seen from Table 2.12 above, although the first wave still shows an increase in the i_{pr}/i_{pf} ratio with the increase of scan rate, the i_{pr}/i_{pf} ratio for the second wave seems to fluctuate, which contradicts the trend seen earlier in the first graph (Table 2.11). This can be explained either by the fact that the peak is not that well resolved, and therefore the experimental error in the calculation is relatively large, or by the other possibility, that the following irreversible chemical reaction (implied by the E_rC_i mechanism) is a reaction that occurs at potentials higher than -1V.

Since 0V is not the potential that the current reaches zero as evident in the graphs, but rather -0.3V is the point where there is no current flow to the electrode, the same sample was taken again and the analysis was repeated. This time the potentials were allowed to reach -1.8V, with the peaks and trends practically remaining unaltered, except the i_{pr}/i_{pf} ratio for the second reduction. Although the decrease is now once again evident it is still close to experimental uncertainty so it is not appropriate to derive from these measurements, any conclusions on the nature of the second peak, and only treat it as a simple quasi-reversible reduction.

	E_{pf} (mV)	Scan Rate (mV/sec)	ΔE_p (mV)	i_{pr}/i_{pf}	$i_{pf}/v^{1/2}$	$i_{pr}/v^{1/2}$
	-572	20	140	1.313	4.159	3.958
	-550	50	134	1.507	4.031	4.624
1st wave	-594	200	206	1.525	3.797	4.377
	-678	1000	350	1.544	3.412	3.820
	-700	2000	404	1.560	3.258	3.591
	-706	20	120	0.664	4.249	1.308
	-706	50	108	0.832	4.144	1.986
2nd wave	-724	200	168	0.836	3.967	1.888
	-760	1000	268	0.877	3.675	1.749
	790	2000	334	0.895	3.540	1.652

Table 2.13. Electrochemical parameters for the two first waves of $(PPN)_2[Fe_8S_6(NO)_8]$ from -0.3V to -1.8V

Upon cooling the solution to lower temperatures (approximately -10ºC) and performing cyclic voltammetry experiments (Figure 2.19), the two waves are practically unchanged, with the only notable difference being that the spacing between the two

consecutive waves increases both with the decrease in temperature and with the increase of scan rate, a trend that is not observed at room temperature. This is basically due to the lowering of the half wave potential of the first reduction much more than the second reduction, which implies a larger influence of temperature to the first electron transfer. This is also in accordance to a C_rE_r mechanism for the first reduction wave, and the temperature dependency of the potential can be calculated according to the following equation:

$$E'^* = E' + \frac{RT}{nF} \ln \frac{K}{K+1} \qquad \text{(eq.6)}$$

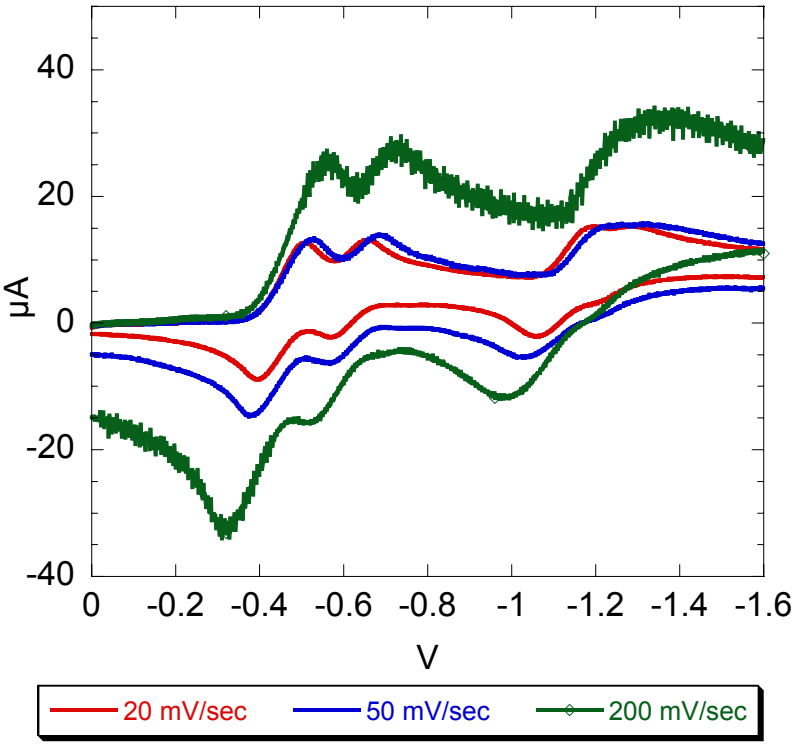

Figure 2.19. Scan rate comparison for $(PPN)_2[Fe_8S_6(NO)_8]$ at low temperature.

The $(PPN)_2[Fe_8S_6(NO)_8]$ cluster was also examined in different solvents (Figure 2.20), to see if the solvent system would affect the appearance of the two waves. The compound is readily soluble in DMF and Dichloroethane and slightly less soluble in

THF, but not very soluble in MeCN. Thus the signal in MeCN is considerably weaker than in other solvents due to poor solubility. In all cases the two waves are still present with the only differences being the exact positions of the waves, as expected in different solvent systems, and the spacing of the two waves, that decreases with solvent polarity by about 10mV.

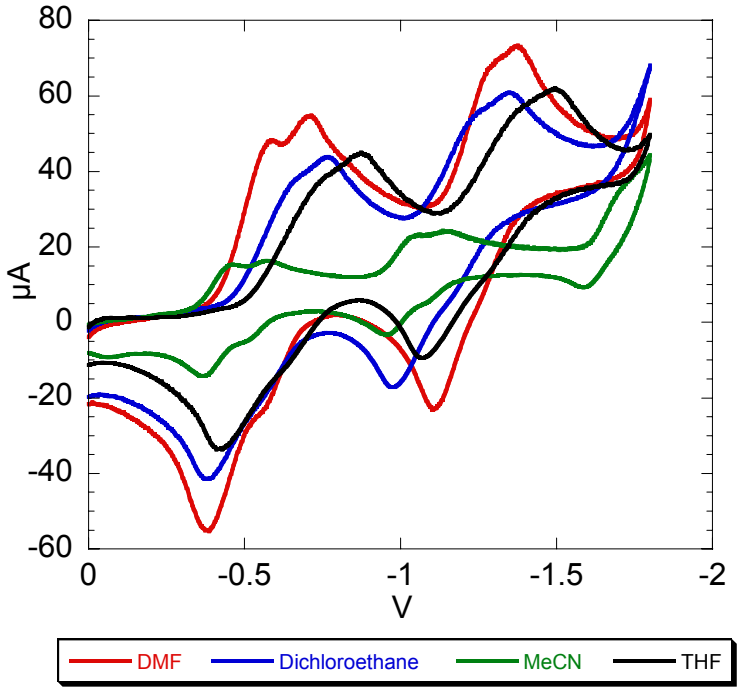

Figure 2.20. Cyclic Voltammetry of $(PPN)_2[Fe_8S_6(NO)_8]$ in different solvents

Since the $(PPN)_2[Fe_4S_3(NO)_7]$ and $(PPN)_2[Fe_6S_6(NO)_6]$ clusters show waves with similar potentials to the reduction waves of $(PPN)_2[Fe_8S_6(NO)_8]$, spiking experiments with these species were performed, by addition of solutions either $(PPN)_2[Fe_4S_3(NO)_7]$ or $(PPN)_2[Fe_6S_6(NO)_6]$ to a solution of $(PPN)_2[Fe_8S_6(NO)_8]$. The results of these experiments (Figures 2.21 and 2.22), showed that both species can be excluded either as possible contaminants in $(PPN)_2[Fe_8S_6(NO)_8]$, either as species formed in solution, since

the appearance of new peaks corresponding to $(PPN)_2[Fe_4S_3(NO)_7]$ and $(PPN)_2[Fe_6S_6(NO)_6]$is evident.

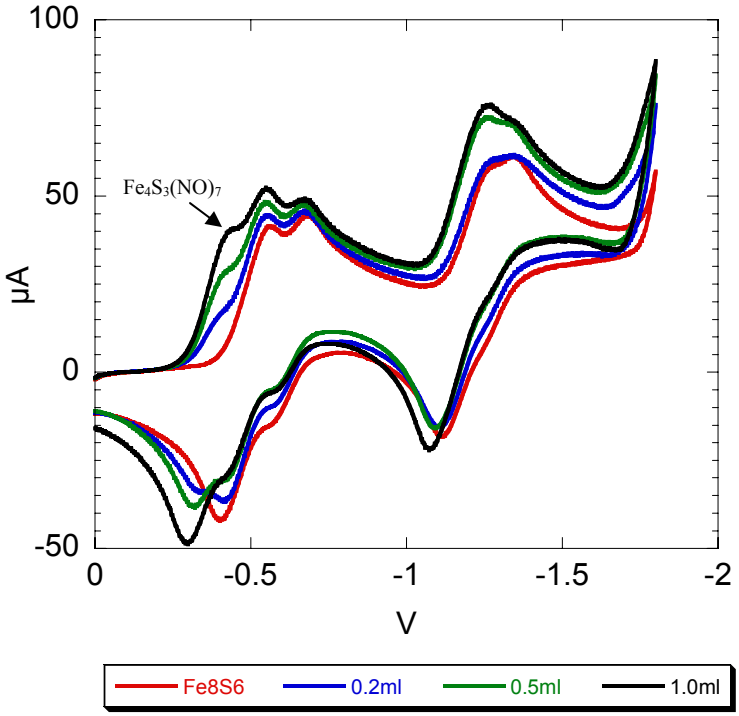

Figure 2.21. Spiking of $(PPN)_2[Fe_8S_6(NO)_8]$ with $(PPN)[Fe_4S_3(NO)_7]$

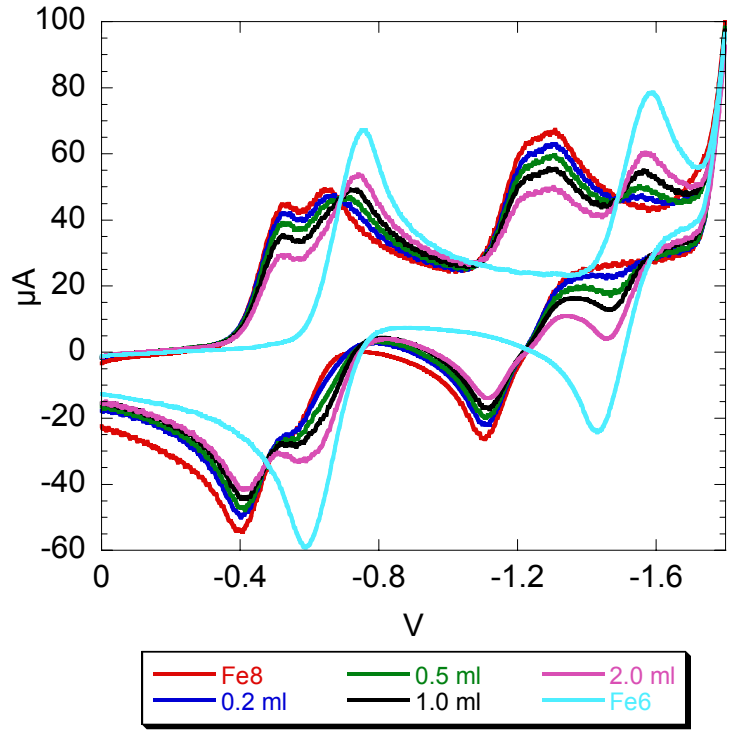

Figure 2.22. Spiking of $(PPN)_2[Fe_8S_6(NO)_8]$ with $(PPN)_2[Fe_6S_6(NO)_6]$

A similar effect on the waves is evident in the case of the addition of $[Fe(Cp)_2]^+$ to a solution of (PPN)$[Fe_8S_6(NO)_8]$ (Figure 2.22). $(PPN)_2[Fe_6S_6(NO)_6]$ forms as the product of oxidation as described in Reaction 9 and is detected by the appearance of the peak at -1.5V. Overall, these results suggest that the two initial waves are not related by a redox process but rather by equilibrium of two species.

In another electrochemical experiment, $[Cu(MeCN)_4]PF_6/PPr_3$ was added to a solution of $(PPN)_2[Fe_8S_6(NO)_8]$ and monitored by cyclic voltammetry over a period of 5 hours as seen in Figure 2.23. The initial shift in potentials from 0 to 30 min is due to the changes in the solvent system as the Cu^+/PPr_3 mixture is added as an acetonitrile solution to a DMF solution of $(PPN)_2[Fe_8S_6(NO)_8]$. As seen in Figure 2.20 however, this fact cannot account for the change in ratio of the currents of the two reductions, as simple solvent system changes would keep the ratio the same. After 30 min, identification of the peaks is not clear as it can either be a shift of the initial waves from -570mV,-684mV to -476mV, -572mV or the appearance of an additional irreversible peak at -476mV superimposed on the initial spectrum.

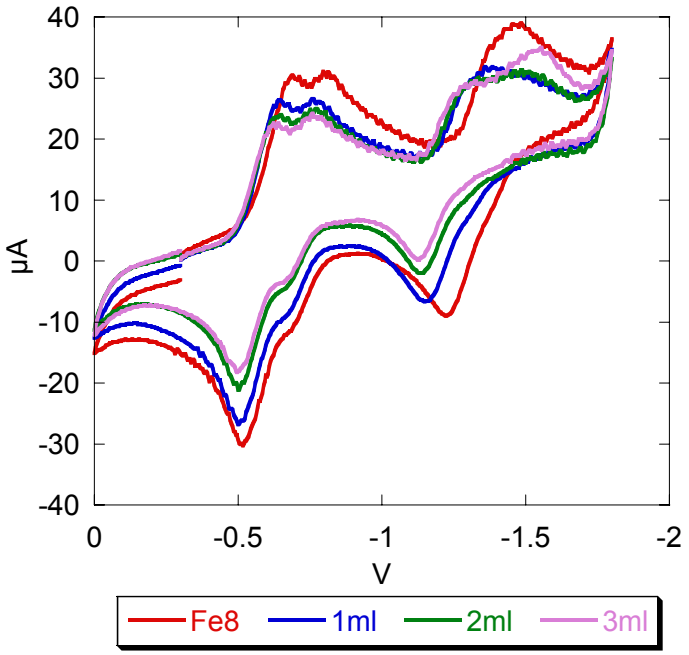

Figure 2.23. Cyclic voltammogram of $(PPN)_2[Fe_8S_6(NO)_8]$ in DMF, with addition of $[Fe(Cp)_2]^+$ 20mM in MeCN. The initial shift in potentials seen in Fe_8 and 1ml lines is normal as the solution becomes a mixture of DMF and MeCN.

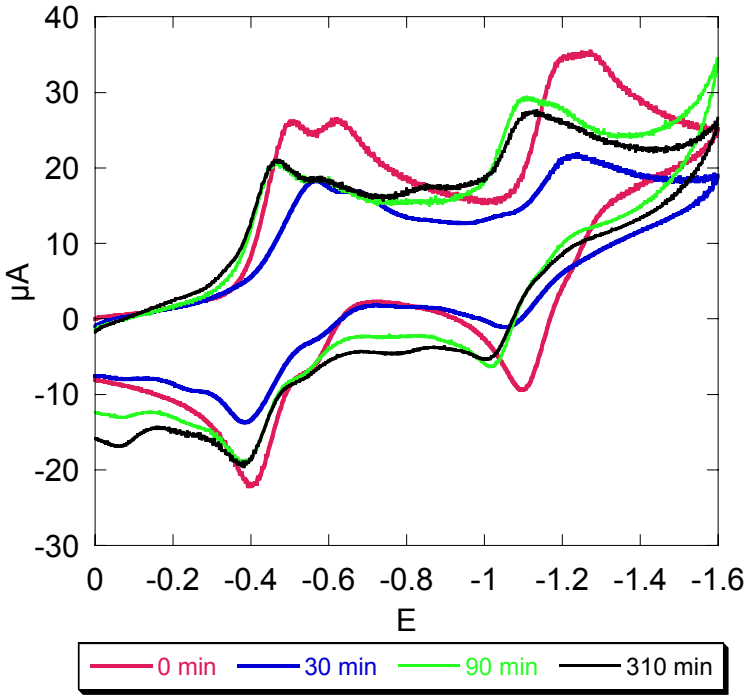

Figure 2.24. Cyclic voltammetry graph of the reaction of $(PPN)_2[Fe_8S_6(NO)_8]$ with Cu^+/PPr_3

As the oxidations of the $[Fe_8S_6(NO)_8]^{2-}$ cluster appear irreversible, two consecutive full range scans were performed. The voltammogram pattern of the $[Fe_8S_6(NO)_8]^{2-}$ cluster remains unaltered within the 1V to -2V window; however, higher positive potentials up to 2V cause the appearance of new peaks. In DMF, there is a new irreversible reduction appearing at approximately -0.3V (Figure 2.24), while in dichloroethane the effect of oxidation is much more prominent, with the appearance of an irreversible reduction peak at -780V (Figure 2.25). The height of the peak, which is more than double the size of the initial peaks, suggests that both species that exist in solution were converted to the same species that gives rise to this irreversible wave.

Despite the several experiments performed, the nature of the two waves is not completely clarified. The data presented indicate that the most likely explanation could be that in solution $[Fe_8S_6(NO)_8]^{2-}$ dissociates to another species that gives rise to the reduction at -480 mV, thus exhibiting characteristics of a C_rE_r reduction mechanism, while the reduction at -620mV is attributed to the $[Fe_8S_6(NO)_8]^{2-}/[Fe_8S_6(NO)_8]^{3-}$ couple. The reductions at -1200V and -1300V can be attributed to the above two species respectively, but due to the difficulty in separating the two peaks it is better not to make any assignments of redox couples.

Regarding the nature of the proposed species formed in solution, it is shown that it is not a known species, but as suggested by EPR, contains an odd number of electrons in its ground state. Two species that can be envisioned as reasonable possibilities to form in solution are a $[Fe_7S_6(NO)_7]^{4-}$ or a $[Fe_4S_3(NO)_4]^{-}$ cluster, since neither requires any change in the oxidation states of the metals and would exhibit an EPR signal in their ground state, in contrast to $(PPN)_2[Fe_8S_6(NO)_8]$ which the $2\{FeNO\}^7$, $6\{FeNO\}^8$ units will provide a S=0 ground state.

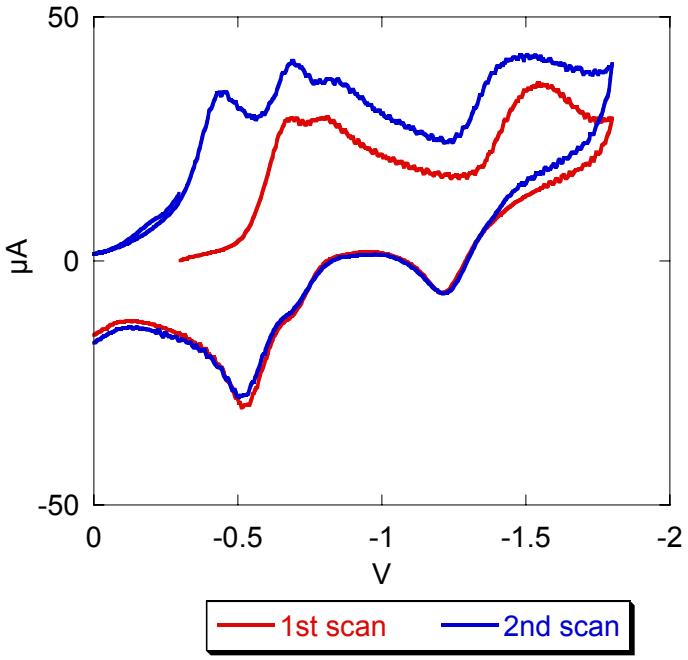

Figure 2.25. Cyclic voltammogram of $(PPN)_2[Fe_8S_6(NO)_8]$ in DMF, with two consecutive scans from +1.5V to-1.8V. The irreversible oxidations appearing below 0V that reach -350 μA are omitted for clarity.

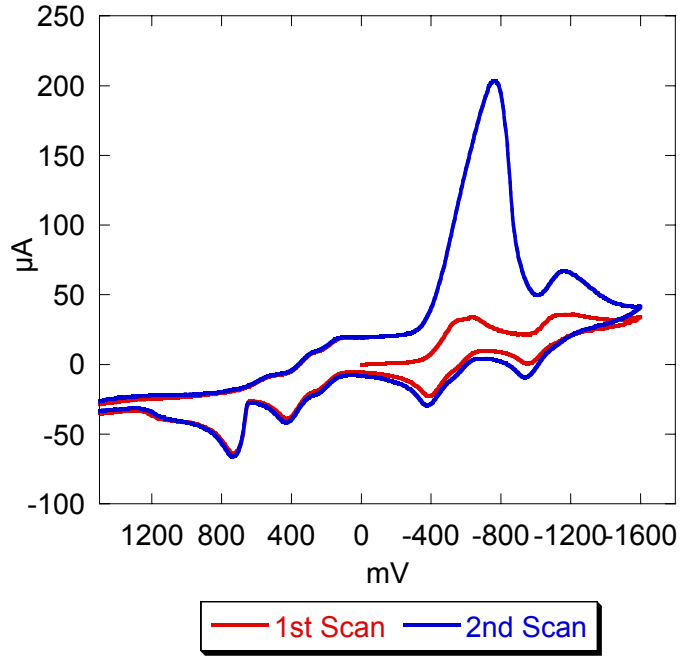

Figure 2.26. Cyclic voltammogram of $(PPN)_2[Fe_8S_6(NO)_8]$ in dichloroethane, with two consecutive scans from +1.5V to-1.8V.

2.4 Conclusions

In this chapter the synthesis and reactivity of octa-, hexa- and tetra- Fe/S/NO species was presented. In terms of synthesis and rearrangements, the Fe/S/NO clusters exhibit a behavior that is almost identical to their Fe/S/X (X=halogen, thiol) analogues. The labile nature of Iron Sulfur clusters in solution governs the formation of the clusters presented herein. This work expands our knowledge about the behavior of Iron Sulfur clusters and their nitrosylated clusters. It was learned that the reactivity of Fe/S/NO clusters does not extend to ligand substitution reactions, because the Fe-NO bond is considerably more covalent than that with halogens or thiols, and removal of NO does not occur without disrupting the Fe/S core. The spectroscopic investigations on these Fe/S/NO clusters, strongly implies that NO^- is a more suitable description for the nitrosyl ligand in this family of compounds than $NO\cdot$ or NO^+. This notation is also in line with the reactivity of these clusters and also their spectroscopic properties. Although not directly related to biological systems, these compounds can be useful tools in elucidating further the interactions of NO with iron/sulfur clusters in biology.

Future goals include studies at a theoretical level in order to clarify further the electronic properties of these clusters, exploring their reactivity towards electrophiles that could lead to new structural rearrangements, and finally, exploring the reactivity of these clusters under conditions (i.e. short reaction times or low temperatures) that will not favor the more stable thermodynamic products and can therefore, provide new and exciting clusters to further increase the knowledge on iron/sulfur clusters.

2.5 References

[1] J.A. McCleverty, Chem. Rev. 104 (2004) 403.
[2] A.R. Butler, I.L. Megson, Chem. Rev. 102 (2002) 1155.
[3] M.P. Murphy, Biochimica Et Biophysica Acta-Bioenergetics 1411 (1999) 401.
[4] R.F. Furchgott, J.V. Zawadzki, Nature 288 (1980) 373.
[5] S. Moncada, R.M.J. Palmer, E.A. Higgs, Pharmacological Reviews 43 (1991) 109.
[6] F. Murad, Angewandte Chemie-International Edition 38 (1999) 1857.
[7] A.R. Butler, C. Glidewell, Chem. Soc. Rev. 16 (1987) 361.
[8] S.A.T. Dillinger, H.W. Schmalle, T. Fox, H. Berke, Dalton Transactions (2007) 3562.
[9] C.E. Cooper, Biochimica Et Biophysica Acta-Bioenergetics 1411 (1999) 290.
[10] J.C. Drapier, Methods 11 (1997) 319.
[11] K. Asanuma, K. Iijima, N. Ara, T. Koike, J. Yoshitake, S. Ohara, T. Shimosegawa, T. Yoshimura, Nitric Oxide-Biology and Chemistry 16 (2007) 395.
[12] F.Z. Roussin, Ann Chim Phys 52 (1858) 285.
[13] F.W. Flitney, I.L. Megson, D.E. Flitney, A.R. Butler, Br. J. Pharmacol. 107 (1992) 842.
[14] F.W. Flitney, I.L. Megson, J.L.M. Thomson, G.D. Kennovin, J. Physiol. (London) 459 (1993) P90.
[15] F.W. Flitney, I.L. Megson, J.L.M. Thomson, G.D. Kennovin, A.R. Butler, Br. J. Pharmacol. 117 (1996) 1549.
[16] O. Einsle, F.A. Tezcan, S.L.A. Andrade, B. Schmid, M. Yoshida, J.B. Howard, D.C. Rees, Science 297 (2002) 1696.
[17] M.A. Tyson, D. Coucouvanis, Inorg. Chem. 36 (1997) 3808.
[18] D. Coucouvanis, J.H. Han, N. Moon, J. Am. Chem. Soc. 124 (2002) 216.
[19] J.H. Han, K. Beck, N. Ockwig, D. Coucouvanis, J. Am. Chem. Soc. 121 (1999) 10448.
[20] W. Cen, F.M. Macdonnell, M.J. Scott, R.H. Holm, Inorg. Chem. 33 (1994) 5809.
[21] L.L. Martin, L.C. West, B. Wu, Eur. J. Biochem. 268 (2001) 5676.
[22] K. Whitmire, J. Ross, C.B. Cooper, D.F. Shriver, Inorg. Synth. 21 (1982) 66.
[23] D. Coucouvanis, M. Kanatzidis, E. Simhon, N.C. Baenziger, J. Am. Chem. Soc. 104 (1982) 1874.
[24] F. Osterloh, C. Achim, R.H. Holm, Inorg. Chem. 40 (2001) 224.
[25] K.H. Pannell, Y.S. Chen, K. Belknap, C.C. Wu, I. Bernal, M.W. Creswick, H.N. Huang, Inorg. Chem. 22 (1983) 418.
[26] N.G. Connelly, C. Gardner, J. Chem. Soc., Dalton Trans. (1976) 1525.
[27] J.H. Enemark, R.D. Feltham, Coord. Chem. Rev. 13 (1974) 339.
[28] M. Jaworska, Z. Stasicka, J. Mol. Struct. 785 (2006) 68.
[29] S.S. Sung, C. Glidewell, A.R. Butler, R. Hoffmann, Inorg. Chem. 24 (1985) 3856.
[30] C.A. Brown, M.A. Pavlosky, T.E. Westre, Y. Zhang, B. Hedman, K.O. Hodgson, E.I. Solomon, J. Am. Chem. Soc. 117 (1995) 715.
[31] R.E. Stevens, W.L. Gladfelter, Inorg. Chem. 22 (1983) 2034.

[32] D.E. Fjare, W.L. Gladfelter, Inorg. Chem. 20 (1981) 3533.
[33] C.T.W. Chu, F.Y.K. Lo, L.F. Dahl, J. Am. Chem. Soc. 104 (1982) 3409.
[34] M.G. Kanatzidis, W.R. Hagen, W.R. Dunham, R.K. Lester, D. Coucouvanis, J. Am. Chem. Soc. 107 (1985) 953.
[35] S. Pohl, W. Saak, Angew. Chem., Int. Ed. Engl. 23 (1984) 907.
[36] S. Pohl, U. Opitz, Angew. Chem., Int. Ed. Engl. 32 (1993) 863.
[37] C. Goh, B.M. Segal, J.S. Huang, J.R. Long, R.H. Holm, J. Am. Chem. Soc. 118 (1996) 11844.
[38] C. Glidewell, R.J. Lambert, M.E. Harman, M.B. Hursthouse, J. Chem. Soc., Dalton Trans. (1990) 2685.
[39] M.J. Scott, R.H. Holm, Angew. Chem., Int. Ed. Engl. 32 (1993) 564.
[40] U. Geiser, J.M. Williams, Acta Crystallographica Section C-Crystal Structure Communications 54 (1998) 292.
[41] M.G. Kanatzidis, A. Salifoglou, D. Coucouvanis, Inorg. Chem. 25 (1986) 2460.
[42] W. Saak, G. Henkel, S. Pohl, Angew. Chem., Int. Ed. Engl. 23 (1984) 150.
[43] M.G. Kanatzidis, A. Salifoglou, D. Coucouvanis, J. Am. Chem. Soc. 107 (1985) 3358.
[44] S.A. Alahmad, A. Salifoglou, M.G. Kanatzidis, W.R. Dunham, D. Coucouvanis, Inorg. Chem. 29 (1990) 927.
[45] T.C. Harrop, D.T. Song, S.J. Lippard, J. Am. Chem. Soc. 128 (2006) 3528.
[46] T.T. Lu, S.J. Chiou, C.Y. Chen, W.F. Liaw, Inorg. Chem. 45 (2006) 8799.
[47] E. Tangen, J. Conradie, A. Ghosh, Inorg. Chem. 44 (2005) 8699.
[48] E. Munck, Aspects of Fe Mossbauer spectroscopy, in: L. Que (Ed.), Physical methods in bioinorganic chemistry : spectroscopy and magnetism, University Science Books, Sausalito, Calif. :, 2000.
[49] D. Sedney, W.M. Reiff, Inorg. Chim. Acta 34 (1979) 231.
[50] P.V. Rao, R.H. Holm, Chem. Rev. 104 (2004) 527.
[51] G. Palmer, Electron paramagnetic resonance of metalloproteins, in: L. Que (Ed.), Physical methods in bioinorganic chemistry : spectroscopy and magnetism, University Science Books, Sausalito, Calif. :, 2000.
[52] S. D' Addario, F. Demartin, L. Grossi, M.C. Iapalucci, F. Laschi, G. Longoni, P. Zanello, Inorg. Chem. 32 (1993) 1153.
[53] P. Zanello, Inorganic electrochemistry : theory, practice and application Royal Society of Chemisty, Cambridge, 2003.

Chapter 3

Synthesis of Heterometallic M/Fe/S (M=Cu, Ni, Co) Clusters with a Pentlandite M_8S_6 Core

3.1 Introduction

Among the plethora of metal sulfide minerals are the cubic pentlandites that can be found as composites of sulfides of several metals with the general formula M_9S_8. Pentlandite is an important ore of nickel and is believed to be composed of equal amounts of nickel and iron $(Ni_{4.5}Fe_{4.5})S_8$ [1-3] although its composition varies slightly with pressure and temperature [4-8]. The pentlandite lends its name and structure to a group of minerals called the pentlandite group that includes also the Argentopentlandite $Ag(Fe_6Ni_2)S_8$ [9, 10], the Cobaltpentlandite Co_9S_8 [11, 12], the Geffroyite $(Ag,Cu,Fe)_9(Se,S)_8$ [13], the Shadlunite $(Pb_{0.75}Cd_{0.25})(Fe_4Cu_4)S$ and the Manganoshadlunite $(Mn_{0.75}Pb_{0.25})(Fe_6Cu_2)S_8$. These minerals are made up of extended lattices of recognizable metal sulfide clusters that are connected by bridging interactions. Their repeating units are M_8S_6 fragments consisting of a cube of metal atoms with each square tetra-metal face symmetrically capped by sulfur atoms that alone inscribe an octahedron (Figure 3.1). The synthesis and characterization of discrete and soluble building blocks of metal sulfur clusters that can be identified in extended lattices is of

extreme importance, and is therefore the focus of extensive research [6, 7, 14-16]. Synthetic cubic metal clusters of the M_8S_6 type are known including the Fe_8S_6 [17, 18], $Mo_2Fe_6S_6$ [19, 20], Ni_8S_6 [21, 22], and Co_8S_6 [23, 24] clusters with the latter being so far the closest synthetic analogue to the natural occurring pentlandites.

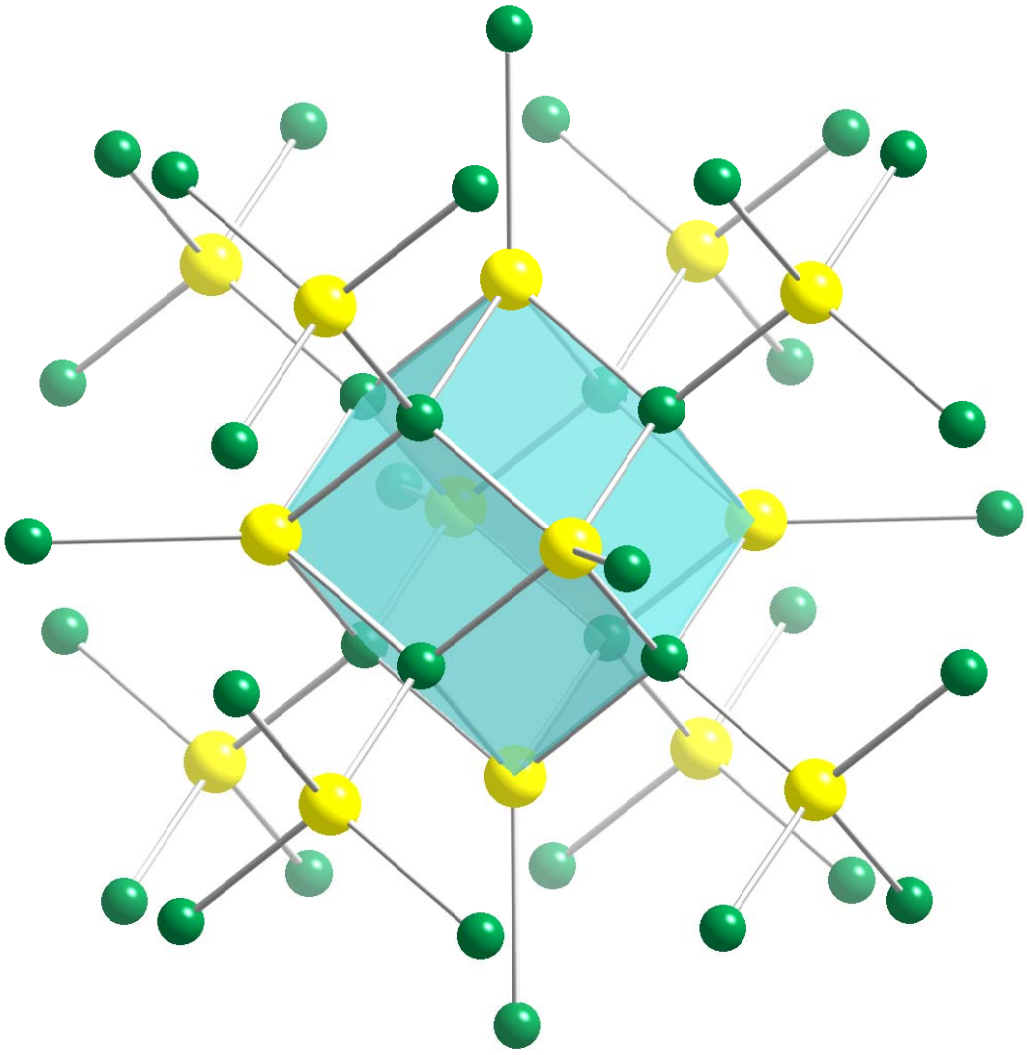

Figure 3.1. The repeating framework unit in pentlandites with a metal cube and sulfur atoms forming an octahedron. The Ni and Fe atoms are depicted with green color whereas S atoms are with yellow.

3.2 Experimental Section

All the reactions were performed under Nitrogen atmosphere in a glove box or by standard Shlenck line techniques. The solvents used were distilled and degassed, except water that was degassed only. Compounds $(Bu_4N)_2[Fe_4S_4Cl_4]$ [25], $(Et_4N)_2[Fe_2S_2Cl_4]$ [26], and $[M(MeCN)_6](BF_4)_2$ (M=Ni, Co) [27] were synthesized according to published procedures, while NaSH, $[(CH_3)_3Si]_2S$, tripropylphosphine (PPr_3), triethylphosphine (PEt_3) and $[Cu(MeCN)_4]PF_6$ were purchased from commercial sources.

IR spectra were collected on a Perkin Elmer Spectrum BX FT-IR spectrometer (mid-IR) and a Nicolet 740 FT-IR spectrometer (Far-IR) in KBr pellets, cyclic voltammetry experiments were carried out with a glassy carbon working electrode and a Ag/AgCl reference electrode with 0.1M Bu_4NPF_6 as supporting electrolyte on a EG&G Princeton Potentiostat/Galvanostat model 263A. The redox potentials are reported vs. SCE. Mössbauer spectra were obtained on a high-sensitivity Mössbauer spectrometer at the Institute of Materials Science, NCSR "Demokritos" Athens, Greece, courtesy of Dr. Yiannis Sanakis. Elemental analysis was performed by the Microanalytical Laboratory at the University of Michigan. Microprobe analyses were performed at the University of Michigan Electron Microbeam Analysis Laboratory.

3.2.1 Bis (Tetrabutylammonium) hexasulfido-hexairon-hexachloro bis(triethylphosphino-copper), $(Bu_4N)_2[(PEt_3)_2Cu_2Fe_6S_6Cl_6]$.*(Reaction 1)*

$[Cu(MeCN)_4]PF_6$ (0.5g, 1.34 mmol) was dissolved in 5ml MeCN followed by the dropwise addition of PEt_3 (0.2 ml, 1.37 mmol) and the mixture was allowed to stir for 30min. The resulting solution was added dropwise to a 15ml solution of $(Bu_4N)_2[Fe_4S_4Cl_4]$ (1.00g, 1.02 mmol) in MeCN. The reaction mixture was left stirring

for one hour before being filtered. The MeCN filtrate was layered with ether (~ 40 ml) and produced 0.4g of crystalline material.

Yield 0.25 mmol, 25% of $(Bu_4N)_2[(PEt_3)_2Cu_2Fe_6S_6Cl_6]$ based on copper.

Elemental analysis calculated for $(Bu_4N)_2[(PEt_3)_2Cu_2Fe_6S_6Cl_6]$, $C_{44}H_{102}Cl_6Cu_2Fe_6N_2P_2S_6$: C: 33.27%, H: 6.47%, N: 1.76%. Found: C: 33.36%, H: 6.75%, N: 1.84%.

IR (KBr, cm^{-1}): 2960(m), 2932(m), 2873(m), 1457(m), 1432(w), 1413(w) 1378(m), 1259(m), 1147(w), 1103(m), 1035(m), 879(w), 840(w), 805(m) ,772(m), 751(w), 733(w), 693(w), 346(s), 322(s)

Microprobe analysis confirmed the Cu/Fe/S/P/Cl ratio of 1:3:3:1:3.

3.2.2 Hexasulfido-Tetrairon-tetrachloro tetra(tripropylphosphino-copper) $(PPr_3)_4Cu_4Fe_4S_6Cl_4$.

Method A. ***(reaction 2)***

$(Et_4N)_2[Fe_2S_2Cl_4]$ (0.36g, 0.62 mmol) and $[Cu(MeCN)_4]PF_6$ (0.46g, 1.24 mmol) were dissolved in a mixture of 20ml MeCN and 0.5ml H_2O, followed by the addition of NaSH (0.070g, 1.24 mmol) and $NaPF_6$ (0.21g, 1.24 mmol) under vigorous stirring. Subsequently PPr_3 (0.50 ml, 2.48 mmol) was added dropwise. The reaction mixture was stirred overnight and then filtered. The filtrate was layered with approximately 100ml of ether and placed in the freezer for several hours. A white crystalline compound was separated by filtration and the filtrate was brought to dryness under a nitrogen stream. The resulting black powder was partially extracted with THF and layered with hexanes affording 0.15g of black crystals, which were isolated after filtration and thoroughly washed with acetonitrile.

Yield 0.10 mmol, 33% of $(PPr_3)_4Cu_4Fe_4S_6Cl_4$ based on iron.

Method B *(Reaction 3)*

Two solutions were prepared. Solution A; $(Et_4N)_2(Fe_2S_2Cl_4)$ (0.3g, 0.52 mmol) was dissolved in 15ml MeCN followed by the dropwise addition of $[(CH_3)_3Si]_2S$ (0.11ml, 0.52mmol) under vigorous stirring. Solution B; $[Cu(MeCN)_4]PF_6$ (0.40g, 1.04 mmol) was dissolved in 10 ml MeCN followed by the dropwise addition of PPr_3 (0.21ml, 1.04 mmol) under vigorous stirring. The two solutions were allowed to stir for 30 min and then solution B was added dropwise to solution A over a period of 5 min. The resulting mixture was stirred for an additional 2 hours, filtered, and the filtrate was taken to dryness under a nitrogen stream. The resulting oily material was partially extracted with 30ml of THF and layered with hexanes affording 0.15g of a black crystalline material.

Yield 0.10 mmol, 40% of $(PPr_3)_4Cu_4Fe_4S_6Cl_4$ based on iron.

Elemental analysis calculated for $(PPr_3)_4Cu_4Fe_4S_6Cl_4$ $C_{36}H_{84}Cl_4Cu_4Fe_4P_4S_6$: C: 29.76%, H: 5.83%, N: 0%. Found: C: 29.89%, H: 5.94%, N: 0%.

IR (KBr, cm^{-1}): 2958(vs), 2929(s), 2891(m), 2869(s), 2801(w), 1456(s), 1416(m), 1377(m), 1341(w), 1301(w), 1261(w), 1230(m), 1080(s), 1050(s), 1040(s), 903(w), 845(m), 841(m), 782(m), 767(m), 727(s), 435(m), 425(m).

Microprobe analysis confirmed the Cu/Fe/S/P/Cl ratio of 2:2:3:2:2.

3.2.3. Hexasulfido-tetrairon-tetrachloro tetra(triporpylphosphino-Nickel) $(PPr_3)_4Ni_4Fe_4S_6Cl_4$.

Method A *(Reaction 4).*

Two solutions were prepared. Solution A; $(Et_4N)_2(Fe_2S_2Cl_4)$ (0.3g, 0.52 mmol) was dissolved in 15ml MeCN followed by the dropwise addition of $[(CH_3)_3Si]_2S$ (0.11ml, 0.52mmol) under vigorous stirring. Solution B; $[Ni(MeCN)_6](BF_4)_2$ (0.49g, 1.04 mmol)

was dissolved in 10 ml MeCN followed by the dropwise addition of PPr_3 (0.21ml, 1.04 mmol) under vigorous stirring. The two solutions were allowed to stir for 30 min and then solution B was added dropwise to solution A over a period of 5 min. The resulting mixture was stirred for an additional 3 hours, filtered, and the filtrate was taken to dryness under a nitrogen stream. The resulting oily material was suspended in 50 ml of ether and stirred for 15 min before filtration. The ether filtrate was transferred in a test tube for slow evaporation of the solvent in the glove box yielding 0.13g of black crystals that were isolated through filtration and were washed with hexanes.

Yield 0.09 mmol, 35% yield based on iron.

Method B *(Reaction 5)*.

$[Ni(MeCN)_6](BF_4)_2$ (0.2g, 0.408 mmol) was dissolved in 5ml MeCN and PPr_3 (0.08ml, 0.408 mmol) was added dropwise and the solution was stirred for 10 min. This solution was then added dropwise to a 25ml MeCN solution containing $(Bu_4N)_2[Fe_4S_4Cl_4]$ (0.2g, 0.204 mmol) and under vigorous stirring. The resulting mixture was allowed to stir for 1.5 hours, filtered and the volume of the filtrate was reduced to approx. 8ml under a nitrogen stream. The solution was placed in the freezer for one day and 0.1g of a black microcrystalline solid was obtained by filtration. Single crystals suitable for X-Ray structural determination were obtained from an ether solution after slow evaporation of the solvent.

Yield 0.07mmol, 34% of $(PPr_3)_4Ni_4Fe_4S_6Cl_4$ based on iron.

Elemental analysis calculated for $(PPr_3)_4Ni_4Fe_4S_6Cl_4$, $C_{36}H_{84}Cl_4Ni_4Fe_4P_4S_6$: C: 30.17%, H: 5.91%, N: 0%. Found: C: 30.25%, H: 6.01%, N: 0%.

IR (KBr, cm^{-1}): 2958(vs), 2928(s), 2890(m), 1456(m), 1409(m), 1372(m), 1341(m), 1298(w), 1260(w), 1220(s), 1070(s), 1044(sh), 1037(s), 1016(m), 894(w), 848(s), 838(m), 819(m), 764(m), 722(s), 433(m), 399(w), 362(s), 318(w), 294(m).

Microprobe analysis confirmed the Ni/Fe/S/P/Cl ratio.

3.2.4. Bis(tetraethylammonium) hexasulfido-hexairon-hexachloro bis (tripropylphosphino-nickel) $(Et_4N)_2[(PPr_3)_2Ni_2Fe_6S_6Cl_6]$.*(Reaction 6)*

Two solutions were prepared: Solution A; $(Et_4N)_2(Fe_2S_2Cl_4)$ (0.3g, 0.52 mmol) was dissolved in 15ml MeCN and $[(CH_3)_3Si]_2S$ (0.11ml, 0.52mmol) were added dropwise under vigorous stirring. Solution B; $NiSO_4$ (0.08g, 0.52 mmol) was dissolved in a solution of 10ml MeCN and 2ml MeOH, followed by the dropwise addition of PPr_3 (0.21ml, 1.04 mmol) under vigorous stirring. The two solutions were left to stir for 30 min and then solution B was added dropwise to solution A over a period of 5 min. The resulting mixture was stirred for 2 hours, filtered, and the filtrate layered with ether (~ 50ml). A mixture of black crystals and a white solid were isolated after filtration. The two solids were separated by washing with MeOH that dissolved the white solid and the remaining black crystals (0.05g) were identified as $(Et_4N)_2[(PPr_3)_2Ni_2Fe_6S_6Cl_6]$. The MeCN/ether filtrate that was still dark colored was taken to dryness under a nitrogen stream. The resulting black powder was partially extracted with 50ml of ether, filtered and the resulting solution was left for slow evaporation affording 0.03g of black crystals that were identified as $[Ni_3S_2(PPr_3)_6][Ni_3Fe_5S_6(PPr_3)_3Cl_5]$.

$(Et_4N)_2[(PPr_3)_2Ni_2Fe_6S_6Cl_6]$

Yield 0.03mmol, 17% of $(Et_4N)_2[(PPr_3)_2Ni_2Fe_6S_6Cl_6]$ based on iron.

Elemental analysis calculated for $(Et_4N)_2[(PPr_3)_2Ni_2Fe_6S_6Cl_6]$ $C_{50}H_{114}Cl_6Ni_2Fe_6N_2P_2S_6$: C: 28.39%, H: 5.75%, N: 1.95%. Found: C: 28.56%, H: 5.92%, N: 2.06%.

IR (KBr, cm^{-1}): 2958(vs), 2929(s), 2890(m), 2869(s), 1488(s), 1478(m), 1457(s), 1438(s), 1416(m), 1406(m), 1393(s), 1373(m), 1364(m), 1341(w), 1329(w), 1295(w), 1218(w), 1173(m), 1080(s), 1039(s), 1032(m), 999(s), 900(w), 850(m), 786(m), 752(m), 726(m), 690(m), 435(m), 420(w), 345(s), 322(s), 282(s).

Microprobe analysis confirmed the Ni/Fe/S/P/Cl ratio of 1:3:3:1:3.

$[Ni_3S_2(PPr_3)_6][Ni_3Fe_5S_6(PPr_3)_3Cl_5]$

Yield 0.01 mmol, 11% of $[Ni_3S_2(PPr_3)_6][Ni_3Fe_5S_6(PPr_3)_3Cl_5]$ based on Ni.

Elemental analysis calculated for $[Ni_3S_2(PPr_3)_6][Ni_3Fe_5S_6(PPr_3)_3Cl_5]$ $C_{81}H_{189}Cl_5Ni_6Fe_5N_2P_9S_8$: C: 38.80%, H: 7.60%, N: 0%. Found: C: 39.06%, H: 7.92%, N: 0%.

IR for III-7 (KBr, cm^{-1}); 2960(vs), 2931(s), 2891(m), 2872(s), 1456(s), 1406(m), 1376(m), 1341(w), 1247(m), 1220(m), 1126(s), 1109(s), 1082(s), 1037(s), 904(w), 847(s), 757(s), 722(s), 698(s), 595(m), 475(w), 433(m). 359(s).

3.2.5. Bis(tetrabutylammonium) hexasulfido-hexairon-hexachloro bis (tripropylphosphino-nickel) $(Bu_4N)_2[(PPr_3)_2Ni_2Fe_6S_6Cl_6]$.*(Reaction 7)*

$[Ni(MeCN)_6]BF_4$ (0.64g, 1.34 mmol) was dissolved in 5ml MeCN followed by the dropwise addition of PPr_3 (0.2 ml, 1.37 mmol), and the mixture was allowed to stir for 30min. The resulting solution was added dropwise to a 15ml solution of $(Bu_4N)_2[Fe_4S_4Cl_4]$ (1.00g, 1.02 mmol) in MeCN. The reaction mixture was left stirring

for one hour before being filtered. The MeCN filtrate was layered with ether (~ 80 ml) affording 0.3g of crystalline material.

Yield 0.18 mmol, 27% of $(Bu_4N)_2[(PPr_3)_2Ni_2Fe_6S_6Cl_6]$ based on nickel.

Elemental analysis calculated for $(Bu_4N)_2[(PPr_3)_2Ni_2Fe_6S_6Cl_6]$, $C_{50}H_{144}Cl_6Ni_2Fe_6N_2P_2S_6$: C: 36.11%, H: 6.91%, N: 1.68%. Found: C: 33.36%, H: 6.75%, N: 1.84%.

IR (KBr, cm^{-1}): 2958(vs), 2929(s), 2890(m), 2869(s), 1488(s), 1478(m), 1457(s), 1438(s), 1416(m), 1406(m), 1393(s), 1373(m), 1364(m), 1341(w), 1329(w), 1295(w), 1218(w), 1173(m), 1080(s), 1039(s), 1032(m), 999(s), 900(w), 850(m), 786(m), 752(m), 726(m), 690(m), 435(m), 420(w), 345(s), 322(s), 282(s).

Microprobe analysis confirmed the Ni/Fe/S/P/Cl ratio of 1:3:3:1:3.

3.2.5. Hexasulfido-tetrairon-dichloro-bis(tripropylphosphido) tetrakis(tripropylphospino-copper) $(PPr_3)_4Cu_4Fe_4S_6(OPPr_3)_2Cl_2$ *(Reaction 8)*.

$FeCl_2$ (0.250g, 1.97mmol) and $CuCl_2$ (0.256g, 1.97mmol) were suspended in 30 ml of THF followed by the addition of PPr_3 (0.79ml, 3.94mmol). The reaction mixture was stirred for 15 min. prior to the dropwise addition of $[(CH_3)_3Si]_2S$ (0.86ml, 3mmol) under vigorous stirring over a period of 5 min. The resulting mixture was stirred for an additional 2 hours, filtered, and the THF filtrate was layered with ether. The mixture was filtered to remove an insoluble black solid, while the filtrate was taken to dryness under a nitrogen stream. The black residue was stirred with 50 ml of ether for 15 min, filtered and the ether filtrate was left for slow evaporation, affording 0.13g of black crystals.

Yield 0.075 mmol, 15% of $(PPr_3)_4Cu_4Fe_4S_6(OPPr_3)_2Cl_2$.

Elemental analysis calculated for $(PPr_3)_4Cu_4Fe_4S_6(OPPr_3)_2Cl_2$ $C_{54}H_{126}Cl_2Cu_4Fe_4O_2P_6S_6$: C: 37.40%; H: 7.32%, N: 0%. Found: C: 37.79%, H: 7.57%, N: 0%.

IR (KBr, cm^{-1}): 2959(vs), 2930(s), 2870(s), 1499(w), 1457(s), 1408(m), 1376(m), 1342(w), 1302 (w), 1260(m), 1165(m), 1100(s), 1082(s), 1051(s), 904(w), 850(m), 800(m), 754(m), 733(m), 580(br, w), 521(w), 481(w), 423(w), 361(m), 300(w).

Microprobe analysis confirmed the Cu/Fe/S/P/Cl ratio.

3.2.6. Hexasulfido-tetrairon tetrachloro tetra(tripropylphosphino cobalt) $(PPr_3)_4Co_4Fe_4S_6Cl_4$

Method A *(Reaction 9)*

Two solutions were prepared. Solution A; $(Et_4N)_2[Fe_2S_2Cl_4]$ (0.50g, 0.86mmol) was dissolved in 10ml MeCN and $[(CH_3)_3Si]_2S$ (0.18ml, 0.86mmol) were added dropwise. Solution B; $[Co(MeCN)_6](BF_4)_2$ (0.83g, 1.73mmol) was dissolved in 5ml MeCN followed by the dropwise addition of PPr_3 (0.35ml, 1.75mmol). The two solutions were stirred for 30 min and solution B was then added dropwise to solution A and the mixture left to stir for an additional two hours. The resulting mixture was filtered, and the precipitate was washed with hexanes and dissolved in ether. Slow evaporation of the ether solution afforded black plate like crystals (0.15g) that were identified as $(PPr_3)_4Co_4Fe_4S_6Cl_4$ by X-Ray Crystallography. The MeCN filtrate was taken to dryness and extracted partially with THF, leaving a blue powder undissolved. The THF solution was layered with ether, affording a mixture of blue crystals and a black powder. The two materials were separated by extracting the black powder with THF leaving the blue crystals undissolved. The resulting THF solution was layered with hexanes and placed in the freezer but again resulted in formation of blue crystals and a black powder suggesting that the species formed is unstable and decomposes fast. Analysis for the blue crystals

was inconclusive about its composition although based on color, infrared and elemental analysis it is believed to contain cobalt and phosphine

Yield 0.10mmol, 23% of $(PPr_3)_4Co_4Fe_4S_6Cl_4$ based on iron

Method B *(Reaction 10)*

$[Co(MeCN)_6](BF_4)_2$ (0.49g, 1.02mmol) was dissolved in 5ml MeCN and PPr_3 (0.21mmol, 1.75mmol) were added dropwise. The solution was stirred for 30 min and then was added dropwise to a solution of $(Bu_4N)_2[Fe_4S_4Cl_4]$ (0.2g, 0.21mmol) in 15ml MeCN. The resulting mixture was stirred for 4h, filtered and the precipitate was washed with hexanes and dissolved in Ether. Slow evaporation of Ether afforded 0.1g of black crystalline plates identified as $(PPr_3)_4Co_4Fe_4S_6Cl_4$ by IR. The MeCN filtrate exhibited the same behavior as mentioned in method A.

Yield 0.07mmol, 33% of $(PPr_3)_4Co_4Fe_4S_6Cl_4$ based on iron

Elemental analysis calculated for $(PPr_3)_4Co_4Fe_4S_6Cl_4 \cdot 2Ether$ $C_{44}H_{104}Cl_4Co_4Fe_4O_2P_4S_6$: C: 33.39%; H: 6.62%, N: 0%. Found: C: 34.00%, H: 6.67%, N: 0%.

IR (KBr, cm^{-1}): 2959(vs), 2929(s), 2868(s), 1495(w), 1456(s), 1404(m), 1375(m), 1338(w), 1301 (w), 1260(m), 1217(m), 1106(s), 1075(s), 1040(s), 901(w), 845(m), 824(w), 807(w) 720(m), 531(w), 442(m), 407(w) 388(m), 362(s), 325(w),319(w).

Microprobe analysis confirmed the Co/Fe/S/P/Cl ratio of 2:2:3:2:2.

3.2.6 Crystallographic Data

All diffraction data were collected at the University of Michigan X-Ray facility, at low temperatures ranging from 85(2) to 153(2) K to avoid decay during data collection, using

a Siemens SMART CCD-based X-Ray diffractometer equipped with an LT-2 low temperature device and normal focus Mo-target X-ray tube (λ = 0.71073 Å). All diffraction data were processed with SADABS for absorption correction. The positions of heavy atoms were found by direct methods in E-maps using the software solution program in SHELXTL v.6.1. Subsequent cycles of least-squares refinement followed by difference Fourier synthesis produced the positions of the remaining non-hydrogen atoms; they were refined anisotropically unless stated otherwise. All hydrogen atoms were placed in ideal positions and refined as riding atoms with individual (or group if appropriate) isotropic thermal displacement parameters. The crystal data and structural parameters are shown in Tables 3.1- 3.7. All space group assignments were determined based on systematic absences and intensity statistics and were confirmed by the program XPREP of the SHELXTL package.

$(Bu_4N)_2[(PEt_3)_2Cu_2Fe_6S_6Cl_6]$	
Color	Black
Habit	Block
Size (mm)	0.12 x 0.12 x 0.14
Formula	$C_{44}H_{102}Cl_6Cu_2Fe_6N_2P_2S_6$
Weight ($g \cdot mol^{-1}$)	1588.52
Crystal System	Monoclinic
Space Group	P21/m
Unit Cell (Å) (a,b,c, α,β,γ)	13.9364(18)
	15.934(2)
	15.719(2)
	90.00
	96.004(4)
	90.00
Volume ($Å^3$)	3471.6(8)
Z	2
Temperature (K)	150(2)
Absorption coefficient	2.304
F(0,0,0)	1644
θ range (deg)	2.85 to 28.35
Reflections	35645
Limiting indices	$-18 < h < 17$
	$-21 < k < 21$
	$-20 < l < 20$
R_{int}	0.0489
Data / restraints / parameters	17041 / 1 / 627
R_1, wR_2 [$I>2\sigma(I)$]	0.0428, 0.0844
R_1, wR_2 (all data)	0.0801, 0.0962
GooF (F^2)	1.010

Table 3.1. Crystallographic and refinement data for $(Bu_4N)_2[(PEt_3)_2Cu_2Fe_6S_6Cl_6]$

$(PPr_3)_4Cu_4Fe_4S_6Cl_4$	
Color	Brown
Habit	Octahedra
Size (mm)	0.22 x 0.20 x 0.18
Formula	$C_{36}H_{84}Cl_4Cu_4Fe_4P_4S_6$
Weight ($g \cdot mol^{-1}$)	1452.72
Crystal System	Orthorhombic
Space Group	Pbca
Unit Cell (Å) (a,b,c, α,β,γ)	16.947(2)
	16.975(2)
	20.846(3)
	90.00
	90.00
	90.00
Volume ($Å^3$)	5996.7(13)
Z	4
Temperature (K)	150(2)
Absorption coefficient	2.848
F(0,0,0)	2944
θ range (deg)	3.10 to 28.31
Reflections	65968
Limiting indices	-22 < h < 22
	-22 < k < 22
	-27 < l < 27
R_{int}	0.0473
Data / restraints / parameters	7442 / 0 / 285
R_1, wR_2 [I>2σ(I)]	0.0336, 0.0792
R_1,wR_2 (all data)	0.0506, 0.0872
GooF (F^2)	1.018

Table 3.2. Crystallographic and refinement data for $(PPr_3)_4Cu_4Fe_4S_6Cl_4$

$(PPr_3)_4Ni_4Fe_4S_6Cl_4$	
Color	Brown
Habit	Multi-faced
Size (mm)	0.40 x 0.40 x 0.24
Formula	$C_{36}H_{84}Cl_4Fe_4Ni_4P_4S_6$
Weight ($g \cdot mol^{-1}$)	1433.31
Crystal System	Trigonal
Space Group	R-3c
Unit Cell (Å) (a,b,c, α,β,γ)	19.9487(16)
	19.9487(16)
	26.536(5)
	90.00
	90.00
	120.00
Volume ($Å^3$)	9145.2(19)
Z	6
Temperature (K)	123(2)
Absorption coefficient	2.641
F(0,0,0)	4440
θ range (deg)	2.81 to 28.29
Reflections	30134
Limiting indices	$-26 < h < 26$
	$-26 < k < 25$
	$-35 < l < 35$
R_{int}	0.0259
Data / restraints / parameters	5037 / 1 / 287
R_1, wR_2 [$I>2\sigma(I)$]	0.0157, 0.0413
R_1, wR_2 (all data)	0.0163, 0.0416
GooF (F^2)	1.083

Table 3.3. Crystallographic and refinement data for $(PPr_3)_4Ni_4Fe_4S_6Cl_4$

$(Et_4N)_2[(PPr_3)_2Ni_2Fe_6S_6Cl_6]$	
Color	Black
Habit	Block
Size (mm)	N/A
Formula	$C_{34}H_{82}Cl_6Fe_6N_2Ni_2P_2S_6$
Weight ($g \cdot mol^{-1}$)	1438.54
Crystal System	Triclinic
Space Group	P-1
Unit Cell (Å) (a,b,c, α,β,γ)	12.420(3)
	12.547(3)
	12.710(3)
	94.592(4)
	117.208(4)
	115.894(4)
Volume ($Å^3$)	1484.6(6)
Z	1
Temperature (K)	153(2)
Absorption coefficient	2.603
F(0,0,0)	740
θ range (deg)	3.08 to 26.42
Reflections	13948
Limiting indices	$15 < h < 15$
	$-15 < k < 15$
	$-15 < l < 15$
R_{int}	0.0660
Data / restraints / parameters	6035 / 0 / 269
R_1, wR_2 [$I>2\sigma(I)$]	0.0669, 0.1974
R_1, wR_2 (all data)	0.1335, 0.2207
GooF (F^2)	1.074

Table 3.4. Crystallographic and refinement data for $(Et_4N)_2[(PPr_3)_2Ni_2Fe_6S_6Cl_6]$

$(PPr_3)_4Cu_4Fe_4S_6(OPPr_3)_2Cl_2$	
Color	Black
Habit	Plates
Size (mm)	0.14 x 0.12 x 0.08
Formula	$C_{54}H_{126}Cl_2Cu_4Fe_4O_2P_6S_6$
Weight ($g \cdot mol^{-1}$)	1734.19
Crystal System	Monoclinic
Space Group	P21/n
Unit Cell (Å) (a,b,c, α,β,γ)	12.9340(19)
	24.440(4)
	12.9433(19)
	90.00
	93.903(3)
	90.00
Volume ($Å^3$)	4081.9(10)
Z	1
Temperature (K)	150(2)
Absorption coefficient	2.080
F(0,0,0)	1812
θ range (deg)	2.85 to 22.91
Reflections	25642
Limiting indices	$-14 < h < 14$
	$-26 < k < 26$
	$-14 < l < 14$
R_{int}	0.0884
Data / restraints / parameters	5595 / 0 / 361
R_1, wR_2 [$I>2\sigma(I)$]	0.0492, 0.1028
R_1, wR_2 (all data)	0.0989, 0.1219
GooF (F^2)	1.000

Table 3.5. Crystallographic and refinement data for $(PPr_3)_4Cu_4Fe_4S_6(OPPr_3)_2Cl_2$

$[Ni_3S_2(PPr_3)_6][(PPr_3)_3Ni_3Fe_5S_6Cl_5]$	
Color	Brown
Habit	Block
Size (mm)	0.22 x 0.08 x 0.02
Formula	$C_{72}H_{168}Cl_5Fe_5Ni_6P_8S_8$
Weight ($g \cdot mol^{-1}$)	2347.07
Crystal System	Triclinic
Space Group	P-1
Unit Cell (Å) (a,b,c, α,β,γ)	14.770(4)
	19.369(5)
	23.025(6)
	108.447(13)
	91.975(13)
	108.198(13)
Volume ($Å^3$)	5871(2)
Z	2
Temperature (K)	150(2)
Absorption coefficient	2.747
F(0,0,0)	3008
θ range (deg)	2.77 to 18.01
Reflections	28621
Limiting indices	$-12 < h < 12$
	$-16 < k < 16$
	$-20 < l < 19$
R_{int}	0.1210
Data / restraints / parameters	8094 / 0 / 891
R_1, wR_2 [$I>2\sigma(I)$]	0.1054, 0.1807
R_1, wR_2 (all data)	0.2880, 0.3477
GooF (F^2)	1.174

Table 3.6. Crystallographic and refinement data for $[Ni_3S_2(PPr_3)_6][(PPr_3)_3Ni_3Fe_5S_6Cl_5]$

$(PPr_3)_4Co_4Fe_4S_6Cl_4$	
Color	Black
Habit	Plates
Size (mm)	0.17 x 0.17 x 0.09
Formula	$C_{36}H_{84}Cl_4Fe_4Co_4P_4S_6$
Weight ($g \cdot mol^{-1}$)	1434.19
Crystal System	Trigonal
Space Group	R3
Unit Cell (Å) (a,b,c, α,β,γ)	19.501(1)
	19.501(1)
	12.912(2)
	90.00
	90.00
	120.00
Volume ($Å^3$)	4252.7(7)
Z	3
Temperature (K)	85(2)
Absorption coefficient	2.681
F(0,0,0)	2208
θ range (deg)	1.99 to 24.54
Reflections	3167
Limiting indices	$-22 < h < 11$
	$0 < k < 22$
	$-15 < l < 15$
R_{int}	0.000
Data / restraints / parameters	3167 / 1 / 172
R_1, wR_2 [$I>2\sigma(I)$]	0.1333, 0.3342
R_1, wR_2 (all data)	0.1741, 0.4253
GooF (F^2)	1.924

Table 3.7. Crystallographic and refinement data for $(PPr_3)_4Co_4Fe_4S_6Cl_4$.

3.3. Results and Discussion

The reactions of Fe/S clusters with heterometals M=Cu^{+}, Ni^{2+} and Co^{2+} affording products containing a pentlandite like M'_8S_6 core are presented in this chapter as summarized in Figure 3.2. All M'_8S_6 clusters presented contain a cubic metal array capped by μ_4-Sulfides. The cubic arrangement of M_2Fe_6 can theoretically be in three isomeric structures with idealized symmetries of D_{3d}, C_{2v} or C_s. The D_{3d} isomer is represented here, while from the three possible M_4Fe_4 isomers (T_d, D_{2h}, C_{4v}) the first two have been obtained.

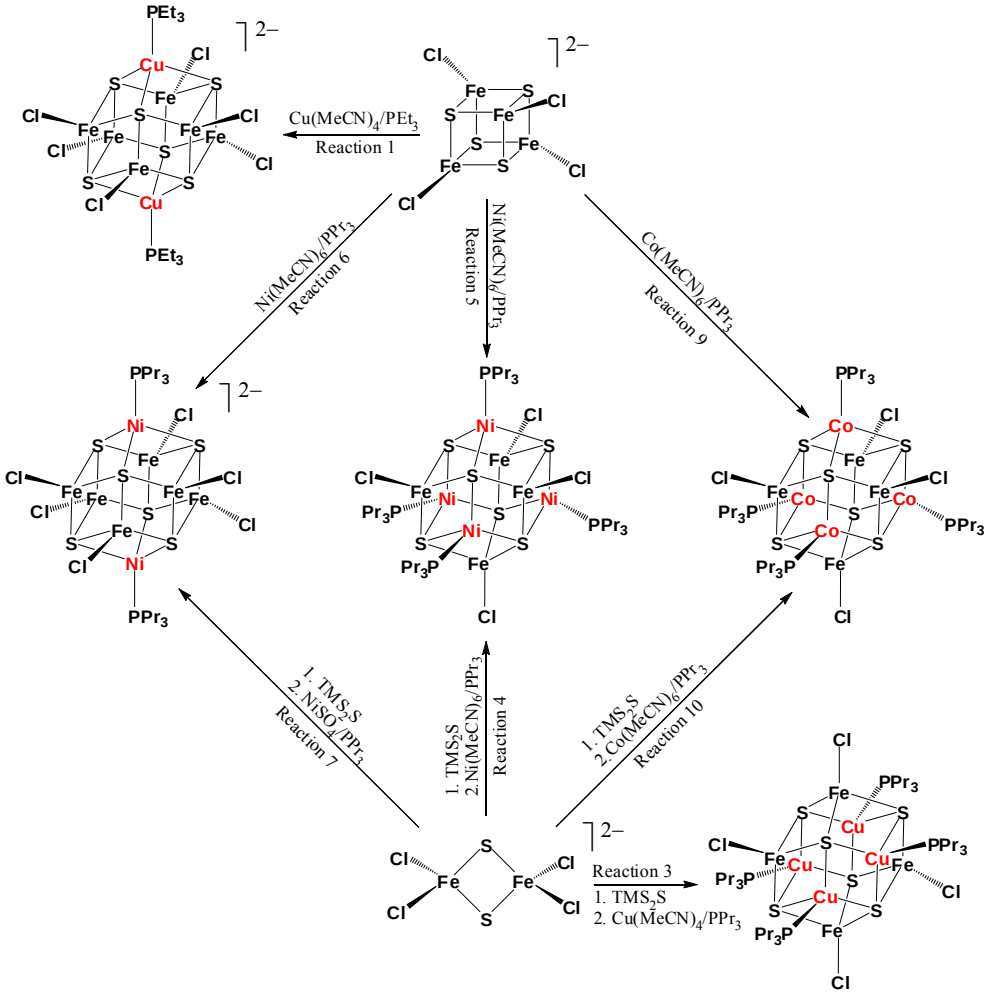

Figure 3.2. Schematic representation of the clusters obtained from the reactions of Fe/S clusters with Cu^{+}, Ni^{2+} and Co^{2+} metal ions. TMS is the trimethylsilane unit of $[(CH_3)_3Si]_2S$.

3.3.1 Synthesis.

The systematic approach towards the synthesis of heterometallic "pentlandite-like" clusters is presented. The general methodology applied in the synthesis of M'_8S_6 clusters is based on the addition of $\{M(PR_3)\}$ units to either the in situ generated, prismatic $[Fe_6S_6]$ core [17, 25] (Figure 3.3-A), or the hypothetical "adamantane", or "dimer of dimers" $[Fe_4S_6]$ cores (Figure 3.3-C and D respectively).

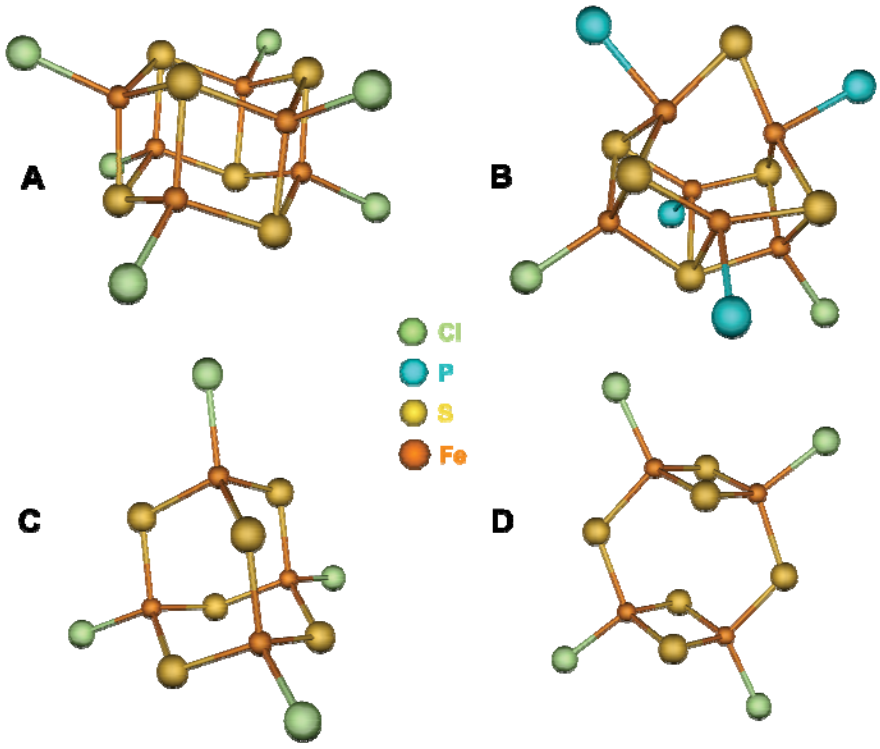

Figure 3.3. Schematic representations of various pentlandite, $Fe_nS_6L_n$ fragments. Examples of A and B have been obtained and structurally characterized[25, 28] while C and D are only hypothetical

The $\{M(PR_3)\}$ units are believed to be generated in solution from $M(MeCN)_n$ (n=4 for Cu^+, n=6 for Ni^{2+} and Co^{2+}) complexes were a phosphine molecule is replacing a MeCN molecule from the coordination sphere of the metal. In all the procedures presented, the heterometal and the phosphine are introduced as a mixture to a solution containing the Fe/S/Cl clusters in order to reduce the probability of any direct reaction of

the phosphine and the Fe/S/Cl cluster, that leads to the formation of known Fe/S/PR_3 clusters, such as $(PR_3)_6Fe_6S_8$ [29] and $(PR_3)_4Fe_6S_6Cl_2$ [28].

The known $[Fe_8S_6L_8]$ [17, 18] and $[(CO)_6Mo_2Fe_6S_6L_6]$ [19, 20] clusters can be envisioned as the addition of iron or molybdenum metal atoms to the known $[Fe_6S_6L_6]$ "prismane" cluster [17, 25] which can be described as a direct fusion of three $[Fe_2S_2L_2]$ units. It has been shown that the $[Fe_6S_6L_6]$ prismane possesses a metastable nature [25, 30] and it is readily converted to the well known $[Fe_4S_4L_4]$ cubane as shown in equation 1, suggesting that dissociation of the $[Fe_6S_6L_6]$ prismanes to the dimeric $[Fe_2S_2L_2]$ subunits may be easily induced.

$$2[Fe_6S_6(L)_6]^{3-} \rightleftharpoons 6\ \{Fe_2S_2L_2\}^{-} \rightleftharpoons 3\ [Fe_4S_4L_4]^{2-} \quad \text{(eq. 1)}$$

The synthesis of the two $[(PR_3)M_2Fe_6S_6Cl_6]^{2-}$ clusters (M=Cu, Ni) from $[Fe_4S_4Cl_4]^{2-}$ cluster can be envisioned as the reverse reaction driven by the thiophilic nature of Cu^{+} and Ni^{2+} that can coordinate to the three sulfur atoms on each side of the prismatic core. For both clusters the stoichiometric 3:4 ratio of $[Fe_4S_4Cl_4]^{2-}$ to $\{M(PR_3\}$ is used to obtain the best results. It should be noted however, that as the irons in both $[(PR_3)M_2Fe_6S_6Cl_6]^{2-}$ (M=Cu, Ni) clusters are formally reduced by one and two electrons respectively compared to $[Fe_4S_4Cl_4]^{2-}$. Therefore these additional electrons have to be provided from the side reaction between PR_3 and S^{2-} by sacrificing some of the $[Fe_4S_4Cl_4]^{2-}$ and thus lowering the overall yield.

As mentioned earlier, the observed D_{3d} isomer of the $M_2Fe_6S_6$ core is obtained from addition of the heterometal atoms to the prismatic $[Fe_6S_6]$ core. The later is theoretically obtainable upon the removal of two iron atoms, from the body diagonal of the Fe_8S_6 pentlandite cube. If however, removal of these two iron atoms takes place from the face

diagonal of the Fe_8S_6 unit then the "basket-like" $[Fe_6S_6]$ isomer (Figure 3.3B) is formed. Attempts to obtain the C_{2v} isomer of $M_2Fe_6S_6$ cluster that would derive from the "basket-like" $[Fe_6S_6]$ isomer have been unsuccessful, mainly due to the similar solubility characteristics of $(PEt_3)_4Fe_6S_6Cl_2$ and the various products that can be obtained.

Further removal of two additional iron atoms from the $[Fe_8S_6]$ parent core leads hypothetically to the two tetranuclear isomeric fragments, Fe_4S_6, with either a square planar (D_{2h}) or a tetrahedral (T_d) Fe_4 array. Molecular examples of either of these two isomers (Figure 3.3C, 3.3D) are not known yet, although an adamantane $Fe_4(SR)_6$ core, with μ_3-RS^- ligands, exists in the $[Fe_4(SR)_6Cl_4]^{2-}$ [31] and $[Fe_4(SR)_{10}]^{2-}$ [32, 33] clusters. The "dimer of dimers" $[Fe_4S_6L_4]$ isomer, with a square planar arrangement of four Fe atoms, (Figure 3.3D) can be envisioned as a result of coupling of two $Fe_2S_2L_4$ dimers that could be accomplished by the following synthetic procedure (equation 2).

$$2[Fe_2S_2Cl_4]^{2-} + 2[(CH_3)_3Si)_2]S \longrightarrow [Fe_4S_6Cl_4]^{4-} + 4\,(CH_3)_3SiCl \quad \text{(eq. 2)}$$

The other "adamantane" $[Fe_4S_6L_4]$ isomer (Figure 3.3C) can possibly be obtained by a structural rearrangement, following reduction of 3.3D. The real and hypothetical structures shown in figure 3.3 possess an important common feature, that makes them viable precursors in the synthesis of heterometallic $(M)_{8-x}(Fe)_xS_6(L')_{8-x}(L)_x$, clusters. They all contain six, octahedrally arranged, μ_3-sulfido ligands and trihapto sites poised for coordination to ML′ units and generation of $L'MS_3$ tetrahedral subunits. Distinct thermodynamically stable isomers are expected to form with different terminal ligands (L′), and specific M-L′ coordination preferences.

The stoichiometric addition of an acetonitrile solution of a $[Cu(MeCN)_4](PF_6)/R_3P$ 2:2 mixture, to a 1:1 mixture of $(Et_4N)_2[Fe_2S_2Cl_4]/[(CH_3)_3Si]_2S$ also in acetonitrile

solution at ambient temperature, leads to the formation of $[(PPr_3)_4Cu_4Fe_4S_6Cl_4]$ at a yield of 40%. The corresponding $[(PPr_3)_4Ni_4Fe_4S_6Cl_4]$ cluster is obtained by a similar reaction using $[Ni(MeCN)_6](BF_4)_2$ at a yield of 35%. When a deficit of copper or nickel with PR_3 is used (less than 2/3 equivalents), the $(Et_4N)_2[(PPr_3)_2Cu_2Fe_6S_6Cl_6]$ cluster (in a very small yield) or $(Et_4N)_2[(PPr_3)_2Ni_2Fe_6S_6Cl_6]$ (at a yield of 28% while the nickel source is $NiSO_4$), are isolated.

As seen in Figure 3.2 and the experimental section, for the cases of copper and nickel, the M_2Fe_6 core units are more easily obtained from $[Fe_4S_4Cl_4]^{2-}$ (Reactions 1 and 7) and in better yields, while the M_4Fe_4 core units are more easily obtained in higher yields from $[Fe_2S_2Cl_4]^{2-}$ (Reactions 3 and 4). However, in the case of cobalt, the main product isolated in both pathways is the $(PPr_3)_4Co_4Fe_4S_6Cl_4$ cluster while the corresponding Co_2Fe_6 analogue has not been isolated. As seen from the synthesis of $(PPr_3)_4Co_4Fe_4S_6Cl_4$ using both methods (Reactions 9 and 10) there is also formation of a product soluble in THF that seems to be unstable. The nature of this unstable product is not known but more likely seems to derive from a Co/Fe/S cluster that could be envisioned as cluster containing the $Co_2Fe_6S_6$ core, which subsequently decomposes in order to form more thermodynamically stable products.

As discussed above, one possible pathway for the formation of these clusters is the use of Fe_2S_2 dimers as building blocks. The other possible pathway would be the use of monomeric units through the formation of $M(\mu_2\text{-}S)_2Fe$ building blocks that could, potentially, provide either higher yields or different isomers. Consequently, we explored the reactivity of $FeCl_2$ in the presence of $CuCl_2$ or $NiCl_2$ with phosphines (PR_3) and hexamethyldisilathiane ($[(CH_3)_3Si]_2S$).

The reaction of $FeCl_2$ and $CuCl_2$ at a 1:1 ratio with two equivalents of PPr_3 and three half equivalents of $[(CH_3)_3Si]_2S$ in THF led to the formation of cluster $(PPr_3)_4Cu_4Fe_4S_6(OPPr_3)_2Cl_2$. The role of hexamethyldisilathiane is dual acting both as an inorganic sulfur (S^{2-}) source and as a Cl^- scavenger by the formation of $(CH_3)_3SiCl$ similar to the behavior presented in Equation 2. Likewise, the reaction utilizing $NiCl_2$ instead of $CuCl_2$, resulted in the formation of a material with analogous, although different, infrared signature. Elemental and microprobe analysis were not conclusive for determining the identity of the produced material, nonetheless they indicated that both Ni and Fe are present in variable ratios of Ni to Fe between 3:5 and 1:1 .

The $(PPr_3)_4Cu_4Fe_4S_6(OPPr_3)_2Cl_2$ cluster is not just another compound with a $Cu_4Fe_4S_6$ pentlandite core but is also the two electron reduced analogue of $(PPr_3)_4Cu_4Fe_4S_6Cl_4$. Assuming that the oxidation states of the $(PPr_3)_4Cu_4Fe_4S_6Cl_4$ cluster are arbitrarily assigned as 4Cu(I)/4Fe(III), then those of the $(PPr_3)_4Cu_4Fe_4S_6(OPPr_3)_2Cl_2$ cluster can be assigned as 4Cu(I)/2Fe(II)/2Fe(III). This assignment is not realistic though, and it does not reflect the actual oxidation states, since the Mössbauer analysis of most of the investigated compounds revealed systems with an extensive charge delocalization. These data will be discussed in more detail later on.

The access into heterometallic M/Fe/S clusters by the use of a simple and facile synthetic approach prompt us to investigate the possible incorporation of other metals besides Ni or Cu such as Cd, Ag, Zn, Co, or Mn. In most cases, intractable and insoluble to all common solvents material were isolated. In the case of $CoCl_2$, the formation of such material was also unavoidable, albeit representing only a small percentage of the products formed. The soluble products could be successfully isolated, but microprobe analysis of the crystalline material obtained revealed the presence of either “all-Fe” or

"all-Co" compounds. In the case of $CdCl_2$, the other extreme was observed, where the majority of the obtained product was an insoluble black powder and the material that remained in solution was found to contain only iron and chloride. In the attempts made by using $[Cd(MeCN)]_4(BF_4)_2$, again, the only product that could be isolated was a Fe/S/P/Cl cluster with no indications of the cadmium presence as shown by microprobe analysis.

In summary, the M_4Fe_4 core was isolated in two isomeric forms. In the case of the Ni_4Fe_4 and Co_4Fe_4 cores the T_d isomer is obtained while the D_{2h} isomer is obtained in the case of Cu_4Fe_4. A possible explanation for this behavior could be through examination of the formal oxidations of the irons in the "adamantane" Fe_4S_6 core (Figure 3.3C) and the "dimer of dimers" Fe_4S_6 core (Figure 3.3D). Assuming Ni(II) and Co(II), the neutral T_d isomer is four electrons reduced compared to the neutral D_{2h} isomer, assuming Cu(I). Therefore the "adamantane" Fe_4S_6 unit can be described as the result of rearrangement under reducing conditions of the "dimer of dimers" Fe_4S_6 unit, in order to create the apparently thermodynamically more stable neutral species. This assumption led to the investigation of the reactivity of Cu(II) in order to see if it would give the T_d isomer of the Cu_4Fe_4 core. As seen from the reactivity of $CuCl_2$ through the monomeric unit pathway, the formation of one isomer versus the other isomer is not only based on the formal oxidation states of the irons but lies also in geometrical preferences of each heterometal.

Although the idea of synthesis through dimeric M_2S_2 building blocks is attractive and to a large extent observed, it is not impossible to obtain these clusters through more extended fragmentation of the Fe/S cluster even to monomeric units, and such behavior is evident in the synthesis of $[Ni_3S_2(PPr_3)_6][(PPr_3)_3Ni_3Fe_5S_6Cl_5]$. This cluster forms as a

byproduct from the synthesis of Ni_2Fe_6 through Reaction 7. Even though the exact mechanism and equation for the assembly of such a compound can not be addressed some assumptions can be made on the basis of some features of the $Ni_3Fe_5S_6$ core structure as presented in Figure 3.4. The positions of the Ni atoms are indicated by arrows in 3.4-A. Removal of these atoms results to the hypothetical Fe_5S_6 core arrangement, an unusual arrangement that is however, found in the $MFe_4S_6(PEt_3)_4Cl$ (M=Mo,V) [34] clusters. Moreover, if the Fe atom indicated by an arrow in figure 3.4B is removed then the "adamantane" $[Fe_4S_6]$ core arrangement is obtained. It is therefore possible that the formation of this hypothetical "adamantane" core is followed by the insertion of three $\{Ni(PR_3)\}$ units and one $\{FeCl\}$ unit instead of four $\{Ni(PR_3)\}$ units (that leads to $Ni_4Fe_4S_6$) in the suitable vacant sites poised for coordination, indicating that fragmentation to monomeric units is possible.

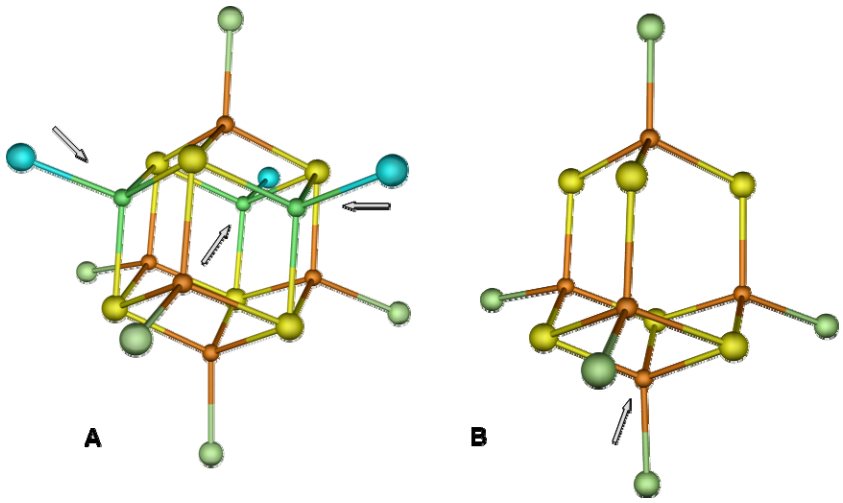

Figure 3.4. Schematic representations of the $Ni_3Fe_5S_6$ A and Fe_5S_6 B fragments.

3.3.2. Structural description.

The core structure of all compounds investigated herein deviates only slightly from the one in naturally occurring pentlandites. Coordination of one terminal chloride (in the case of the iron atoms) or one terminal phosphine (in the case of the heterometal atoms) completes tetrahedral coordination and results in a trigonally distorted, local D_{3d} symmetry, $(\mu_4\text{-S})_3$ML sites.

The clusters $[(PEt_3)_2Cu_2Fe_6S_6Cl_6]^{2-}$ (Figure 3.5) and $[(PPr_3)_2Ni_2Fe_6S_6Cl_6]^{2-}$ (Figure 3.6) are isostructural and exhibit similar average Fe-S and Fe-Cl distances at 2.307Å, 2.197Å and 2.281Å, 2.221Å respectively. The interatomic distances in $(Bu_4N)_2[(PEt_3)_2Cu_2Fe_6S_6Cl_6]$ and $(Et_4N)_2[(PPr_3)_2Ni_2Fe_6S_6Cl_6]$ can be compared to the corresponding distances in the isostructural $[(MePh_2P)_2Ni_2Fe_6S_6I_6]^{2-}$ [35] and $[(CO)_6Mo_2Fe_6S_6Cl_6]^{n-}$ (n=3,4) [36] clusters (Table 3.8). Comparing these structures, $[(PEt_3)_2Cu_2Fe_6S_6Cl_6]^{2-}$ exhibits larger interatomic distances than the two Nickel equivalents and slightly shorter than the Molybdenum equivalent. Although it has to be noted that the presence of the larger second row transition element will affect the individual comparisons.

Compound	Interatomic Distances in Å					
	M-Fe	Fe-Fe	M-S	Fe-S	M-P	Fe-Cl
$[(PEt)_2Cu_2Fe_6S_6Cl_6]^{2-}$	2.784	2.772	2.385	2.310	2.243	2.229
$[(PPr_3)_2Ni_2Fe_6S_6Cl_6]^{2-}$	2.615	2.752	2.255	2.296	2.222	2.231
$[(Ph_2MeP)_2Ni_2Fe_6S_6I_6]^{2-}$	2.645	2.719	2.261	2.289	2.259	-
$[(CO)_6Mo_2Fe_6S_6Cl_6]^{3-}$	2.930	2.742	2.582	2.292	-	2.226
$[(CO)_6Mo_2Fe_6S_6Cl_6]^{4-}$	3.005	2.761	2.619	2.353	-	2.244

Table 3.8. Comparison of selected average interatomic distances in M_2Fe_6 clusters.

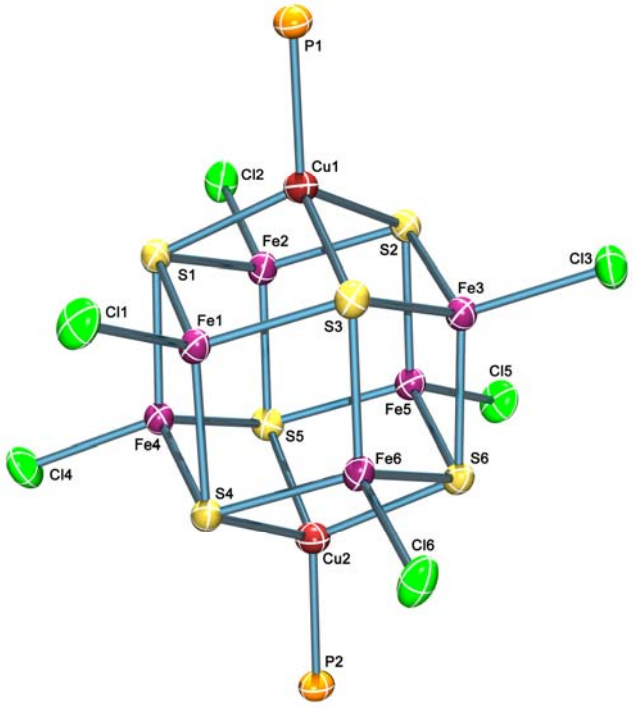

Figure 3.5. Ortep diagram of $(Bu_4N)_2[(PEt_3)_2Cu_2Fe_6S_6Cl_6]$ with thermal ellipsoids at 50% probability. The carbon atoms of the phosphines have been omitted for clarity.

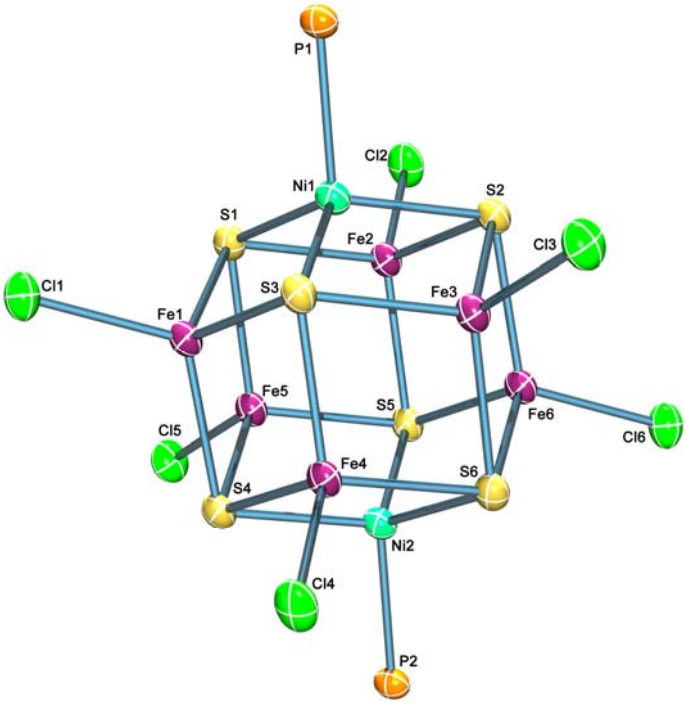

Figure 3.6. Ortep diagram of $(Et_4N)_2[(PPr_3)_2Ni_2Fe_6S_6Cl_6]$ with thermal ellipsoids at 50% probability. The carbon atoms of the phosphines have been omitted for clarity.

The $M_4Fe_4S_6$ clusters that have been isolated are isomeric, with copper affording the D_{2h} isomer of M_8S_6, while nickel and cobalt afford the T_d isomer that has been described previously. Structurally these clusters can be compared to the previously isolated $(MePh_2P)_4Ni_4Fe_4S_6I_4$ [35] cluster. As seen in table 3.9 the $(PPr_3)_4Cu_4Fe_4S_6Cl_4$ cluster exhibits larger M-P and M-S distances than the nickel and cobalt analogues by approximately 0.1Å with only the Fe-S and Fe-Cl distances being comparable, which is in line with the larger ionic radius of Cu(I) compared to Ni(II) and Co(II).

The structures of $(PPr_3)_4Cu_4Fe_4S_6Cl_4$ (Figure 3.7) and $(PPr_3)_4Cu_4Fe_4S_6(OPPr_3)_2Cl_2$ (Figure 3.8) show structures with very similar distances that can be described as two intersecting rectangles of metals, while $(PPr_3)_4Ni_4Fe_4S_6Cl_4$ (Figure 3.9) and $(PPr_3)_4Co_4Fe_4S_6Cl_4$ (Figure 3.10) can be described as two interpenetrating tetrahedra of metals. Another notable feature is that the structure of $(PPr_3)_4Co_4Fe_4S_6Cl_4$ exhibits a considerably more distorted cube of metals with the average tetrahedral edge of Co_4 being 2.889Å compared to the 4.193Å edge of Fe_4. In the case of $(PPr_3)_4Ni_4Fe_4S_6Cl_4$ and $(MePh_2P)_4Ni_4Fe_4S_6I_4$ the M_4 tetrahedra are more or less equal with the Ni_4 distances at 3.630Å and 3.684Å respectively while the Fe_4 distances are at 3.821Å and 3.808Å.

Compound	**Interatomic Distances in Å**						
	M-M[a]	**Fe-Fe[a]**	**M-Fe**	**M-S**	**Fe-S**	**M-P**	**Fe-Cl**
$(PPr_3)_4Cu_4Fe_4S_6Cl_4$	3.379	3.321	2.787	2.366	2.270	2.252	2.198
$(PPr_3)_4Cu_4Fe_4S_6(OPPr_3)_2Cl_2$	3.429	3.248	2.802	2.385	2.311	1.974	2.271
$(PPr_3)_4Co_4Fe_4S_6Cl_4$	2.889	4.193	2.587	2.158	2.387	2.166	2.197
$(PPr_3)_4Ni_4Fe_4S_6Cl_4$	3.630	3.821	2.636	2.242	2.283	2.215	2.219
$(PPr_3)_3Ni_3Fe_5S_6Cl_5$	3.714	3.842	2.674	2.264	2.291	2.210	2.218
$(MePh_2P)_4Ni_4Fe_4S_6I_4$	3.684	3.808	2.650	2.248	2.275	2.236	-

Table 3.9. Comparison of selected average interatomic distances in M_4Fe_4 clusters.

[a] The M-M bond in the case of the Cu complexes is the average Cu-Cu distance of the rectangle, while for Ni and Co clusters it is the average distance in the tetrahedral of metals. The same applies for the reported Fe-Fe distances.

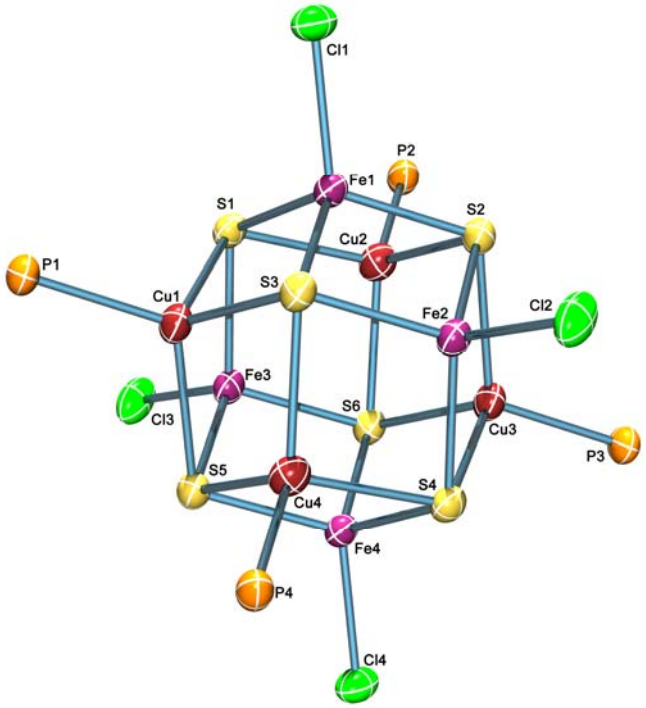

Figure 3.7. Ortep diagram of $(PPr_3)_4Cu_4Fe_4S_6Cl_4$ with thermal ellipsoids at 50% probability. The carbon atoms of the phosphines have been omitted for clarity.

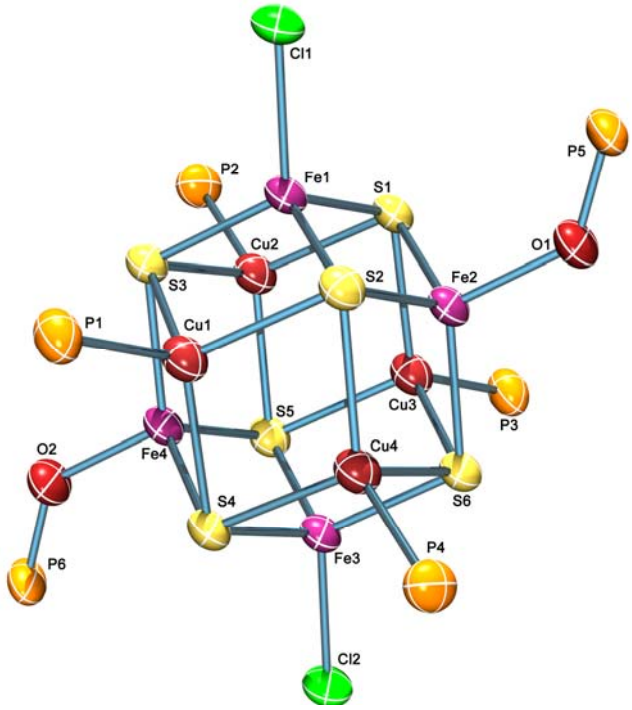

Figure 3.8. Ortep diagram of $(PPr_3)_4Cu_4Fe_4S_6(OPPr_3)_2Cl_2$ with thermal ellipsoids at 50% probability. The carbon atoms of the phosphines have been omitted for clarity.

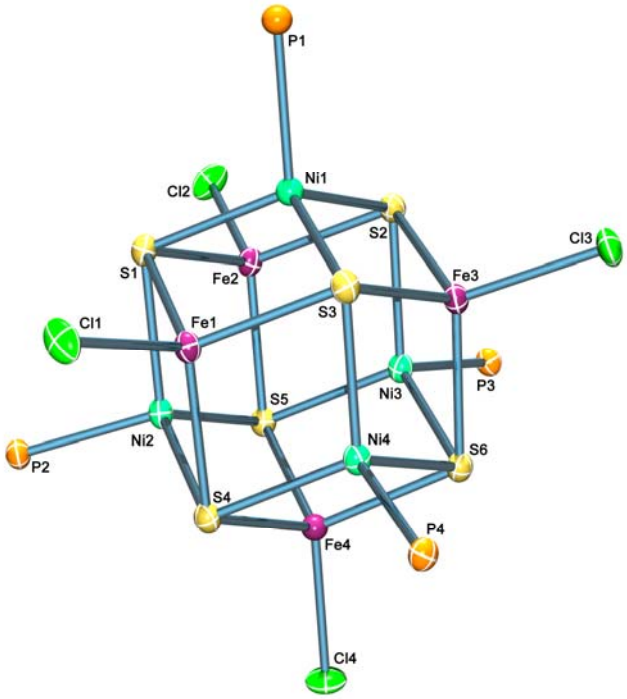

Figure 3.9. Ortep diagram of $(PPr_3)_4Ni_4Fe_4S_6Cl_4$ with thermal ellipsoids at 50% probability. The carbon atoms of the phosphines have been omitted for clarity.

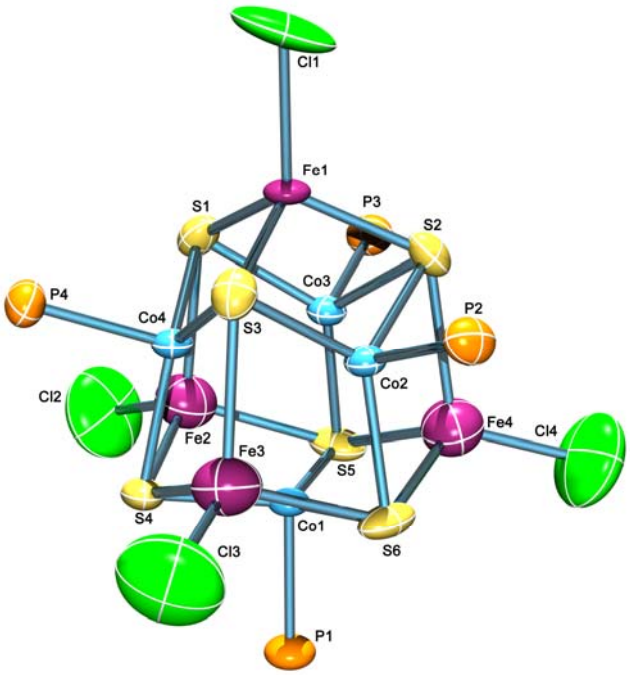

Figure 3.10. Ortep diagram of $(PPr_3)_4Co_4Fe_4S_6Cl_4$ with thermal ellipsoids at 50% probability. The carbon atoms of the phosphines have been omitted for clarity.

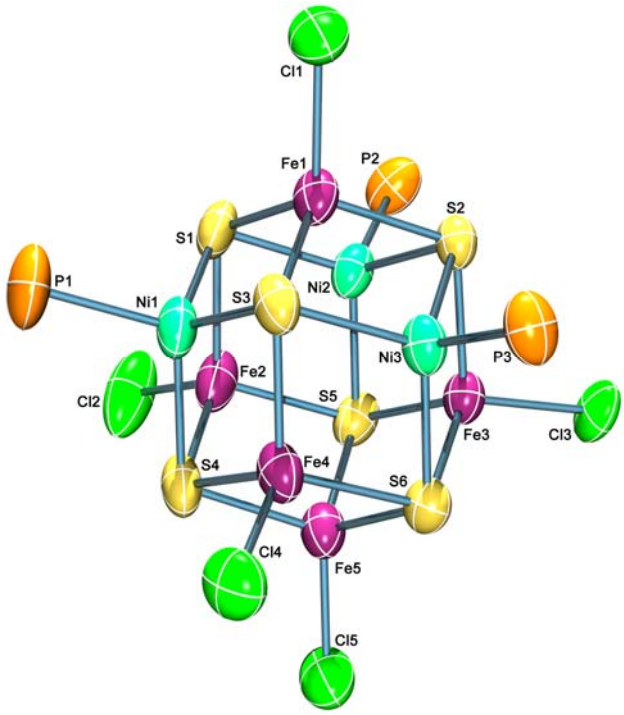

Figure 3.11. Ortep diagram of $(PPr_3)_3Ni_3Fe_5S_6Cl_5$ with thermal ellipsoids at 50% probability. The carbon atoms of the phosphines have been omitted for clarity.

In all the M_8S_6 clusters, the structure can be described either as a cube of metals with μ_4-*S* atoms capping the faces of the cube or as an octahedral arrangement of sulfur atoms with the μ_3-metals capping the triangular faces of the octahedral. In all these clusters the individual metals are four coordinated and are arranged in tetrahedral geometries with the exception of cobalt that exhibits an almost trigonal pyramidal geometry with the P-Co-S angle at 95º and S-Co-S angle at 121º. This distortion is the basis of the differences observed in the $(PPr_3)_4Co_4Fe_4S_6Cl_4$ cluster with the unequal Co_4 and Fe_4 tetrahedra mentioned previously as the cobalt atoms move closer to the triangular face of the sulfur octahedra while the iron atoms remain in a tetrahedral geometry. A possible explanation for this behavior of cobalt is the odd number of electrons, d^7 assuming Co(II), that leads to higher Janh-Teller distortions compared to Nickel, d^8

assuming Ni(II), making a trigonal pyramidal geometry more favorable than a tetrahedral.

The structure of $(PPr_3)_3Ni_3Fe_5S_6Cl_5$ (Figure 3.11) is almost identical to the structure of $(PPr_3)_4Ni_4Fe_4S_6Cl_4$ (Figure 3.9) with one nickel atom replaced by an iron atom in the tetrahedral arrangement of nickels. This substitution leads to elongation on the iron corner of the Ni_3Fe tetrahedral and the distances change accordingly as seen in Table 3.9. Nevertheless, the interatomic distances of the tetrahedral of Ni_3Fe and Fe_4 have average metal distances of 3.713Å and 3.842Å respectively making the overall structure much closer to $(PPr_3)_4Ni_4Fe_4S_6Cl_4$ than $(PPr_3)_4Co_4Fe_4S_6Cl_4$. A cluster with a similar $[Ni_5Fe_3S_6I_8]^{4-}$ core structure has been reported by Pohl et al [37] obtained from the reaction of $[Fe_6S_6I_6]^{2-}$ with $[NiI_4]^{2-}$. While the authors can not differentiate between the Ni and Fe atoms based on crystallographic criteria (all the metal atoms are also bound to I- ligands) they do not address how the Ni/Fe ratio was determined. The counterion $[Ni_3S_2(PPr_3)_6]^{2+}$ fragment can be described as a trigonal planar Ni_3 unit capped by two μ_3-S^{2-} ligands. Each Nickel site exhibits a tetragonal NiP_2S_2 geometry with a mean Ni-μ_3-S bond length and Ni-P found at 2.178Å and at 2.193Å respectively. Moreover the average Ni-Ni distance is 2.911Å (range: 2.843-2.984) The Ni_3S_2 core is not without precedence and can be encountered in the $[Ni_3S_2(PEt_3)_5SH]B(Ph)_4$ cluster. Both clusters exhibit similar Ni-P and Ni-S distances.

The $(PPr_3)_4Cu_4Fe_4S_6(OPPr_3)_2Cl_2$ cluster has the same core structure with cluster $(PPr_3)_4Cu_4Fe_4S_6Cl_4$. The only difference between the two compounds is the substitution of two Cl^- in with two neutral $OPPr_3$ ligands, thus rendering the latter two electrons reduced compared to the former. The $(PPr_3)_4Cu_4Fe_4S_6(OPPr_3)_2Cl_2$ cluster exhibits mean Cu-S bond lengths of 2.385Å comparable to the ones found in $(PPr_3)_4Cu_4Fe_4S_6Cl_4$ and

Fe-S distances of 2.311Å which are slightly longer than the corresponding ones in $(PPr_3)_4Cu_4Fe_4S_6Cl_4$. The average Cu-P bond distance is 2.232Å whereas the Fe-Cl and Fe-O bond lengths are 2.271Å and 1.974Å respectively. The average Cu-Cu and Fe-Fe body diagonals distances can be found at 4.947Å (range: 4.911Å -4.983Å) and 4.657Å (range: 4.581Å -4.733Å) respectively. When these distances are compared to the corresponding ones in the $(PPr_3)_4Cu_4Fe_4S_6Cl_4$, cluster, an increase of ~ 0.09Å in the Cu-Cu body diagonal distances is evident. A more pronounced difference is revealed when the Fe-Fe body diagonal distances are compared. While the body diagonal distance between the Fe atoms bound by Cl^- ligands is comparable with the ones in cluster $(PPr_3)_4Cu_4Fe_4S_6Cl_4$ the body diagonal distance between the Fe atoms bound by the phosphine oxides is significantly shorter (~0.13Å -0.19Å). In conclusion, upon reduction by two electrons of $(PPr_3)_4Cu_4Fe_4S_6Cl_4$ the volume of the cluster only slightly increases from 21.647$Å^3$ to 21.999$Å^3$. This increase is in line with the expected increase in electron density of the clusters as slightly antibonding M-M orbitals are populated and it is within range of the increase observed in the $[Co_8S_6(SPh)_8]^{4-/5-}$ [24] and $[Fe_8S_6I_8]^{3-/4-}$ [17, 18] cluster pairs.

By comparison, the Cu_2Fe_6 and the Cu_4Fe_4 core structures are larger than the corresponding nickel and cobalt structures. In particular, the average Cu-Cu and Fe-Fe body diagonal distances can be found at 4.860Å (range: 4.843Å -4.877Å) and 4.756Å (range: 4.719Å -4.793Å) for $(PPr_3)_4Cu_4Fe_4S_6Cl_4$, at 4.954Å and 4.763Å (range: 2.727Å - 2.785Å) for $[(PEt_3)_2Cu_2Fe_6S_6Cl_6]^{2-}$. The average Ni-Ni and Fe-Fe body diagonal distances for $[(PPr_3)_2Ni_2Fe_6S_6Cl_6]^{2-}$ can be found at 4.297Å and 4.755Å, respectively while the corresponding average Ni-Fe distance for $(PPr_3)_4Ni_4Fe_4S_6Cl_4$ is 4.576Å (range: 4.549Å -4.603Å). These differences undoubtedly, are mainly due to the longer Cu-S

bonds in $(PPr_3)_4Cu_4Fe_4S_6Cl_4$ and $[(PEt_3)_2Cu_2Fe_6S_6Cl_6]^{2-}$ at 2.336Å and 2.385Å when compared to the Ni-S bonds in $(PPr_3)_4Ni_4Fe_4S_6Cl_4$ and $[(PPr_3)_2Ni_2Fe_6S_6Cl_6]^{2-}$ at 2.243Å and 2.255Å respectively.

3.3.4. Mössbauer Spectroscopy, Magnetic and Electrochemical Studies.

The Mössbauer spectra of $(Bu_4N)_2[(PEt_3)_2Cu_2Fe_6S_6Cl_6]$, $(Et_4N)_2[(PPr_3)_2Ni_2Fe_6S_6Cl_6]$, $(PPr_3)_4Cu_4Fe_4S_6Cl_4$, $(PPr_3)_4Ni_4Fe_4S_6Cl_4$ and $(PPr_3)_4Co_4Fe_4S_6Cl_4$ clusters (at room temperature, vs Fe metal) display isomer shifts and quadruple splittings as presented in Table 3.10. Not unexpectedly, the Fe atoms in $(Et_4N)_2[(PPr_3)_2Ni_2Fe_6S_6Cl_6]$ and $(PPr_3)_4Ni_4Fe_4S_6Cl_4$ appear more reduced than those in $(Bu_4N)_2[(PEt_3)_2Cu_2Fe_6S_6Cl_6]$ and $(PPr_3)_4Cu_4Fe_4S_6Cl_4$. Based on the initial assignment of the heterometals as Cu(I), Ni(II) and Co(II) the formal oxidation states of the irons should be Fe^{+3} for Cu_4Fe_4, $Fe^{+2.33}$ for Cu_2Fe_6 and Fe^{+2} for the nickel and cobalt analogues. If this was true, the expected isomer shifts should have a considerably larger range, as in the reported Fe/S clusters [38], where the isomer shift decreases by approximately 0.4 $mm{\cdot}s^{-1}$ as the oxidation state changes from Fe^{2+} to Fe^{3+} with values approximately at 0.55 $mm{\cdot}s^{-1}$ and 0.15 $mm{\cdot}s^{-1}$ respectively (at room temperature).

Compound	Formal oxidation of the metals	δ ($mm{\cdot}s^{-1}$)	ΔE_Q ($mm{\cdot}s^{-1}$)	μ_{eff} (5K)	μ_{eff} (300K)
$[(PEt_3)_2Cu_2Fe_6S_6Cl_6]^{2-}$	2Cu(I), 2Fe(III), 4Fe(II)	0.34	0.39	1.28	5.38
$[(PPr_3)_2Ni_2Fe_6S_6Cl_6]^{2-}$	2Ni(II), 6Fe(II)	0.36	0.68	diam.	diam.
$(PPr_3)_4Cu_4Fe_4S_6Cl_4$	4Cu(I), 4Fe(III)	0.34	0.64	diam.	diam.
$(PPr_3)_4Cu_4Fe_4S_6(OPPr_3)_2Cl_2$	4Cu(I), 2Fe(II), 2Fe(III)	-	-	0.84	6.92
$(PPr_3)_4Ni_4Fe_4S_6Cl_4$	4Ni(II), 4Fe(II)	0.40	0.70	2.76	4.61
$(PPr_3)_4Co_4Fe_4S_6Cl_4$	4Co(II), 4Fe(II)	0.41	0.80	2.05	2.87
Natural Pentlandites	N/A	0.31-0.38	0.10-0.22	diam.	diam.

Table 3.10. Mössbauer and magnetic susceptibility measurements on the main M/Fe/S clusters presented in this chapter. Mossbauer parameters for natural occurring pentlandites are taken from reference 40.

The observed values however, have a range of 0.07 $mm \cdot s^{-1}$ indicating that the oxidation states of the irons are much more similar and closer to $Fe^{+2.5}$. Therefore, while Cu(I)/2Fe(III)/4Fe(II) can be an adequate description for $[(PEt_3)_2Cu_2Fe_6S_6Cl_6]^{2-}$, the isomer shifts suggests that for the rest of the cluster measured, there is partial charge transfer from the heterometals as well, with Cu(I) being slightly oxidized to Cu(II) and Ni(II) and Co(II) partially reduced to Ni(I) and Co(I) in order to obtain delocalized Fe(II)/Fe(III) systems that fit the data. A more precise assignment of oxidation states is not however possible unless we could have obtained reduced or oxidized species of these clusters.

Similar delocalization of charge and a more ferric character has been observed in naturally occurring $(Fe,Ni)_8S_6$ pentlandites that exhibit isomer shifts in the 0.3-0.4 $mm \cdot s^{-1}$ range [39, 40]. Unfortunately, no Mössbauer spectra ware reported for the structurally similar $(Et_4N)_3Fe_8S_6I_8$ [17], $(PhCH_2NEt_3)_4Fe_8S_6I_8$, $[Fe(dppe)(MeCN)_4]_2Fe_8S_6I_8$ [18] and $Fe_8S_6(PCy_3)_4Cl_4$ [41] clusters that would provide a better assignment of the oxidation states of the metals on the clusters reported herein.

The magnetic moments for $(Bu_4N)_2[(PEt_3)_2Cu_2Fe_6S_6Cl_6]$ are μ_{eff}= 0.49 (5K), 1.38 (40K), 3.89 (300K), whereas $(Et_4N)_2[(PPr_3)_2Ni_2Fe_6S_6Cl_6]$ appears to be diamagnetic. $(PPr_3)_4Cu_4Fe_4S_6Cl_4$ is also diamagnetic at either 5K or room temperatures, which is also observed in natural occurring pentlandites [39]. The $(PPr_3)_4Ni_4Fe_4S_6Cl_4$, $(PPr_3)_4Co_4Fe_4S_6Cl_4$ and $(PPr_3)_4Cu_4Fe_4S_6(OPPr_3)_2Cl_2$ clusters exhibit magnetic moments with values of μ_{eff}= 2.76 (5K), 3.22 (40K), 4.61 (300K), μ_{eff}= 2.05 (5K), 2.27 (40K), 2.87 (300K) and μ_{eff}= 0.47 (5K), 1.35 (40K), 3.68 (300K) respectively.

The diamagnetic nature of $(Et_4N)_2[(PPr_3)_2Ni_2Fe_6S_6Cl_6]$ and $(PPr_3)_4Cu_4Fe_4S_6Cl_4$ clusters is difficult to explain without the calculation of the molecular orbital diagram of these clusters. However calculations on $M_8(\mu_4\text{-}E)_6L_4Cl_4$ T_d clusters [42] suggests that clusters with 102, 110, 114 or 120 metal valence electrons would be diamagnetic. The clusters $(PPr_3)_4Ni_4Fe_4S_6Cl_4$, $(PPr_3)_4Co_4Fe_4S_6Cl_4$ that have a T_d geometry have 108 and 104 metal valence electrons respectively are expected to be paramagnetic since the HOMO level is $(2a_1,4t_2)$ with four and two unpaired electrons respectively, which is reflected in the room temperature magnetic moments that approximate those of S=2 (μ_S=4.9) and S=1 (μ_S=2.83) respectively. At 5K the values in both cases approximate S=1 suggesting therefore that there is a small separation of the $2a_1$ and $4t_2$ orbitals in $(PPr_3)_4Ni_4Fe_4S_6Cl_4$ allowing a $2a_1^2,4t_2^2$ state to appear instead of the $2a_1^1,4t_2^3$ electron configuration observed at room temperature. In the other cases the change in geometry to D_{2h} for $(PPr_3)_4Cu_4Fe_4S_6Cl_4$ ($112e^-$) and $(PPr_3)_4Cu_4Fe_4S_6(OPPr_3)_2Cl_2$ ($114e^-$); or D_{3d} for $(Bu_4N)_2[(PEt_3)_2Cu_2Fe_6S_6Cl_6]$ ($106e^-$) and $(Et_4N)_2[(PPr_3)_2Ni_2Fe_6S_6Cl_6]$ ($104e^-$); would cause additional splitting to the t and e symmetry orbitals making predictions on the resulting molecular orbital diagrams unrealistic. The complexity of the molecular orbital diagrams for D_{2h} and D_{3h} symmetries is also evident by observing the two paramagnetic species. Both $(PPr_3)_4Cu_4Fe_4S_6(OPPr_3)_2Cl_2$ and $(Bu_4N)_2[(PEt_3)_2Cu_2Fe_6S_6Cl_6]$ clusters differ from the diamagnetic $(PPr_3)_4Cu_4Fe_4S_6Cl_4$ and $(Et_4N)_2[(PPr_3)_2Ni_2Fe_6S_6Cl_6]$ clusters by two electrons. However, at room temperature, the magnetic values correspond to six unpaired electrons for $(PPr_3)_4Cu_4Fe_4S_6(OPPr_3)_2Cl_2$, and four unpaired electrons for $(Bu_4N)_2[(PEt_3)_2Cu_2Fe_6S_6Cl_6]$. This result suggests that there is significant difference in the molecular orbital levels for the two geometries as the metal or the ligand changes,

making theoretical calculations necessary for explaining the observed magnetic properties.

The temperature dependence of the effective magnetic moment for the paramagnetic species is presented in Figure 3.12. It is of interest to note that in the cases of the two paramagnetic Cu/Fe/S clusters antiferromagnetic coupling is considerably stronger than in the case of the paramagnetic nickel and cobalt clusters that appear to approximate more the curie law, although there is antiferromagnetic coupling to some extent.

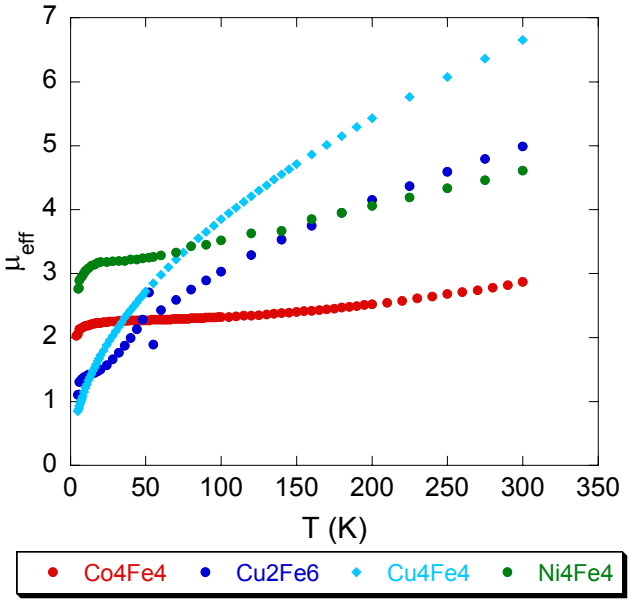

Figure 3.12. Temperature dependence of the effective magnetic moment of $(PPr_3)_4Co_4Fe_4S_6Cl_4$, $[(PEt_3)_2Cu_2Fe_6S_6Cl_6]^{2-}$, $(PPr_3)_4Cu_4Fe_4S_6(OPPr_3)_2Cl_2$ and $(PPr_3)_4Ni_4Fe_4S_6Cl_4$ clusters

Cyclic voltammetry experiments were performed as well. The $(PPr_3)_4Cu_4Fe_4S_6Cl_4$ cluster (Figure 3.13) shows two reductions, one reversible at -17mV and an irreversible at -635mV, while it exhibits one irreversible oxidation at 672mV. In contrast, the $(Bu_4N)_2[(PEt_3)_2Cu_2Fe_6S_6Cl_6]$ (Figure 3.14) shows one reversible reduction at -587mV

(the peak at approximately -200mV is due to strong absorption of the species on the surface of the electrode [43]) and one irreversible oxidation at 883mV.

$(PPr_3)_4Ni_4Fe_4S_6Cl_4$ (Figure 3.15) reveals two reversible reduction waves at -228mV and -555mV and two irreversible oxidation waves at 384mV, 854mV, while $(Et_4N)_2[(PPr_3)_2Ni_2Fe_6S_6Cl_6]$ (Figure 3.16) shows only one reversible reduction wave at -585mV and irreversible oxidations at 342mV 1058mV. The cyclic voltammetry of $(PPr_3)_4Co_4Fe_4S_6Cl_4$ (Figure 3.17) reveals two reversible reductions at -478mV and -776mV. In all cases as shown in Figure 3.17 above -1V, there are irreversible reductions as well.

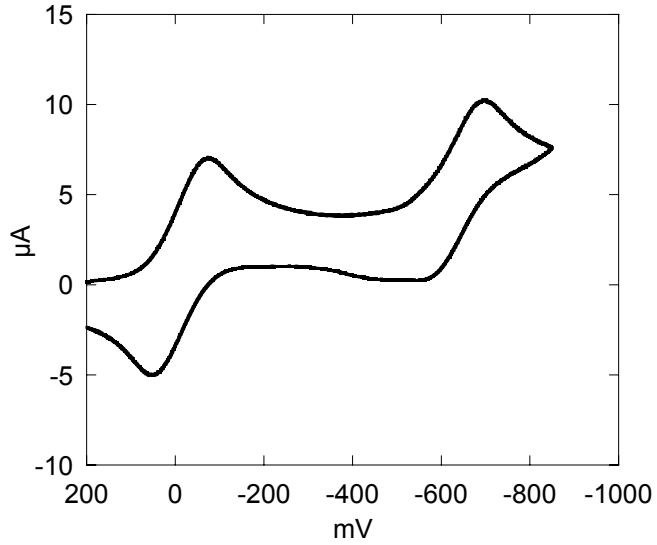

Figure 3.13. Cyclic Voltammogram of $(PPr_3)_4Cu_4Fe_4S_6Cl_4$ from 0.2V to -0.9V

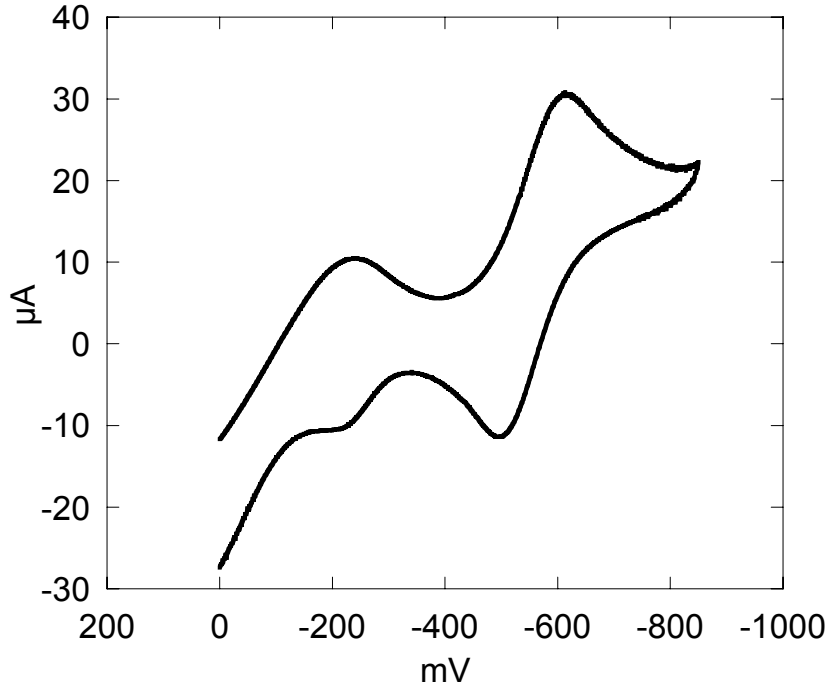

Figure 3.14. Cyclic Voltammogram of $(Bu_4N)_2[(PEt_3)_2Cu_2Fe_6S_6Cl_6]$ from 0V to -0.9V.

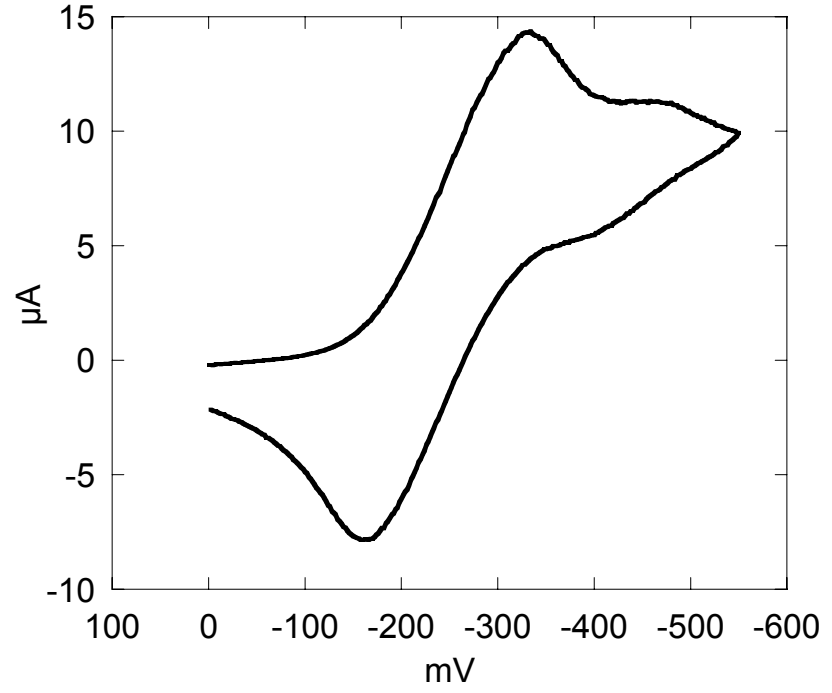

Figure 3.15. Cyclic Voltammogram of $(PPr_3)_4Ni_4Fe_4S_6Cl_4$ from 0V to -0.55V.

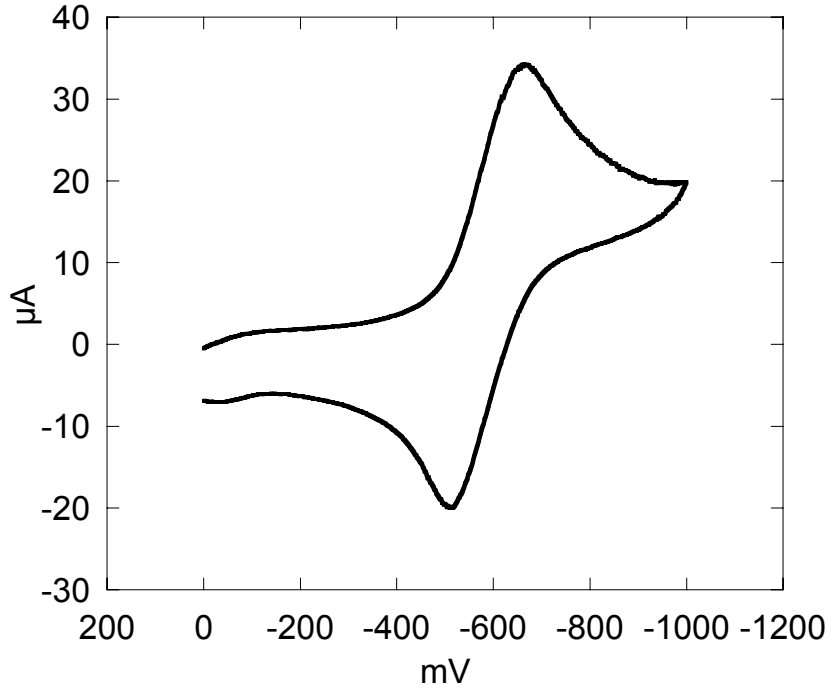

Figure 3.16. Cyclic Voltammogram of $(Et_4N)_2[(PPr_3)_2Ni_2Fe_6S_6Cl_6]$ from 0V to -1V.

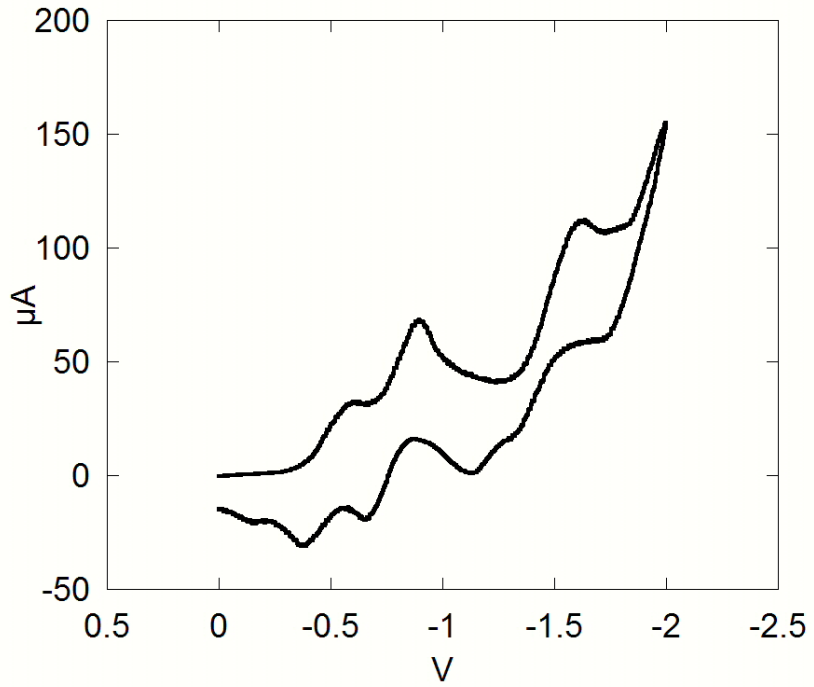

Figure 3.17. Cyclic Voltammogram of $(PPr_3)_4Co_4Fe_4S_6Cl_4$ from 0V to -2V.

3.4. Conclusions

The interest in expanding our knowledge of Fe/S clusters led us to the investigation of the reactions of discrete known Fe/S compounds such as the $Fe_2S_2Cl_4$ dimer and the $Fe_4S_4Cl_4$ cubane with monomeric compounds containing copper, nickel of cobalt. This resulted in the isolation of a large number of new compounds, including a series of heterometallic M/Fe/S clusters containing a pentlandite-like core structure. Although two structures have been previously reported, they have not been fully characterized, nor more importantly, were their chemical properties investigated. The use of Fe_2S_2 dimeric units as building blocks provides yet another example of how the synthesis of high nuclearity M/Fe/S clusters can be approached by design. Future goals can be summarized in the three following: 1) Expand the family of these heterometallic compounds including different metals such as Silver and Cadmium. 2) Further investigate the properties of these clusters. Substituting the phosphine and chloride with sulfur containing ligand might not only provide us with an insight and understanding of the properties of the natural occurring pentlandites, but also lead to novel chemistry with exciting properties. 3) Use the discrete soluble building blocks with suitable bridging ligands (and metals in certain cases) for the synthesis of extended networks whose properties would be finely tuned by the use of the appropriate different starting building blocks or ligands.

3.5 References:

[1] V. Rajamani, C.T. Prewitt, Canadian Mineralogist 12 (1973) 178.
[2] V. Rajamani, C.T. Prewitt, American Mineralogist 60 (1975) 39.
[3] J.F. Riley, Mineralogical Magazine 41 (1977) 345.
[4] K. Tsukimura, H. Nakazawa, Acta Crystallographica Section B-Structural Science 40 (1984) 364.
[5] A. Sugaki, A. Kitakaze, American Mineralogist 83 (1998) 133.
[6] B. Etschmann, A. Pring, A. Putnis, B.A. Grguric, A. Studer, American Mineralogist 89 (2004) 39.
[7] C. Tenailleau, B. Etschmann, R.M. Ibberson, A. Pring, American Mineralogist 91 (2006) 1442.
[8] K. Tsukimura, H. Nakazawa, T. Endo, O. Fukunaga, Physics and Chemistry of Minerals 19 (1992) 203.
[9] S.D. Scott, E. Gasparrini, Canadian Mineralogist 12 (1973) 165.
[10] S.R. Hall, J.M. Stewart, Canadian Mineralogist 12 (1973) 169.
[11] S. Geller, Acta Crystallographica 15 (1962) 1195.
[12] V. Rajamani, C.T. Prewitt, Canadian Mineralogist 13 (1975) 75.
[13] M. Fleischer, L.J. Cabri, G.Y. Chao, J.A. Mandarino, A. Pabst, American Mineralogist 67 (1982) 1074.
[14] A. Kitakaze, A. Sugaki, Canadian Mineralogist 42 (2004) 17.
[15] I. Bezverkhyy, P. Afanasiev, M. Danot, Journal of Physical Chemistry B 108 (2004) 7709.
[16] G.V. Gibbs, R.T. Downs, D.F. Cox, N.L. Ross, C.T. Prewitt, K.M. Rosso, T. Lippmann, A. Kirfel, Zeitschrift Fur Kristallographie 223 (2008) 1.
[17] S. Pohl, W. Saak, Angewandte Chemie-International Edition in English 23 (1984) 907.
[18] S. Pohl, U. Opitz, Angewandte Chemie-International Edition in English 32 (1993) 863.
[19] D. Coucouvanis, M.G. Kanatzidis, Journal of the American Chemical Society 107 (1985) 5005.
[20] M.G. Kanatzidis, D. Coucouvanis, Journal of the American Chemical Society 108 (1986) 337.
[21] D. Fenske, J. Ohmer, J. Hachgenei, K. Merzweiler, Angewandte Chemie-International Edition in English 27 (1988) 1277.
[22] D. Fenske, H. Krautscheid, M. Muller, Angewandte Chemie-International Edition in English 31 (1992) 321.
[23] G. Christou, K.S. Hagen, R.H. Holm, Journal of the American Chemical Society 104 (1982) 1744.
[24] G. Christou, K.S. Hagen, J.K. Bashkin, R.H. Holm, Inorganic Chemistry 24 (1985) 1010.
[25] M.G. Kanatzidis, W.R. Hagen, W.R. Dunham, R.K. Lester, D. Coucouvanis, Journal of the American Chemical Society 107 (1985) 953.
[26] Y. Do, E.D. Simhon, R.H. Holm, Inorganic Chemistry 22 (1983) 3809.

[27] R.A. Heintz, J.A. Smith, P.S. Szalay, A. Weisgerber, K.R. Dunbar, Homoleptic transition metal acetonitrile cations with tetrafluoroborate or trifluoromethanesulfonate anions, Inorganic Syntheses, Vol 33, 2002, pp. 75.
[28] B.S. Snyder, M.S. Reynolds, I. Noda, R.H. Holm, Inorganic Chemistry 27 (1988) 595.
[29] F. Cecconi, C.A. Ghilardi, S. Midollini, Journal of the Chemical Society-Chemical Communications (1981) 640.
[30] D.J. Evans, G. Garcia, M.D. Santana, M.C. Torralba, Inorganica Chimica Acta 284 (1999) 296.
[31] D. Coucouvanis, M. Kanatzidis, E. Simhon, N.C. Baenziger, Journal of the American Chemical Society 104 (1982) 1874.
[32] K.S. Hagen, D.W. Stephan, R.H. Holm, Inorganic Chemistry 21 (1982) 3928.
[33] K.S. Hagen, R.H. Holm, Inorganic Chemistry 23 (1984) 418.
[34] W. Cen, F.M. Macdonnell, M.J. Scott, R.H. Holm, Inorg. Chem. 33 (1994) 5809.
[35] C. Junghans, W. Saak, S. Pohl, Journal of the Chemical Society-Chemical Communications (1994) 2327.
[36] D. Coucouvanis, A. Salifoglou, M.G. Kanatzidis, W.R. Dunham, A. Simopoulos, A. Kostikas, Inorganic Chemistry 27 (1988) 4066.
[37] W. Saak, S. Pohl, Angew. Chem., Int. Ed. Engl. 30 (1991) 881.
[38] P.V. Rao, R.H. Holm, Chemical Reviews 104 (2004) 527.
[39] O. Knop, C.H. Huang, K.I.G. Reid, J.S. Carlow, F.W.D. Woodhams, Journal of Solid State Chemistry 16 (1976) 97.
[40] G.A. Fatseas, J.B. Goodenough, Journal of Solid State Chemistry 33 (1980) 219.
[41] C. Goh, B.M. Segal, J.S. Huang, J.R. Long, R.H. Holm, Journal of the American Chemical Society 118 (1996) 11844.
[42] E. Furet, A. Lebeuze, J.F. Halet, J.Y. Saillard, Journal of the American Chemical Society 116 (1994) 274.
[43] P. Zanello, Inorganic electrochemistry : theory, practice and application Royal Society of Chemisty, Cambridge, 2003.

Chapter 4

Synthesis and Characterization of new Heterometallic Iron Sulfur Nitrosyl Clusters with Mo, Cu and Ni

4.1 Introduction

The diversity of Fe/S cluster chemistry is expressed in a multitude of stoichiometries, ligand (L) types, and structures. In a general, broad sense, the Fe/S/L clusters can be classified as Fe/S/X (X=halogens, thiols), Fe/S/CO, Fe/S/PR_3 and Fe/S/NO species. Examples of these clusters (Figure 4.1) include the $[Fe_4S_4(L)_4]^{n-}$ cubanes [1, 2], the sulfur voided $[Fe_4S_3]$ cube of $(Ph_4As)[Fe_4S_3(NO)_7]$[3], the iron voided $[Fe_3S_4]$ cube in $(Et_4N)_3[Fe_3S_4(LS_3)]$, (LS_3=1,3,5-Tris((4,6-dimethyl-3-mercaptophenyl)thio)-2,4,6-tris(p-tolylthio)benzene) [4], the Fe_6S_6 prism in the $[Fe_6S_6(L)_6]^{n-}$ prismanes (L=halogens, $MeOC_6H_4O$ or nitrosyl)[5-7], the "bow-tie" $[Fe_6S_6]$ core in $(PPN)_2[Fe_6S_6(CO)_{12}]$[8], the edge-fused double cubane $[Fe_8S_8]$ core in $Fe_8S_8(PCy_3)_6$ [9] (PCy_3= Tricyclohexylphosphine) and the $Fe_8S_7(SR)_4(SR')$ (SR =2,6bis(mesityl)-thiophenol, SR´=2,4,6,tris(isopropyl)-thiophenol)[10]

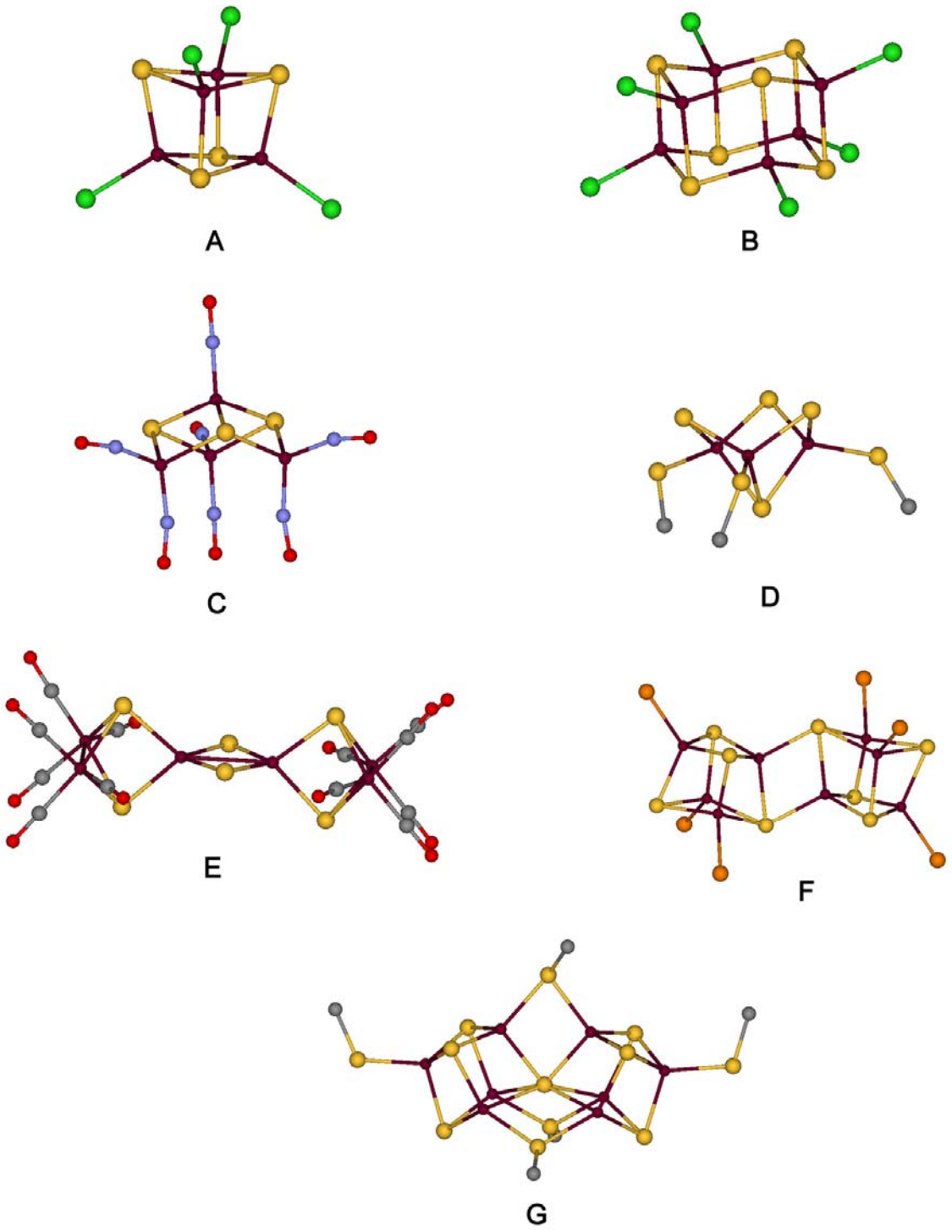

Figure 4.1: Examples of Fe/S clusters in different arrangements with various ligands. Clusters shown are $[Fe_4S_4Cl_4]^{2-}$ (A), $[Fe_6S_6Cl_6]^{3-}$ (B), $[Fe_4S_3(NO)_7]^{-}$ (C), $[Fe_3S_4(LS_3)]^{3-}$ (D) (LS_3=1,3,5-Tris((4,6-dimethyl-3-mercaptophenyl)thio)-2,4,6-tris(p-tolylthio)benzene), $[Fe_6S_6(CO)_{12}]^{2-}$ (E), $Fe_8S_8(PCy_3)_6$ (F) (PCy_3= Tricyclohexylphosphine) and $Fe_8S_7(SR)_4(SR')$ (G) (SR =2,6 bis(mesityl)-thiophenol, SR´=2,4,6, tris(isopropyl) -thiophenol). In (D), (F) and (G) the carbon atoms have been omitted for clarity.

The diversity of Fe/S clusters is expanded further by the addition of thiophilic metals and the consequent alterations in the coordination and the properties of these clusters. An important class of heterometallic iron sulfur clusters are the cuboctahedral M_8S_6 "pentlandite-like" core with a cubic array of metal atoms inscribed in an S_6 octahedron of μ_4-sulfido ligands that have been observed in minerals [11], and also in molecular clusters with halides [12-16] as terminal ligands as was discussed in more detail in Chapter 3.

4.2. Experimental Section

All the reactions have been performed under a nitrogen atmosphere in a glove box or by using standard Shlenck line techniques. The solvents used have been distilled and degassed prior to use, except of DMF that was only degassed. $(PPN)_2[Fe_6S_6(NO)_6]$ was synthesized according to the method described in Chapter 2, while $Mo(CO)_3(MeCN)_3$ [17] and $[Ni(MeCN)_6](BF_4)_2$ [18] were synthesized according to published procedures. $[Cu(MeCN)_4]PF_6$ and tripropylphosphine (PPr_3), were purchased from commercial sources.

IR spectra were obtained on a Perkin Elmer BX FT-IR spectrometer (mid-IR) and a Nicolet 740 FT-IR spectrometer (Far-IR) in KBr pellets, and cyclic voltammetry experiments were carried out on a glassy carbon working electrode and Ag/AgCl reference electrode in saturated KCl/AgCl aqueous solution, with 0.1M Bu_4NPF_6 supporting electrolyte on a EG&G Princeton Potentiostat/Galvanostat model 263A. The reduction potentials are reported against a standard calomel electrode SCE. Magnetic susceptibility measurements were carried out on a MPMS SQUID magnetometer and the

data were corrected for diamagnetic contributions. X-Band EPR spectra were collected on a Bruker EMX electron spin resonance spectrometer equipped with a Varian liquid nitrogen cryostat at approximately 100K. Elemental analysis was performed by the Microanalytical Laboratory at the University of Michigan. Microbeam Electron Analysis was performed at the University of Michigan Electron Microbeam Analysis Laboratory (EMAL). Mössbauer spectra were obtained with the high-sensitivity Mössbauer spectrometer in the Institute of Materials Science, NCSR "Demokritos" Athens, Greece, courtesy of Dr. Yiannis Sanakis.

4.2.1. Bis (Bis(triphenylphospine)iminium) hexasulfido-hexairon-hexanitrosyl bis(tricarbonyl-molybdenum) $(PPN)_2[Mo_2Fe_6(NO)_6(CO)_6]$. *(Reaction 1)*

$(PPN)_2[Fe_6S_6(NO)_6]$ (0.5g, 0.28 mmol) and $Mo(CO)_3(MeCN)_3$ (0.17g, 0.56 mmol) were dissolved in 15ml dichloroethane and the solution was stirred overnight. The mixture was filtered, and the filtrate layered with ~ 60ml ether, affording 0.45 g of a crystalline material.

Yield 0.20 mmol, 71.3 % of $(PPN)_2[(CO)_6Mo_2Fe_6S_6(NO)_6]$

Elemental analysis calculated for $(PPN)_2[(CO)_6Mo_2Fe_6S_6(NO)_6]\cdot 2DMF$ $C_{78}H_{60}N_8O_{12}P_4S_6Fe_6Mo_2$ C: 43.68%, H: 2.82%, N: 5.22%. Found: C: 43.48%, H: 2.70%, N: 5.16%.

IR (KBr, cm^{-1}): 3055(w), 2957(w), 2926(w), 2861(w), 1926(vs) (ν_{C-O}), 1877(ν_{C-O}), 1723(sh) (ν_{N-O}), 1695(vs) (ν_{N-O}), 1670(sh) (ν_{N-O}), 1437(m), 1384(m), 1258(m), 1113(m), 744(w), 723(m), 691(m), 690(m), 594(m) (ν_{Mo-C}), 548(m), 532(m), 498(w).

CV: (DMF solution, 0.031 M) $E_{1(rev)}$ = -641 mV, $E_{2(rev)}$ = -1247 mV

4.2.2. Hexasulfido- hexairon- hexanitrosyl bis(tripropylphosphino-copper) $(PPr_3)_2Cu_2Fe_6S_6(NO)_6$ and Hexasulfido- tetrairon- tetranitrosyl tetrakis(tripropylphosphino-copper) $(PPr_3)_4Cu_4Fe_4S_6(NO)_4$. *(Reaction 2)*

$[Cu(MeCN)_4]PF_6$ (0.21g, 0.56 mmol) was dissolved in 5 ml MeCN followed by the dropwise addition of tripropylphosphine (PPr_3) (0.12ml, 0.60 mmol) and the solution stirred for 30 min. This solution was added dropwise to a dichloroethane solution (15ml) containing $(PPN)_2[Fe_6S_6(NO)_6]$ (0.5g, 0.28 mmol) and the mixture was stirred overnight. The mixture was filtered and the precipitate was washed with small amounts of ether, extracted with a THF/Ether 1:1 mixture and layered with hexanes affording 0.2g of crystalline $(PPr_3)_2Cu_2Fe_6S_6(NO)_6$. The filtrate was taken to dryness and the residue stirred in ether affording a colored solution and a white powder identified as $PPNPF_6$. Following filtration, the ether solution was dried affording approx. 0.05g of oily $(PPr_3)_4Cu_4Fe_4S_6(NO)_4$. Crystals suitable for X-Ray diffraction were obtained by redissolving in ether and allowing for slow evaporation of the solvent to occur.

$(PPr_3)_2Cu_2Fe_6S_6(NO)_6$

Elemental analysis calculated for $(PPr_3)_2Cu_2Fe_6S_6(NO)_6$ $C_{18}H_{42}N_6O_6P_2S_6Fe_6Cu_2$ C: 18.72%, H: 3.67%, N: 7.28%. Found: C: 18.51%, H: 3.63%, N: 7.05%

Yield 0.17 mmol, 60 % of $(PPr_3)_2Cu_2Fe_6S_6(NO)_6$ based on iron

IR (KBr, cm^{-1}): 2957(m), 2927(m), 2867(w), 1766(sh) (ν_{N-O}), 1750(sh) (ν_{N-O}), 1729(vs) (ν_{N-O}), 1660(sh) (ν_{N-O}), 1450(m), 1410(m), 1080(m), 1000(m), 851(w), 736(w).

Microprobe analysis confirms the 2:6 ratio of copper to iron.

CV: (THF solution, 0.029 M) $E_{1(rev)}$ = -169 mV, $E_{2(rev)}$ = -1035 mV, $E_{3(rev)}$= -1667 mV

$(PPr_3)_4Cu_4Fe_4S_6(NO)_4$

Elemental analysis calculated for $(PPr_3)_4Cu_4Fe_4S_6(NO)_4$ $C_{36}H_{84}N_4O_4P_4S_6Fe_4Cu_4$ C: 30.22%, H: 5.92%, N: 3.92%. Found: C: 32.90%, H: 6.35%, N: 3.08%

Yield 0.04 mmol 28.5% $(PPr_3)_4Cu_4Fe_4S_6(NO)_4$ based on copper

IR (KBr, cm^{-1}): 2957(m), 2928(m), 2869(w), 1724(vs) (ν_{N-O}), 1712(vs) (ν_{N-O}), 1457(m), 1080(m), 840(w).

Microprobe analysis confirms the 1:1 ratio of copper to iron.

CV: (THF solution, 0.011 M) $E_{1(rev)}$ = -153 mV, $E_{2(rev)}$ = -1021 mV, $E_{3(rev)}$= -1537 mV, $E_{4(irr)}$ =-2077 mV

4.2.3. Hexasulfido- hexairon- hexanitrosyl bis(tripropylphosphino-nickel) $(PPr_3)_2[Ni_2Fe_6S_6(NO)_6]$, Hexasulfido- tetrairon- tetranitrosyl tris(tripropylphosphino-nickel) $(PPr_3)_3[Ni_3Fe_4S_6(NO)_4]$ and Hexasulfido- tetrairon- tetranitrosyl tetra(tripropylphosphino-nickel) $(PPr_3)_4Ni_4Fe_4S_6(NO)_4$. *(Reaction 3)*

$[Ni(MeCN)_6](BF_4)_2$ (0.27g, 0.56mmol) was dissolved in 5ml MeCN followed by the dropwise addition of PPr_3 (0.12ml, 0.60mmol) and the solution stirred for 30 min. This solution was added dropwise to a dichloroethane solution (15ml) containing $(PPN)_2[Fe_6S_6(NO)_6]$ (0.5g, 0.28 mmol) and the mixture was stirred overnight. The mixture was filtered and the precipitate was washed with small amounts of ether and extracted with a THF/Ether 1:1 mixture and layered with hexanes affording 0.15g of crystalline $(PPr_3)_2Ni_2Fe_6S_6(NO)_6$. The filtrate was taken to dryness and the residue stirred in ether affording a colored solution and a white powder which was identified as $PPNBF_4$. The resulting ether solution was dried and washed with hexanes and extracted partially with ether and partially with THF using silica gel as a filtration agent. The ether fraction afforded approx 0.02g of oily $(PPr_3)_4Ni_4Fe_4S_6(NO)_4$ and the THF fraction

afforded approx. 0.04g of oily $(PPr_3)_3Ni_3Fe_4S_6(NO)_4$. Crystals suitable for X-Ray diffraction were obtained by slow evaporation of ether and recrystalization from THF/Hexanes respectively.

$(PPr_3)_2Ni_2Fe_6S_6(NO)_6$

Elemental analysis calculated for $(PPr_3)_2Ni_2Fe_6S_6(NO)_6$ $C_{18}H_{42}N_6O_6P_2S_6Fe_6Ni_2$ C: 18.88%, H: 3.70%, N: 7.34%. Found: C: 19.12%, H: 3.77%, N: 7.26%.

Yield 0.13 mmol, 46% of $(PPr_3)_2Ni_2Fe_6S_6(NO)_6$ based on iron.

IR (KBr, cm^{-1}): 2958(m), 2927(m), 2868(w), 1763(s) (ν_{N-O}), 1745(sh) (ν_{N-O}), 1725(vs) (ν_{N-O}), 1663(sh) (ν_{N-O}), 1449(m), 1405(m), 12181(m), 1076(m), 1041(m), 851(m), 762(w), 731(m), 586(w), 435(w)

Microprobe analysis confirms the 2:6 ratio of nickel to iron.

CV: (THF solution, 0.029 M) $E_{1(rev)}$ = -1 mV, $E_{2(rev)}$ = -717 mV, $E_{3(rev)}$= -1431 mV

$(PPr_3)_3Ni_3Fe_4S_6(NO)_4$

Elemental analysis calculated for $(PPr_3)_3Ni_3Fe_4S_6(NO)_4$ $C_{27}H_{63}N_4O_4P_3S_6Fe_4Ni_3$ C: 27.19%, H: 5.32%, N: 4.70%. Found; C: 31.57%, H: 5.91%, N: 5.31%.

Yield 0.033 mmol, 17.83% $(PPr_3)_3Ni_3Fe_4S_6(NO)_4$ based on nickel.

IR (KBr, cm^{-1}): 2957(m), 2927(m), 2868(w), 1720(s) (ν_{N-O}), 1698(vs) (ν_{N-O}), 1679(s) (ν_{N-O}), 1452(m), 1404(m), 1221(m), 1073(m), 1038(m), 849(m), 724(m), 584(w), 440(w)

Microprobe analysis confirms the 3:4 ratio of nickel to iron.

$(PPr_3)_4Ni_4Fe_4S_6(NO)_4$

Elemental analysis calculated for $(PPr_3)_4Ni_4Fe_4S_6(NO)_4$ $C_{36}H_{84}N_4O_4P_4S_6Fe_4Ni_4$ C: 30.63%, H: 6.00%, N: 3.97%. Found; C: 31.57%, H: 5.91%, N: 5.31%.

Yield 0.014 mmol, 10% $(PPr_3)_4Ni_4Fe_4S_6(NO)_4$ based on nickel.

IR (KBr, cm^{-1}): 2959(m), 2927(m), 2870(w), 1745(m) (ν_{N-O}), 1716(vs) (ν_{N-O}), 1456(m), 1404(m), 1377(m), 1260(w), 1216(w), 1081(m), 1033(m), 847(m), 808(w), 729(m), 582(w), 433(w)

Microprobe analysis confirms the 1:1 ratio of nickel to iron.

4.2.4. Crystallographic Data

All diffraction data were collected at the University of Michigan X-Ray facility, at low temperatures ranging from 85(2) to 123(2) K to avoid decay during data collection, using a Siemens SMART CCD-based X-Ray diffractometer equipped with an LT-2 low temperature device and normal focus Mo-target X-ray tube (λ = 0.71073 Å). All diffraction data were processed with SADABS for absorption correction. The positions of heavy atoms were found by direct methods in E-maps using the software solution program in SHELXTL v.6.1. Subsequent cycles of least-squares refinement followed by difference Fourier synthesis produced the positions of the remaining non-hydrogen atoms; they were refined anisotropically unless stated otherwise. All hydrogen atoms were placed in ideal positions and refined as riding atoms with individual (or group if appropriate) isotropic thermal displacement parameters. The crystal data and structural parameters are shown in Tables 4.1, 4.2, 4.3, 4.4, and 4.5. All space group assignments were determined based on systematic absences and intensity statistics and were confirmed by the program XPREP of the SHELXTL package.

$(PPN)_2[(CO)_6Mo_2Fe_6S_6(NO)_6]$	
Color	Black
Habit	Needle
Size (mm)	044 x 0.44 x 0.34
Formula	$C_{90}H_{86}Fe_6Mo_2N_{12}O_{16}P_4S_6$
Weight ($g \cdot mol^{-1}$)	2434.93
Crystal System	Triclinic
Space Group	P -1
Unit Cell (Å) (a,b,c, α,β,γ)	12.373(2)
	14.386(3)
	15.495(3)
	97.037(3)
	91.936(3)
	110.014(2)
Volume ($Å^3$)	2563.4(8)
Z	1
Temperature (K)	123(2)
Absorption coefficient	1.311
F(0,0,0)	1234
θ range (deg)	1.88 to 28.39
Reflections	81490
Limiting indices	-16 < h < 16
	-19 < k < 19
	-20 < l < 20
R_{int}	0.0292
Data / restraints / parameters	12725 / 0 / 617
R_1,wR_2 [I>2σ(I)]	0.0396, 0.1050
R_1,wR_2 (all data)	0.0456, 0.1098
GooF (F^2)	1.024

Table 4.1. Crystallographic and refinement data for $(PPN)_2[(CO)_6Mo_2Fe_6S_6(NO)_6]$

$(PPr_3)_2Cu_2Fe_6S_6(NO)_6$	
Color	Black
Habit	Polyhedron
Size (mm)	0.44 x 0.40 x 036
Formula	$C_{18}H_{42}Cu_2Fe_6N_6O_6P_2S_6$
Weight ($g \cdot mol^{-1}$)	1155.06
Crystal System	Cubic
Space Group	P a -3
Unit Cell (Å) (a,b,c, α,β,γ)	15.9081(9)
	15.9081(9)
	15.9081(9)
	90.00
	90.00
	90.00
Volume ($Å^3$)	4025.8(4)
Z	4
Temperature (K)	108(2)
Absorption coefficient	3.563
F(0,0,0)	2320
θ range (deg)	2.22 to 28.29
Reflections	82778
Limiting indices	$-21 < h < 21$
	$-21 < k < 21$
	$-21 < l < 21$
R_{int}	0.0332
Data / restraints / parameters	1671 / 0 / 72
R_1,wR_2 [$I>2\sigma(I)$]	0.0134, 0.0343
R_1,wR_2 (all data)	0.0142, 0.0348
GooF (F^2)	1.090

Table 4.2. Crystallographic and refinement data for $(PPr_3)_2Cu_2Fe_6S_6(NO)_6$

$(PPr_3)_4Cu_4Fe_4S_6(NO)_4$	
Color	Black
Habit	Plate
Size (mm)	0.30 x 0.28 x 0.05
Formula	$C_{36}H_{84}Cu_4Fe_4N_4O_4P_4S_6$
Weight ($g \cdot mol^{-1}$)	1430.87
Crystal System	Monoclinic
Space Group	P 21/c
Unit Cell (Å) (a,b,c, α,β,γ)	11.299(3)
	15.292(5)
	17.404(5)
	90.00
	98.193(4)
	90.00
Volume ($Å^3$)	2976.4(15)
Z	2
Temperature (K)	123(2)
Absorption coefficient	2.700
F(0,0,0)	1472
θ range (deg)	1.78 to 26.43
Reflections	51829
Limiting indices	$-14 < h < 14$
	$-19 < k < 19$
	$-21 < l < 21$
R_{int}	0.0806
Data / restraints / parameters	6079 / 0 / 286
R_1,wR_2 [$I>2\sigma(I)$]	0.0738, 0.1753
R_1,wR_2 (all data)	0.1290, 0.2281
GooF (F^2)	0.990

Table 4.3. Crystallographic and refinement data for $(PPr_3)_4Cu_4Fe_4S_6(NO)_4$

$(PPr_3)_2Ni_2Fe_6S_6(NO)_6$	
Color	Black
Habit	Polyhedron
Size (mm)	0.38 x 0.34 x 030
Formula	$C_{18}H_{42}Fe_6Ni_2N_6O_6P_2S_6$
Weight ($g \cdot mol^{-1}$)	1145.40
Crystal System	Cubic
Space Group	P a -3
Unit Cell (Å) (a,b,c, α,β,γ)	15.7773(10)
	15.7773(10)
	15.7773(10)
	90.00
	90.00
	90.00
Volume ($Å^3$)	3927.3(4)
Z	4
Temperature (K)	108(2)
Absorption coefficient	3.528
F(0,0,0)	2312
θ range (deg)	2.24 to 28.30
Reflections	85115
Limiting indices	-21 < h < 21
	-20 < k < 20
	-21 < l < 21
R_{int}	0.0383
Data / restraints / parameters	1636 / 0 / 71
R_1,wR_2 [I>2σ(I)]	0.0147, 0.0395
R_1,wR_2 (all data)	0.0158, 0.0399
GooF (F^2)	1.139

Table 4.4. Crystallographic and refinement data for $(PPr_3)_2Ni_2Fe_6S_6(NO)_6$

$(PPr_3)_3Ni_3Fe_4S_6(NO)_4$	
Color	Black
Habit	Block
Size (mm)	0.40 x 0.24 x 0.16
Formula	$C_{24}H_{63}Fe_4N_4Ni_3O_4P_3S_6$
Weight ($g \cdot mol^{-1}$)	1192.61
Crystal System	Cubic
Space Group	P a -3
Unit Cell (Å) (a,b,c, α,β,γ)	21.3741(18)
	21.3741(18)
	21.3741(18)
	90.00
	90.00
	90.00
Volume ($Å^3$)	9764.8(14)
Z	8
Temperature (K)	108(2)
Absorption coefficient	2.675
F(0,0,0)	4912
θ range (deg)	1.65 to 28.32
Reflections	194707
Limiting indices	-28 < h < 28
	-28 < k < 28
	-28 < l < 28
R_{int}	0.0571
Data / restraints / parameters	4069 / 0/ 157
R_1,wR_2 [I>2σ(I)]	0.0199, 0.0413
R_1,wR_2 (all data)	0.0345, 0.0497
GooF (F^2)	1.239

Table 4.5. Crystallographic and refinement data for $(PPr_3)_3Ni_3Fe_4S_6(NO)_4$

4.3. Results and Discussion

As discussed in Chapter 3, the cyclohexane-like Fe_3S_3 units of the $[Fe_6S_6]$ core can serve as ligands for two additional metal ions to form $[M_2Fe_6S_6]$ clusters [12, 19, 20]. The latter were obtained in reactions carried out with coordinatively unsaturated complexes containing Mo, Cu and Ni. Similar reactions were carried out with $(PPN)_2[Fe_6S_6(NO)_6]$ affording structures with the same coordination environment as seen in Figure 4.2.

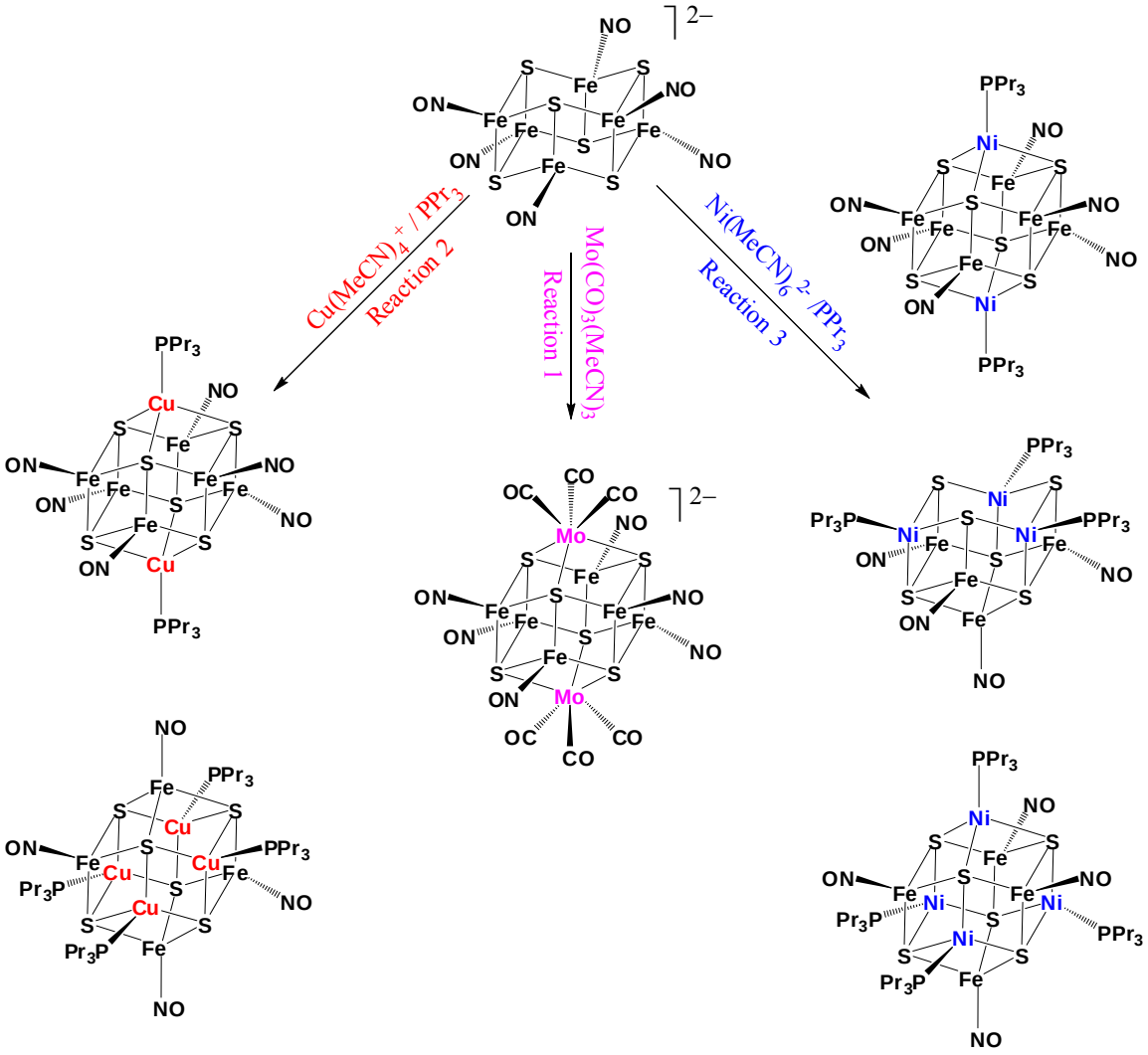

Figure 4.2. Schematic representation of the reactions presented in this chapter. It is noted that the reaction involving copper and nickel result in a mixture of products that were separated and characterized.

4.3.1. Synthesis

As in the case of $(Et_4N)_2[Fe_6S_6Cl_6]$ [19], the reaction between the $(PPN)_2[Fe_6S_6(NO)_6]$ and $Mo(CO)_3(MeCN)_3$ complexes leads to a single product, the $(PPN)_2[(CO)_6Mo_2Fe_6S_6(NO)_6]$ cluster in high yields (75%). This cluster forms even in molar ratios less than 1:1 suggesting that the $[MoFe_6S_6]$ core, if it forms at all, disproportionates to the $[Mo_2Fe_6S_6]$ and $[Fe_6S_6]$ clusters.

The reaction between $(PPN)_2[Fe_6S_6(NO)_6]$ and $[Cu(MeCN)_4]^+/PPr_3$ affords two products. The main product being $(PPr_3)_2Cu_2Fe_6S_6(NO)_6$, and in a lower yield the $(PPr_3)_4Cu_4Fe_4S_6(NO)_4$ cluster with the two clusters being separated due to their different solubilities. The reaction mechanism for the formation of $(PPr_3)_2Cu_2Fe_6S_6(NO)_6$ appears to be a simple addition with $(PPr_3)Cu(MeCN)_3^+$, with the copper replacing its weakly bound acetonitrile atoms from its coordination sphere with the more thermodynamically favored sulfur atoms of $[Fe_6S_6(NO)_6]^{2-}$. In coordinating solvents, such as DMF or THF, the $(PPr_3)_2Cu_2Fe_6S_6(NO)_6$ cluster does not form as a pure product but rather as a mixture with $[Cu(DMF)_4]_2[Fe_6S_6(NO)_6]$, as seen in infrared were there is the appearance of the characteristic coordinated DMF peaks, similar to $[Fe(DMF)_6][Fe_6S_6(NO)_6]$ presented in Chapter 2. This favors the use of the non-coordinating dichloroethane as the preferred solvent for the synthesis of $(PPr_3)_2Cu_2Fe_6S_6(NO)_6$.

The formation of the $(PPr_3)_4Cu_4Fe_4S_6(NO)_4$ cluster could be explained in terms of fragmentation of the $[Fe_6S_6(NO)_6]^{2-}$ cluster to smaller Fe/S/NO units (i.e. $\{Fe_2S_2(NO)_2\}$ units), as presented in Chapters 2 and 3. The latter in the presence of $Cu(PR_3)$ are transformed into $(PR_3)CuS_2Fe(NO)$ units which couple to form the final product. There is no solvent effect in obtaining the $(PPr_3)_4Cu_4Fe_4S_6(NO)_4$ cluster, since it is soluble in ether and can be easily separated from the mixture of compounds.

Similarly the reaction of $[Fe_6S_6(NO)_6]^{2-}$ with $[Ni(MeCN)_6]^{2+}/PPr_3$, give the neutral $(PPr_3)_2Ni_2Fe_6S_6(NO)_6$ cluster as the main product and other byproducts. Unlike the case of copper where the byproduct formed is exclusively $(PPr_3)_4Cu_4Fe_4S_6(NO)_4$, with nickel the isolated byproducts are the $(PPr_3)_4Ni_4Fe_4S_6(NO)_4$ cluster and the unique Ni/Fe/S cluster $(PPr_3)_3Ni_3Fe_4S_6(NO)_4$. The later contains the "voided–cubic" M_7S_6 core which previously has been found in $(PPr_3)_4Fe_7S_6Cl_3$ [21], $Co_7S_6I_3(PEt_3)_4$ [22], and $Co_7S_6X_3(PPh_3)_4$ (X= Cl^- [15], Br^- [23]) but not in mixed metal systems. The Ni_4Fe_4 and the Ni_3Fe_4 clusters were isolated from a mixture that appears to contain three compounds. The separation of these species is relatively difficult as their solubilities are similar, with $(PPr_3)_3Ni_3Fe_4S_6(NO)_4$ being less soluble in ether and hexanes than the other two species therefore it is obtained more easily. All three species contain phosphine and nitrosyls as shown by infrared spectroscopy, with the main N-O stretching peak at 1696 cm^{-1} for $(PPr_3)_3Ni_3Fe_4S_6(NO)_4$ (THF fraction), 1739 cm^{-1} for $(PPr_3)_4Ni_4Fe_4S_6(NO)_4$ (Ether fraction) and 1711 cm^{-1} (Hexanes Fraction). Unfortunately we were unable to obtain a detailed structural description for the $(PPr_3)_4Ni_4Fe_4S_6(NO)_4$ cluster as the crystals were twin, and due to the poor quality of data a satisfactory solution could not be obtained. Nevertheless, the appearance of a Ni_4Fe_4 core were the nickel and iron atoms form two interpenetrating tetrahedra was observed with an overall structure resembling the $(PPr_3)_4Ni_4Fe_4S_6Cl_6$ cluster presented in Chapter 3.

As in the case of copper, the formation of the $(PPr_3)_4Ni_4Fe_4S_6(NO)_4$ cluster can be explained by the coupling of $(PR_3)NiS_2Fe(NO)$ units although the resulting product has a different symmetry than the copper analogue. Formation of $(PPr_3)_3Ni_3Fe_4S_6(NO)_4$ seems to be much more complex, it can be viewed either as the coupling of a $Fe_4S_3(NO)_4$ unit to a $(PPr_3)_3Ni_3S_3$ unit, or as a smaller Fe(NO) unit coupling three $(PR_3)NiS_2Fe(NO)$ units.

However, the formation of a $Fe_4S_3(NO)_4$ unit is not impossible as implied from the reactivity of $[Fe_6S_6(NO)_6]^{2-}$ with $Fe(H_2O)_6^{2+}/PPr_3$, as already discussed in Chapter 2, that forms exclusively $[Fe_8S_6(NO)_6]^{2-}$. The $[Fe_8S_6(NO)_6]^{2-}$ cluster, is also capable of dissociating in solution into smaller units, with $Fe_4S_3(NO)_4$ being the most probable.

In all the cases described herein, and the previous chapters, the underlying property of the Fe/S clusters, in terms of synthesis, that leads to the diversity of the products obtained under different conditions is their kinetic lability in solution. The M/Fe/S/NO clusters presented are not an exception. Another interesting feature is that, like the heterometallic Fe/S/Cl clusters presented in chapter 3, the M_4Fe_4 clusters obtained from the reactions with copper and nickel give the exact same isomers of D_{2h} and T_d respectively, despite the use of different starting materials and procedures. Although the synthesis of the $(PPr_3)_4M_4Fe_4S_6(NO)_6$ clusters has not been described in terms of Fe_4S_6 units, the formation of such a unit from $[Fe_6S_6(NO)_6]^{2-}$ by the loss of two FeNO units cannot be excluded. Therefore, the two M_4Fe_4 clusters could also be obtained through addition of {$M(PPr_3)$ units to a Fe_4S_6 unit as the "dimer of dimers" Fe_4S_6 core and, after rearrangement upon reduction, the "adamantane" Fe_4S_6 core can be obtained as shown in Figure 4.3.

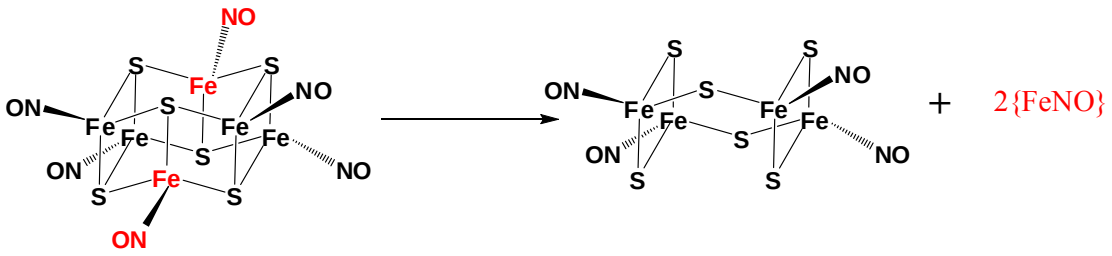

Figure 4.3. Schematic representation of the relation between the prismatic Fe_6S_6 core and the hypothetical "dimer of dimers" Fe_4S_6 core.

4.3.3. Structural Description.

Crystallographic determination the $(PPN)_2[(CO)_6Mo_2Fe_6S_6(NO)_6]$ cluster (Figure 4.4) reveals a M_8S_6 cuboctahedral core exhibiting average Mo-Fe and Fe-Fe distances at 2.89Å and 2.69Å respectively, while the Mo-S and Fe-S distances are found at 2.58Å and 2.25Å, respectively. As expected, the Mo_2Fe_6 cluster in comparison to $[Fe_8S_6(NO)_8]^{2-}$, is elongated along the three-fold axis that contains the Mo atoms with a cluster topology identical to the MoFe/S/Cl analogues $(Et_4N)_3[(CO)_6Mo_2Fe_6S_6Cl_6]$ and $(Et_4N)_4[(CO)_6Mo_2Fe_6S_6Cl_6]$ [19].

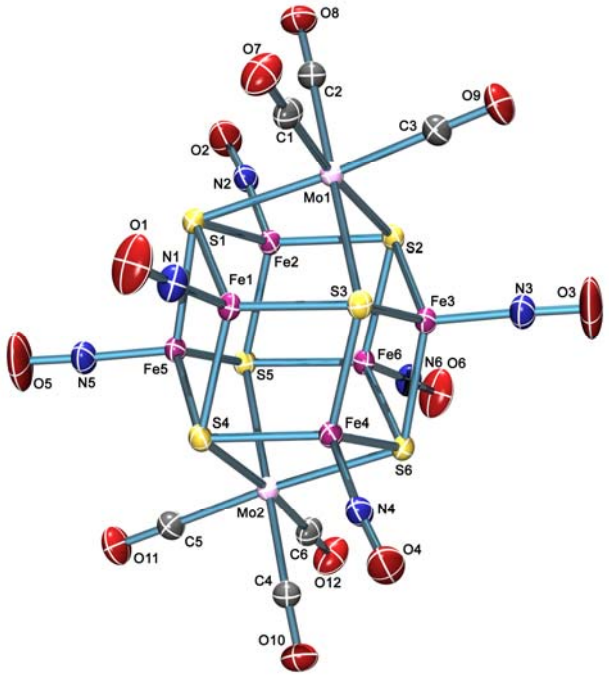

Figure 4.4. Ortep Diagram of $[(CO)_6Mo_2Fe_6S_6(NO)_6]^{2-}$ showing thermal ellipsoids with 50% probability.

Since the three $[(CO)_3Mo_2Fe_6S_6X_6]^{n-}$ clusters can be described as addition of $[Mo(CO)_3]^0$ units to $[Fe_6S_6(NO)_6]^{n-}$ units, the increase of charge will result in the increase of interatomic distances as the irons are more reduced (Table 4.7). The Mo-Fe distances increase from 2.893Å in $(PPN)_2[(CO)_6Mo_2Fe_6S_6(NO)_6]$ to 2.930Å in

$(Et_4N)_3[(CO)_6Mo_2Fe_6S_6Cl_6]$ and 3.005Å in the case of $(Et_4N)_4[(CO)_6Mo_2Fe_6S_6Cl_6]$. The respective Fe-Fe distances are at 2.672Å, 2.742Å and 2.761Å , the Mo-S distances at 2.580Å, 2.582Å, 2.619Å and the Fe-S distances at 2.247Å, 2.292Å and 2.353Å. In all four distances, there is an increase of approximately 0.1Å between $[(CO)_6Mo_2Fe_6S_6(NO)_6]^{2-}$ and $[(CO)_6Mo_2Fe_6S_6Cl_6]^{4-}$.

Both of the Cu/Fe/S/NO structures exhibit the typical cubic arrangement of metals capped by sulfur atoms and posses structures similar to their respective Cu/Fe/S/Cl analogues $(Bu_4N)_2[(PPr_3)_2Cu_2Fe_6S_6Cl_6]$ and $(PPr_3)_4Cu_4Fe_4S_6Cl_6$ [12]. In the case of $(PPr_3)_2Cu_2Fe_6S_6(NO)_6$ (Figure 4.5) the average Cu-Fe and Fe-Fe distances are 2.70Å and 2.65Å respectively, while the Cu-S and Fe-S bonds are found at 2.38Å and 2.24Å. for the $[(PPr_3)_2Cu_2Fe_6S_6Cl_6]^{2-}$ cluster that the core is reduced by two electrons, assuming NO^-, there is again an increase in metal-metal and metal sulfur distances of approximately 0.1Å with the exception of the Cu-S distance that remains practically unaltered as in $[(PPr_3)_2Cu_2Fe_6S_6Cl_6]^{2-}$ it is 2.385Å.

In $(PPr_3)_4Cu_4Fe_4S_6(NO)_4$ (Figure 4.6) the metals in the Cu_4Fe_4 core are arranged in D_{2h} geometry (mutually perpendicular Fe_4 and Cu_4 rectangles) with average metal-metal distances of 2.74Å and average Cu-S and Fe-S bond distances of 2.36Å and 2.26Å respectively. The $(PPr_3)_4Cu_4Fe_4S_6(NO)_4$ is structurally and electronically equivalent to $(PPr_3)_4Cu_4Fe_4S_6Cl_6$, as the charge of the core is the same and therefore the distances should be identical which applies for the Cu-Cu, Cu-Fe Cu-S and Fe-S distances as seen in Table 4.7. However, the Fe-Fe distance shows an increase of approximately 0.1Å between the two clusters. This unexpected difference could be attributed to the more covalent nature of the iron-nitrosyl bond that withdraws electron density from the metal which could be compensated by an increase of the Fe-Fe interaction.

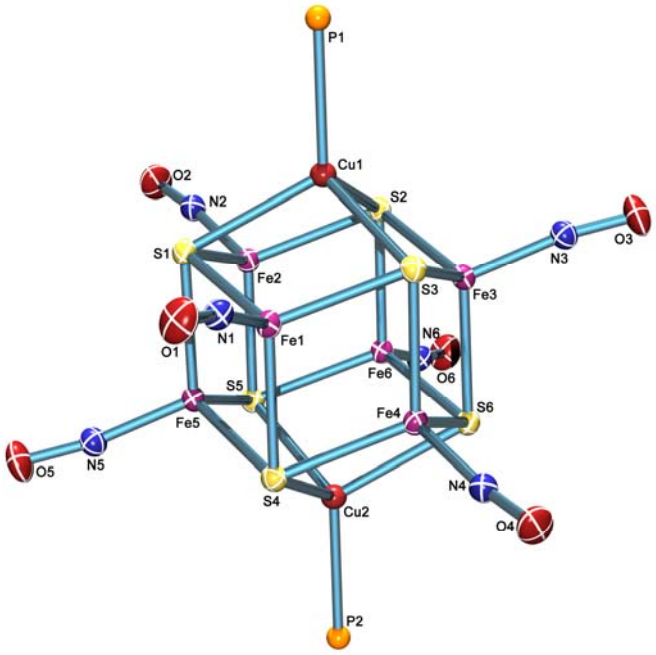

Figure 4.5. Ortep Diagram of $(PPr_3)_2Cu_2Fe_6S_6(NO)_6$ showing thermal ellipsoids with 50% probability. The carbons of the phosphines have been omitted for clarity.

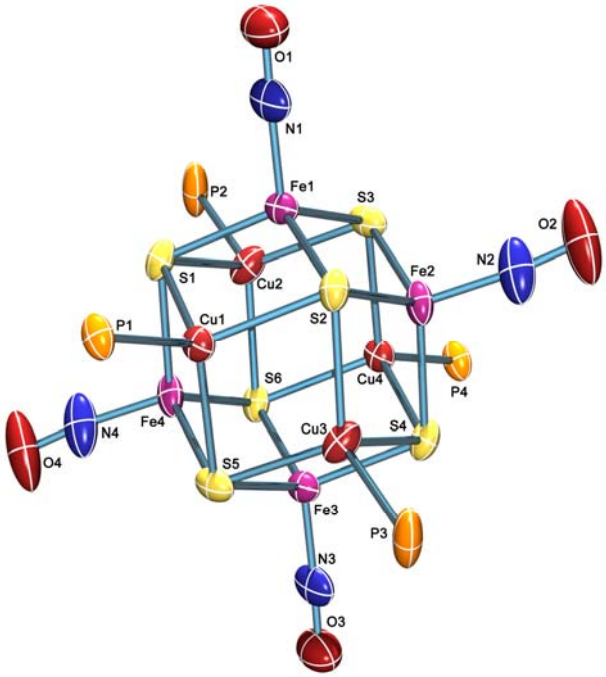

Figure 4.6. Ortep Diagram of $(PPr_3)_4Cu_4Fe_4S_6(NO)_4$ showing thermal ellipsoids with 50% probability. The carbons of the phosphines have been omitted for clarity.

The neutral $(PPr_3)_2Ni_2Fe_6S_6(NO)_6$ cluster (Figure 4.7) possesses the same geometry as its copper analogue, but with a slightly more compact core structure . The average Ni-S and Fe-S distances of 2.25Å and 2.26Å respectively, while Ni-Fe and Fe-Fe distances are 2.59Å and 2.65Å respectively. A similar core is also found in the halide analogues, $(Et_4N)_2[(PPr_3)_2Ni_2Fe_6S_6Cl_6]$[12] and $[PhCH_2NEt_3]_2[(Ph_2MeP)_2Ni_2Fe_6S_6I_6]$[13].

Comparing the $(PPr_3)_2Ni_2Fe_6S_6(NO)_6$ and $(PPr_3)_2Cu_2Fe_6S_6(NO)_6$ clusters the Ni-Fe and the Ni-S distances are shorter by approximately 0.1Å, in respect to the Cu-Fe and Cu-S distances, that can be attributed to the smaller ionic radius of nickel. In comparison to the halide analogue $[(PPr_3)_2Ni_2Fe_6S_6Cl_6]^{2-}$, the additional electrons on the core do not affect the distances significantly with only the Fe-Fe bond being elongated by 0.1Å.

The $(PPr_3)_3Ni_3Fe_4S_6(NO)_4$ cluster (Figure 4.8) can be viewed as a $Fe_4S_3(NO)_4$ unit coupled with a nearly trigonal planar $Ni_3S_3(PPr_3)_3$ unit. In this structure the iron atoms adopt a tetrahedral coordination geometry while the nickel atoms adopt a trigonal pyramidal geometry. The Fe-Fe distances in the equatorial triangle (defined by Fe1, Fe2 and Fe3) have a mean value of 3.82Å. These irons are located at 2.74 Å from the capping iron. The Ni-Fe and Ni-Ni distances are at found at 2.61 and 2.79Å, respectively, and the Fe-S and Ni-S distances are 2.23Å and 2.25Å, respectively.

The $(PPr_3)_3Ni_3Fe_4S_6(NO)_4$ structure shows a similar arrangement of metals with the $(PPr_3)_3Ni_3Fe_5S_6Cl_5$ cluster described in Chapter 3 were the capping iron atom between the three nickel atoms is the main difference. Structurally, the insertion of the additional iron results in an increase of distance in the trigonal plane of the nickel atoms. The explanation lies on the movement of the three sulfur atoms (S1,S2 and S3) that move closer in order to coordinate to the capping iron atom as evident by comparison of the corresponding distances and angles in Table 4.6

	Triangular distances in Å			Angles	
Compound	**Ni-Ni**	**Fe-Fe**	**S-S**	**Fe-S-Ni**	**S-Ni-S**
$(PPr_3)_3Ni_3Fe_4S_6(NO)_4$	2.790	3.823	4.087	104.47º	104.86º
$(PPr_3)_3Ni_3Fe_5S_6Cl_5$	3.614	3.839	3.655	113.35º	111.06º

Table 4.6. Comparison of the interatomic distances and angles between the $(PPr_3)_3Ni_3Fe_4S_6(NO)_4$ and $(PPr_3)_3Ni_3Fe_5S_6Cl_5$ clusters. The triangular distances are the Ni1-Ni2-Ni3, Fe1-Fe2-Fe3 and S1-S2-S3 while the angles noted are Fe4-S6-Ni1 and S1-Ni1-S6 as shown in figure 4.8.

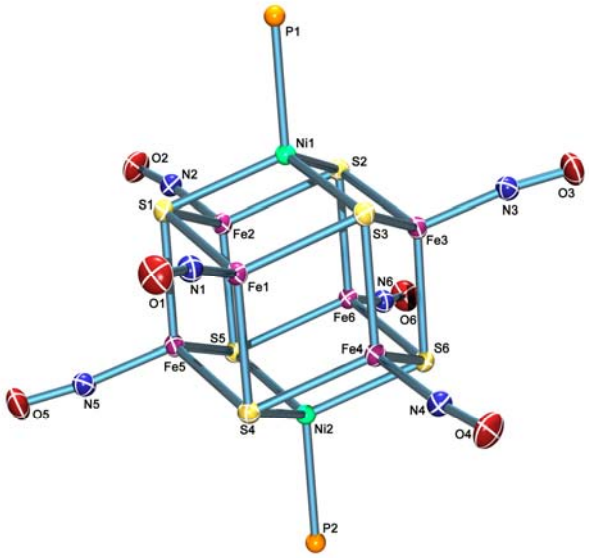

Figure 4.7. Ortep Diagram of $(PPr_3)_2Ni_2Fe_6S_6(NO)_6$ showing thermal ellipsoids with 50% probability. The carbons of the phosphines have been omitted for clarity.

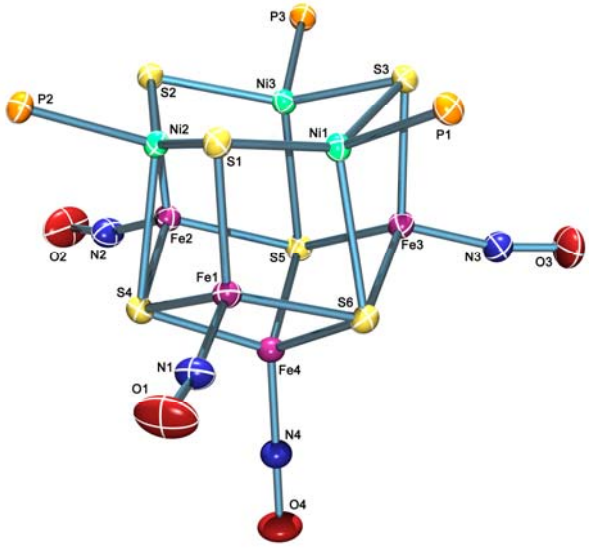

Figure 4.8. Ortep Diagram of $(PPr_3)_3Ni_3Fe_4S_6(NO)_4$ showing thermal ellipsoids with 50% probability. The carbons of the phosphines have been omitted for clarity.

Comparison of the M/Fe/S/NO clusters with the parent ion $[Fe_6S_6(NO)_6]^{2-}$ and the cuboidal $[Fe_8S_6(NO)_8]^{2-}$ ion (Table 4.7) does not reveal any significant changes in their overall structures. The only exception being the M_8 cuboidal volume that reflects the difference in the M-Fe distances, which are larger for the copper and molybdenum clusters and smaller for nickel in respect to the Fe-Fe distances.

	Average bond distance in Å				M_8	Fe-N-O
Compound	**Fe-Fe**	**Fe-S**	**Fe-N**	**N-O**	**Volume**	**angle**
$[Fe_6S_6(NO)_6]^{2-}$	2.651	2.220	1.669	1.181	-	175.3
$[Fe_8S_6(NO)_8]^{2-}$	2.659	2.265	1.674	1.181	18.800	177.1
$[(CO)_6Mo_2Fe_6S_6(NO)_6]^{2-}$	2.672	2.247	1.678	1.166	21.535	176.8
$(PPr_3)_2Cu_2Fe_6S_6(NO)_6$	2.647	2.240	1.676	1.171	19.098	171.0
$(PPr_3)_2Ni_2Fe_6S_6(NO)_6$	2.649	2.257	1.676	1.172	17.933	173.0
$(PPr_3)_4Cu_4Fe_4S_6(NO)_4$	2.710	2.264	1.709	1.137	20.593	176.0
$(PPr_3)_3Ni_3Fe_4S_6(NO)_4$	2.744	2.223	1.668	1.184	-	168.0

Table 4.7. Comparative table of selected distances between the Fe/S/NO and M/Fe/S/NO complexes

As shown in Table 4.8 the M/Fe/S (M=Mo,Cu,Ni) clusters reported in this chapter have shorter metal-metal and iron-sulfur distances with a more compact overall structure than their corresponding analogues with halogens. An exception is the $(PPr_3)_3Ni_3Fe_4S_6(NO)_4$ cluster which has similar size to the structurally related $[Fe_7S_6]$ and $[Co_7S_6]$ clusters. In the M_7S_6 clusters the "uncapped" M_3S_3 unit shows a triangular M_3 array with distances of nearly 1Å shorter than the distances found in the hexagonal faces of the M_6S_6 prismanes. The data are consistent with the expected π back bonding from the Fe atoms into the NO π^* orbital, which in turn, results in electron deficient Fe atoms, significant M-Fe and Fe-Fe bonding and Fe-S multiple bonding.

Distance (Å)	$[(CO)_6Mo_2Fe_6S_6(NO)_6]^{2-}$	$[(CO)_6Mo_2Fe_6S_6Cl_6]^{3-}$	$[(CO)_6Mo_2Fe_6S_6Cl_6]^{4-}$
Mo-Fe	2.893	2.930	3.005
Fe-Fe	2.672	2.742	2.761
M_8 Volume	21.535	22.810	23.983
Mo-S	2.580	2.582	2.619
Fe-S	2.247	2.292	2.353
	$(PPr_3)_2Cu_2Fe_6S_6(NO)_6$		$[(PEt_3)_2Cu_2Fe_6S_6Cl_6]^{2-}$
Cu-Fe	2.699		2.784
Fe-Fe	2.647		2.772
M_8 Volume	19.098		21.435
Cu-S	2.381		2.385
Fe-S	2.240		2.310
	$(PPr_3)_4Cu_4Fe_4S_6(NO)_4$		$(PPr_3)_4Cu_4Fe_4S_6Cl_6$
Cu-Cu	3.374		3.379
Cu-Fe	2.747		2.787
Fe-Fe	3.239		3.321
M_8 Volume	20.593		21.431
Cu-S	2.363		2.366
Fe-S	2.264		2.269
	$(PPr_3)_2Ni_2Fe_6S_6(NO)_6$	$(PPr_3)_2Ni_2Fe_6S_6Cl_6^{2-}$	$(Ph_2MeP)_2Ni_2Fe_6S_6I_6^{2-}$
Ni-Fe	2.586	2.615	2.645
Fe-Fe	2.649	2.752	2.719
M_8 Volume	17.933	19.328	19.281
Ni-S	2.250	2.255	2.261
Fe-S	2.257	2.296	2.289
	$(PPr_3)_3Ni_3Fe_4S_6(NO)_4$	$(PEt_3)_4Fe_7S_6Cl_3$	$(PPh_3)_4Co_7S_6Br_3$
Ni-Ni[a]	2.790	2.746	2.883
Ni-Fe	2.618	2.624	2.590
$Fe\text{-}Fe_{(planar)}$[b]	3.823	4.148	3.955
$Fe\text{-}Fe_{(capping)}$	2.744	2.584	2.607
$Ni\text{-}S_{(equatorial)}$	2.144	2.179	2.139
$Ni\text{-}S_{(axial)}$	2.470	2.231	2.197
$Fe\text{-}S_{(capping)}$	2.223	2.193	2.168
$Fe\text{-}S_{(equatorial)}$	2.242	2.363	2.254
$Fe\text{-}S_{(axial)}$	2.204	2.276	2.184

Table 4.8.Comparison of selected bond distances between different M/Fe/S clusters. The volume of the Metal formed cuboidal unit has been calculated approximating it as a cube, using average metal-metal distances.

a) The distances of interest are denoted as shown in figure 4.8 using the equivalent metal positions for Fe_7S_6 and Co_7S_6 since in the case of $Ni_3Fe_4S_6$ they are more easily defined and recognized.

b) The Fe-Fe (planar) distance is the trigonal plane defined by Fe1-Fe2-Fe3, and the Fe-Fe (capping) is the distance of Fe4 to the trigonal Fe plane. Fe-S (capping) is the Fe4-S3 distance, Fe-S (equatorial) is the Fe3-S3 distance and Fe-S (axial) is the Fe3-S4 distance

4.3.4. Spectroscopic Characterization

As already discussed in Chapter 2, in the metal nitrosyl complexes it is difficult to determine precisely the oxidation states for the metal atoms since the NO ligand could be described as NO^+, NO or NO^-. Based on the characteristics of the clusters described in chapter 2 the most appropriate description that explains both the reactivity and the spectroscopic data appears to be NO^-, although the use of the Enemark-Feltham notation is adequate to describe the reactivity of the clusters formed as they all contain tetrahedrally coordinated $\{FeNO\}^n$ (n=7 or 8) units.

Compound	Formal oxidation	Average Fe oxidation
$[Fe_8S_6(NO)_8]^{2-}$	6Fe(II), 2Fe(III)	2.25
$[Fe_6S_6(NO)_6]^{2-}$	2Fe(II), 4Fe(III)	2.67
$[(CO)_6Mo_2Fe_6S_6(NO)_6]^{2-}$	2Mo(0), 2Fe(II), 4Fe(III)	2.67
$(PPr_3)_2Cu_2Fe_6S_6(NO)_6$	2Cu(I), 2Fe(II), 4Fe(III)	2.67
$(PPr_3)Ni_2Fe_6S_6(NO)_6$	2Ni(II), 4Fe(II), 2Fe(III)	2.33
$(PPr_3)_4Cu_4Fe_4S_6(NO)_4$	4Cu(I), 4Fe(III)	3
$(PPr_3)_4Ni_3Fe_4S_6(NO)_4$	3Ni(II), 2Fe(II), 2Fe(III)	2.5
$(PPr_3)_4Ni_4Fe_4S_6(NO)_4$	4Ni(II), 4Fe(II)	2

Table 4.9. Formal oxidation states of the metals assuming NO^- for the M/Fe/S/NO clusters.

Mössbauer spectra for clusters $[(CO)_6Mo_2Fe_6S_6(NO)_6]^{2-}$, $(PPr_3)_2Cu_2Fe_6S_6(NO)_6$ and $(PPr_3)Ni_2Fe_6S_6(NO)_6$ exhibit a single doublet, which is consistent with delocalized charge on the irons with isomer shifts and quadrupole splittings shown in Table 4.9. In all three $M_2Fe_6S_6$ clusters the isomer shifts lie between those of $[Fe_8S_6(NO)_8]^{2-}$ and $[Fe_6S_6(NO)_6]^{2-}$

suggesting that the oxidation states of the irons are between these two compounds, or between $Fe^{+2.25}$ and $Fe^{+2.67}$ assuming NO^-. This in turn, suggests that the initial Cu(I) and Mo(0) metal atoms are more oxidized and closer to Cu(II) and Mo(I) respectively while Ni(II) might be an adequate description since in this case the oxidation state of the irons in $(PPr_3)Ni_2Fe_6S_6(NO)_6$ will be $Fe^{+2.33}$.

	78K		250K		5K	300K
Compound	**δ (mm·s^{-1})**	**ΔE_Q**	**δ (mm·s^{-1})**	**ΔE_Q**	**μ_{eff}**	**μ_{eff}**
$[Fe_8S_6(NO)_8]^{2-}$ [a]	0.37	0.24	0.29	0.22	1.47	5.86
$[Fe_6S_6(NO)_6]^{2-}$ [a]	0.26	0.32	0.18	0.30	2.01	5.86
$[Fe_6S_6Cl_6]^{3-}$ [b]	0.48	0.73	-	-	-	-
$[(CO)_6Mo_2Fe_6S_6(NO)_6]^{2-}$	0.34	0.21	0.29	0.22	0.81	1.84
$[(CO)_6Mo_2Fe_6S_6Cl_6]^{3-}$ [b]	0.58	1.1	-	-	-	-
$[(CO)_6Mo_2Fe_6S_6Cl_6]^{4-}$ [b]	0.63	1.0	-	-	-	-
$(PPr_3)_2Cu_2Fe_6S_6(NO)_6$	0.31	0.42	0.24	0.42	0.37	2.78
$[(PPr_3)_2Cu_2Fe_6S_6Cl_6]^{2-}$ [c]	-	-	0.34	0.39	0.49	3.89
$(PPr_3)_2Ni_2Fe_6S_6(NO)_6$	0.32	0.34	0.25	0.34	0.66	3.54
$[(PPr_3)_2Ni_2Fe_6S_6Cl_6]^{2-}$ [c]	-	-	0.36	0.68	diam.	diam.
$(PPr_3)_4Cu_4Fe_4S_6(NO)_4$	0.24	0.74	-	-	1.87	7.82
$(PPr_3)_4Cu_4Fe_4S_6Cl_4$ [c]	-	-	0.34	0.64	diam.	diam.
$(PPr_3)_4Ni_4Fe_4S_6(NO)_4$	0.36	0.19	0.29	0.16	2.00	5.15
$(PPr_3)_4Ni_4Fe_4S_6Cl_4$ [c]	-	-	0.40	0.70	2.76	4.61
$(PPr_3)_4Ni_3Fe_4S_6(NO)_4$	0.19	0.82	0.15	0.78	1.09	7.01
	0.49	0.55	0.41	0.64		
$[Fe_4S_3(NO)_7]^{-}$ [d]	0.15	0.96	-	-	-	-
	0.16	0.73				

Table 4.10. Mössbauer and magnetic parameters for the M/Fe/S/NO clusters presented herein and comparison with the equivalent Mössbauer data M/Fe/S/Cl clusters.

[a] As reported in chapter 2

[b] Taken from Reference [19]

[c] As reported in chapter 3

[d] Taken from Reference [24]

A similar behavior is also evident in the case of M/Fe/S/Cl clusters presented in Chapter 3 and also in the $[(CO)_6Mo_2Fe_6S_6Cl_6]^{n-}$ (n= 3 and 4) clusters [19] that also exhibit a similar delocalization of charges and partial electron transfer from the heterometals to the iron atoms. As mentioned in Chapter 2, the presence of nitrosyl ligands might affect the observed isomer shifts by decreasing the observed values making correlations between M/Fe/S/Cl and M/Fe/S/NO clusters difficult. However, some correlations can be made. The $[(CO)_6Mo_2Fe_6S_6Cl_6]^{n-}$ (n= 3 and 4) clusters exhibit isomer shifts at 80K of 0.58 $mm \cdot s^{-1}$ and 0.63 $mm \cdot s^{-1}$ respectively, while the irons are described as $Fe^{+2.5}$ and $Fe^{+2.33}$ with the isomer shift decreasing by 0.05 $mm \cdot s^{-1}$ as the charge lowers by one electron. By comparison to $[Fe_6S_6Cl_6]^{3-}$ (δ=0.46 $mm \cdot s^{-1}$, ΔE_Q=0.73 $mm \cdot s^{-1}$, 80K), the increase of 0.1 $mm \cdot s^{-1}$ in isomer shift of $[(CO)_6Mo_2Fe_6S_6Cl_6]^{3-}$ suggests partial oxidation of Mo(0) to Mo(I). Comparing the $[Fe_6S_6(NO)_6]^{2-}$ and $[(CO)_6Mo_2Fe_6S_6(NO)_6]^{2-}$ clusters, the increase is 0.08 $mm \cdot s^{-1}$, therefore in similar levels suggesting that the charge transfer from molybdenum to the irons is at a similar extent. $[(CO)_6Mo_2Fe_6S_6(NO)_6]^{2-}$ and $[(CO)_6Mo_2Fe_6S_6Cl_6]^{3-}$ have an isomer shift difference of 0.2 $mm \cdot s^{-1}$ which is primarily attributed to the difference between NO^- and Cl^- since the difference between the (hypothetical) $[(CO)_6Mo_2Fe_6S_6Cl_6]^{2-}$ and the $[(CO)_6Mo_2Fe_6S_6Cl_6]^{3-}$ cluster would be 0.05 $mm \cdot s^{-1}$, making the shift between NO^- and Cl^- being approximately 0.15 $mm \cdot s^{-1}$. It should be noted however that changing the ligands, the relationships between isomer shifts change as well. For example in the $[(CO)_6Mo_2Fe_6S_6Br_6]^{n-}$ (n= 3 and 4) series the difference in isomer shift is only 0.02 $mm \cdot s^{-1}$ opposed to 0.05 $mm \cdot s^{-1}$ for the chloride analogues, suggesting that the 0.15 $mm \cdot s^{-1}$ shift between NO^- and Cl^- calculated for the Mo/Fe clusters cannot be used directly for the cases of Cu/Fe and Ni/Fe clusters. The

general trend however of isomer shifts is similar in both nitrosyl and halide analogues with Mo_2Fe_6>Ni_2Fe_6>Cu_2Fe_6.

For the $(PPr_3)_4Cu_4Fe_4S_6(NO)_4$ and $(PPr_3)_4Ni_4Fe_4S_6(NO)_4$ clusters, the isomer shifts are 0.24 $mm{\cdot}s^{-1}$ and 0.36 $mm{\cdot}s^{-1}$ respectively. These values are in agreement with the assignment of completely delocalized systems as in the case of $M_2Fe_6S_6$ clusters. The more oxidized nature of $(PPr_3)_4Cu_4Fe_4S_6(NO)_4$ is expected since the localized assignment (Table 4.9) gives all ferric irons, while for $(PPr_3)_4Ni_4Fe_4S_6(NO)_4$, the localized assignment is all ferrous system. Again, both systems are closer to an average $Fe^{+2.5}$ oxidations which means that the Cu(I) atoms are partially oxidized to Cu(II) in $(PPr_3)_4Cu_4Fe_4S_6(NO)_4$ and the Ni(II) atoms are partially reduced to Ni(I) in $(PPr_3)_4Ni_4Fe_4S_6(NO)_4$. For the $(PPr_3)_3Ni_3Fe_4S_6(NO)_4$ cluster, the Mössbauer spectra reveals a more complex case, that fits a system with two different types of iron in a 3 to 1 ratio with isomer shift values at 0.19 $mm{\cdot}s^{-1}$ and 0.49 $mm{\cdot}s^{-1}$ respectively. The deviation of $(PPr_3)_3Ni_3Fe_4S_6(NO)_4$ from the completely delocalized systems in all the other M/Fe/S/NO clusters can be explained in terms of the coordination environment that is not identical for all the irons. The cluster can be viewed as a Fe_4S_3 fragment coupled to a triangular Ni_3S_3 fragment with one apical and three basal iron atoms. A similar trend is evident for the $[Fe_4S_3(NO)_7]^-$ that previous studies [24, 25] distinguished between the apical and the three basal iron atoms with again a 3 to 1 ratio as seen in Table 4.10. However, for $[Fe_4S_3(NO)_7]^-$ the cluster is described better as a 4Fe(III) system and therefore the isomer shift values for the two iron types differs only by 0.01 $mm{\cdot}s^{-1}$. In the case of $(PPr_3)_3Ni_3Fe_4S_6(NO)_4$ the isomer shifts suggest that the three basal irons are better described as ferric irons, while the apical iron has a more ferrous character.

The magnetic susceptibility measurements reveal strong antiferromagnetic coupling for all the M/Fe/S/NO clusters with the values presented in Table 4.9 and illustrated in Figures 4.9 and 4.10 for M_2Fe_6 and M_4Fe_4 clusters respectively. Furthermore, it is interesting to note the strong paramagnetic character of $(PPr_3)_4Cu_4Fe_4S_6(NO)_4$ compared to the diamagnetic character of $(PPr_3)_4Cu_4Fe_4S_6Cl_4$ cluster that is structurally similar and share the same number of metal valence electrons ($112e^-$). This can be attributed to the presence of NO^- that, unlike Cl^-, contains two unpaired electrons in the π^* orbitals for which antiferromagnetic coupling might not be as effective as the coupling of the metals in this case. The value of 7.82 BM at 300K for the $(PPr_3)_4Cu_4Fe_4S_6(NO)_4$ cluster is close to the value for seven unpaired electrons, while the maximum number of unpaired electrons that NO^- can contribute in this case is eight. This feature however, is not observed comparing $(PPr_3)_4Ni_4Fe_4S_6(NO)_4$ to $(PPr_3)_4Ni_4Fe_4S_6Cl_4$ that again share the same number of metal valence electrons ($108e^-$) and are structurally similar, since the magnetic susceptibility measurements provide almost identical results, which could infer that the unpaired electrons of NO^- are effectively cancelled.

In the case of $(PPr_3)Ni_2Fe_6S_6(NO)_6$ and $[(PPr_3)_2Ni_2Fe_6S_6Cl_6]^{2-}$ there is a formal 2 electron difference between the clusters, that alone could account for the paramagnetic nature of the $(PPr_3)Ni_2Fe_6S_6(NO)_6$. $[(PPr_3)_2Ni_2Fe_6S_6Cl_6]^{2-}$ and $(PPr_3)Cu_2Fe_6S_6(NO)_6$ share the same geometry and metal valence electrons ($104e^-$) however the former is paramagnetic, which can be attributed to some extent on the presence of NO^- ligands, although the magnetic measurements of $(PPr_3)Cu_2Fe_6S_6(NO)_6$ and $[(PPr_3)_2Cu_2Fe_6S_6Cl_6]^{2-}$ are almost identical.

Further investigation on the magnetic properties of these clusters would require the calculation of the molecular orbital diagrams. It has been already discussed in chapter 3

that the MO diagrams of $M_8(\mu_4\text{-}E)_6L_4Cl_4$ T_d clusters [26] could provide some information about the M_8S_6 clusters, however, the presence of different geometries, different ligands and in the case of $[(CO)_6Mo_2Fe_6S_6(NO)_6]^{2-}$ different total number of ligands, will affect significantly the MO diagram. Also as mentioned previously the presence of NO ligands that contain unpaired electrons will increase the complexity to an even higher extent making any further discussion unrealistic.

EPR measurements on all the clusters were performed as well and with the exception of $(PPr_3)_3Ni_3Fe_4S_6(NO)_4$ all species were EPR silent. This is in line with antiferromagnetic coupling in the ground state for all the M/Fe/S/NO species.

The EPR spectra of the $(PPr_3)_3Ni_3Fe_4S_6(NO)_4$ cluster taken at 100K exhibits a rhombic signal g values g_x=1.98, g_y=2.00 and g_z= 2.02 as seen in Figure 4.11.

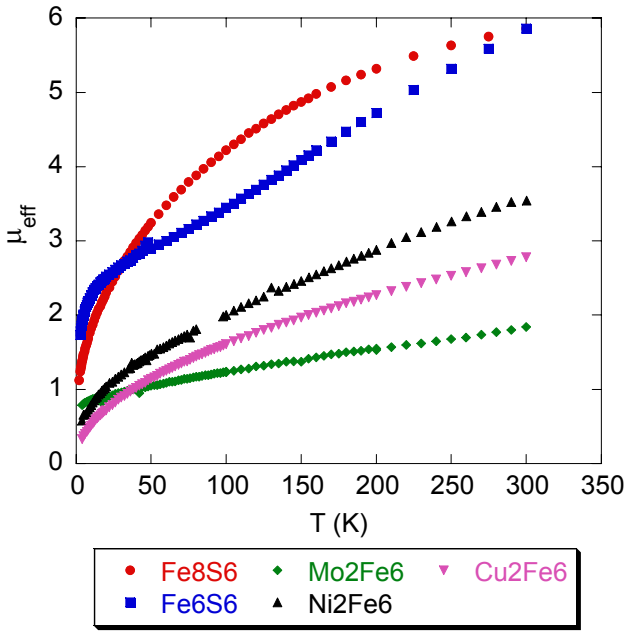

Figure 4.9. Temperature dependence of the effective magnetic moment for the $M_2Fe_6S_6(NO)_6$ (M= Mo, Ni and Cu) clusters. The $[Fe_6S_6(NO)_6]^{2-}$ and $[Fe_8S_6(NO)_8]^{2-}$ clusters are presented for comparison.

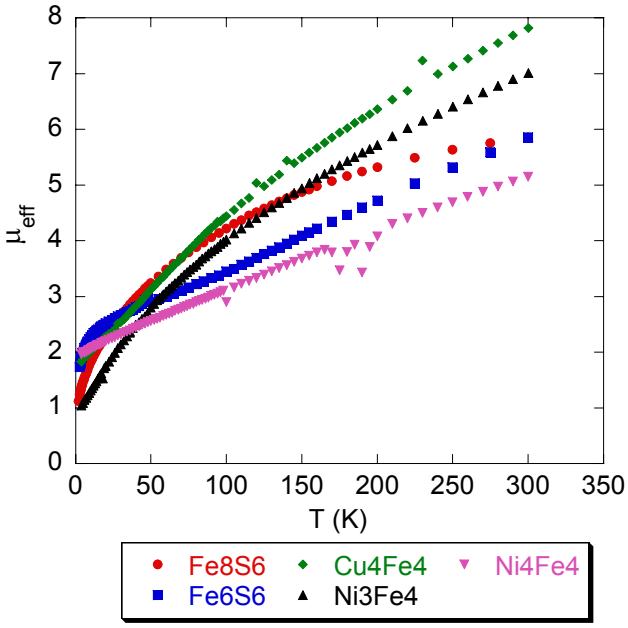

Figure 4.10. Temperature dependence of the effective magnetic moment for the $(PPr_3)_4M_4Fe_4S_6(NO)_4$ (M= Ni and Cu) and $(PPr_3)_3Ni_3Fe_4S_6(NO)_4$ clusters. The $[Fe_6S_6(NO)_6]^{2-}$ and $[Fe_8S_6(NO)_8]^{2-}$ clusters are presented for comparison.

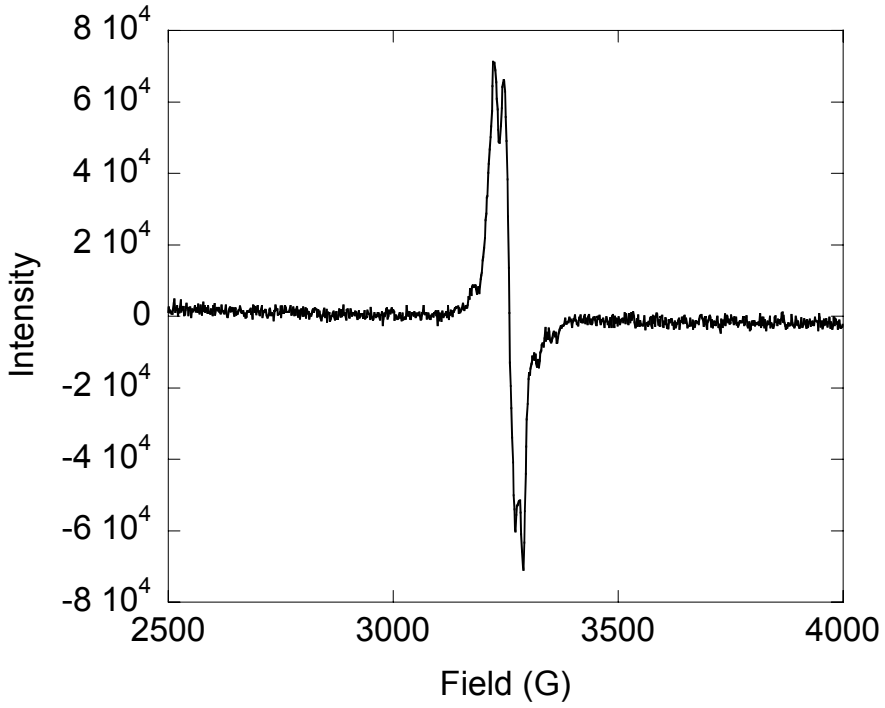

Figure 4.11. X-Band EPR spectrum obtained of a THF solution of $(PPr_3)_3Ni_3Fe_4S_6(NO)_4$.

4.3.5. Electrochemical studies.

Electrochemical studies of the clusters reported here, show mainly reversible, multi-electron reductions (Table 4.9).

Compound	0/-1 couple			-1/-2 couple			-2/-3 couple			-3/-4 couple		
	$E_{1/2}$	ΔE	i_{pr}/i_{pf}	$E_{1/2}$	ΔE	i_{pr}/i_{pf}	$E_{1/2}$	ΔE	i_{pr}/i_{pf}	$E_{1/2}$	ΔE	i_{pr}/i_{pf}
$(PPr_3)_2Cu_2Fe_6S_6(NO)_6$	-169	152	0.84	-1035	148	0.99	-1667	152	1.02			
$[(PEt_3)_2Cu_2Fe_6S_6Cl_6]^{2-}$							-228	26		-555	120	
$(PPr_3)_4Cu_4Fe_4S_4(NO)_4$	-153	172	0.39	-1021	156	0.57	-1537	116	0.73	-2065		irr
$(PPr_3)_4Cu_4Fe_4S_4(NO)_4$	-17	124		-635	130							
$(PPr_3)_2Ni_2Fe_6S_6(NO)_6$	+140	168	1.10	-717	156	0.61	-1431	334	0.71			
$[(PPr_3)_2Ni_2Fe_6S_6(NO)_6]^{2-}$							-585	156				
$[(CO)_6Mo_2Fe_6S_6(NO)_6]^{2-}$							-641	192	070	-1247	176	0.68
$[(CO)_6Mo_2Fe_6S_6Cl_6]^{3-}$										+50	92	1.00

Table 4.11. Reduction potentials of the three $M_2Fe_6S_6(NO)_6$ (M=Cu, Ni, Mo) clusters and $(PPr_3)_4Cu_4Fe_4S_6(NO)_4$ with comparison with their Fe/S/Cl equivalents. All reductions are reversible unless denoted otherwise.

The $(PPr_3)_2Cu_2Fe_6S_6(NO)_6$ cluster shows three reversible reduction waves (Figure 4.11) at -169mV, -1035mV, -1667mV. Following a cyclic scan from 1.8 V to -2V, the voltammogram shows the appearance of two additional irreversible reduction waves at about 0mV and -633mV respectively, which suggest that the small peak that appears in that region in the 0 to -2.0V scan is due to partial oxidation of the cluster during the experiment rather than to the presence of an impurity. The cluster is stable upon oxidation to potentials up to +1.0V but further oxidation results in the appearance of these two irreversible peaks.

In the case of $(PPr_3)_4Cu_4Fe_4S_6(NO)_4$, although the voltammogram appears to be very similar to $(PPr_3)_2Cu_2Fe_6S_6(NO)_6$ as the first two reductions coincide, (Figure 4.12) at potentials above -1.5V there are different peaks with an irreversible reduction appearing at approximately -2V. In addition when two consecutive full scans from -2V to 1.8V are

performed, there is no appearance of the peak at -0.6V indicating that it is not a mixture of two species.

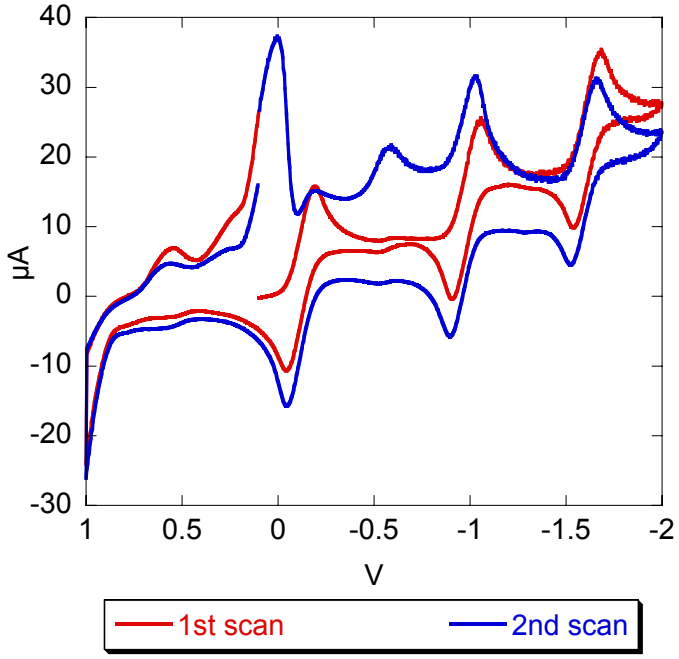

Figure 4.12. Cyclic voltammogram of $(PPr_3)_2Cu_2Fe_6S_6(NO)_6$ performing two consecutive scans from +1.8V to -2V. The irreversible oxidation below 1V that reaches -200µA is not shown for clarity.

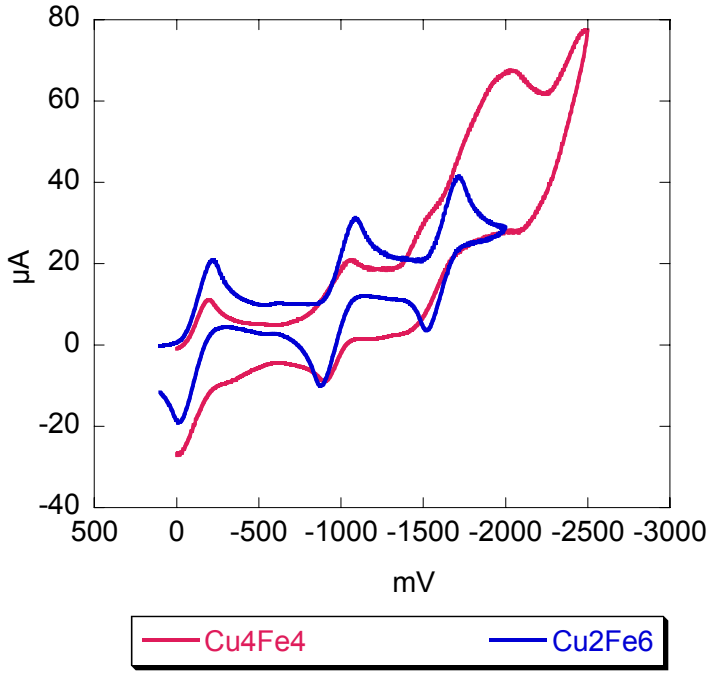

Figure 4.13. Cyclic Voltammogram of $(PPr_3)_4Cu_4Fe_4S_6(NO)_6$ from 0 to -2.5V in comparison with $(PPr_3)_2Cu_2Fe_6S_6(NO)_6$

For the $(PPr_3)_2Ni_2Fe_6S_6(NO)_6$ cluster the cyclic voltammogram (Figure 4.13) shows three reversible waves at +140 mV, -717 mV and -1431mV and overall the voltammogram of $(PPr_3)_2Ni_2Fe_6S_6(NO)_6$ is very similar to that of $(PPr_3)_2Cu_2Fe_6S_6(NO)_6$ shifted by approx 0.2V towards more positive potentials. Again after a full range scan (Figure 4.14) there is an emergence of two new irreversible waves at -0.2V and -1.3Vwhich is also evident in the initial scan but with smaller intensity suggesting that part of the sample had been oxidized during the experimental process. Again, the cluster is stable in the range of +1V to -2V as the copper analogue.

Cyclic voltammograms for the $(PPr_3)_3Ni_3Fe_4S_6(NO)_4$ and $(PPr_3)_4Ni_4Fe_4S_6(NO)_4$ clusters were not conclusive as both appear to have very complex consecutive reduction waves but contaminations from other byproducts cannot be excluded in order to present reliable electrochemical data for these two clusters.

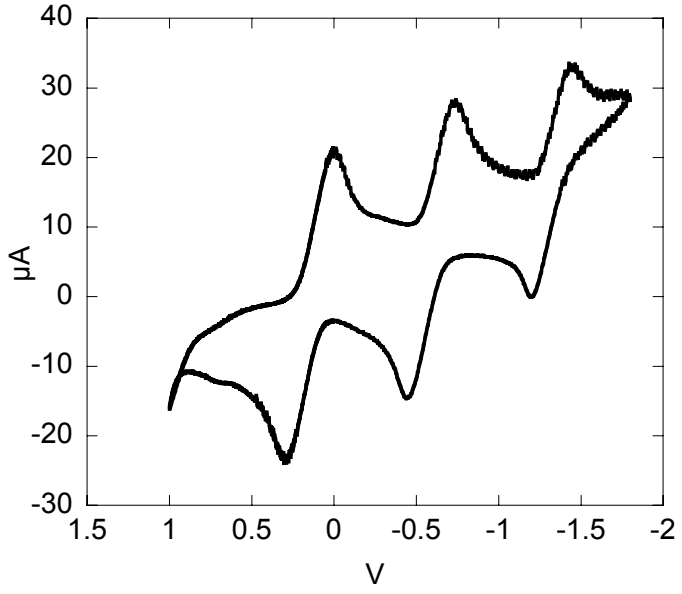

Figure 4.14. Cyclic Voltammogram of $(PPr_3)_2Ni_2Fe_6(NO)_6$ from 1V to -1.8V.

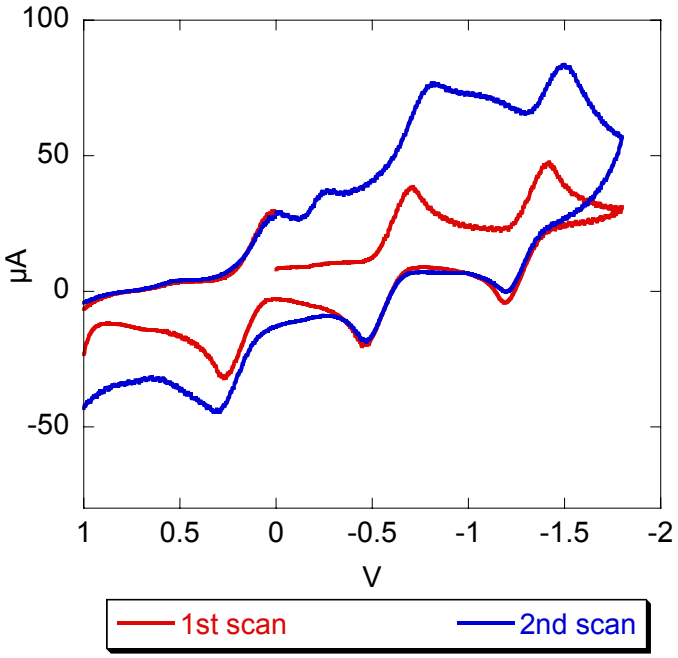

Figure 4.15. Cyclic voltammogram of $(PPr_3)_2Ni_2Fe_6S_6(NO)_6$ performing two consecutive scans from +1.8V to -1.8V. The irreversible oxidation below 1V that reaches -180μA is not shown for clarity.

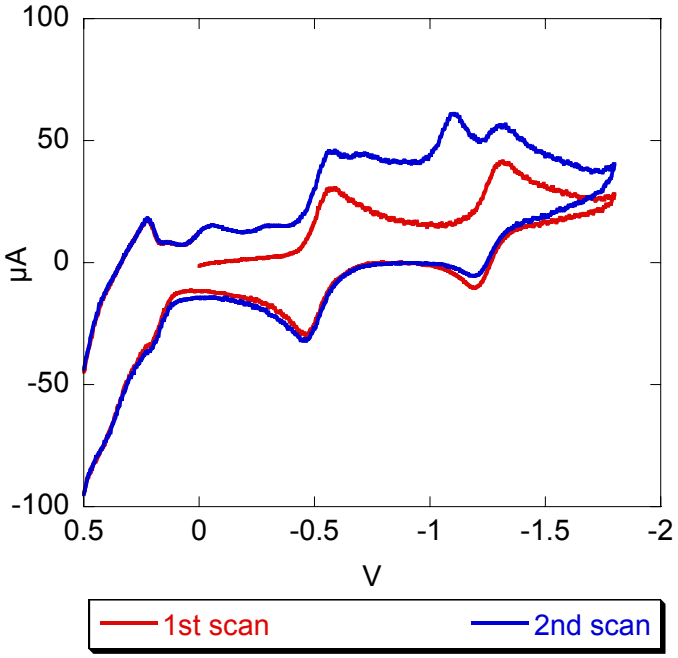

Figure 4.16. Cyclic voltammogram of $(PPN)_2[(CO)_6Mo_2Fe_6S_6(NO)_6]$ performing two consecutive scans from +1.5V to -1.8V. The irreversible oxidation below 1V that reaches -250μA is not shown for clarity.

For $(PPN)_2[(CO)_6Mo_2Fe_6S_6(NO)_6]$ (Figure 4.15) there are two reduction waves observed at -641mV and -1247mV that appear to be stable up to 0.5V. As in the cases of copper and nickel further oxidation to 1V causes the appearance of additional peaks. As evident from the positive potentials $(PPN)_2[(CO)_6Mo_2Fe_6S_6(NO)_6]$ retains its integrity only up to 0.5V unlike copper and nickel analogues that are stable up to 1V.

As shown in table 4.9, by comparison to the corresponding M/Fe/S/Cl species and equivalent couples, the clusters presented herein are more difficult to reduce which is reasonable given that these clusters appear to be more electron rich than their corresponding halogen analogues due to the more covalent nature of the Fe-NO bond that eventually disturbs the ability of the metals to accept additional electrons. However these species appear to be considerably more stable, as implied by the reversibility of the reductions, in a wider range of potentials as opposed to the M/Fe/S/Cl analogues that the reversibility window is limited to ranges of 0 to -1V.

In addition, the reversibility of the reductions of these pentlandite like clusters suggests that various reduced clusters may be obtainable. However, the isolation of such species must await further studies.

4.4. Conclusions

The clusters presented in this chapter can be described as a link between the chemistry of the Fe/S/NO clusters presented in chapter 2 and the M/Fe/S/Cl clusters presented in chapter 3.

Structurally, the M/Fe/S/NO clusters are almost identical to their M/Fe/S/Cl analogues, suggesting that similar pathways of formation are followed. However, the electronic properties of the M/Fe/S/NO clusters differ from those of their M/Fe/S/Cl analogues, with generally higher magnetic susceptibilities and a wider range of electrochemical stability. Future goals can include theoretical studies in order to gain more insight in the electronic properties of these clusters, expansion of this family of clusters with additional heterometals such as cobalt, silver, cadmium or platinum, that would lead to possibly different structures and properties, and also using these clusters as building blocks with suitable bridging ligands in order to obtain extended networks.

The higher stability of the M/Fe/S/NO clusters compared to the M/Fe/S/Cl clusters make these compounds better candidates as building blocks for extended networks that would be capable of multi-electron catalysis.

4.5 References

[1] P.V. Rao, R.H. Holm, Chem. Rev. 104 (2004) 527.
[2] H. Ogino, S. Inomata, H. Tobita, Chem. Rev. 98 (1998) 2093.
[3] C.T.W. Chu, L.F. Dahl, Inorg. Chem. 16 (1977) 3245.
[4] J. Zhou, Z.G. Hu, E. Munck, R.H. Holm, J. Am. Chem. Soc. 118 (1996) 1966.
[5] M.G. Kanatzidis, W.R. Hagen, W.R. Dunham, R.K. Lester, D. Coucouvanis, J. Am. Chem. Soc. 107 (1985) 953.
[6] D. Coucouvanis, M.G. Kanatzidis, W.R. Dunham, W.R. Hagen, J. Am. Chem. Soc. 106 (1984) 7998.
[7] M.J. Scott, R.H. Holm, Angew. Chem., Int. Ed. Engl. 32 (1993) 564.
[8] F. Calderoni, F. Demartin, M.C. Iapalucci, F. Laschi, G. Longoni, P. Zanello, Inorg. Chem. 35 (1996) 898.
[9] C. Goh, B.M. Segal, J.S. Huang, J.R. Long, R.H. Holm, J. Am. Chem. Soc. 118 (1996) 11844.
[10] Y. Ohki, Y. Ikagawa, K. Tatsumi, J. Am. Chem. Soc. 129 (2007) 10457.
[11] K.C. Misra, M.E. Fleet, Economic Geology 68 (1973) 518.
[12] M. Koutmos, H. Kalyvas, Y. Sanakis, A. Simopoulos, D. Coucouvanis, J. Am. Chem. Soc. 127 (2005) 3706.
[13] C. Junghans, W. Saak, S. Pohl, J. Chem. Soc., Chem. Commun. (1994) 2327.
[14] D. Fenske, H. Krautscheid, M. Muller, Angew. Chem., Int. Ed. Engl. 31 (1992) 321.
[15] D. Fenske, J. Hachgenei, J. Ohmer, Angew. Chem., Int. Ed. Engl. 24 (1985) 706.
[16] D. Fenske, J. Ohmer, J. Hachgenei, K. Merzweiler, Angewandte Chemie-International Edition in English 27 (1988) 1277.
[17] M.D. Curtis, M.S. Hay, Inorg. Synth. 28 (1990) 150.
[18] R.A. Heintz, J.A. Smith, P.S. Szalay, A. Weisgerber, K.R. Dunbar, Inorg. Synth. 33 (2002) 75.
[19] D. Coucouvanis, A. Salifoglou, M.G. Kanatzidis, W.R. Dunham, A. Simopoulos, A. Kostikas, Inorg. Chem. 27 (1988) 4066.
[20] S. Pohl, W. Saak, Angew. Chem., Int. Ed. Engl. 23 (1984) 907.
[21] I. Noda, B.S. Snyder, R.H. Holm, Inorg. Chem. 25 (1986) 3851.
[22] F. Cecconi, C.A. Ghilardi, S. Midollini, A. Orlandini, Inorg. Chim. Acta 184 (1991) 141.
[23] F.L. Jiang, L.G. Huang, X.J. Lei, H.Q. Liu, B.S. Kang, Z.Y. Huang, M.C. Hong, Polyhedron 11 (1992) 361.
[24] N.A. Sanina, Chuev, II, S.M. Aldoshin, N.S. Ovanesyan, V.V. Strelets, Y.V. Geletii, Russian Chemical Bulletin 49 (2000) 444.
[25] D. Sedney, W.M. Reiff, Inorg. Chim. Acta 34 (1979) 231.
[26] E. Furet, A. Lebeuze, J.F. Halet, J.Y. Saillard, J. Am. Chem. Soc. 116 (1994) 274.

Chapter 5
Conclusions

The data presented in this thesis provide information about formation, electronic properties and coordination of a variety of metal iron sulfur clusters, in order to understand better the chemistry of this important class of molecules, which are found broadly in minerals and biological systems.

The common theme observed from these studies is that the structural diversity of these clusters derives from the kinetic lability of iron, which leads to fragmentation of the clusters in solution and subsequent rearrangements of the structures. This process is to a large extent dependent on the exact conditions of the experiment performed and consequently, is to some extent unpredictable. In the last forty years of research on iron sulfur cluster chemistry, synthetic chemists have relied heavily on trial and error methods, varying reagents and conditions slightly and observing the obtained products. To a large extent these methods have provided excellent results with the majority of the known structures of iron sulfur clusters obtained from simple monomeric compounds of iron and sulfur. Of course, after so many years of studies some synthetic aspects are now understood and to some extent the products obtained can be predicted, when using established methods developed by other researchers. Thus, even more new and exciting compounds can now be obtained. The synthetic processes described herein are no exception; they provide information about the utility of different reagents that have

specific characteristic properties, expanding the toolbox for future synthetic chemists in the quest for new compounds. Such methodology can be used either for the synthesis of model compounds for naturally occurring clusters, or as building blocks for new materials with interesting properties.

In particular, the iron sulfur clusters presented in chapter 2 expand significantly the family of iron sulfur nitrosyl clusters. Up to date the known iron sulfur nitrosyl clusters, were derivatives of three [Fe-S] core structures; the dimeric [Fe_2S_2], the cubic [Fe_4S_4] and the sulfur voided cubic [Fe_4S_3]. In this work, the prismatic [Fe_6S_6] and the cuboctahedral [Fe_8S_6] cores have been synthesized and characterized, and the yet elusive chair-like edge fused dimer of dimers $[Fe_4S_4(NO)_6]^{2-}$ has been observed, although not synthesized in a reproducible manner in this work. Nevertheless, these results can provide some direction for future work in order to obtain this new iron sulfur chair-like cluster core structure. This work also provides some insight into what can possibly happen in solution and how these clusters were formed.

From a biological perspective, both iron sulfur clusters and nitrosyl compounds are of extreme importance in almost all biological processes. Therefore, the synthesis of new iron sulfur nitrosyl clusters is essential for understanding the interactions of these two biologically significant molecules. It cannot be claimed that the clusters synthesized in this work are direct models for the interaction of nitric oxide with iron sulfur proteins; nevertheless, these clusters can provide valuable insights for some aspects of this biologically important compounds. For instance, the electronic structure of iron sulfur nitrosyl clusters has not been unequivocally established. Up to date, the biologically important $\{Fe\text{-}NO\}^7$ and $\{Fe\text{-}NO\}^8$ configurations have been mainly examined only for six and five coordinated geometries, as models for the interaction of heme molecules with

nitric oxide. The elucidation of the electronic configuration for these geometries relied on the vast amount of model compounds available, as the theoretical models were fine-tuned over the years to support the experimental observations. As a result, the interaction of nitric oxide with heme containing proteins is well understood. In terms of oxidation states for iron and nitric oxide, the current consensus for five and six coordinated $\{Fe\text{-}NO\}^7$ systems is that they are better described as Fe(III)/NO^- systems.

For four coordinated complexes, theoretical calculations have predicted that for $\{Fe\text{-}NO\}^7$ and $\{Fe\text{-}NO\}^8$ systems, the Fe-NO bond should be linear and that nitric oxide is most likely better described as NO^-. These predictions were supported however by a limited number of model compounds, and in this work we have provided additional experimental evidence supporting the linearity of the Fe-NO bond in $\{Fe\text{-}NO\}^7$ and $\{Fe\text{-}NO\}^8$ systems. More importantly however, this work has provided solid evidence to support the assignment of nitric oxide as NO^-. Up to date, there were only a handful of complexes studied and especially for Mössbauer studies, the assignment of nitric oxide as NO^- was dubious. With the series of clusters reported in chapter 2, for which different formal oxidation states were accessed, the Mössbauer spectra reveal a trend similar to the trends reported for iron sulfur clusters with thiols and halogens, and therefore, the assignment of nitric oxide as NO^- is the most accurate description.

At this point it should be noted that although there has been a tremendous amount of work on elucidating the compound formed upon interaction of nitric oxide with iron sulfur proteins such as aconitase and endonuclease III, there is no concrete evidence about its structure, because no crystal structures of this adduct have been obtained by protein crystallographers. Based on the spectroscopic observation of the characteristic g=2.04 EPR signal, and the similarity with known iron sulfur compounds containing

{$Fe(NO)_2$} units, the consensus is that interaction of nitric oxide with iron sulfur clusters provides a cysteine ligated dinitrosyl iron complex (DNIC). This adduct initially was thought to be a soluble compound derived from iron abstraction, although there are indications that the cluster remains bound to the protein. Other data suggests that heme proteins can also form adducts with the same signal. There are only a handful of known four coordinated iron nitrosyl clusters for the biologically important {$Fe(NO)\}^7$ and {$Fe(NO)\}^8$ units. These are two monomeric iron compounds with thiols and the two $[Fe_4S_4(NO)_4]^n$ (n=0,1) clusters. The work presented here has expanded this family to an additional three compounds that are EPR silent and therefore, cannot provide information about the observed EPR signal. Interestingly, though, the $[Fe_8S_6(NO)_8]^{2-}$ cluster exhibits a weak g=2.00 EPR signal, which is believed to be the result of dissociation of the cluster in solution. This dissociation in solution has been suggested by the electrochemical experiments presented as well, although the nature of the product that forms is yet to be determined. However, these results can be potentially associated with the EPR signal observed in biological systems raising the question if DNIC's are the only possible sources of this signal. It would be interesting to see in future studies more iron sulfur nitrosyl clusters, especially asymmetrical clusters containing nitrosyl and thiol ligands that can confirm or refute the assignment of DNIC's as the source of the g=2.03 EPR signal.

In chapters 3 and 4, compounds of mixed metal clusters are presented. The synthetic routes employed in the synthesis of the clusters provides information about the possible fragments that form these clusters and also provides some good models for the naturally occurring pentlandites, for which the exact positioning of nickel and iron are not known.

The different arrangements of the metals in the structures depends to a great extent on the metal used, which can initiate some investigation on what are the exact properties of the heterometals that define the different structural arrangements and a more detail analysis on the electronic structure of these clusters based on the spectroscopic data obtained. Again, prior to this work, there were only a few known mixed metal clusters of the pentlandite core, and their properties have not been thoroughly investigated, limiting the data available for theoretical analysis. The most important feature of these clusters, besides the systematic synthesis that enables the extension of the pentlandite family to even more metals, is their potential use as building blocks for the synthesis of extended lattices.

Extended lattices of metals are important in materials science and can be used for several applications. These can include semiconductors, nanowires, and most importantly heterogeneous catalysts for several industrially important reactions. The use of iron sulfur clusters as building blocks for extended networks is intriguing due to the unique properties of clusters opposed to single metallic centers. These include the more rapid electron transfer within a cluster and their ability to perform multi-electron redox reactions. The six electron conversion of dinitrogen to ammonia and the two electron conversion of protons to dihydrogen are of great importance for humans. While the known industrial methods of production of these molecules are extremely energy consuming, Nature, produces these molecules with considerable less energy utilizing metal sulfur clusters. The success of Nature in these conversions is due to the fact that metal sulfur clusters are capable of delivering two electrons almost simultaneously unlike single metallic centers. Therefore, the use of clusters as building blocks, instead of single metals, can provide us with catalysts that are much more efficient electron donors,

making the whole industrial production of ammonia and dihydrogen, less energy consuming process.

The work done so far has shown that different metallic compositions can be obtained in a systematic way, with the use of a variety of metals. These different metals affect the reduction potentials and magnetic properties of the clusters, as shown by electrochemical and magnetic studies. In addition, Mössbauer studies indicate a complete delocalization of electron density throughout the metals, which is a property that facilitates fast electron transfer. Therefore, although it is not possible to predict what the properties of materials formed by polymerization of these clusters will be, the chemical features of these clusters makes them good candidates for such investigations.

The comparison of the M/Fe/S/Cl and the M/Fe/S/NO clusters (chapters 3 and 4 respectively) as potential building blocks, shows that the chloride analogues have slightly better synthetic advantages. M/Fe/S/Cl clusters are more easily obtained than the nitrosyl analogues, and can provide a larger variety of structures because both phosphines and chlorides are more easily replaced from the coordination sphere of the metal than nitrosyls. However, the nitrosyl analogues exhibit a slightly better stability with respect to redox chemistry because they have a much larger window of reversible potentials, as demonstrated by electrochemical studies. This stability of M/Fe/S/NO clusters might also be important, from a synthetic point of view, for any future work towards extended lattices as well. As it has been shown throughout this work, and in line with the previous knowledge of iron sulfur chemistry, the lability of iron sulfur clusters in solution has to be taken into account. Therefore, in any attempts to synthesize extended networks from clusters, caution must be taken in order not to compromise the structural integrity of the

clusters that would lead to almost complete loss of the interesting properties that these clusters have.

Appendix 1
Structural Characterization of $(PPN)_3[Fe_8S_6(NO)_8]$

The crystal structure of $(PPN)_3[Fe_8S_6(NO)_8]$ had been obtained from a reaction of one equivalent of $(PPN)_2[Fe_8S_6(NO)_8]$ with 4.5 equivalents of K(anthracenite) and 6 equivalents of NaN_3, in DMF. The reaction was stirred overnight and layered with ether affording a mixture of crystals and powder. The IR of the crystals showed a peak at 2036 and the NO stretch at 1684. The first peak was due to contamination from the powder (small amounts on the surface of the crystals) as the results of the X-Ray showed.

Attempts to isolate this compound again were performed, however use of the same synthetic method is not optimal since it creates a mixture of a powder and crystals that are not easily separated.

The use of one equivalent of K(anthracenite) was attempted affording a powder, it was however not possible to determine the presence of this cluster beyond doubt, since the elemental analysis although in line with the $(PPN)_3[Fe_8S_6(NO)_8]$ formula it is also in line with a $K(PPN)_3[Fe_8S_6(NO)_8]$ cluster or a mixture of $(PPN)_3[Fe_8S_6(NO)_8]$ and $(PPN)_2[Fe_8S_6(NO)_8]$, and the lack of characteristic peaks in the IR makes the synthetic routes followed not suitable for synthesis of this clusters in bulk amounts and further spectroscopic characterization.

$(PPN)_3[Fe_8S_6(NO)_8]$	
Color	Black
Habit	Block
Size (mm)	0.14 x 0.24 x 0.58
Formula	$C_{108}H_{90}Fe_8N_{11}O_8P_6S_6$
Weight ($g \cdot mol^{-1}$)	2494.93
Crystal System	Triclinic
Space Group	P -1
Unit Cell (Å) (a,b,c, α,β,γ)	14.586(3)
	16.166(3)
	27.408(6)
	102.370(3)
	93.872(3)
	108.743(3)
Volume ($Å^3$)	5913(2)
Z	3
Temperature (K)	123(2)
Absorption coefficient	1.205
F(0,0,0)	2786
θ range (deg)	1.98 to 28.33
Reflections	29289
Limiting indices	-19 < h < 19,
	-21 < k < 21,
	-36 < l < 36
R_{int}	0.0374
Data / restraints / parameters	29289 / 0 / 1465
R_1, wR_2 [I>2σ(I)]	0.0397, 0.1000
R_1, wR_2 (all data)	0.0539, 01102
GooF (F^2)	1.017

TableA1.1. Crystallographic and refinement data for $(PPN)_3[Fe_8S_6(NO)_8]$

Appendix 2
Synthesis of dimers $(Et_4N)_2[(mida)(O)MoS_2FeCl_2]$ and $(Et_4N)_2[(tdga)(O)MoS_2FeCl_2]$.

The synthesis of these dimers $(Et_4N)_2[(mida)(O)MoS_2FeCl_2]$ and $(Et_4N)_2[(tdga)(O)MoS_2FeCl_2]$ (mida= methylimminodiacetic acid, tdga= thiodiglycolic acid) was performed in order to use as building blocks for the synthesis of $[MoFe_3S_4]$ and $[Mo_2Fe_6S_8]$ clusters containing a dicarboxylate coordinated to the molybdenum that approximates better the coordination site of Mo in the FeMoco cluster of nitrogenase. The compound $(Et_4N)_2[(mida)MoFe_3S_4Cl_3]$ [1] was known but obtained through a different route which required more steps. These two clusters were made in order to obtain clusters of this type using the reductive coupling method developed in our lab [2].

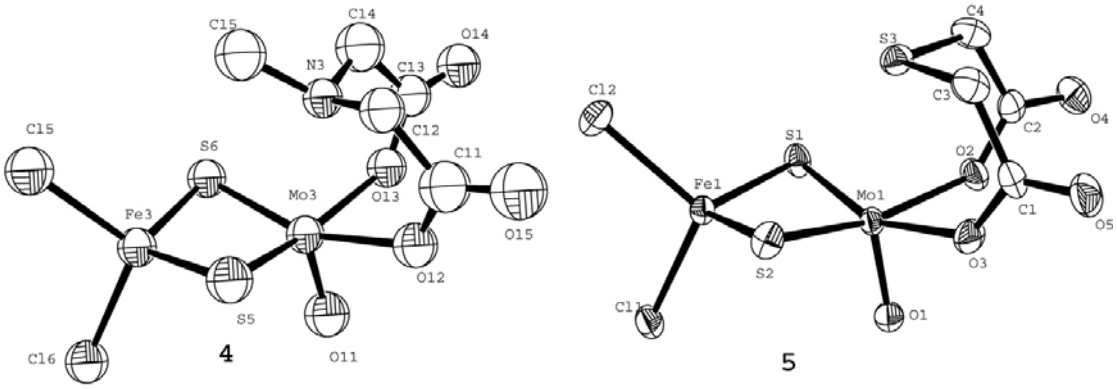

Figure A2.1. Ortep diagrams of $[(mida)(O)MoS_2FeCl_2]^{2-}$ and $[(tdga)(O)MoS_2FeCl_2]^{2-}$ with 50% probability.

The initial synthesis of these clusters were obtained in good yields from the reaction of $(Et_4N)_2[O_2MoS_2FeCl_2]$ with one equivalent of the carboxylate ligand. The

second step involving the reductive coupling of the Mo-Fe dimer with $(Et_4N)_2[Fe_2S_2Cl_4]$ did not provide the desired results.

With the use of phosphines as a reducing agent, in different stoichiometries resulted in the removal of the polycarboxylate from the molybdenum coordination as it was observed in the IR by the loss of the characteristic peak at ~ 1670 cm^{-1}.

The use of Et_4NBH_4 as a reducing agent for the reductive coupling, with $(Et_4N)_2[(mida)(O)MoS_2FeCl_2]$ provided a MeCN soluble powder that the IR showed the characteristics of $(Et_4N)_2[(mida)MoFe_3S_4Cl_3]$ although the elemental analysis was not identical to this product. Borohydride reductive coupling of $(Et_4N)_2[(tdga)(O)MoS_2FeCl_2]$ did not provide the same result as no polycarboxylate stretches were seen in the MeCN soluble fraction. IR of this product and cyclic voltammetry showed that the MeCN soluble product was $(Et_4N)_3[Fe_6S_6Cl_6]$, the product of reductive coupling of $(Et_4N)_2[Fe_2S_2Cl_4]$ on its own. Cyclic voltammetry of the product containing $(Et_4N)_2[(mida)MoFe_3S_4Cl_3]$ showed that the $(Et_4N)_3[Fe_6S_6Cl_6]$ was present as well and that the powder was a mixture of these two compounds.

Further studies on this system were abandoned as the desired product containing a $[Mo_2Fe_6S_8]$ core was not obtained, and this route for obtaining $[MoFe_3S_4]$ cubes did not provide an easier route of synthesis.

Experimental

$(Et_4N)_2[(mida)MoOFeS_2Cl_2]$ (4) In 20 ml DMF 1.5 g $(Et_4N)_2[O_2MoFeS_2Cl_2]$ (2.59 mmol) and 0.39 g methyliminodiacetic acid (2.65 mmol) were dissolved and stirred for 4 h. The solution is filtered and the product is precipitated with ether. The resulting powder

is recrystallized from acetone and ether. Yield 1.60 g (87.4%). Crystals suitable for X-ray analysis were obtained by a second recrystalization from acetone/ether.

Elemental microanal. Calcd for $C_{21}H_{47}Cl_2FeMoN_3O_5S_2$ (708.44): C, 35.60; H, 6.69; N, 5.93. Found: C, 35.52; H, 6.56; N, 5.81. IR (KBr pellet, cm-1): 410 cm-1(w), 433 cm-1 (vs), 469 cm-1 (s), (vC=O) 1661 cm-1 (vs)¬, 1635 cm-1 (vs), 1368 cm-1 (s) (v Mo=O) 937cm-1(s), 904 cm-1(s), (vMo-S-Fe) 433 cm-1 (m). UV-Vis (MeCN): 236 nm (s), 280 nm (s), 322 nm (sh) 472 nm (w).

$(Et_4N)_2$[(tdga)MoOFeS_2Cl_2] (5) In 20 ml MeCN 1.5 g $(Et_4N)_2[O_2MoFeS_2Cl_2]$ (2.59 mmol) and 0.39 g thiodiglycolic acid (2.60 mmol) were dissolved and stirred for 4 h. The solution is filtered and the product is layered with ether, affording crystalline material. Yield 1.70 g (92.4%).

Elemental microanal. Calcd for $C_{20}H_{44}Cl_2FeMoN_2O_5S_3$ (711.46): C, 33.67; H, 6.23; N, 3.94. Found: C, 33.79; H, 6.32; N, 3.99. IR (KBr pellet, cm-1): (vC=O) 1649 cm-1 (vs)¬, 1631 cm-1 (vs), 1324 cm-1 (vs) (v Mo=O) 935cm-1(s), 927 cm-1 (s), 919 cm-1 (s) (vMo-S-Fe) 431 cm-1 (m). UV-Vis (MeCN): 255 nm (s), 283 nm (s), 317 nm (sh) 473 nm (w).

$(Et_4N)_2$[(mida)Mo$Fe_3S_3Cl_3$] In 20 ml MeCN 1.0 g $(Et_4N)_2$[(mida)MoOFeS_2Cl_2] (1.41 mmol), 0.83g $(Et_4N)_2[Fe_2S_2Cl_4]$ (1.44 mmol) and 0.21 g Et_4NBH_4 (1.45 mmol) were dissolved and stirred for 5 min prior to the addition of 0.72 g $NaPF_6$ (4.29 mmol). The mixture is stirred for 4 h, filtered and layered with ether, affording 0.38 g (30 %) of $(Et_4N)_2$[(mida)Mo$Fe_3S_3Cl_3$].

IR (KBr pellet, cm-1): (vC=O) 1649 cm-1 (vs)¬, 1631 cm-1 (vs), 1324 cm-1 (vs) (v Mo=O) 935cm-1(s), 927 cm-1 (s), 919 cm-1 (s) (vMo-S-Fe) 431 cm-1 (m). UV-Vis (MeCN): 255 nm (s), 283 nm (s), 317 nm (sh) 473 nm (w).

X-Ray crystallographic Studies: Diffraction data were collected on a Bruker P4 X-ray diffractometer operated at 153 K, ($2\theta max$ = 46.80, 56.86 for **4**, and **5** respectively). The space groups Cc, Monoclinic for **4**, and Pca2(1), Orthorhombic for **5** were determined based on systematic absences and intensity statistics. Cell dimensions (Å, deg) are for **4**: a = 33.333(8), b = 25.624(6), c = 14.845(4) with $\alpha = \gamma = 90.00$, β = 93.413(4) and V = 12657(5) Å3, z = 16; for **5**: a = 12.901(3), b = 15.891(3), c = 14.777(3) with $\alpha = \beta = \gamma = 90.00$ and V = 3029.6(11) Å3, z=4. Full matrix least-squares refinement based on F2 converged to an R1 [$I > 2\sigma$] value of 0.0800, 0.0325 and a wR2 value of 0.2064, 0.0670, GooF 1.029, 0.666, **4**, and **5** respectively.

[1] K.D. Demadis, D. Coucouvanis, Inorg. Chem. 34 (1995) 436.
[2] J. Han, M. Koutmos, S. Al Ahmad, D. Coucouvanis, Inorg. Chem. 40 (2001) 5985.